INFORMATION TO USERS

This manuscript has been reproduced from the microfilm master. UMI films the text directly from the original or copy submitted. Thus, some thesis and dissertation copies are in typewriter face, while others may be from any type of computer printer.

The quality of this reproduction is dependent upon the quality of the copy submitted. Broken or indistinct print, colored or poor quality illustrations and photographs, print bleedthrough, substandard margins, and improper alignment can adversely affect reproduction.

In the unlikely event that the author did not send UMI a complete manuscript and there are missing pages, these will be noted. Also, if unauthorized copyright material had to be removed, a note will indicate the deletion.

Oversize materials (e.g., maps, drawings, charts) are reproduced by sectioning the original, beginning at the upper left-hand corner and continuing from left to right in equal sections with small overlaps.

Photographs included in the original manuscript have been reproduced xerographically in this copy. Higher quality 6" x 9" black and white photographic prints are available for any photographs or illustrations appearing in this copy for an additional charge. Contact UMI directly to order.

Bell & Howell Information and Learning
300 North Zeeb Road, Ann Arbor, MI 48106-1346 USA

UMI®
800-521-0600

ROOM TEMPERATURE INDENTATION OF MOLYBDENUM DISILICIDE

By

PAUL HENRY BOLDT, B.ENG

A Thesis

Submitted to the School of Graduate Studies

in the Partial Fulfillment of the Requirements

for the Degree

Doctor of Philosophy

McMaster University

ROOM TEMPERATURE INDENTATION OF $MoSi_2$

Doctor of Philosophy (1998) McMaster University

(Materials Science and Engineering) Hamilton, Ontario

TITLE: Room Temperature Indentation of Molybdenum Disilicide

AUTHOR: Paul Boldt, B.Eng (McMaster University)

SUPERVISOR: Professors G.C. Weatherly and J.D. Embury

NUMBER OF PAGES: xv, 210

ABSTRACT

The proposed use of molybdenum disilicide (MoSi2) in gas turbines can only be properly evaluated when mechanical property information is available for all temperatures that are encompassed in this application. Because molybdenum disilicide is brittle at room temperature special testing techniques are required to obtain deformation information at this temperature. An indentation test is one method of obtaining room temperature deformation information of brittle materials. Indentations were made on two surfaces of molybdenum disilicide single crystals at room temperature. The indentations were made with a range of applied loads and the indenter was aligned in two different orientations on each surface. The deformation and fracture produced by the indentations was studied with Scanning Electron Microscopy (SEM), Atomic Force Microscopy (AFM) and Transmission Electron Microscopy (TEM). The results from these analyses are discussed in terms of the micro-mechanisms of deformation and fracture and related to both the hardness and changes in applied load.

ACKNOWLEDGMENTS

There are many people to whom I owe gratitude for their help with this study. I would like to thank my supervisors Drs. G.C. Weatherly and J.D. Embury for presenting this topic and guiding me through the study. I would like to particularly thank Dr. Weatherly for his continued interest in my work and critical review of my experimental results throughout the length of my study.

I owe thanks to several people for helping with various elements of the work. First, I would like to thank Jim Garrett for the growth of the single crystals used in this study. Second, I would like to thank Dr. M. Niewczas for providing me with the image simulation program used in this study. I must also thank Marek for his insightful discussions and advice on TEM techniques. Third, I would like to thank Dr. M. Hawley of Los Alamos National Lab for her AFM work. Fourth, I would like to thank Dr. Y.P. Lin for his advice on TEM techniques and training on how to abtain useful information from the TEM.

I would like to pay particular thanks to Dr. Z.S. Basinski for his insightful advice and colourful discussions. Dr. Basinski gave me a glimpse of 'true' science and an unadultered pursuit of knowledge.

Finally, I would like to pay the largest thanks to Tamara McCaw who stuck by me all these years. Tamara helped me put life and the thesis in perspective. This work would not have been finished without her support.

One last word.....

"We who revel in nature's diversity and feel instructed by every animal tend to brand homosapiens as the greatest catastrophe since the Cretaceous extinction."

Stephen Jay Gould

Table of Contents

List of Tables

List of Figures

Chapter 1.0

Introduction

In the past several decades there has been a major initiative to use intermetallics as monolithic structural materials in aircraft turbine engines rather than as strengthening agents embedded in a metallic matrix, for example Ni_3Al or Ni_3Si in Ni based superalloys. This initiative required a large number of compounds be screened. Fleischer (1987) compared the melting temperature and specific gravity of nearly 300 intermetallic compounds with melting temperatures $\geq$ 1550 °C. Comparison of these two structure insensitive properties allowed promising candidates to be identified from a large number of compounds with different crystal structures. One of the early candidates to emerge from the screening process was molybdenum disilicide ($MoSi_2$).

In a review of molybdenum disilicide and molybdenum disilicide composites Vasudevan and Petrovic (1992) presented a compelling case for the use of $MoSi_2$ in aircraft engine turbine blades. They saw $MoSi_2$ as a primary candidate for use in the 1000-1600 °C temperature range because of its high melting temperature, excellent oxidation resistance and good retention of strength at high temperature. This temperature range is higher than that for existing Ni-based super alloys and is comparable to the operating temperature envisioned for silicon-based ceramics. $MoSi_2$ is more desirable than these ceramics because it is ductile at temperatures above 1300 °C (Aikin 1992) while offering comparable strength and oxidation resistance. However, before such a proposed use can be realized there is a need for basic data concerning all aspects of its mechanical properties. This understanding requires information on plasticity and fracture behaviour. A vital first

step towards an adequate knowledge of the mechanical properties is an understanding of deformation modes operative in single crystals. From this base one can move to the more complicated cases of deformation and fracture of polycrystals and composites.

Accurate mechanical property data can only be obtained from well characterized high purity material. Polycrystalline $MoSi_2$ samples are often obtained by the consolidation of $MoSi_2$ powder. These powders usually have a SiO_2 coating on their surface which produces a glassy layer along the grain boundaries during consolidation (Cotton, Kim and Kaufman 1992). This coating can drastically alter the high temperature mechanical properties. There is also some evidence of intergranular fracture in polycrystalline $MoSi_2$ because of this layer (Maloy, Lewandowski, Heuer and Petrovic 1992). The best way of avoiding these problems is through the use of single crystals which allow the mechanical properties to be studied without the complications brought about by grain boundaries and the possible impurities found there.

To date most mechanical property studies of $MoSi_2$ have used compression testing at temperatures above 1000 °C. One way of expanding the study of deformation to room temperature is through indentation testing. Indentation testing has been effectively used to study room temperature plasticity in materials that are brittle in tension at this temperature. The ability to produce plastic deformation with an indentation test at temperatures well below those possible during uniaxial tests, is a result of the stress state produced during the test. Material under an indenter is subjected to both very high shear stresses and large hydrostatic pressures. This large hydrostatic pressure suppresses brittle fracture, thus allowing plastic deformation in a zone both beneath and around the indentation.

Indentation testing has traditionally been used to determine the yield stress of brittle materials. The accuracy of this determination relies on the accuracy of the correlation between yield stress and measured hardness. Because the shape of the plastic zone produced during indentation determines which hardness-yield stress correlations should be

used, knowledge of the true shape of the plastic zone is critical. The plastic zone shape and yield stress correlation are reasonably well understood for large indentations in polycrystalline samples. However, the situation is much different for small indentations in single crystals of ceramics.

The goal of obtaining yield information from a single crystal is much more difficult as one now has to relate a macroscopic hardness value to the critical resolved shear stress on individual slip systems. Thus, the motion of individual dislocations has to be considered instead of an overall pattern of material movement. While a hardness-yield stress relationship is not a practical goal for single crystal tests, the controlled nature of the test allows other valuable information to be gathered. With a single crystal test the available slip systems which accommodate the indenter are known and one can then use this information to explore the slip-fracture relationship, slip system activity at stresses approaching the theoretical strength and material movement during the loading and unloading stages of the test. In this work by combining indentation techniques and single crystal specimens, information on the deformation and fracture of $MoSi_2$ at room temperature has been gathered.

Indentation techniques were used to study deformation for two orientations of $MoSi_2$ single crystals at room temperature. Neither of these orientations exhibit plasticity below 1000 °C when tested in compression. In all cases the indenter was aligned with either its edges or diagonals parallel to a low index direction and three microscopic techniques, Transmission Electron Microscopy (TEM), Scanning Electron Microscopy (SEM) and Atomic Force Microscopy (AFM) were employed to study the plastic zone. Through the use of these three techniques a complete picture of deformation during indentation has been formed. The slip system results obtained from this study were compared to those from high temperature compression tests and the differences considered in terms of both test temperature and the stress state operative under the indenter.

While indentation testing has been used to gather deformation information for $MoSi_2$, information concerning the nature of indentation testing was also gathered. This latter information arose from the non-cubic structure of $MoSi_2$ and the extensive use of TEM in this study. First, the tetragonal structure of $MoSi_2$ allowed indentation along either an axis with four fold symmetry, matching that of the Vicker's tip, or an axis with two mirror planes. This lower symmetry axis allowed one to differentiate between effects related to the symmetry of the indenter and ones related to the symmetry of the crystal. Second, TEM has not been extensively used to study indentations because the large strains and strain gradients produced by an indentation make it difficult to fully characterize the dislocations in the plastic zone. For this reason dislocation identity has often been inferred from a knowledge of the slip system. However, by reducing the size of the indentation many of the problems that reduce the effectiveness of TEM have been minimized and the deformation directly under an indentation was fully characterized. Thus, indenting single crystals of $MoSi_2$ has yielded information about slip system activity in $MoSi_2$ and the nature of indentation testing.

In Chapter 2 the relevant literature concerning $MoSi_2$ and indentation testing will be reviewed. The experimental procedure will be outlined in Chapter 3 and the results presented in Chapter 4. These results will be discussed in Chapter 5. It will be shown that the results of this study agree with both slip system observations in $MoSi_2$ single crystals that have been deformed at low temperatures, and with models of small indentations in single crystals. Conclusions drawn from this study will be presented in Chapter 6 and suggestions for future work are given in Chapter 7.

Chapter 2.0

Literature Review

The proper interpretation of mechanical property test data requires a thorough knowledge of the material being tested. Therefore the first literature to be discussed concerns the structure and physical properties of $MoSi_2$. Once the crystallography, basic physical properties and polymorphs of $MoSi_2$ have been outlined the basics of plastic deformation can be considered. These ideas will then be applied to $MoSi_2$. After these theoretical issues have been outlined mechanical testing results in the literature will be reviewed. The majority of plasticity information about $MoSi_2$ has been acquired through compression testing. Therefore, the results of these compression tests will be presented first. The results of the three previous indentation studies of $MoSi_2$ will then be presented.

The second area of importance is indentation testing. This literature will be divided into two groups: indentation of polycrystals and the indentation of single crystals. In the former group the deformation and fracture are controlled by macroscopic patterns of material movement i.e. the crystallography of the sample does not influence the accommodation processes. In the latter group, the indentation of single crystals, crystallography will be shown to govern all aspects of the material's response during an indentation test. In each of these sections, indentation of polycrystals and single crystals, the material's response will be considered in terms of elastic deformation, plastic deformation and fracture.

The final section of the literature review will consider the origins of plasticity and fracture during an indentation test. It is important to consider the initiation of these responses and how each develops in small volumes of material. These concepts are

important in understanding the development of a large plastic zone and fracture pattern from a volume of crystal that was initially void of defects.

2.1. $MoSi_2$

2.1.1. Physical Properties

In the search for materials that are suitable for aircraft engine applications Fleischer, Dimiduk and Lipsitt (1989) considered the intrinsic properties of melting temperature and specific gravity to be the most important parameters in the initial screening process. With a melting temperature of 2030 °C and a specific gravity of 6.34 $g.cm^{-3}$ $MoSi_2$ became an early candidate for further study. Some other important physical properties are shown in Table 2.1. $MoSi_2$ is a non-metal rich intermetallic compound in the Mo-Si alloy system (Figure 2.1) with a small solubility range on the Mo rich side. The six stiffness constants of $MoSi_2$ were measured by Nakamura, Matsumoto and Hirano (1990), using ultrasonic methods at room temperature. The measured constants are presented in Table 2.2. From their data Nakamura et.al. (1990) calculated that Poisson's ratio is 0.15.

Property		Reference
Resistivity (μΩ.cm)	(010) (001) ρ(273K) 16.9 12.6 ρ(4K) 9.6 9.2	Thomas, Senateur, Madar and Rasincher (1985)
Thermal Expansion Coefficient	a-axis $8.2x10^{-6}$/°C c-axis $9.4x10^{-6}$/°C	Thomas et.al. (1985)
Thermal Conductivity (W/m)	41-49	Shaffer (1964)
Heat Capacity (cal/g°C)	0.092	Shaffer (1964)

Table 2.1 Selected Physical Properties of $MoSi_2$.

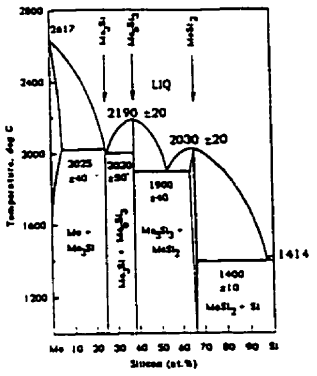

Figure 2.1 The Mo-Si phase diagram.

Constant	C11	C33	C44	C66	C12	C13
GPa	417	515	204	194	104	84

Table 2.2 Stiffness Constants of $MoSi_2$ (Nakamura et. al. 1990).

2.1.2. Crystallography

$MoSi_2$ can crystallize in either a tetragonal $C11_b$ or hexagonal C40 structure. The $C11_b$ structure is body centered tetragonal with space group I4/mmm (Figure 2.2) having Mo atoms at 0 0 0 and 1/2 1/2 1/2 and Si atoms at 0 0 1/3, 0 0 2/3, 1/2 1/2 1/6 and 1/2 1/2 5/6 (Pearson (1972)). It can be seen in Figure 2.2 that the $MoSi_2$ unit cell is composed of three sub-cells that have body centered symmetry. With lattice parameters: a=3.202 Å and c=7.851 Å $MoSi_2$ has a c/a ratio of 2.452. This c/a ratio is very close to the value of 2.449 which produces a perfect hexagonal arrangement of Si atoms around each Mo atom on the $\{110\}^*$ planes.

---

* In the current crystallographic notation { } denotes a family of planes, ( ) denotes a specific plane, < > denotes a family of directions and [ ] denotes a specific direction.

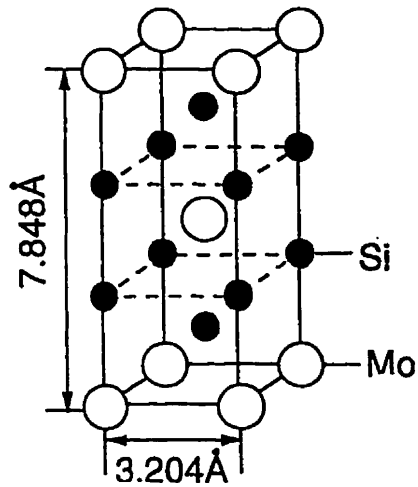

Figure 2.2 $C11_b$ unit cell of $MoSi_2$.

The $C11_b$ and C40 structures are related by the stacking sequence of {110} planes. Mo atoms in successive {110} planes rest at saddle points between Si atoms on the adjacent layer, Figure 2.3 (a). This results in four equivalent locations for stacking compared to three for {111} planes in the FCC case where subsequent layers rest in the valleys. For the tetragonal structure the stacking sequence is ABABAB while it is ABCABC for the hexagonal structure. Another possible stacking sequence, ADBCADBC, results in the orthorhombic, C54, structure which is not found in $MoSi_2$.

Movement from one Mo site to another requires a shear of $\frac{1}{4}\langle 111\rangle$ (Figure 2.3 (a)). One unit cell of the hexagonal structure can be produced from the tetragonal structure by moving an 'A' layer by $\frac{1}{4}[1\,\bar{1}\,1]$ and then moving the subsequent layer by $\frac{1}{4}[\bar{1}\,1\,1]$. Repetition of this sequence of shears will fully transform the tetragonal structure into the hexagonal structure. After a single $\frac{1}{4}\langle 111\rangle$ shear (the case of a stacking fault between two partial dislocations) there are four {110} planes where Mo atoms occupy each possible location i.e. **ABABCDCDCD**.

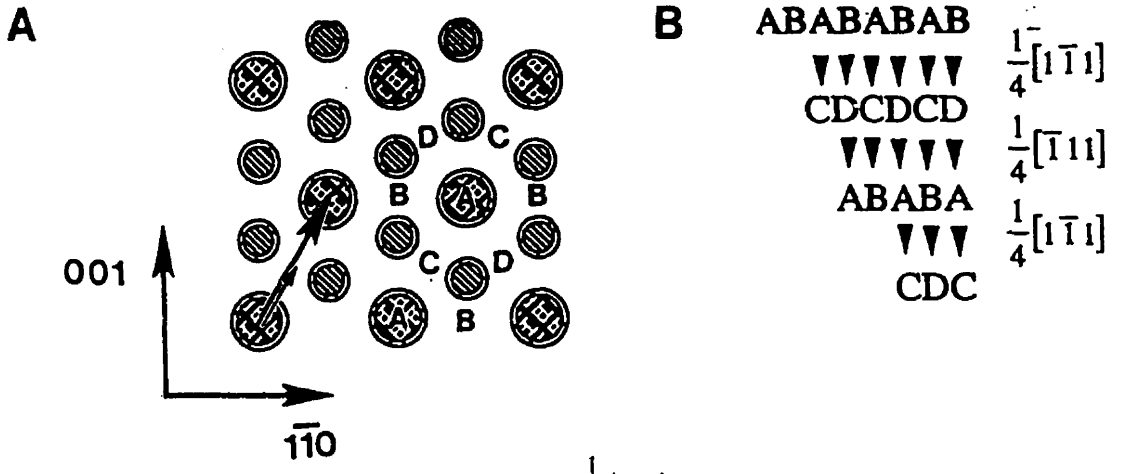

Figure 2.3 {110} plane of $MoSi_2$ showing a $\frac{1}{4}\langle 111\rangle$ vector and the possible Mo locations (a) and {110} stacking sequence after several $\frac{1}{4}\langle 111\rangle$ shears (b).

2.1.3. Polymorphs

There has been some discrepancy in the literature concerning the ranges of stability of the various polymorphs of $MoSi_2$, in particular, the temperature range over which the $C11_b$ and C40 phases are stable. It has been widely accepted that the $C11_b$ structure transforms to the C40 structure at 1900 °C (Svechnikov, Kocherzhinskii and Yupko (1970)). However, in a recent study of psuedo-ternary silicide phase diagrams Boettinger, Perepezko and Frankwicz (1992) found the $C11_b$ structure to be stable up to the melting temperature. The temperature ranges over which the various structures are stable has also been considered in studies of $MoSi_2$ for electronic applications.

There is a large body of research concerning the use of silicide films as interconnects in very large scale integrated (VLSI) circuits. Films with the correct stoichiometry were produced at low temperatures by either co-deposition of the elements or by reacting thin layers of each element to produce crystalline $MoSi_2$. van Ommen, Reader and deVries (1988) looked at the influence of microstructure on resistivity for films produced by both of these routes. They found that films annealed at 600 °C had the

hexagonal structure while those annealed at 900 °C were tetragonal. A similar result was obtained by de'Heurle, Peterson and Tsai (1980). Again only the tetragonal phase was present in samples annealed at 900 °C while there was only a trace of tetragonal phase found in samples annealed at 800 °C. It is interesting to note that this literature describes the hexagonal phase as the phase that is stable at low temperatures one while the mechanical properties literature considers the tetragonal polymorph to be the low temperature phase.

One might question the possible role of epitaxial stresses in the low temperature stability of the hexagonal phase. However, there are similar observations in plasma spray studies. For example, Alman, Shaw, Stoloff and Rajan (1992), in a study of plasma sprayed composites, found the hexagonal phase of $MoSi_2$ in both the as-sprayed case and after annealing at 700 °C. When the sample was annealed at 900 °C only the tetragonal form was present. Again the hexagonal phase appears to be formed at low temperatures and it is only when annealed at temperatures between 800 and 900 °C that the tetragonal phase forms.

2.1.4. Slip System Selection

The strength of a crystal is often several orders of magnitude smaller than the crystal's theoretical strength. This is due to the presence of dislocations. Glide of dislocations occurs on a plane (slip plane) that is defined by the Burgers vector (slip direction) and line direction of the dislocation. The first step in understanding the choice of these two elements is to look at a model of the theoretical shear strength. Frenkel (1926) modeled the shear stress required to move two planes past one another assuming a sinusoidal force.

$$\tau = k \sin \frac{2\pi x}{b} \qquad 2.1$$

where x is the displacement in the direction of shear, b is the repeat distance in the direction of shear (Burgers vector) and k is a constant equal to $\frac{Gb}{2\pi h}$ (G is the shear modulus and h is the spacing between adjacent planes). If it is assumed that the maximum stress occurs at x=b/4, equation 2.1 becomes

$$\tau_{max} = \frac{G|\mathbf{b}|}{2\pi h} \qquad 2.2$$

From equation 2.2 it is evident that a slip system which has a small $\frac{|\mathbf{b}|}{h}$ value will be favoured due to the lower value of τ_{max}. $\frac{|\mathbf{b}|}{h}$ values for several slip systems in $MoSi_2$ are presented in Table 2.3. The value of $\frac{|\mathbf{b}|}{h}$ is also an indication of the lattice resistance to the movement of dislocations. A large value of $\frac{|\mathbf{b}|}{h}$ indicates there is a large resistance to the movement of dislocations. This very simple analysis assumes non-directional bonding in the crystal. While the bonding in $MoSi_2$ has been shown to have limited directionality (Bhattacharyya, Bylander and Kleinman 1985), the above approach is still a good first step when looking at the choice of slip systems.

So far only dislocations with a perfect Burgers vector have been considered. Since the strain energy of a dislocation is directly proportional to the square of the magnitude of its Burgers vector any reduction in the length of the Burgers vector will significantly reduce the energy of the dislocation, as summarized by Frank (1949). Frank's rule states that a reaction or dissociation will take place if the square of the resultant Burgers vector is less than the sum of the squares of the reacting dislocations i.e. a reaction is favourable if

$$b_1^2 + b_2^2 \rangle b_3^2 \qquad \text{where} \quad b_1 + b_2 \Rightarrow b_3 \qquad 2.3$$

and a dissociation is favourable if

$$b_1^2 \rangle b_2^2 + b_3^2 \qquad \text{where} \quad b_1 \Rightarrow b_2 + b_3 \qquad 2.4$$

Burgers Vector	Possible Slip Plane	$\|\mathbf{b}\|$(Å)	Interplanar Spacing (Å)	$\frac{\|\mathbf{b}\|}{h}$
⟨100⟩	011 013 010	3.21	2.96 2.02 3.2	1.09 1.59 1.0
$\frac{1}{2}$⟨111⟩	110 101	4.53	2.26 2.96	2.0 1.53
$\frac{1}{2}$⟨331⟩	110 103	7.85	2.26 2.02	3.47 3.89
⟨001⟩	110	7.85	2.26	3.47

Table 2.3 $\frac{|\mathbf{b}|}{h}$ values for various slip systems in $MoSi_2$.

In the case of an ordered structure dissociation can create one of two stacking errors. If the stacking error produces an incorrect atom positioning with no order violation a Superlattice Intrinsic Stacking Fault (SISF) is produced. If, on the other hand, atoms are in the correct sites but the ordering is disrupted, an Anti Phase Boundary (APB) is formed. The separation of the dissociated dislocations (partials) will be determined by the balance between the repulsive force between partials and the attractive force, due to the surface energy of the fault created during the dissociation. Some of the theoretical dissociation reactions in $MoSi_2$ are presented in Table 2.4.

In Equation 2.2 it was seen that the stress required for slip varies inversely with interplanar spacing. Since interplanar spacing varies inversely with packing density, slip preferentially takes place on the most densely packed planes. In a material with an FCC

structure slip takes place on the close-packed {111} planes. However, the absence of close-packed planes in crystals with a BCC structure allows slip to take place on several different planes. This tendency towards multiple slip planes has been found in $MoSi_2$ (Unal, Petrovic, Carter and Mitchell 1990).

	REACTION	Fault Type	$\|\mathbf{b}_{initial}\|^2$	$\sum\|\mathbf{b}_{product}\|^2$
1.	$\frac{1}{2}\langle 111\rangle \Rightarrow \frac{1}{4}\langle 111\rangle + \frac{1}{4}\langle 111\rangle$	SISF	20.57	10.28
2.	$\langle 001\rangle \Rightarrow \frac{1}{3}\langle 001\rangle + \frac{1}{3}\langle 001\rangle + \frac{1}{3}\langle 001\rangle$	APB	61.62	20.54
3.	$\langle 001\rangle \Rightarrow \frac{1}{2}\langle 001\rangle + \frac{1}{2}\langle 001\rangle$	SISF	61.62	30.81
4.	$\langle 001\rangle \Rightarrow \frac{1}{2}\langle 001\rangle + \frac{1}{4}\langle 111\rangle + \frac{1}{4}\langle \bar{1}\,\bar{1}\,1\rangle$	SISF	61.62	25.68
5.	$\langle 001\rangle \Rightarrow \frac{1}{4}\langle \bar{1}\,\bar{1}\,1\rangle + \frac{1}{4}\langle 111\rangle + \frac{1}{4}\langle \bar{1}\,\bar{1}\,1\rangle + \frac{1}{4}\langle 111\rangle$	SISF	61.62	20.56
6.	$\frac{1}{2}\langle 331\rangle \Rightarrow \frac{1}{6}\langle 331\rangle + \frac{1}{6}\langle 331\rangle + \frac{1}{6}\langle 331\rangle$	APB	61.78	20.59
7.	$\frac{1}{2}\langle 331\rangle \Rightarrow \frac{1}{4}\langle 331\rangle + \frac{1}{4}\langle 331\rangle$	SISF	61.78	30.89

Table 2.4 Possible dissociations in $MoSi_2$.

2.1.5. Mechanical Testing

2.1.5.1. Compression Studies

The largest body of mechanical testing data is based on high temperature compression tests. Umakoshi, Hirano, Sakagami and Yamane (1989 a) conducted compression tests at 900 °C on single crystals of three orientations. Tests that were attempted at temperatures below 900 °C resulted in brittle fracture with no noticeable plastic strain. Slip traces were evident on samples deformed at 900 °C and, depending on the crystal orientation, the slip system was either $\{110\}\langle 331\rangle$or $\{013\}\langle 331\rangle$. They proposed that the $\frac{1}{2}\langle 331\rangle$ dislocations split into three collinear partials, separated by APB's according to the following reaction

$$\frac{1}{2}\langle 331\rangle \Rightarrow \frac{1}{6}\langle 331\rangle + \frac{1}{6}\langle 331\rangle + \frac{1}{6}\langle 331\rangle \qquad 2.5$$

It was further postulated that the partials may cross slip from $\{110\}$ to $\{013\}$ planes due to a lower APB energy on $\{103\}$ planes. However, the slip direction determination was based on optical slip trace results, casting doubt on the slip system determination.

Umakoshi, Yamane, Sakagami and Hirano (1989 b) looked at the nature of stacking faults created by the dissociation of $\frac{1}{2}\langle 111\rangle$ dislocations on $\{110\}$ planes according to the reaction

$$\frac{1}{2}\langle 111\rangle \Rightarrow \frac{1}{4}\langle 111\rangle + \frac{1}{4}\langle 111\rangle \qquad 2.6$$

A series of micrographs were presented (Umakoshi et.al. 1989b, Figure 3) to illustrate such stacking faults in a foil deformed at 1100 °C . However, neither the **g.R** nor **g.b** results were consistent . Further, it appears that the fault actually lies on (001) not (110) (Umakoshi et.al. 1989b, Figure 3.e).

Kad, Vecchio, Bewlay and Asaro (1994) studied the character of extended stacking faults seen in as-grown single crystals of $MoSi_2$. The authors identified the displacement vector of the faults to be $\frac{1}{6}[001]$. Such faults were attributed to the loss of a Si layer in the (001) sequence of Mo and Si layers during crystal growth. The loss of Si is a well known occurrence during crystal growth. After examining the results presented by Umakoshi et.al. (1989b) the authors suggested Umakoshi et.al. (1989b) were observing the same $\frac{1}{6}[001]$ growth fault. With this explanation the inconsistencies in the **g.R** and **g.b** analysis stated above disappear.

Recently, Kad Vecchio and Asaro (1995) studied stacking faults in plasma sprayed polycrystals and single crystals that were grown at either 1 or 30 $cm.h^{-1}$. The authors found the stacking faults in the plasma sprayed material had displacement vectors equal to $\frac{1}{4}\langle 331\rangle$ and $\frac{1}{2}[001]$. Since these faults were only found in unannealed samples the authors postulated that these faults were metastable. Furthermore, they proposed possible dissociation reactions for each of the observed stacking faults. The fault with $\mathbf{R}=\frac{1}{2}[001]$ resulted from the dissociation

$$[001] \Rightarrow \frac{1}{4}[1\bar{1}1] + \frac{1}{2}[001] + \frac{1}{4}[\bar{1}11] \qquad 2.7$$

and the stacking fault with $\mathbf{R}=\frac{1}{4}\langle 331\rangle$ was a product of the dissociation of a $\frac{1}{2}\langle 331\rangle$ dislocation according to the reaction

$$\frac{1}{2}\langle 331\rangle \Rightarrow \frac{1}{4}\langle 331\rangle + \frac{1}{4}\langle 331\rangle \qquad 2.8$$

Reaction 2.8 was originally proposed by Evans, Court, Hazzledine and Fraser (1993). In single crystals that were grown at a growth rate of 1 $cm.h^{-1}$, Kad et.al. (1995) only

observed stacking faults with **R**= $\frac{1}{2}$ or $\frac{1}{6}[001]$ and there were no faults seen in crystals grown at the higher growth rate. They proposed that the faults in the single crystal were a result of Si loss during the growth process as described in their earlier study (Kad et.al. 1994).

Umakoshi, Sakagami, Hirano, and Yamane (1990) expanded their study of high temperature compression of single crystals to temperatures between 900-1500 °C. Again, they reported two slip systems, $\{110\}\langle 331\rangle$ and $\{013\}\langle 331\rangle$, depending on orientation, for crystals deformed at 900 °C. A **g.b** analysis for this Burgers vector was not presented. At temperatures greater than 1300 °C, dislocations with [100] and [110] type Burgers vectors were found. Finally, the authors proposed that $\langle 331\rangle$ type dislocations could cross-slip from $\{110\}$ to $\{013\}$ planes due to the lower APB energy on the $\{013\}$ planes. Two observations were presented as evidence for this event. First, circular defects (Umakoshi et.al. 1990, Figure 6 and 7) on $\langle 331\rangle$ type dislocations were said to be ellipsoidal faults formed by this cross-slip process. Second, a peak in the hardness versus temperature curve was reported at 800 °C (Umakoshi et.al. 1989 a, Figure 2) for the $\{013\}$ orientation. The authors attributed this peak to cross-slip of $\frac{1}{6}\langle 331\rangle$ partials. However, the valley to peak change in hardness in this curve is around 10 kg/mm^2 at a hardness of 450 kg/mm^2. Since no error bars were presented with the data the significance of the observed change in hardness at 800 °C is unclear.

Unal et.al. (1990) studied the deformation of hot pressed $MoSi_2$/ SiC composites using four point bend tests at 1200 °C. They found a large variation in dislocation structure from one grain to another. In grains with a low dislocation density, dislocations having $\langle 100\rangle$ Burgers vectors were commonly observed while grains with high dislocation

densities contained $\langle 100\rangle$, $\langle 110\rangle$ and $\frac{1}{2}\langle 111\rangle$ dislocations. All the dislocations were perfect. In grains with a high dislocation density the dislocations were often found in networks based on the following reactions

$$\langle 100\rangle + \langle 010\rangle \Rightarrow \langle 110\rangle \qquad 2.9$$

$$\frac{1}{2}[111] + \frac{1}{2}[\bar{1}1\bar{1}] \Rightarrow [010] \qquad 2.10$$

$$\frac{1}{2}[1\bar{1}1] + \frac{1}{2}[11\bar{1}] \Rightarrow [100] \qquad 2.11$$

The observation of perfect dislocations at elevated temperatures is in agreement with the results of Umakoshi et.al. (1990). Unal et.al. (1990) compiled an extensive list of slip planes and postulated that the abundance of slip planes could be a result of cross-slip at elevated temperatures.

Mitchell, Maloy and Heuer (1993) studied the compression of single crystals of three orientations: [001],[021] and [771]. Four slip systems: $\{013\}\langle 100\rangle$, $\{011\}\langle 100\rangle$, $\{1\bar{1}0\}\frac{1}{2}\langle 111\rangle$ and $\{0\bar{1}3\}\frac{1}{2}\langle 331\rangle$ were observed. At temperatures between 900 °C and 1000 °C most of the dislocations were dissociated. For example, in [021] and [771] samples, $\frac{1}{2}\langle 111\rangle$ dislocations were found to be dissociated according to Reaction 2.6. At higher temperatures (T=1300 °C) $\langle 100\rangle$ dislocations on $\{011\}$ planes were found to be dominant for the above two orientations. The $\frac{1}{2}\langle 331\rangle$ dislocations on $(0\bar{1}3)$ planes were dissociated according to Reaction 2.5, i.e. three co-linear partials separated by APB's were observed.

The authors also noted the very high strength of [001] samples at temperatures above 1300 °C. They noted that the Schmid factor is zero for many slip systems when stress is applied along [001]. At lower temperatures (<1200 °C) slip occurred on the $\{013\}\frac{1}{2}\langle 331\rangle$ system. However, at temperatures above 1200 °C this system is unavailable due to the decomposition of $\frac{1}{2}\langle 331\rangle$ dislocations. It was then assumed that the $\{123\}\frac{1}{2}\langle 111\rangle$ and $\{011\}\frac{1}{2}\langle 111\rangle$ slip systems were activated.

Evans et.al. (1993) studied compression of polycrystalline samples at 1400 °C. Both $\langle 100\rangle$ and $\frac{1}{2}\langle 111\rangle$ dislocations were found, with the latter being dissociated. This dissociation was found to take place according to Equation 2.6. From weak beam observations, a partial separation of 65 Å was determined, corresponding to a stacking fault energy of 261 $mJ.m^{-2}$.

Recently, Ito, Inui and Yamaguchi (1995) studied the compression of four orientations of single crystals: [0 15 1], [1 1 0], [2 2 1] and [0 0 1]. In contrast to other studies these authors found that crystals having the first three orientations could be plastically deformed at room temperature while [0 0 1] crystals could only be deformed at temperatures above 1300 °C. This latter temperature is higher than that reported by Maloy et.al. (1993). Five slip systems were observed: $\{1\bar{1}0\}\langle 111\rangle$, $\{011\}\langle 100\rangle$, $\{010\}\langle 100\rangle$, $(023)\langle 100\rangle$ and $\{013\}\langle 3\bar{3}1\rangle$. For those crystals displaying room temperature plasticity, there was an anomalous strengthening peak seen at intermediate temperatures with the exact range depending on orientation.

Many of the slip system observations of Ito et.al. (1995) agree with those of previous studies. $\{011\}\langle 100\rangle$ slip was present at all temperatures while $\{110\}\langle 111\rangle$ slip

was only operative above 300 °C. The ⟨111⟩ dislocations were dissociated according to Reaction 2.6. A weak beam analysis found the partials to have a separation between 44 and 68 Å, depending on whether the dislocation was in edge or screw orientation. {010}⟨100⟩ slip was only observed for [110] crystals that had been deformed at temperatures between 600-900 °C i.e. in the range of anomalous strengthening. While the authors note the absence of $\frac{1}{2}\langle 331\rangle$ dislocations on {110} planes, as reported by Umakoshi et.al. (1989 a.), $\frac{1}{2}\langle 331\rangle$ dislocations were seen on {013} planes for samples tested at temperatures between 300 and 1000 °C. $\frac{1}{2}\langle 331\rangle$ dislocations found in samples deformed above 1000 °C had a [100] line direction and the dislocations were absent in samples deformed at higher temperatures.

In all of the above studies $\frac{1}{2}\langle 331\rangle$ dislocations were not observed in samples deformed at temperatures above 1200 °C. The absence of $\frac{1}{2}\langle 331\rangle$ dislocations in samples tested at these temperatures appears to have been explained by Maloy, Mitchell, Lewandowski and Heuer (1993). These authors found {013}⟨331⟩ slip in samples deformed at 1000 °C with the dislocations having either a ⟨331⟩ or ⟨100⟩ line direction. When the line direction ,**u**, equaled ⟨331⟩ the dislocation remained intact while dislocations with **u**=⟨100⟩ were found to decompose according to the reaction

$$\frac{1}{2}\langle 331\rangle \Rightarrow \frac{1}{2}\langle 111\rangle + \langle 110\rangle \qquad 2.12$$

The fraction of $\frac{1}{2}\langle 331\rangle$ dislocations decreased with increasing temperature and none were seen at temperatures at or above 1200 °C. Thus, these dislocations are unstable at high temperatures explaining their absence in other work.

There now appears to be a consensus that $\frac{1}{2}\langle 331\rangle$ dislocations become unstable and dissociate at temperatures above 1100 °C (Maloy et.al. 1993, Ito et.al. 1995). This explains their absence in the high temperature studies of Unal et.al. (1990) and Evans et.al. (1993). Below 1100 °C $\frac{1}{2}\langle 331\rangle$ dislocations split into three co-linear partials separated by APB's (Mitchell et.al. 1993), supporting the suggestion of Umakoshi et.al. (1990). However, only Umakoshi et.al. (1990) report $\{110\}$ as a possible slip plane for $\frac{1}{2}\langle 331\rangle$ dislocations. All other studies have found that these dislocations lie on only $\{013\}$ planes.

The nature of $\frac{1}{2}\langle 111\rangle$ dislocations is not as clear. The first observations of $\frac{1}{2}\langle 111\rangle$ dislocations found they were not dissociated (Unal et.al. 1990 and Maloy et.al. 1992). Evans et.al. 1993, Mitchell et.al. 1993 and Ito et.al. 1995 observed that $\frac{1}{2}\langle 111\rangle$ dislocations were dissociated into two co-linear partials separated by a stacking fault.

Lastly, slip processes involving $\langle 100\rangle$ dislocations appear to be operative at all temperatures. Many studies (Unal et.al. 1990, Mitchell et.al. 1993, Umakoshi et.al. 1990 and Ito et.al. 1995) have found these dislocations to be the most abundant during deformation above 1200 °C. However, Ito et.al. (1995) found $\langle 100\rangle$ dislocations in samples deformed at temperatures as low as -100 °C.

2.1.5.2. Indentation Studies

Vahldiek and Mersol (1968) used indentation testing to gather hardness and slip system information for the various intermetallic phases in the Mo-Si system. The tests were conducted with both Knoop and Vickers indenters. For indentations on a (100) plane of $MoSi_2$ they found slip traces along [001]. They reported $\{100\}\langle001\rangle$ as the primary slip system and $\{110\}\langle001\rangle$ as the secondary slip system during indentation on an (001) plane. It appears that these slip plane and direction determinations were based on observations from a single surface, namely the plane of indentation. If this was the case the results have to be questioned as slip plane identification requires a two surface analysis while the slip direction is difficult to identify in the absence of TEM information. Since this study, there have been two other studies which have used indentation to study the mechanical properties of $MoSi_2$.

Umakoshi et.al. (1989 a) conducted hot hardness tests between 100 and 1200 °C for three orientations of $MoSi_2$ single crystals. The hardness versus temperature curves were found to follow similar trends (Figure 2.4): there was an initial rapid decrease in hardness followed by a plateau and subsequent decrease until a final plateau was reached at approximately 1050 °C. The (001) plane showed the highest hardness until 800 °C where the hardness dropped below that of the other two orientations. The authors noted that, for indentations on (001), many slip traces were seen along $\langle110\rangle$ directions and cracks were seen along $\langle100\rangle$ directions. There was no further microstructural analysis presented.

Maloy, Heuer, Lewandowski and Mitchell (1992) also studied hardness as a function of temperature. However, in this study the $MoSi_2$ was polycrystalline and TEM was used to study the dislocation structure around the indentations. For indentations made between 100 and 500 °C $\{011\}\langle100\rangle$ slip was observed with the dislocations cross-slipping

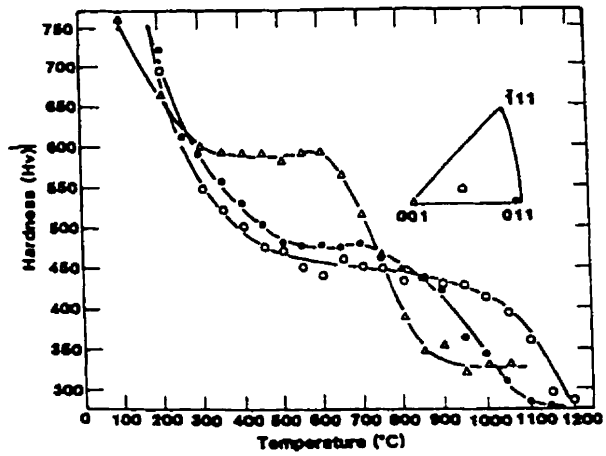

Figure 2.4 Hardness versus temperature for three orientations of $MoSi_2$ single crystals (Umakoshi et.al. 1989 a)

between (011) and $(0\bar{1}1)$ planes. They noted that the dislocations were very long and straight but did not identify their line direction. At higher temperatures, between 600 and 900 °C, both $\{011\}\langle 100\rangle$and $\{1\bar{1}0\}\frac{1}{2}\langle 111\rangle$ slip systems were active. Maloy et.al. (1992) noted that the $\frac{1}{2}\langle 111\rangle$ dislocations were perfect and had a $[1\bar{1}0]$ line direction. Also, in cases where both of the above slip systems were active reactions between the dislocations from these systems were observed i.e.

$$\frac{1}{2}[\bar{1}11]\Rightarrow[100]+\frac{1}{2}[111] \qquad 2.13$$

2.2. Indentation

Because of the diversity of conditions under which an indentation study can be conducted, it is important to divide the literature into groups, where studies within a group have been conducted under similar conditions. The most important demarcation is between tests on single crystals and polycrystals. The latter group contains any test that is not influenced by crystallography. This includes large indentations in fine grain polycrystals and amourphous materials. The other grouping contains indentation tests in which crystallography is an important factor. This includes tests on single crystals and large grain size polycrystals, if the indentation only samples a few grains. Indentation studies that have been conducted on polycrystalline samples will be considered first, since the most common notions about indentation testing result from tests on polycrystals.

The second important consideration is the geometry of the indenter, which can either be blunt or sharp. Blunt indentations are most commonly made with a spherical indenter. This geometry is attractive because the stress state produced during indentation has an analytical solution. However, a sphere is not self-similar. This implies that the stress and strain produced during indentation are functions of the indenter's penetration. On the other hand, sharp indenters produce self-similar indentations. The self-similarity of pointed indenters has made them more popular than spherical indenters, because the hardness from different tests can be readily compared. However, there is no analytical solution for the stress field produced by sharp indenters.

An indentation can be formed by a combination of elastic deformation, plastic deformation and fracture. The fraction of the total deformation provided by these three processes will be shown to be a function of the size of the indentation and the geometry of the indenter. For example, the fraction of elastic deformation increases with decreasing indentation size and with increasing bluntness of the indenter. Thus, the discussion of

indentations in single crystals and polycrystals will look at each of these modes of deformation.

2.2.1. Indentation of Polycrystalline Samples

2.2.1.1. Elastic Deformation

Elastic deformation during indentation of a polycrystal is most obvious during indentation with a spherical indenter. Hertz (1881) determined that such a contact will produce purely elastic deformation until the mean pressure over the circle of contact is equal to 1.1Y, where Y is the yield stress of the material. This well defined onset of plastic deformation occurs at a distance equal to $\frac{1}{2}$ the contact radius below the surface. With further increases in the applied load the size of the plastic zone increases until all of the material around the indentation has deformed plastically.

Theoretically, plastic deformation is instantaneous during indentation with a pointed indenter. There are no known examples of purely elastic deformation during indentation of a polycrystal with pointed indenters. However, it will be shown in the next section that a fraction of the total deformation can be elastic. This fraction increases as the ratio of Young's modulus divided by yield stress $\left(\frac{E}{Y}\right)$ decreases or the included angle of the indenter increases i.e. the indenter becomes blunter. Any deformation that occurs elastically will recover once the applied load is removed. The nature of this recovery was studied by Stilwell and Tabor (1961). They found that only the depth of the indentation changes when the load was removed. There were no changes in the in-plane dimensions, which implies that the included angle of the indentation was larger than the indenter. This

distinction between recovery of the depth versus the in-plane dimensions is important in the analysis of hardness measurements.

2.2.1.2. Plastic Deformation

The plastic deformation produced during indentation of polycrystals can be described by models based on either slip-line fields or the radial compression of an elastic plastic solid. Since the assumption of rigid-plastic deformation works well for many polycrystalline metals, slip-line fields have been quite successful in describing the movement of material away from an indentation in these specimens. However, it was found that this approach begins to break down when the included angle of the indenter is greater than 60° or when the material deviates from the rigid-plastic assumption. This latter condition occurs when $\frac{E}{Y}$ is below approximately 100. In these cases the radial compression models have been found to work reasonably well. Considerable effort has been put into the development of a relationship between hardness and yield stress for each model of deformation. Of particular concern has been the inclusion of the indenter geometry in this relationship.

Hill, Lee and Tupper (1947) used slip-line fields to describe the plastic deformation created by a wedge shaped indenter. By using slip-line fields to describe the plasticity the authors assumed the materials were rigid plastic and that there was no friction between the wedge and sample. They found that the normal pressure at the indenter face was given by

$$P_{normal} = 2k\left(1+\frac{\phi}{2}\right) \qquad 2.13$$

where ϕ is the included angle of the wedge and k is the maximum shear stress. Depending on the yield criterion used, Tresca or von Mises, 2k is either equal to Y or 1.15Y, respectively, where Y is the yield stress. A plot of P/Y versus wedge angle, assuming the

von Mises yield criterion, is shown in Figure 2.5. As $\phi \Rightarrow 0$ the hardness approaches Y while as $\phi \Rightarrow \pi$ (flat punch) the much quoted relationship H=3Y is reached. This model has been widely used to describe indentation with axially symmetric indenters. Experimentally, Hill et.al. (1947) found that the shape of the plastic zone predicted by slip-line fields was only accurate for sharp wedges i.e. the included angle is less than 60°. For larger wedge angles, deformation was observed under the apex of the wedge and the plastic zone began to show radial symmetry, neither of which are predicted by slip-line field theory. These deviations from the predictions of slip-line field theory prompted several studies of the influence of indenter geometry.

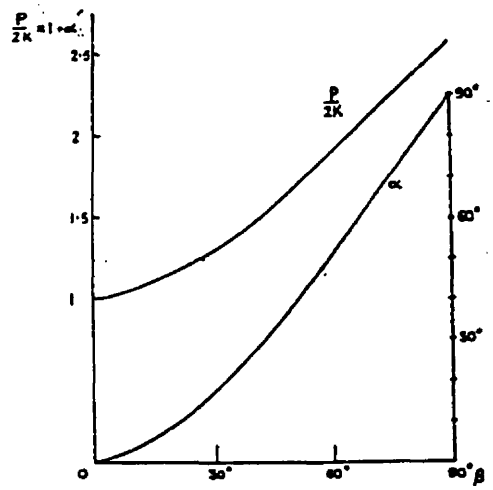

Figure 2.5 Variations of pressure (P) with wedge semi-angle (β). (Hill et.al. 1947)

Atkins and Tabor (1965) conducted an extensive series of cone indentation tests on copper and steel specimens with various amounts of work-hardening. They used cones with different included angles to explore how hardness varied with changes in the indenter angle. A plot of hardness versus cone angle for steel is shown in Figure 2.6. In the fully work-hardened case (top curve) the hardness fell to a minimum at a cone angle of 105°, increased to a maximum at an angle of 170° and then fell once again. As the degree of

work-hardening was reduced, the increase in hardness for indenter angles between 105° and 170° as also reduced, until the hardness continually decreased, with increasing angle, for the fully annealed case. Between 105° and 170° the curves looked similar to the calculated curve, from slip-line field theory (Figure 2.5).

Atkins and Tabor (1965) noted that the quantitative agreement with the predictions of the slip-line field theory was in contrast to the experimental observations which found the plastic zone was hemispherically shaped (Samuels and Mulhearn 1957 and Mulhearn 1959). Atkins and Tabor (1965) also noted

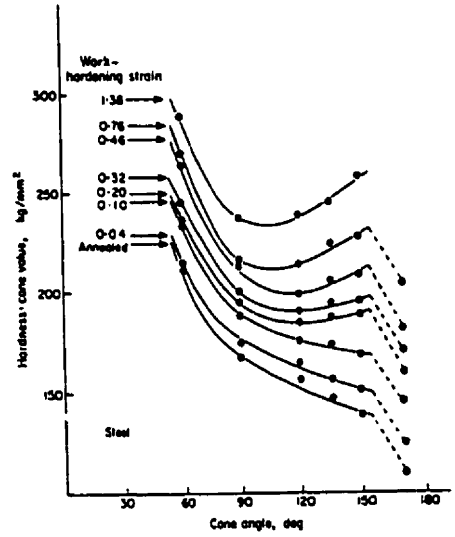

Figure 2.6 Hardness versus cone angle for indentations in steel. (Atkins and Tabor 1965)

that the sharp drop in hardness at a cone angle of 170° was likely due to the geometry of the indenter. The amount of plastic strain imposed by an indenter with this included angle is quite small, thus increasing the importance of any elastic deformation. As the material deviated from the ideal rigid-plastic assumption this decrease in hardness was found to occur at smaller indenter angles. Finally, the increase in hardness seen at small indenter angles was not predicted by slip-line field models.

The role of friction in hardness testing is not well understood. At small angles the indenter 'cuts' the material with considerable movement between the indenter face and the surface. Friction should be important in this regime. If this is the case, the observed hardness would increase because of the extra work necessary to overcome friction. This intuitive model appears to agree with the above experimental results.

Samuels and Mulhearn (1957) studied the size and shape of the deformed zone for Brinell and Vickers hardness impressions to investigate the deviations from rigid-plastic deformation seen by Hill et.al. (1947). Blocks of annealed 70:30 brass were bolted together and indentations made across the parting plane with unlubricated indenters. Etching techniques were then used to delineate the plastic zone. The indentations were at least one order of magnitude larger than the grain size to eliminate any influence of grain size. When indentations were made on a semi-infinite substrate the plastic zone was found to be almost perfectly hemispherical for both indenter geometries. Only in regions directly below the indenter did the strain patterns appear to be different for Brinell and Vickers indentations. Thus, the plastic zones created by blunt indenters were found to bear little resemblance to those predicted by slip-line field theory even when the material was nearly rigid-plastic.

To pursue these observations, Mulhearn (1959) studied the change in plastic zone shape as the indenter (wedge) geometry was changed from 40 to 80 to 136°. Deformation from the wedge with an included angle of 136° was compared to that from a Vickers pyramid indenter to investigate the importance of the plane strain assumption. Annealed 70:30 brass and cold rolled low carbon steel were tested. The low carbon steel was selected because of its better approximation to an ideal rigid-plastic material. In all tests the indenter was coated with high pressure lubricant.

No difference was detected in the deformation pattern for the 136° wedge and Vickers pyramid indenters. Thus, in this limit, large wedges and axially symmetric

indenters behave in a similar fashion. There was also little difference noted between the plastic zone shape found in the low carbon steel and the brass when indenting with a Vickers pyramid. However, the extent of deformation was greater in the brass (lower E/Y ratio). For the 40° wedge, deformation followed the rigid-plastic predictions but, as the wedge angle was increased, the plastic zone took on a more hemispherical shape until there was no evidence of flow along slip-lines for the 136° wedge. This series of experiments clearly showed how the plastic zone shape deviated from the predictions of slip-line field theory when the included angle of the indenter was increased. This was in contrast to the results of Atkins and Tabor (1965), who found close agreement between the measured hardness and that predicted by slip-line field theory, at similar indenter angles.

Marsh (1964) studied indentations in glass. After noting that the relationship, H=3Y, produced yield stresses below those obtained from other testing techniques, he developed a relationship between the pressure (P), which is equal to hardness, and Y for materials that deform in a radial fashion. He started with Hill's (1950) solution for the pressure needed in the expansion of a hemispherical cavity in an elastic-plastic medium:

$$\frac{P}{Y} = \frac{2}{3}\left(1 + \frac{3}{3-\lambda}\ln\frac{3}{\lambda + 3\mu - \lambda\mu}\right) \qquad 2.13$$

Here $\lambda=(1-2\upsilon)Y/E$ and $\mu=(1+\upsilon)Y/E$, Y = yield stress, E = Young's modulus and υ is Poison's ratio. This can be generalized and rewritten to give the more common expression

$$\frac{P}{Y} = C + KB\ln Z \qquad 2.14$$

where C and K are constants while B and Z contain the ratio Y/E. Marsh then indented numerous materials with a standard Vickers tip (136 °) and plotted the results as P/Y versus BlnZ, Figure 2.7. The agreement between the measured and calculated P/Y ratios was quite good over the wide range of materials tested. The plateau at large values of P/Y corresponds to the rigid-plastic regime. A transition from the radial compression model to

the rigid- plastic line (P/Y=3) is clearly seen when BlnZ =4, which corresponds to an E/Y value of 100. Thus, this approach of predicting the hardness-yield stress relationship appears to work well for blunt indenters.

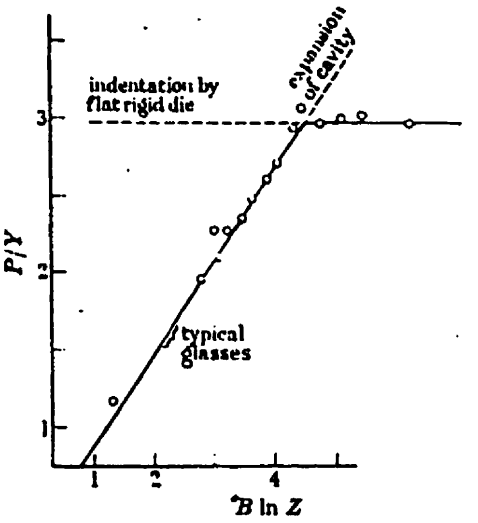

Figure 2.7 P/Y versus BlnZ for Vicker's indentations (Marsch 1964).

Hirst and Howse (1969) explored the affect of wedge angle on P/Y for six different materials. In this study all of the materials were fully work-hardened (where possible) and the indenter was lubricated before testing. E/Y ratios ranged from a high of 830 for lead to a low of 13 for nylon. The results of these experiments are shown in Figure 2.8. The experimental P/Y versus wedge angle curve for lead followed the same trends as the rigid-plastic (broken) line up to an angle of 150°, where the pressure dropped off. As the value of E/Y decreased, i.e. in more elastic materials, the angular range over which the P/Y curve resembled the predictions of slip-line field models decreased until the case of nylon, where there was no qualitative agreement. There are several points that arise from these results. First, even though lead has such a large E/Y value, deviations from rigid-plastic theory were seen at large indenter angles. This agrees with the results of Hill et.al. (1947) and Atkins and Tabor (1965). Once again, quantitative deviations from slip-line field theory

were seen at much larger indenter angles than the qualitative deviations seen in plastic zone shape. This discrepancy suggests that microstructural evidence of radial compression occurs well before it dominates the measured hardness. Second, the deviation from rigid-plastic theory depended on E/Y. As the material showed a greater degree of elastic deformation (low E/Y) the indenter had to be more acute for the rigid-plastic model to hold. These results are remarkably similar to those of Atkins and Tabor (1965) where the curve of P/Y versus indenter angle was altered, in a similar manner, by decreasing the amount of work-hardening.

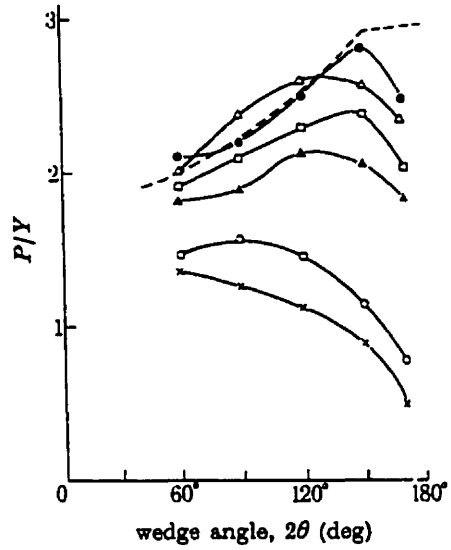

Figure 2.8 P/Y versus wedge angle for six different materials. (Hirst and Howse 1969).

Moreover, plastic deformation and hardness of polycrystalline samples can be adequately described by slip-line field models of deformation when the material approaches rigid-plastic behaviour $\left(\frac{E}{Y})100\right)$ and the included angle of the indenter is <150°. As the value of E/Y decreases the indenter angle where slip-line field models break down also decreases. In these cases the plastic deformation is more accurately described by models based on the radial compression of an elastic-plastic solid.

2.2.1.3. Fracture

Indentation cracking is probably the most unpredictable aspect of indentation testing. While cracking is relatively well understood for spherical indentation it is poorly understood for indentations made with pointed indenters. However, regardless of indenter geometry, crack formation requires a crack nucleus and a tensile stress to propagate the cracks nucleus. Crack formation during indentation with either a blunt or sharp indenter will now be considered.

The first study of cracks created during indentation with a spherical indenter was conducted by Hertz (1882). A detailed description of the formation of these cracks, and the nature of the stress field causing their formation was given by Lawn and Wilshaw (1975). They describe how the first crack to form is a ring crack, which forms at the edge of the contact region between the sphere and the surface. These authors noted that this is the location of the maximum tensile stress. This crack then forms a nucleus for the 'Hertzian' cone crack that grows into the material. Lawn and Wilshaw (1975) cited several studies of spherical indentations in single crystals where the shape of the cone was influenced by the crystallography. In his study, Hertz (1882), found that the stress required to initiate fracture varied significantly from sample to sample. This point can be understood by considering the work of Argon, Hori and Orowan (1960). These authors studied the formation of cracks in glass when the surface finish was varied. They found that the formation of cracks was directly related to the surface finish, with the stress required to form cracks varying with the distribution of Griffith flaws.

The situation is more complicated when the indentation is made with a pointed indenter. Lawn and Wilshaw (1975) pointed out that the stress field around a pointed indenter will always contain singularities and large gradients at points and edges, respectively. Such large stresses will result in plastic deformation. They stated that this deformation is often the source of crack nuclei. However, it can also impede the

propagation of cracks that have formed within the plastic zone. Lawn and Wilshaw (1975) stated that crack propagation requires that any crack nuclei that are formed during deformation are formed in a favourable location, with respect to the tensile stresses produced during indentation.

Cook and Pharr (1990) conducted an extensive study of indentation cracking using pointed indenters. Tests were conducted on both glass and crystalline materials. They found that the cracks that were formed could be described with reference to five basic crack geometries (Figure 2.9). It was found that the cracks in glass generally obeyed predictions based on the geometry of the stresses developed by a point contact (Lawn and Wilshaw 1975) i.e. cracks formed at locations of maximum tensile stress. However, the authors found that the cracks formed during indentation of crystalline materials were influenced by crystallography. In the end Cook and Pharr (1990) noted the absence of a general crack pattern that spans a wide range of materials.

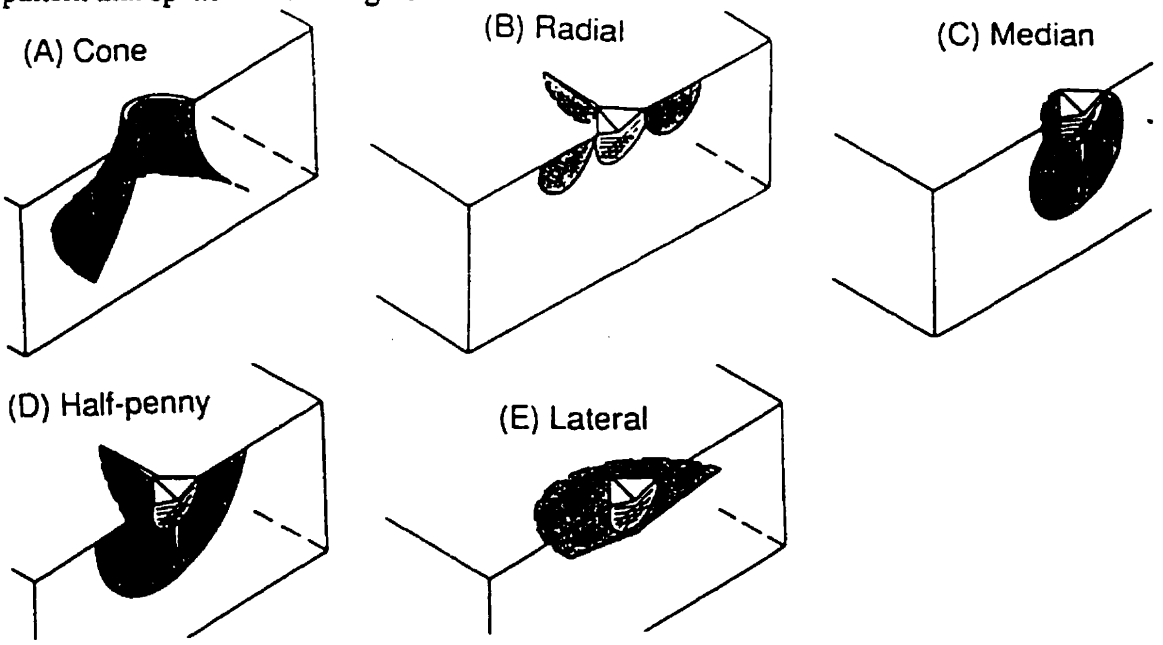

Figure 2.9 Five crack geometries commonly found during indentation of polycrystalline samples. (Cook and Pharr 1990)

2.2.2. Indentation of Single Crystals

2.2.2.1. Elastic Deformation

The strength of a solid is determined by the presence of and ability to move dislocations. In a well annealed metal the dislocation density usually lies between 10^{10} and 10^{12} /m^2. Using the lower density, the spacing between dislocations is around 10 μm. If a mechanical test could be performed within this spacing the test would be on an essentially defect free crystal. This is often the case during indentation of single crystals. When the indentation is smaller than the spacing between defects the crystal will deform elastically until the theoretical strength is reached and dislocations are nucleated. Therefore, elastic deformation can form a substantial fraction of the overall deformation during indentation of single crystals.

The nature of the indenter tip-surface contact can also affect the amount of elastic deformation before the onset of plasticity. As noted by Tabor (1951) the onset of plasticity should be instantaneous after contact of a geometrically perfect pointed indenter. However, pointed indenters often have a blunted tip. This will reduce the stress concentration at the tip which, in turn, delays the onset of plasticity. Contamination on the sample surface can also reduce the stress concentration. Gane (1970) noted that a higher load was required for indentation when a layer of polymeric contamination was present on the surface. Similar results were found by Pethica and Tabor (1979). They found that the hardness of a clean nickel surface was one quarter of the hardness that was found when there was a film on the surface. It appears that any surface film distributes the applied load over a larger area thereby reducing the stress. Moreover, considerable elastic deformation will take place if the stress concentration is reduced by a blunt indenter tip or a surface film.

Recently, Page, Oliver and McHargue (1992) demonstrated the importance of elastic deformation during indentation of single crystals. Single crystals of Al_2O_3, SiC and Si were indented with a Berkovich tip. The authors were able to record the load-displacement curves for each indentation. These curves were then compared to microstructural observations made with SEM and TEM techniques. Two load-displacement curves for (0001) faces of carefully annealed Al_2O_3 are shown in Figure 2.10. In Figure 2.10 (a) the loading and unloading curves are identical, indicating the deformation was completely elastic. There was no visible trace of this indentation when the sample was examined in either the SEM or TEM. If the applied load was increased above 15 mN the load-displacement curve showed a discontinuity in the loading cycle, Figure 2.10 (b). A residual impression was found on the surface during SEM observations. Strain contrast and very localized arrays of dislocations were seen during TEM analysis of indentations displaying this discontinuity. It appears that this discontinuity in the load-displacement curve is related to the nucleation of the first dislocations in this defect free volume.

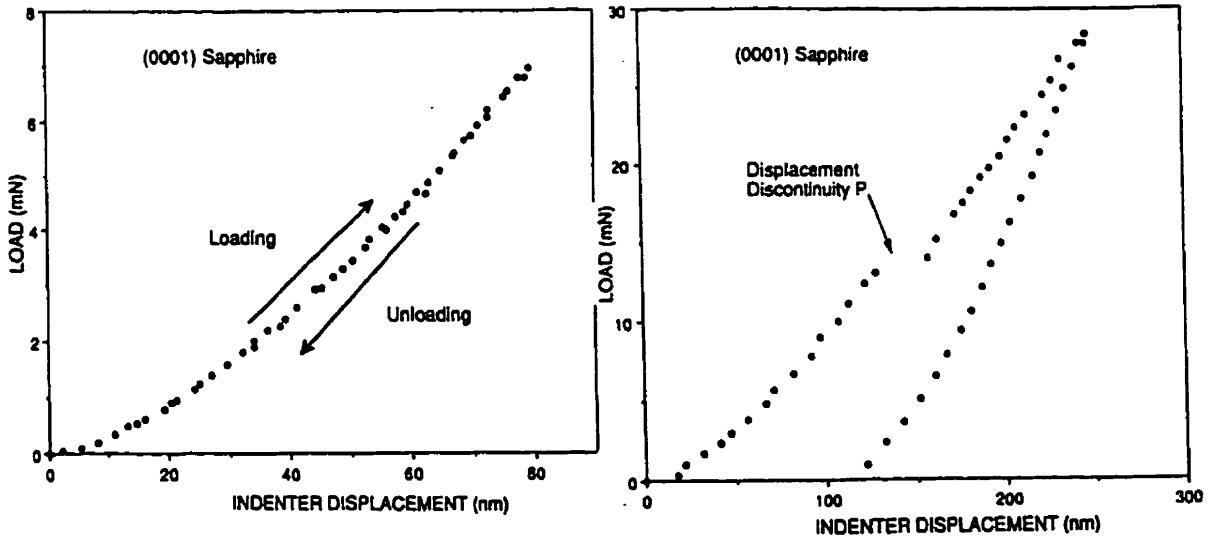

Figure 2.10 Load versus displacement curves for indentations made in sapphire. (a) shows purely elastic loading while (b) shows a mixture of elastic and plastic loading. (Page et.al. 1992)

There is another important point raised by the load displacement curve shown in Figure 2.10 (b). During the unloading portion of the curve there was substantial recovery in the indentation depth. The depth after the load has been removed was approximately one half of that at full load. This clearly shows that a substantial fraction of the total deformation of a small indentation, in a high yield stress material, can be elastic. Because of this large fraction of elastic deformation, which is recovered with load removal, it has been cited as the origin of Indentation Size Effect (ISE) in such materials. However, it is important to consider exactly how such recovery takes place.

Elastic recovery should be considered in terms of recovery of the depth and recovery of the in-plane dimensions. It is a simple matter of geometry to show that the depth recovery will not significantly alter the hardness. On the other hand, any recovery in the in-plane dimensions has a significant impact on hardness. It has often been assumed that only recovery of the depth takes place (Stilwell and Tabor 1961) but, this assumption is incorrect for single crystals. Sargent and Page (1985) pointed out that the amount of elastic deformation, and thus recovery, depends on the yield stress (Y_θ) and "effective modulus" (E_θ) in a given direction. They state that a direction with a higher yield stress will have a larger fraction of elastic deformation. Thus, the direction and magnitude of elastic recovery depends on the yielding characteristics along specific directions of the crystal.

2.2.2.2. Plastic Deformation

Plastic flow during indentation of polycrystalline material can be reasonably well described by either slip-line field or radial compression models (Section 2.2.1.2.). This is not the case for indentation of single crystals. Several questions must be answered to sort through the issue of plasticity in single crystals: What is the pattern of material movement ?

What number of slip-systems are required to accommodate an indenter ? and What effect do dislocation mobility and Peierls stress have on the previous two questions ?

In one of the earliest single crystal indentation studies Smakula and Klein (1949) indented crystals of Th(Br, I). Crystals were indented with a conical indenter having an apex angle of 80°. The experiments may be divided into two groups depending on the thickness of crystal being indented. In the first group of experiments, indentations were made in thick crystals (more than 10 mm thick), at regular intervals, along one of three paths. For example, in one series, indentations were made along a path from one cube face to another. When an indentation was made on a (100) plane, material was found to be piled up in the four ⟨100⟩ directions, reflecting the four fold symmetry of this axis. As the direction of indentation was moved away from [100], the piled up material lost this symmetry. The piled-up material was seen to have two fold symmetry for indentations along [110]. Once again it was symmetrical about the ⟨100⟩ directions. In the second group of experiments indentations were made along either [100], [110] or [111] directions in thin (a few millimeters thick) crystals. When this experiment was conducted along [100] a raised square of material was seen on the opposite face of the crystal. Prior to indenting along either [110] or [111] directions, the authors cut the opposite surface of the crystal to produce (100) facets. Indentations along [110] produced a raised square on each (100) facet, while three raised squares were formed during indentation along [111]. At the time this paper was written the authors were not able to provide an explanation for their results.

An interpretation using concepts from dislocation theory was later provided by Seitz (1950) and Nabarro (1950). Seitz (1950) explained the transmitted patterns in terms of [100] prismatic loops traveling along a glide cylinder bounded by {011} planes. The symmetry in the observed patterns reflected the number of [100] axes found around a given zone, e.g. two ⟨100⟩ axes inclined 45° to the [110] axis. Seitz postulated that these

prismatic loops were nucleated at Frank-Read sources on the glide plane. However, Nabarro (1950) pointed out that the loops might also be nucleated at the surface of the crystal.

In such a prismatic punching system the Burgers vector of the loop must be parallel to the axis of the glide column. This system is the simplest means of accommodating an indenter. Only one slip system is necessary as long as that system is able to move material freely along the axis of indentation, producing an outline of the indenter on the opposite face. However, this is only possible if the Peierls stress of this slip system is low enough that material can be moved the required distance without a pile-up forming along the glide column. In experiments on thicker crystals Smakula and Klein (1949) observed piled up material on the indented surface, indicating the activation of other slip systems when the crystal was too thick for the prismatic punching system to move material to the opposite surface. Thus, transmitted patterns are probably very rare as most materials do not contain both a suitable slip system and a suitably low Peierls stress.

Swain and Lawn (1969) used etch pitting techniques to study the dislocation activity around indentations, of various sizes, on (001) planes of LiF. LiF was chosen for study because of its anisotropy and limited slip systems. Indentation information could then be gathered for a group of materials where there is little knowledge of the indentation behaviour. Spherical indenters were chosen because of the mathematical tractability of the stress field. Nylon and steel indenters allowed a wide range of indentation strains to be produced. The observed deformation was divided into three categories: elastic, initial yielding and growth of the plastic zone. At the smallest loads only one slip system, $\{110\}_{45}$[†], was activated and slip activity was concentrated on one of four possible slip planes. It was determined that internal dislocation sources were activated, in agreement

[†] In this notation the subscript indicates the angle between the slip plane and sample surface

with the predictions of Hertzian theory. As the applied load was increased a second system, $\{110\}_{90}$, became active. Dislocation activity on the $\{110\}_{90}$ slip system was found to increase at a faster rate than activity on $\{110\}_{45}$. By the time the plastic zone became symmetrical dislocations on the $\{110\}_{90}$ system extended away from the indent into the crystal. It was noted that the $\{110\}_{90}$ slip system is not activated during compression tests (along [001]) as the resolved shear stress is zero on these planes for this orientation. The authors believed this discrepancy results from the complexity of the stress state during an indentation test. To summarize, it was found that dislocations were nucleated within the crystal and slip system activity was not independent of scale. These findings are quite different than the plastic flow characteristics of polycrystals discussed in Section 2.2.1.2.

A very comprehensive study of indentation plasticity in GaAs was undertaken by Hirsch, Pirouz, Roberts and Warren (1985). The extensive knowledge of slip systems and dislocations in GaAs was used by the authors to determine the nature of plastic flow during loading and unloading, to explain the observed differences in hardness between Ga and As faces and to explore the formation of cracks during indentation. Vickers indentations were made at several temperatures on {111} type Ga and As faces of GaAs. Once again etch pitting was used to reveal the dislocation structure around an indentation. However, instead of looking at a cross-section the authors removed specific amounts of material from the reverse surface and then re-etched it to reveal the pattern of cracks and slip traces at that position in the deformed volume.

An important result was the observation of reverse plastic flow after the load had been removed. Slip lines due to recovery were seen 5-10 seconds after the load was removed. The authors were able to explain the observed slip patterns with a model based on cross-slip. The compressive stresses present after indentation could be relieved by cross-slip of dislocations which were then free to create the observed reverse flow. This mechanism was proven correct by the slip line observations on both the Ga and As faces.

Another material that has received considerable attention is MgO. There have been several studies, using a variety of characterization techniques, that have demonstrated the importance of slip system knowledge in understanding indentations in single crystals. Armstrong and Wu (1974) looked at Vickers indentations made on (100) surfaces with SEM and X-ray diffraction microscopy. The SEM micrographs (Armstrong and Wu 1974, Figure 5) clearly showed the surface topography after indentation with the diagonals of the indenter either parallel to ⟨100⟩ or ⟨110⟩. In both cases three important features were found. First, long troughs extending into the crystal along ⟨100⟩ were observed. These troughs resulted from the movement of material into the crystal on $\{110\}_{45}$ planes via screw dislocations. The width of these troughs was found to be dependent on the orientation of the indenter in the plane of indentation. Troughs were as wide as the longest indenter dimension along ⟨100⟩, i.e. the trough was wider when the diagonals were aligned parallel to ⟨100⟩. Second, slip traces resulting from edge dislocations on $\{110\}_{45}$ planes formed a series of nested squares with edges parallel to ⟨100⟩.

Brown, Khan and Chaudri (1988) also looked at the deformation produced during indentation on (100) surfaces of MgO. In this study cathodoluminescence and high voltage TEM were used to study the indentations. These methods were chosen because they yield information from the deformed volume surrounding an indentation. An absence of luminescence in the centre of the indentation was attributed to the high defect density and a strain of at least 5% in this region. The HVEM study found rotations of approximately 10° around the [100] axis of indentation and rotations that brought other diffraction spots into the [001] pattern (Brown et.al. 1988, Figure 3). Unfortunately the authors were unable to carry out a complete dislocation analysis because of the high dislocation density and large strains around the indentation. After the foil was annealed at 900 °C for 1h, the rotations were no longer present and the dislocations that lay along ⟨100⟩ extended further into the

crystal. It was also observed that the cracks along [110], which were very visible before annealing were barely visible after annealing and cathodoluminescence was now seen under the indenter. These observations suggest that the large residual stresses and high dislocation densities produced during indentation were reduced upon annealing.

The above studies have demonstrated that plastic deformation created by indentation of a single crystal is both complicated and governed by crystallography. Both Smakula and Klein (1949) and Swain and Lawn (1969) found that different slip systems were activated at different stages of the indentation cycle and the former authors demonstrated that under certain conditions only a single slip system is required to form the indentation. The complexity of slip is well illustrated in the studies of indentation in MgO (Armstrong and Wu 1974 and Brown et.al. 1988). In the latter study it was determined that the dislocation density at the centre of the indentation is extremely high and this density is lowered with annealing.

2.2.2.3. Fracture

Just as the plastic deformation produced during the indentation of single crystals are dictated by crystallography so are the fracture processes. The patterns of fracture cannot be described by the models presented in Section 2.2.1.3. Two examples will be discussed. In their study of MgO Armstrong and Wu (1974) observed long cracks along ⟨110⟩ directions around indentations made on (001) surfaces (Armstrong and Wu 1974, Figure 5). When the indenter was aligned such that its diagonals were parallel to ⟨110⟩ directions the cracks appeared to be radial type i.e. they emanate from the diagonals of the indentation. However, when the indenter was rotated such that the diagonals of the indenter were parallel to [100] and [010] directions the cracks remain parallel to ⟨110⟩. This clearly indicates that the observed crack geometry was based on crystallography not

on the local stress state around the indenter which is the reverse of the situation presented in Section 2.2.1.3. A similar situation was found by Hirsch et.al. (1985) in their study of indentations in GaAs. Again the fracture pattern was not influenced by the orientation of the indenter. The only exceptions to this influence of crystallography might occur where there is an absence of crack sources for the particular orientation of indenter.

2.2.3. Development of Plasticity

In Section 2.2.2.2. it was shown that the shape of the plastic zone is a function of the active slip system. It is now important to consider why certain slip systems are activated during indentation and how plasticity occurs on these systems. The question of slip system activation is related to the distribution of stresses under an indenter while the development of the plastic zone can be considered in terms of plasticity processes in micron sized volumes of material.

In Section 2.2.2.2. it was shown that not all possible slip systems are activated during indentation. There are differences in both the timing of slip system activation and differences in the location of slip system activity i.e. a particular slip system might only be active directly under the indenter and not at the periphery of the plastic zone. This variation in slip system activity is a result of the distribution of stresses in the plastic zone. Thus, an important step in the understanding of plasticity created during indentation of a single crystal has been the determination of the resolved stresses on the available slip systems.

In their study of indentations in LiF, Swain and Lawn (1969) calculated the stress state under the indenter just before the onset of plasticity using the solution developed by Hertz (1881). The authors then resolved the shear stresses on to the $\{110\}_{45}$ and $\{110\}_{90}$ slip systems. They were able to show that the largest stresses were on the $\{110\}_{45}$ system, at the correct distance below the surface (according to Hertzian theory). This is in agreement with their experimental observations (Section 2.2.2.2). The situation is not as

well defined when a pointed indenter is used because there is no analytical solution for the stress state. In such cases approximations about the stress state must be made. In their study of indentation made in GaAs, Hirsch et.al. (1985) approximated the stress state of a Vickers indenter with the stress field of a infinitely long flat punch. The stresses were then resolved onto the appropriate slip systems. It was found that even this crude approximation of the stress state was able to explain the slip system observations. This demonstrates the importance of crystallography during the indentation of single crystals.

Another approach used to study the resolution of stresses on individual slip systems was developed by Brookes, O'Neill and Redfern (1971). The authors developed this method of resolving stresses to rationalize the anisotropy of hardness of single crystals. The geometry of this calculation is shown in Figure 2.11. The approach was based on the Schmid and Boas (1950) relationship for the resolution of a normal stress onto slip systems

$$\tau = \frac{F}{A}\cos\lambda\cos\phi \qquad 2.15$$

In Schmid and Boas' (1950) model the slip plane will rotate during deformation, In the case of an indentation test this rotation is constrained by the indenter and the surrounding elastic material. Daniels and Dunn (1949) considered this constraint in terms of the angle between the indenter facet and the axis of rotation of the slip plane. Brookes et.al. (1971) found that this single constraint could not describe the activity on all slip systems. They determined that a further constraint of the slip plane rotation was required. This constraint was based on the angle between the slip direction and the indenter facet. Their final equation for the Effective Resolved Shear Stress (ERSS) is

$$\tau = \frac{F}{A}\cos\lambda\cos\phi(\cos\varphi + \sin\gamma) \qquad 2.16$$

where λ, ϕ, ψ and γ are defined in Figure 2.11. It was found that this approach was able to give good qualitative agreement with their experimental results. Moreover, several

different approaches have been taken to explain the hardness and slip system observations in terms of the resolved stresses on the individual slip systems.

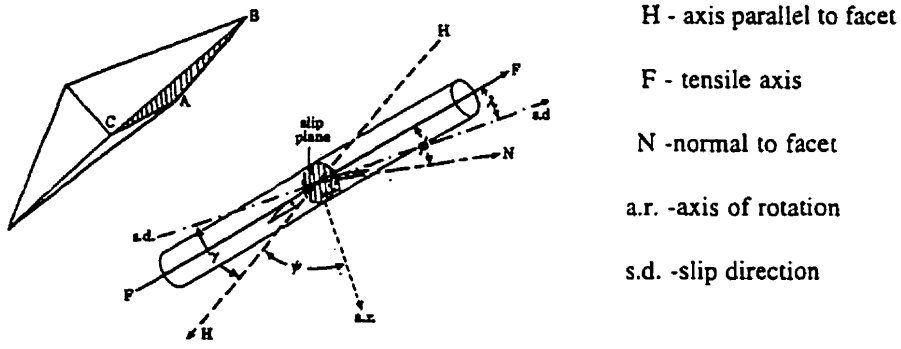

Figure 2.11 Schematic diagram showing the 'tensile' cylinder used to calculate the Effective Resolved Shear Stress. (Brookes et.al. 1971)

Dislocation generation and accumulation in micron size volumes was considered by Gane (1970) and Gane and Cox (1970). Gane (1970) conducted a series of in-situ (SEM and TEM) experiments where the volume of deformed material was below the spacing between dislocations in a well annealed crystal, which is approximately 10 μm. These experiments included: indentation, blunting of a soft metal tip against a hard surface, compression of spheres and bending of wires. There were several interesting points that arose from this study. Many of the experiments showed an increase in the stress required to deform the samples stress with decreasing volume of deformed material. This suggests that this behaviour is a function of the scale of deformation, and not a specific feature of indentation testing. Furthermore, this increase in stress occurred without any apparent work hardening.

In a related study Gane and Cox (1970) indented gold with a spherical tungsten tip. These experiments were also conducted in-situ in an SEM. The gold samples were in either an annealed or work-hardened state. The size of the indentation was varied from 0.5 mm to 0.2 μm, such that a large portion of the hardness versus applied load curve could be

studied. Furthermore, because a spherical indenter produces a strain that varies with penetration a stress strain curve of indentation could be plotted. There was no work hardening observed for the smallest indentations. For larger indentations there was no work hardening when the indented material was cold worked while the annealed specimens work hardened. When the authors plotted the hardness versus indentation size (corrected for the spherical geometry), Figure 2.12 it was found that the hardness increased with decreasing indentation size for both annealed and work hardened samples. Further, the point where this increase begins is the same in both conditions of starting material. Gane and Cox (1970) suggested this increase in hardness is independent of the original dislocation density. For this reason the authors proposed the increase in strength with decreasing size is a result of an increased stress required to operate dislocation sources at small sizes.

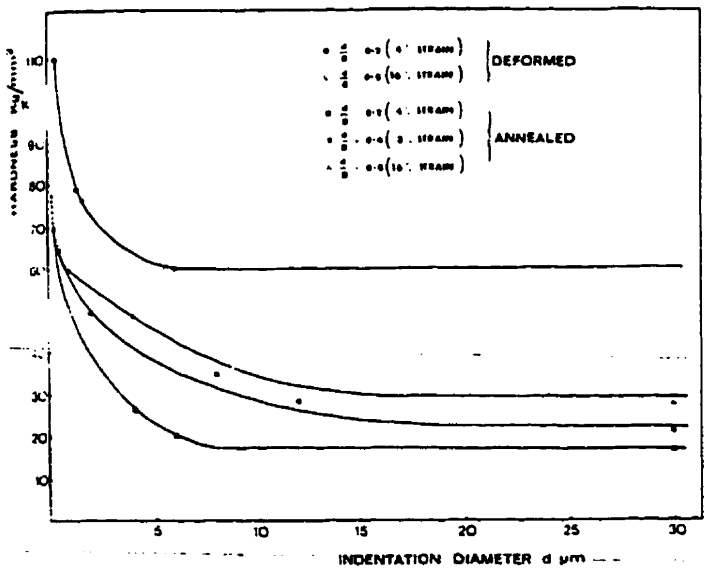

Figure 2.12 Hardness versus indentation diameter for indentations made in gold. (Gane and Cox 1970)

The above studies suggest that traditional concepts of work hardening are not applicable to micron size volumes of deformed material. Ashby (1970) states that

geometrically necessary dislocations can control work hardening when their density (ρ_G) exceeds the density of statistically stored dislocations (ρ_S). This occurs at small length scales as the density of geometrically necessary dislocations varies inversely with the length over which deformation takes place. Ashby (1970) described the density of geometrically necessary dislocations by

$$\rho_G \approx \frac{4\gamma}{b\lambda} \qquad 2.17$$

where γ is the macroscopic plastic shear, b is the magnitude of the Burgers vector and λ is the local length scale. Such scale dependent plasticity was recently discussed by Fleck, Muller, Ashby and Hutchinson (1994). Fleck et. al. (1994) presented a diagram showing ρ_G and ρ_S as a function of shear strain (Figure 2.13). It can be seen that for length scales below 10 μm ρ_G exceeds ρ_S over all strains. Thus, geometrically necessary dislocations probably control the hardness of small indentations.

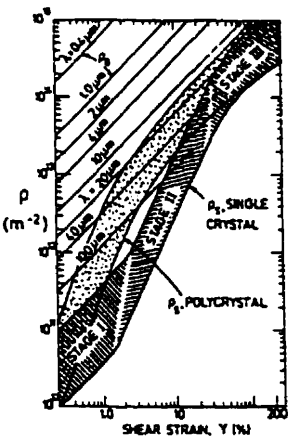

Figure 2.13 Dislocation density versus shear strain. Straight lines represent length scale of deformation. The hatched bands show experimental densities of statistically stored dislocations. (Fleck et.al. 1994)

A model of plastic flow around an indentation, based on geometrically necessary dislocations, was developed by Brown (1988). In this model the movement of material was modeled in terms of rotating blocks and the movement of these blocks was determined by geometrically necessary dislocations. The density of these dislocations was defined in terms of the indenter angle i.e.

$$\rho = \frac{\tan\beta}{bd} \qquad 2.18$$

where β is the angle between the indenter face and the surface, b is the Burgers vector and d is the indent dimension. Since β and b are constant any decrease in the size of an indentation increases the dislocation density. This increase in dislocation density causes an increase in the hardness. Flow stress can be described in terms of dislocation density by the relationship

$$\sigma_y = \mu\alpha b d^{\frac{1}{2}} \qquad 2.19$$

where μ is the shear modulus and α is a constant. Brown separated dislocation density into statistically stored and geometrically necessary dislocations. The density of statistically stored dislocations will remain constant while the density of geometrically necessary dislocations is described by Equation 2.18. The hardness can then be described as

$$H = A\mu\alpha b\left(\rho_o + \frac{\tan\beta}{bd}\right)^{\frac{1}{2}} \qquad 2.20$$

where ρ_o is the density of statistically stored dislocations and A is a constant, whose value depends on the material, that relates flow stress to hardness. It was found that Equation 2.20 produced good agreement with experimental results on MgO.

In a recent study of indentations in single crystals of Ag, Ma and Clarke (1995) used a strain gradient plasticity approach (Fleck, Muller, Ashby and Hutchinson (1994)) to interpret their ISE results. Ma and Clarke observed ISE behaviour for the two orientations tested; the [110] hardness curve showed a larger increase in hardness than indentation along [100].

2.2.4. Development of Fracture

The discussion of Section 2.2.2.1. described how an indentation can be made small enough that there are no background (statistically stored) dislocations in the deformed volume. In this case plasticity commences when the theoretical strength is reached. A similar argument can be made for indentation fracture. A common source of cracking is the distribution of flaws on a surface. In a study of the flaw distribution in glasses, Argon et.al. (1960) etched boro-silicate glass with a sodium vapour. After this treatment the flaw density was 1000/mm^2 or roughly 1 flaw every 30 μm. With this separation between flaws indentations could be easily made in a region free of flaws. In this case the crack nucleus must be formed during indentation.

A dislocation pile-up in the plastic zone in a region of tensile stress is a possible crack nucleus. In their study of GaAs Hirsch et.al. (1985) found cracks originated at the apices of either slip tetrahedra or rosette triangles. In both of these locations the slip planes intersect such that a dislocation reaction which forms a Lomer-Cottrell lock might occur. This lock then becomes a potential crack nucleus. When such crack nuclei are formed within the plastic zone they are prevented from propagating because of the large compressive stresses. However, if they form at the edge of the plastic zone tensile stresses

in this region will cause the cracks to open. It should be noted that Hirsch et.al. (1985) do not identify the proposed dislocation reaction.

A similar situation was found by Farber, Chiarelli and Heuer (1994). These authors compared indentations on {111} planes of 9.4 and 21 mol% Y_2O_3 stabilized ZrO_2 single crystals. The authors found the plastic zones in the two crystals to be quite different. In the 9.4% crystal $\langle 0\bar{1}1 \rangle$ dislocations were found on both {100} and {111} planes. In the more heavily alloyed crystal $\langle 0\bar{1}1 \rangle$ dislocations were only found on {100} planes. Two $\langle 0\bar{1}1 \rangle$ dislocations can react according to the reaction

$$\frac{1}{2}[1\bar{1}0]+\frac{1}{2}[\bar{1}01]=\frac{1}{2}[0\bar{1}1] \qquad 2.21$$

If the reacting dislocations lie on {100} and {111} planes (9.4 mol% crystal) the product dislocation would be from the $\{100\}\langle 0\bar{1}1 \rangle$ slip system, which is a primary slip system in ZrO_2. Therefore, a dislocation lock will not form in the 9.4 mol% crystal. In the 21 mol% alloy the original dislocations lay on {100} planes. In this case the product dislocation will be from the $\{011\}\langle 0\bar{1}1 \rangle$ slip system and this slip system is not active at temperatures below 1400° C (Dominguez-Rodriguez, Cheong and Heuer 1991). The authors noted that these dislocations would have a low mobility at the test temperature of this study and thus, a pile-up that can create a crack nuclei may be formed. Therefore, the difference in slip plane behaviour between the two alloys appears to result in the formation of dislocation based cracks in the 21 mol% Y_2O_3 case and not in the 9.4 mol% crystal.

Chapter 3.0

Experimental

3.1. Crystal Growth

A study of deformation produced during indentation requires well characterized, high quality samples. The best way of ensuring this sample quality is to use oriented single crystals. Single crystals were grown from a stoichiometric mixture of semiconductor grade Si and 99.99 Mo. This mixture was melted and homogenized several times before being transferred into the crystal-growing furnace. Oriented single crystals were grown by the Czochralski method in a tri-arc furnace, Figure 3.1. Crystals were grown at rates around 250 mm/hr under high purity argon.

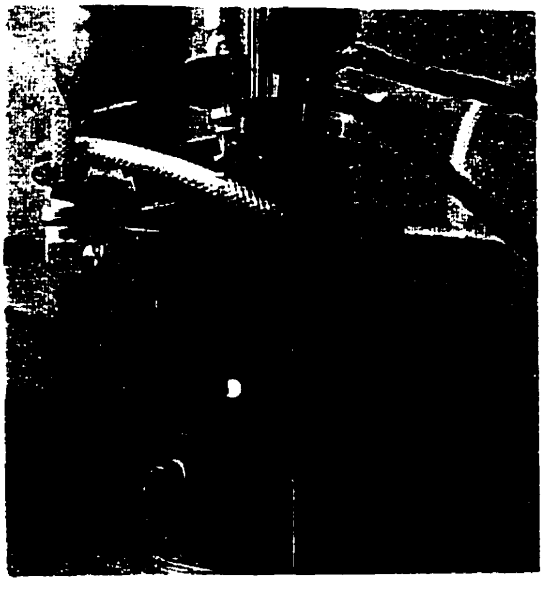

Figure 3.1 Tri-arc furnace used for crystal growth.

The two crystals used in the current study are shown in Figure 3.2.

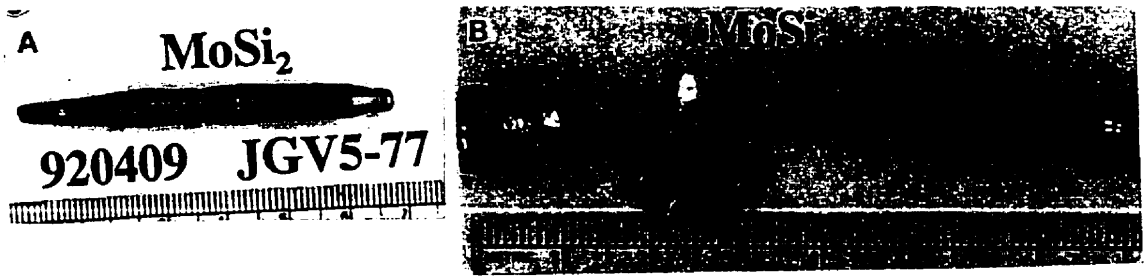

Figure 3.2 Single crystals used in this study. The crystal in (a) was grown parallel to the [001] axis while the crystal in (b) was grown parallel to [010] axis.

Because Si has a high vapour pressure at the melting temperature of $MoSi_2$, there will be loss of Si during crystal growth. Some early attempts at $MoSi_2$ single crystal growth (Lograsso 1992) were unsuccessful due to excessive Si loss at slow growth rates. It has been found that this loss of Si results in the precipitation of Mo_5Si_3 (the next intermetallic on the Mo rich side of $MoSi_2$). Maloy, Xiao, Heuer and Garrett (1993) studied the precipitation of Mo_5Si_3 in $MoSi_2$ single crystals grown at 300 mm/hr. It was found that precipitates were usually in the shape of laths with their long axes lying along $[110]_{MoSi_2}$ directions. The orientation relationship between matrix and precipitate was found to be:

$$[110]_{MoSi_2} \| [110]_{Mo_5Si_3}$$

and

$$(002)_{MoSi_2} \| (2\bar{2}0)_{Mo_5Si_3}$$

The distribution of Mo_5Si_3 precipitates in the crystals used in the current study was determined by compositional back scattering analysis in the SEM. Micrographs of the

crystal cross sections are shown in Figure 3.3. Only a few regions of higher Mo content were visible (Mo_5Si_3) and this second phase did not appear to have any preferred distribution across the cross section. It was thus determined that samples could be cut from all regions of the crystal cross section. As a further precaution to avoid Mo_5Si_3 precipitates samples were only taken from the upper regions of a crystal. Precipitates that were visible on the surface of the foil were avoided during indentation. There were no examples of precipitates contained in the plastic zone of an indentation found during TEM analysis.

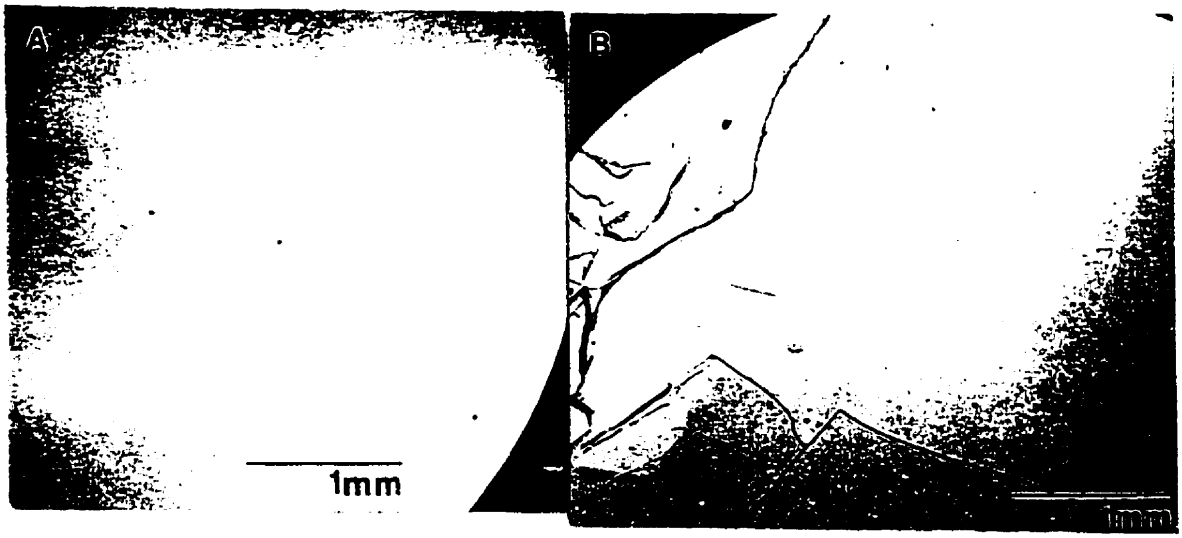

Figure 3.3 SEM micrographs of the cross-sections of the above crystals (a) [001] (b) [010]. The bright streaks and spots (marked) are regions of higher Mo content.

3.2. Crystal Orientation and Disc Preparation

Because the indentations and resulting deformation volumes were micron sized it was important to ensure samples were well aligned and had a defect free surface. Sample preparation techniques were chosen to ensure this result. Standard Laue back reflection x-

ray techniques, using a Cu K-α source, were used to verify crystal alignment. The goiniometer used during the alignment procedure was then transferred to a slow speed diamond saw such that an oriented cut could be made. Electro-Discharge Machining was then used to cut slices that were parallel to the face cut with diamond tooling. 3 mm discs were then cut from these slices.

A two step polishing procedure was employed to produce a defect free surface for indentation. Samples were mechanically thinned to a thickness of 200 μm and then polished electrochemically. Mechanical polishing procedures were selected to produce surfaces that were free of large scratches or pullout that would be enlarged during electropolishing. Discs were initially ground with 600 grit SiC paper. This was followed by 6 μm and 1 μm diamond paste. The diamond paste was impregnated in a nylon cloth which was mounted on a hard polishing wheel.

Electropolishing was conducted in a solution of 10% H_2SO_4 in methanol at a temperature of -40 °C with an applied voltage of 30 V. If the electropolishing conditions were correct a current of 45 mA was observed. The amount of current increased to 60 mA as the foil was thinned. Polishing prior to indentation was initially performed in a beaker. However because of difficulties producing a consistent surface with this technique, jet polishing techniques were adopted. Polishing times of one minute allowed sufficient material to be removed to achieve the desired surface quality without removing sufficient material to invalidate the assumption of indentation on a semi-infinite surface. Polished samples were rinsed in a 10% HF solution to remove any oxide. Finally, samples were washed in distilled water, high purity acetone and high purity methanol prior to indentation.

3.3. Indentation

A complete picture of the deformation resulting from an indentation test requires both detailed surface topography information and a detailed picture of material movement within the plastic zone. Two regimes of indentation tests were required to produce the desired information. First, indentations that were made with a range of applied loads, producing indentations with an edge length between 1 and 30 μm, were examined with SEM and AFM techniques. Second, TEM studies were conducted on indentations that had been made with an applied load of 5 grams. All indentations were made with a Vickers pyramid attached to either a Leitz or Shimadzu micro-hardness machine. The Vickers tip was aligned such that either its edges or diagonals were parallel to a low index direction for both (100) and (001) samples. Thus, in the case of the (100) plane the indenter was aligned with [010] and [001] directions while it was aligned with ⟨110⟩ directions on the (001) plane.

Indentations to be studied by SEM were made with applied loads of: 5, 10, 15, 30, 55, 105, 200, 300 and 500 grams. Three indentations were made at each load and there was a minimum of five edge lengths between indentations. This spacing was necessary to ensure the deformed zones around the indentations did not overlap. In order to improve the resolution of slip traces in the SEM, indented samples were etched in a solution of $4H_2O$:$2HNO_3$:1 HF for one minute. This procedure was repeated until the desired slip trace resolution was obtained.

Indentations to be studied with TEM methods were made with an applied load of 5 grams. This produced indentations with an edge length of approximately 2 μm and a depth of 400 nm at the apex. This load was selected to both minimize the amount of fracture and reduce the size of the plastic zone. A small plastic zone was desired such that it could be

viewed in its entirety during TEM analysis. A total of sixty four indents were made in a 1mm^2 area in the centre of a disc. This number of indents ensured that several indents would be contained in the thin area of the foil. Further, additional indentations could be studied by expanding the thin area of the foil.

3.4. Scanning Electron Microscopy

SEM techniques were used to study the deformation and fracture patterns around an indentation. In particular, the spatial distribution and orientation of these features was readily determined with these techniques. SEM studies were conducted with a Philips 515 microscope. The choice between Secondary Electron (SE) and Back Scattered (BS) imaging modes was based on the information desired and the resolution capabilities of these imaging modes. BS mode was found to give the best resolution of etch pits and slip traces. This appeared to be a result of shadowing due to the 15° tilt between the sample normal and the electron beam. This tilt increased the contrast between edges (trace or pit) tilted towards and away from the detector. This in turn enhanced the visibility of these features. However, at the higher magnifications required to image smaller indentations the resolution available in the BS mode was inadequate. In these cases the SE mode was used to image the indentations.

3.5. Atomic Force Microscopy

While SEM studies provided information on the spatial distribution of deformation and fracture around an indentation they did not provide detailed depth information. AFM studies provided the high resolution spatial and depth information required to fully characterize the surface around an indentation. A Digital Nanoscope III was used for AFM

studies. AFM images of the indentations made with at least two different loads, for each orientation, were collected. The scan size used during imaging was set such that the indentation and entire plastic zone could be imaged. Smaller scan sizes were then used to produce high resolution images of important features. In a second series of experiments, line traces were made across the indent to obtain a detailed picture of the indentation shape. These traces were made along both diagonals of indentations made on (001) planes with the indenter's edges aligned parallel to [110] directions. Three indentations were examined at each load.

3.6. Transmission Electron Microscopy

Transmission Electron Microscopy studies were conducted on a Philips CM12 microscope operating at 120 KeV. Beam alignment was checked at the beginning of each session and periodically during the session, particularly when there was a large change in magnification. Rotation between the image and diffraction pattern was calibrated with MoO_3 crystals. A double tilt sample holder was used to reach the desired crystal orientations. Annealing experiments were conducted in a single tilt heating stage that had a maximum temperature of 800 °C.

In order to accurately determine the pattern of material movement during indentation the identity and distribution of defects in the plastic zone must be determined. Therefore, TEM techniques of defect analysis were very important in this study. The quantities to be determined included the Burgers vector (**b**), line direction (**u**) and slip plane of dislocations and the displacement vector (**R**) of any stacking faults. While the techniques used to determine these quantities in cubic isotropic materials are well established, certain precautions had to be taken when working with a non-cubic anisotropic material, such as

$MoSi_2$. The basic techniques used for defect analysis and the extra precautions taken will now be outlined.

3.6.1. Burgers Vector Determination

Burgers vector determinations were based on the invisibility criteria, **g.b**=0. A dislocation creates distortions in the surrounding crystal that affects the intensity of the incident and diffracted beams. A screw dislocation only produces displacements that are parallel to the Burgers vector. Thus all displacements are contained in the slip plane. If the crystal is tilted such that the Burgers vector lies in the diffracting plane there is no distortion normal to this plane and thus there will be no additional contrast from the dislocation. This is the case of **g.b**=0. By finding several diffracting conditions where this criterion (**g.b**=0) is satisfied, the Burgers vector of the dislocation can be determined.

This criterion for determining the Burgers vector of a dislocation is complicated when the dislocation has an edge component. The displacement normal to the slip plane of the edge dislocation implies that contrast may be produced even when **g.b**=0. Complete invisibility is only possible when both **g.b** and $\mathbf{g.b} \wedge \mathbf{u}$ are equal to zero (Hirsch et.al. 1977). However the contrast produced by an edge dislocation in the case where **g.b**=0 is often recognizable. For example, a double image, which is symmetrical about the dislocation line, is produced by a pure edge dislocation when **g.b**=0.

The above invisibility criteria, and thus the determination of **b** are only valid for elastically isotropic materials. The situation becomes more complicated when the crystal is elastically anisotropic, because there are no planes that remain undistorted in the presence of a dislocation, even for the pure screw or pure edge cases (Head et.al. 1973). In these

cases the contrast that is observed experimentally must be compared to computed images to verify the identity of the Burgers vector.

3.6.2. Displacement Vector Determination

A stacking fault is a planar defect that disrupts the regular stacking sequence of a crystal. The crystal below the fault has been displaced from the crystal above the fault by a constant vector **R**, where **R** lies in the plane of the fault. In electron diffraction studies there is a change in the phase factor (α) equal to $2\pi\mathbf{g}.\mathbf{R}$ on crossing the fault plane. There is again a simple invisibility criterion that can be used to determine **R**. If the fault is not visible for a given **g** then α must be either 0 or an integral multiple of 2π, i.e. there is no phase difference due to the presence of the fault. By finding several examples where the fault is invisible the identity of **R** can be determined.

The above discussion assumes that **R** lies in the fault plane. If **R** is not contained in the fault plane the component out of the plane may create residual contrast when the fault is expected to be invisible. An example of this was given by van Tendeloo and Amelinckx (1974). In this case the out of plane displacement produced residual contrast for an APB when imaged with a fundamental reflection.

3.6.3. Trace Analysis

The standard trace analysis techniques were outlined by Head et.al. (1973). Because $MoSi_2$ is tetragonal, directions and plane normals are not necessarily parallel. Therefore the procedure outlined for cubic materials by Head et.al. (1973) has been modified to reflect the non-cubic structure. Trace analyses were used to determine the

dislocation line direction (**u**) and to confirm slip plane identity. A trace analysis required the diffracting vector, **g**, the beam direction, **B**, and the direction of the dislocation trace for each image (at least three). Figure 3.4 shows a sample stereographic projection. Three great circles have been drawn for the planes that are normal to **B** for each image. **g** and the dislocation trace will both lie on this great circle, they will be separated by the measured angular separation. A plane trace is drawn between the beam direction, **B**, and the point on its trace representing the above mentioned angular separation. The point of intersection for the traces connecting the beam direction and the respective dislocation trace will be the line direction of the dislocation **u**.

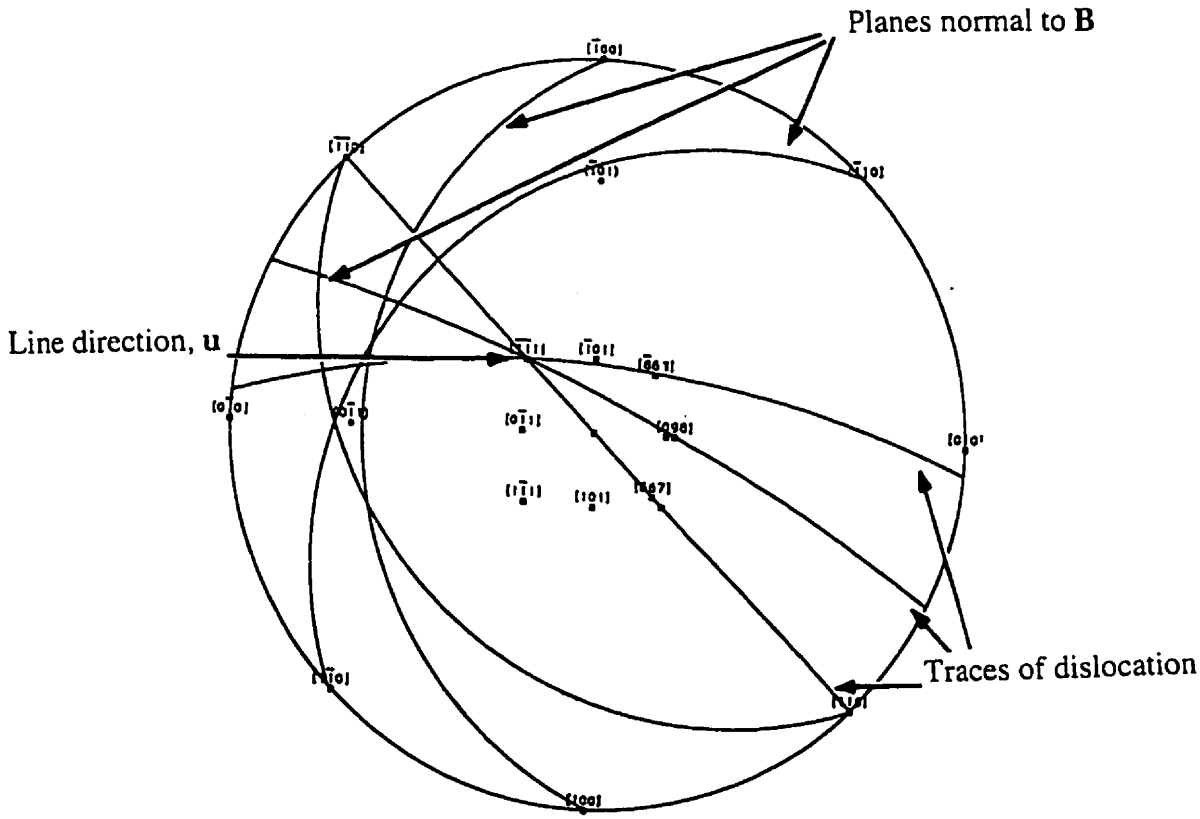

Figure 3.4 [010] stereographic projection showing the plotting procedure used for trace analyses. Round brackets denote plane normals and square brackets denote directions.

3.6.4. Stereo Microscopy

Knowledge of the spatial distribution of defects within the plastic zone is very useful when mapping the movement of material during indentation. This requires a three dimensional view of the plastic zone. Stereo microscopy can provide this three dimensional information. A stereo image requires that two TEM images be taken at symmetrical positions about the indentation axis under identical diffracting conditions i.e. **g** and s are the same for the two images. For example, a stereo image of an indentation on an (010) surface was formed from images formed with $\mathbf{g}= 10\bar{3}$ and **B** equal to either $[3\bar{9}1]$ or $[391]$. When the positive prints of these images were viewed in a stereo viewer the distribution of defects throughout the depth of the foil could be determined.

3.7. Image Simulation

Computer simulated images were used to confirm Burgers vector determinations based on the **g.b** invisibility criteria. The computer program used for image simulation was a highly modified version of the two beam program of Head et.al. (1973). The modifications allowed up to four stacking faults and five dislocations to be simulated. Crystals could be anisotropically elastic and have any crystal structure. Operation of the program required the following inputs: atomic positions, elastic constants, crystal thickness, slip plane normal, partial separation, **g**, **s**, $\mathbf{b}_p$, **R** and **B**. The anomolous absorption coefficient was calculated by the program using the input data. The calculated images were then output to the monitor and stored as a jpeg file which was later printed. Sufficient resolution for defect identification was achieved with a 600 dpi laser printer.

Chapter 4.0

Results

Four techniques have been used to characterize indentations made on (001) and (010) surfaces of $MoSi_2$. These techniques are: hardness measurements, SEM, AFM, and TEM. The results from these techniques have enabled the structure associated with plasticity and fracture to be examined at a variety of scales. Information from these characterization techniques has been used to develop a picture of indentation that begins with a very basic macroscopic view and ends with a detailed understanding of the micro-mechanisms of deformation and fracture.

The first results to be presented will be hardness versus applied load measurements. These will be followed by SEM observations of indentations. AFM images will then be presented. AFM imaging provided greater detail about specific features of the surface topography. Of particular importance is the depth information that was gathered with AFM techniques. AFM was also used to collect information on the shape of indentations, which was used to quantify the change in shape that occurred with unloading. Finally, TEM results will be presented. These will provide detailed defect information from the entire plastic zone. The TEM results will also be presented in order of decreasing scale. Low magnification images of the entire plastic zone will be presented first. Stereo images will then be presented to construct a three dimensional picture of the plastic zone. Lastly, a detailed analysis of the defects within the plastic zone will be given. The microscopic picture of deformation that is created can then be used to rationalize the macroscopic observations.

The microstructural observations will be grouped according to orientation. Results from indentations on (001) planes will be presented first. This will allow the pattern of deformation and fracture that results from the four fold rotational symmetry of the [001] zone to be analyzed first. The more complicated case of indentation on an (010) plane will be presented second. For each orientation the results of the four characterization techniques will be presented in order of decreasing scale.

4.1 (001) Surface

4.1.1 Hardness Measurements

The first insight into the accommodation processes that take place during an indentation test was provided by a plot of hardness versus applied load. Vickers hardness is defined as the applied force divided by the contact area between the indenter and the sample surface. Vickers hardness was calculated using the equation

$$H = \frac{18.19m}{d^2} \qquad 4.1$$

where m is the applied load in kilograms and d is the diagonal length in meters. The constant, 18.19, incorporates gravitational acceleration, the conversion from diagonal to edge length and the constant 0.927. This last factor converts the projected area into a contact area (Tabor 1951). The length of the two diagonals of each indentation was measured with the SEM. These measurements were then averaged to produce a single 'composite' diagonal length, d, which was used to calculate hardness, using Equation 4.1.

A plot of hardness versus applied load for indentations made with the edges of the indenter aligned parallel to $\langle 110 \rangle$ directions is shown in Figures 4.1. The hardness was found to be constant at 8 GPa for applied loads greater than 200 grams. As the load was reduced below 200 grams the hardness increased to approximately 10 GPa, at the smallest loads. When indentations were made with the indenter's diagonals aligned parallel to $\langle 110 \rangle$

directions, the hardness versus applied load curve followed a similar trend, but the magnitude of the change in hardness was much larger (Figure 4.2). The hardness at large loads was constant at 9.5 GPa. When the applied load was reduced below 200 grams the hardness once again increased. However, in this case, the maximum hardness was 14 GPa. Thus, both the absolute magnitude of hardness and the magnitude of the change in hardness were larger for indentations made with this orientation of indenter.

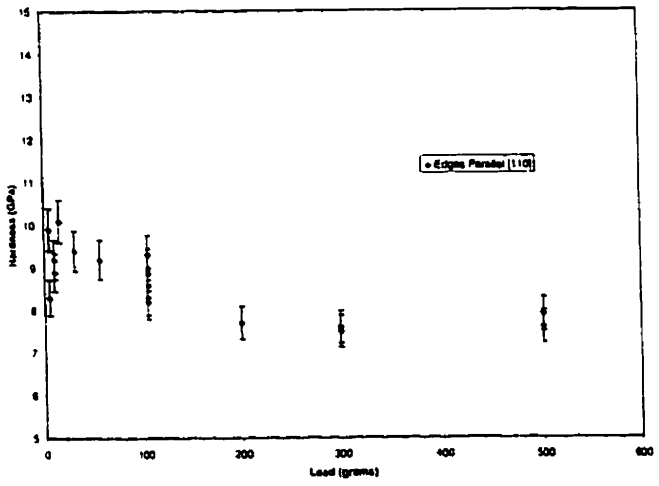

Figure 4.1 Hardness versus applied load, edges of the indenter aligned with ⟨110⟩.

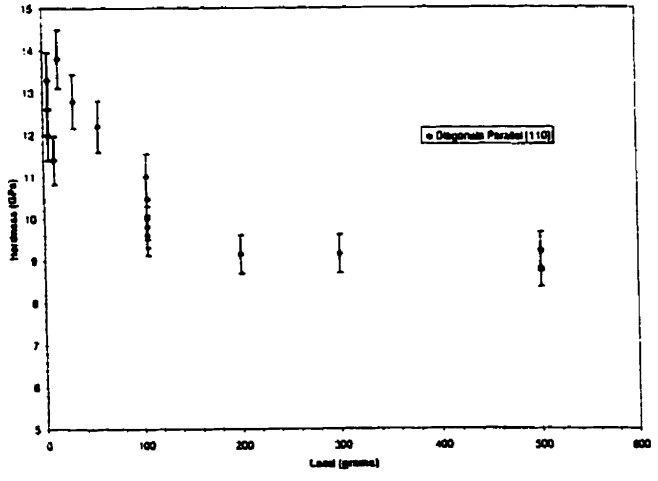

Figure 4.2 Hardness versus applied load, diagonals of the indenter aligned with ⟨110⟩.

4.1.2. SEM

The hardness versus applied load curves showed that the accommodation of an indenter (as seen through hardness) is dependent on the volume of material being displaced (applied load) and the orientation of the indenter. An understanding of the mechanisms responsible for this accommodation requires microstructural characterization of the deformed material surrounding the indentation. The spatial distribution of deformation and fracture patterns on the surface surrounding the indent were determined by SEM.

An SEM micrograph of an indentation made with an applied load of 500 grams and with the indenter's edges aligned parallel to ⟨110⟩ directions is shown in Figure 4.3 (a). Long cracks extend from the corners of the indentation into the matrix, producing traces along ⟨100⟩ directions. Another crack, producing a trace along ⟨100⟩, has formed in the plastic zone away from the indentation. Two sets of slip traces are visible in Figure 4.3 (a). The most prominent set lies along ⟨100⟩ directions and is locally perpendicular to the crack traces described above. The density of these traces was very high in the region around the ⟨100⟩ crack traces, while there were no visible traces at the indentation edge mid-point. This configuration of slip formed a V-shaped trough that extended along ⟨110⟩ from the edge mid-points. The second set of slip traces lie parallel to ⟨110⟩ directions. These traces extended further from the indentation than those along ⟨100⟩ directions. They were also unevenly distributed around the indentation with a cluster lying approximately 5 μm from the edges of the indentation.

Indentations made with an applied load of between 200 and 500 grams produced a hardness that fell on the constant hardness portion of the hardness versus applied load curve (Figure 4.1). Therefore, one might expect the deformation and fracture around these indentations to be very similar. An indentation made with an applied load of 200 grams is

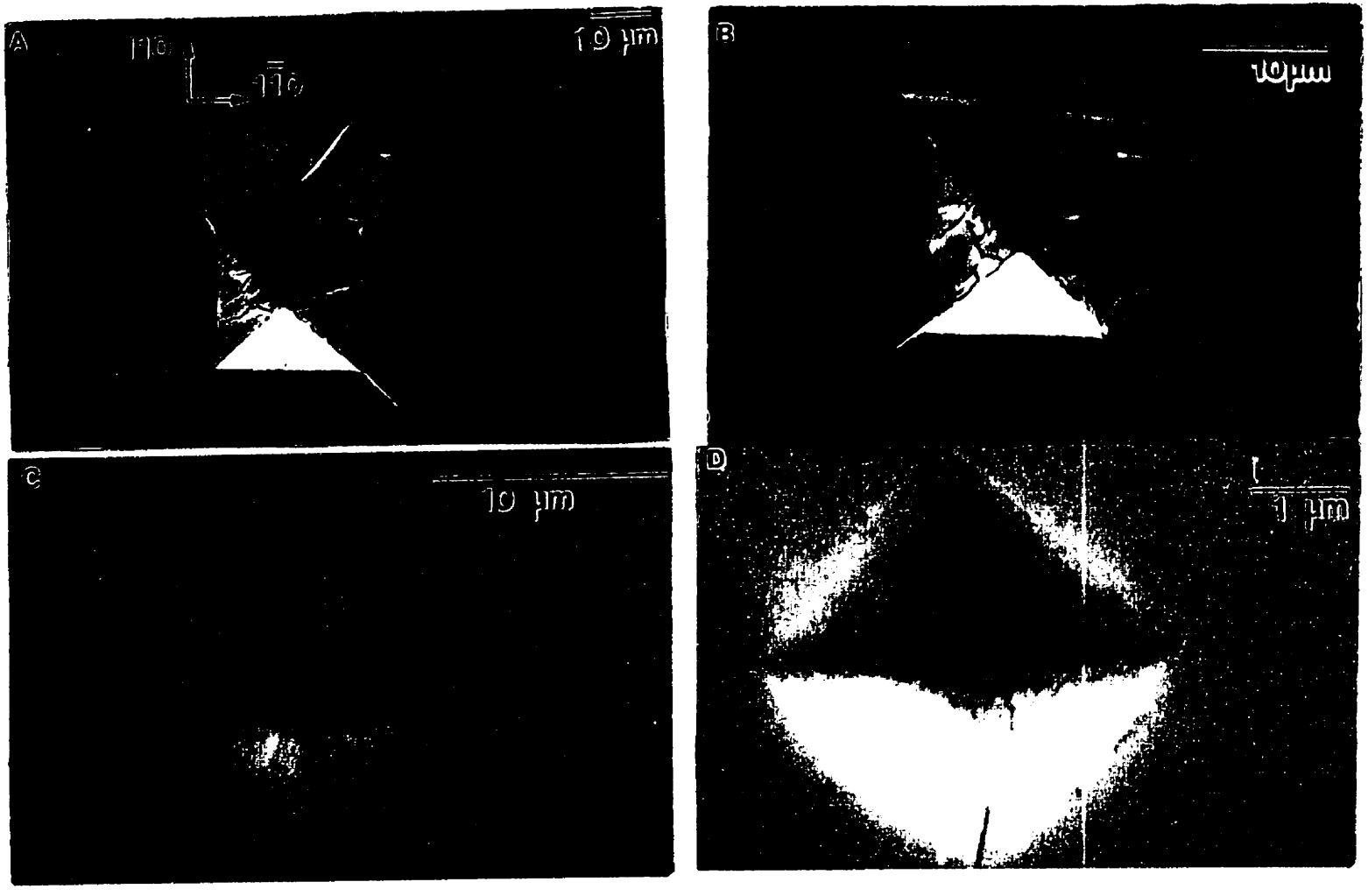

Figure 4.3 SEM micrographs of indentations made with the edges of the indenter aligned parallel to $\langle 110 \rangle$. The applied load is 500, 200, 55 and 10 grams in (a), (b), (c) and (d), respectively.

shown in Figure 4.3 (b). The crack traces that extend along ⟨100⟩ directions, from the corners of the indentation, are still present while the traces that are more remote from the indentation are no longer seen. The slip traces along ⟨100⟩ and ⟨1 1 0⟩ directions were in the same configuration as found at the indentation made with a 500 gram load (Figure 4.3(a)). However, in this case neither set of traces extended as far from the indentation. For example, the traces along ⟨100⟩ no longer extend beyond the ⟨100⟩ cracks. In this micrograph (Figure 4.3(b)) the V-shaped trough discussed above is clearly visible on the left side of the indentation.

When an indentation was made with an applied load of 105 grams or less the hardness fell on the ascending portion of the hardness versus applied load curve. An SEM micrograph of an indentation made with an applied load of 55 grams is shown in Figure 4.3 (c). There were no crack traces along ⟨100⟩ directions. There were no slip traces seen along ⟨100⟩ directions and only a single slip trace extended from each corner of the indentation along ⟨1 1 0⟩. Finally, Figure 4.3 (d) shows an indentation made with an applied load of 10 grams. Again, only ⟨1 1 0⟩ slip traces are seen, with a single ⟨1 1 0⟩ trace extending from each corner. However, slip traces along ⟨1 1 0⟩ are now visible on the faces of the indentation.

Similar trends in the deformation and fracture pattern were observed for indentations made with edges of the indenter aligned parallel to ⟨100⟩ directions. An SEM micrograph of an indentation made with an applied load of 500 grams is shown in Figure 4.4 (a). As in the previous orientation, crack traces are seen along ⟨100⟩ directions. However, in this case the traces extended from the edges of the indentation not the corners. The longest cracks were found half way from the edge corner to the edge mid-point. Thus, the formation of ⟨100⟩ crack traces appears to be independent of the orientation of the

indenter. This suggests that these cracks were nucleated at a source that is determined by crystallography and not the stress field. A second set of cracks can be seen at the edge mid-points. This location corresponds to the point where the ⟨110⟩ slip traces intersect. The cracks expand out from the edge of the indentation in a semi-circular shape. In this orientation, the slip traces along ⟨110⟩ directions were actually broad slip bands that were elevated above the original surface. These bands extended a maximum of one diagonal length from the indentation. Faint slip traces (arrowed) along ⟨100⟩ directions extended from the corners of the indentation. These traces were only visible after the sample had been etched. In a higher magnification image (Figure 4.4(b)) these traces are visible as a series of discrete etch pits. This suggests that the dislocation density on this family of slip planes is fairly low and the Burgers vector of the dislocations does not have a component along [001]. By following these ⟨100⟩ traces from the corner of the indentation into the surrounding material the ⟨110⟩ slip bands are seen to end at these traces, suggesting that the slip activity forming the etch pits along ⟨100⟩ occurred before the slip that formed the bands along ⟨110⟩ directions.

Figure 4.4 (c) shows an SEM micrograph of an indentation made with a 200 gram load. While the elements of the deformation and fracture pattern are similar to the 500 gram indentation, the size of these elements is smaller around the 200 gram indentation. For example, the length of the ⟨100⟩ crack traces seen in Figure 4.4(b) is approximately one third the indentation diagonal length, while they are approximately one half of the indentation diagonal length in the 500 gram case (Figure 4.4(a)). The semi-circular cracks also appear to be smaller than those observed around indentations made with larger loads. The arrangement of slip traces along ⟨100⟩ is very clear in Figure 4.4(c). The ⟨110⟩ slip bands still extend

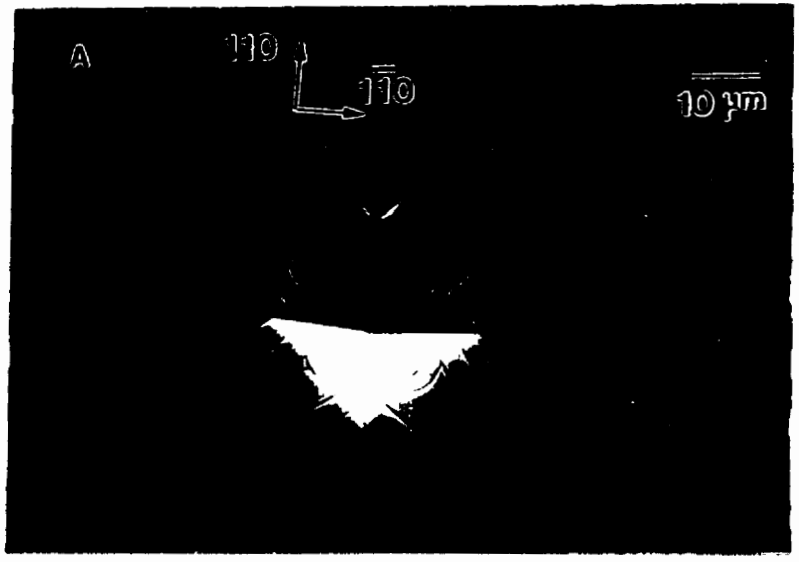

Figure 4.4 SEM micrographs of indentations made with the diagonals of the indenter aligned parallel to ⟨110⟩. The applied load was 500 grams in (a), 200 grams in (c), 55 grams in (d) and 10 grams in (e). Micrograph (b) is a high magnification image of the indent shown in (a).


D
10 µm


E
1 µm

approximately one diagonal length away from the indentation. However, the density of these bands is lower than it is for the 500 gram indentation. In this case only a few slip bands extend from the corner of the indentation.

As in the previous orientation there is a dramatic change in the deformation and fracture pattern around an indentation when the applied load is reduced below 55 grams (Figure 4.4(d)). First, the length of the crack traces along ⟨100⟩ is now only one fifth of the indentation's diagonal length while there are no semi-circular cracks at the edge mid-points. Second, there are longer etch pits visible along ⟨100⟩ directions. A single slip trace extends along ⟨110⟩ from the corner of the indentation instead of the broad slip bands observed for indentations made with larger applied loads. The ⟨110⟩ traces now form a series of nested squares whose edges form an angle of 45° with the edges of the indentation. The edge length of the largest square is equal to the diagonal length of the indentation. This pattern of ⟨110⟩ traces was not seen around indentations made with larger applied loads. When the indentation was made with an applied load of 5 grams (Figure 4.4(e)) the deformation pattern was very similar to the 55 gram case. The same pattern of nested squares is created by the slip traces along ⟨110⟩. In this case ⟨100⟩ traces can also be seen along the faces of the indentation.

Several conclusions can be drawn from the orientation of slip and fracture seen in these SEM observations. First, the slip traces along ⟨110⟩ directions are a result of slip on {110} planes, since this is the only slip plane in $MoSi_2$ that produces a trace along ⟨110⟩ directions on an (001) surface. Second, when the applied load was greater than 100 grams the slip traces along ⟨100⟩ directions were different for indentations made with the two indenter orientations. When the edges of the indenter were aligned along ⟨110⟩ directions, slip traces were formed i.e. there was a displacement normal to the surface. However,

when the edges were aligned along ⟨100⟩ only etch pits were observed (Figure 4.4(b)). This suggests that the Burgers vector of the dislocations forming these etch pits does not have an [001] component. Thus, it appears that different slip systems have been activated at applied loads larger than 100 grams.

The SEM observations of the surface have shown that many of the elements of the slip and fracture patterns were the same for indentations made with the two orientations of indenter. It was also found that these patterns underwent considerable change when the load used to make the indentation was reduced below 200 grams. There is a general decrease in the magnitude of cracking and slip activity with decreasing load. However, there is a significant change in these patterns when the applied load is reduced from 200 to 55 grams. When the applied load was less than 100 grams there was no cracking observed and there were very few slip bands seen beside the indentation. Slip bands were now seen on the facets of the indentation. These changes occurred at roughly the same load as the hardness increase in the hardness versus applied load curves (Figures 4.1 and 4.2).

4.1.3. AFM Observations

High resolution images and quantifiable shape information of an indentation are not readily obtainable with SEM methods. However, AFM can readily provide this information. AFM offers both qualitative and quantitative three dimensional surface topography information.

Two AFM images of an indentation made with the edges of the indenter aligned parallel to ⟨110⟩ are shown in Figure 4.5. In Figure 4.5(a) the indentation is viewed from a direction that is at an angle to the surface normal. This image clearly shows the elevation of the {110} slip bands that were observed in the SEM. It is also apparent that the elevation to which material was raised decreases away from the indentation. Three steps in

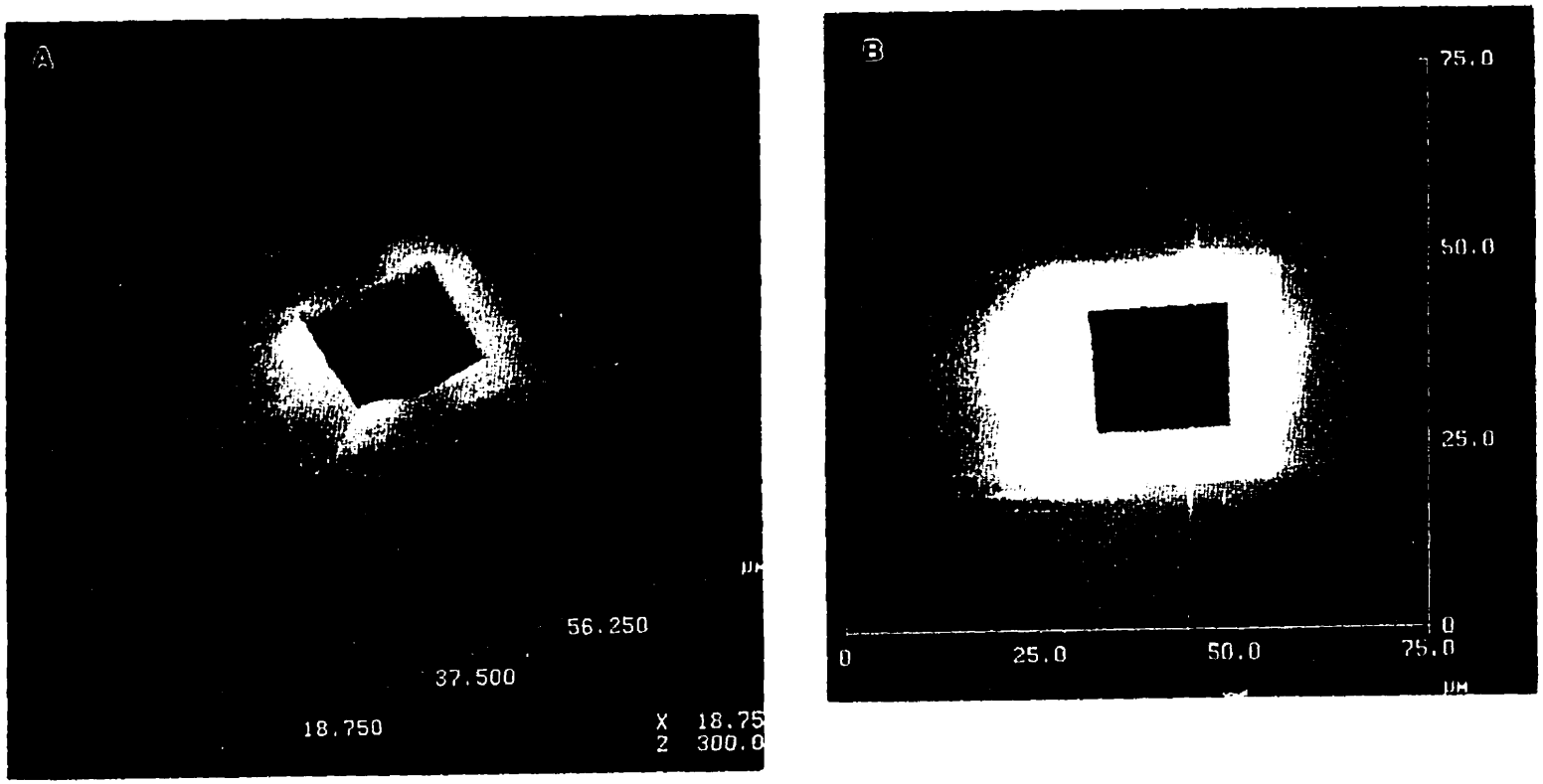

Figure 4.5 AFM images of an indentation made with an the edges of the indenter aligned parallel to ⟨110⟩. The applied load is 300 grams. The image in (a) is at an angle to the surface normal while that in (b) looks along the surface normal.

elevation are seen along the front edge of the indentation in Figure 4.5 (a). Furthermore, within these {110} bands there is a depression at the edge mid-point. This corresponds to the V-shaped trough noted in Figure 4.3(a). Figure 4.5(b) shows the same indent seen in Figure 4.5(a), but the viewing direction is now parallel to the plane normal. This image gives a clearer picture of the height variations within the deformed zone around the indentation. The change in height as one moves away from the indentation across ⟨110⟩ slip traces, is clear. For example, there is a change in height of approximately 200 nm across a ⟨110⟩ trace 6 μm away from the indentation edge. There is also a difference in elevation between the two sides of the ⟨100⟩ cracks (upper and lower left corners of the indentation). Lastly, the shape of the deformed zone is seen to be defined by both the slip traces along ⟨110⟩ and those along ⟨100⟩. Along ⟨100⟩ directions the plastic zone is bounded by slip traces along ⟨110⟩ while the traces along ⟨100⟩ directions define the plastic zone along ⟨110⟩. This agrees with the SEM observations of indentations made with the edges of the indenter parallel to ⟨100⟩ directions.

An indentation made with an applied load of 200 g, with the edges of the indenter parallel to ⟨100⟩ directions, is shown in Figure 4.6. Once again, the slip traces along ⟨110⟩ directions, framing the indentation, are seen to be raised above the sample surface. The indentation appears to have eight corners because of four clam shell shaped depressions that are located at the edge mid-points. This is also the location of the semi-circular cracks observed in the SEM. A higher magnification image of this area in an indentation made with an applied load of 300 grams is shown in Figure 4.7. In this image, this area is darker than its surroundings, confirming that it is at a lower elevation. It is also apparent that the bottom lies at a shallow angle to the sample surface. Figure 4.7 clearly

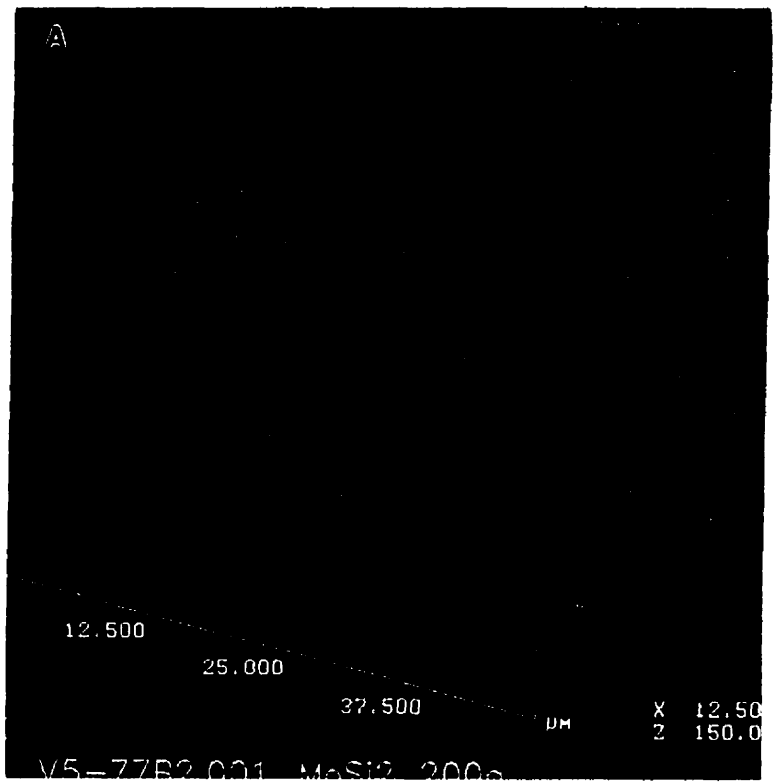

Figure 4.6 AFM image of an indentation that was made with the diagonals of the indenter aligned parallel to ⟨110⟩. The applied load is 200 grams.

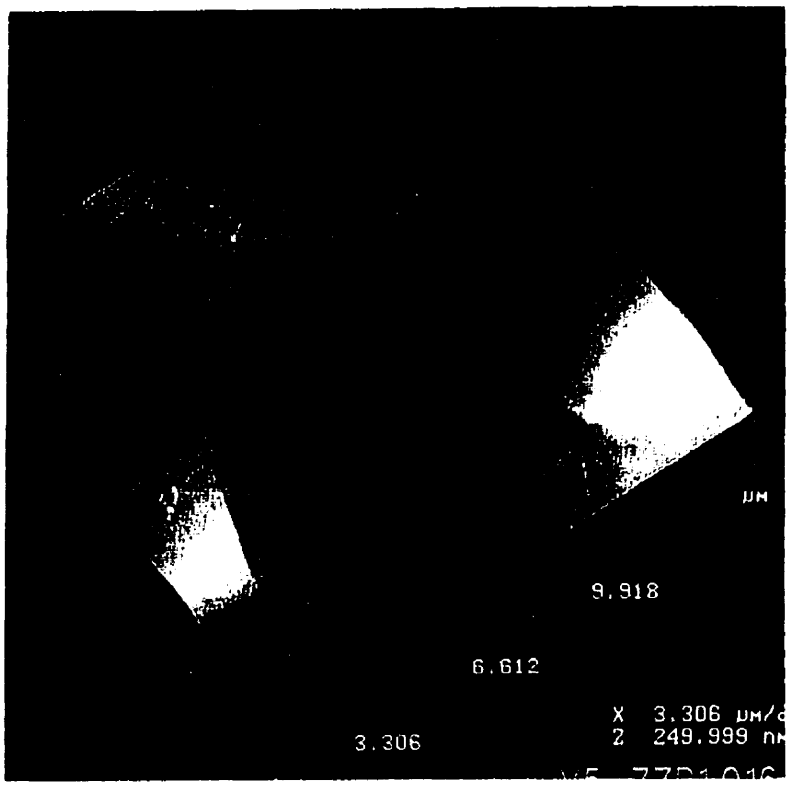

Figure 4.7 Higher resolution image of clam shell shaped depressions.

shows the intersection of the two sets of slip bands along ⟨110⟩ directions. These slip bands appear finer than those seen beside the indentation. The above observations suggest that the formation of this region is a result of shallow cracks which, in turn, are related to the intersection of slip bands along⟨110⟩ directions.

The data acquired during AFM imaging is stored digitally and can thus be manipulated to produce a wide range of information. For example, the image can be inverted ie. any areas below the surface appear elevated above the surface in the image. An inverted image of an indentation made with an applied load of 300 grams is shown in Figure 4.8. The colour scheme was selected to contrast features above the surface with those on the surface. Slip traces along ⟨110⟩ directions are seen running parallel to the indentation diagonals. These traces follow the shape of the indenter, decreasing in size towards the apex. While this pattern of slip traces was only visible in the SEM when the indentation was made with small applied loads (eg. Figure 4.4(d)), it now appears that this pattern of slip on {110} planes occurs at all applied loads. In Figure 4.6 it was shown that the slip bands along ⟨110⟩, lying outside the indentation, were raised above the surface.

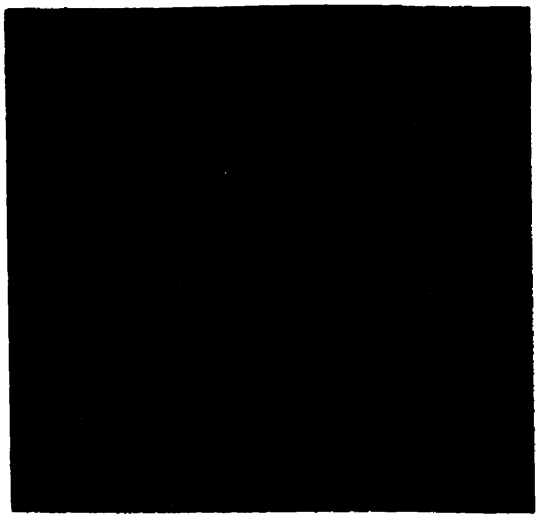

Figure 4.8 Inverted AFM image of an indentation made with an applied laod of 300 g.

4.1.3.1 Shape Change of an Indentation

Vickers hardness is calculated by dividing the applied force by the contact area between the indenter and the sample. Since area measurements are made after the load has been removed the validity of any hardness calculation is based on the correspondence between the measured area and that actually supporting the load. This correspondence can be determined by studying changes in the shape of the indentation that occurs after the load is removed. AFM was used for this task because of its ability to accurately profile a surface and the flexibility provided for analysing the data. All of the shape change experiments were conducted on indentations that were made with the edges of the indenter aligned with ⟨110⟩ directions.

The volume of an indentation, after load removal, was calculated from the projected diagonal length and the depth of the indentation at the apex. Line traces along diagonals of an indentation provided both of these measurements. An example of such a trace is shown in Figure 4.9. Markers placed at the corners of the indentation were used to measure the length of the indentation's diagonal while markers at the apex and on the surface, far from the indenter, were used to measure its depth. These two values were then used to calculate the angle between the surface and the sides of the indentation and the angle measurements were in turn used to calculate the volume of the indentation after load removal. Any decrease in the volume of material displaced by the indenter indicates elastic recovery and/or reverse plastic flow.

Quantification of the shape changes that accompany load removal required assumptions be made about the in-plane dimensions of the indentation. It was assumed that there was no change of these dimensions when the load was removed. This assumption was made with knowledge of the SEM observations. In Figure 4.4 (a) the slip

traces along $\langle 1\,1\,0 \rangle$ directions were observed on the facets of the indentation. These slip traces did not extend beyond the edges of the indentation with the largest traces having a length equal to the diagonal length of the indentation. If the diagonal length changed during unloading then it would be anticipated that the slip traces on $\{1\,1\,0\}$ planes would be distorted, which is not the case. Therefore, the in-plane dimensions of the indentation remained the same during unloading. This will be confirmed with the TEM results in Section 4.1.4.

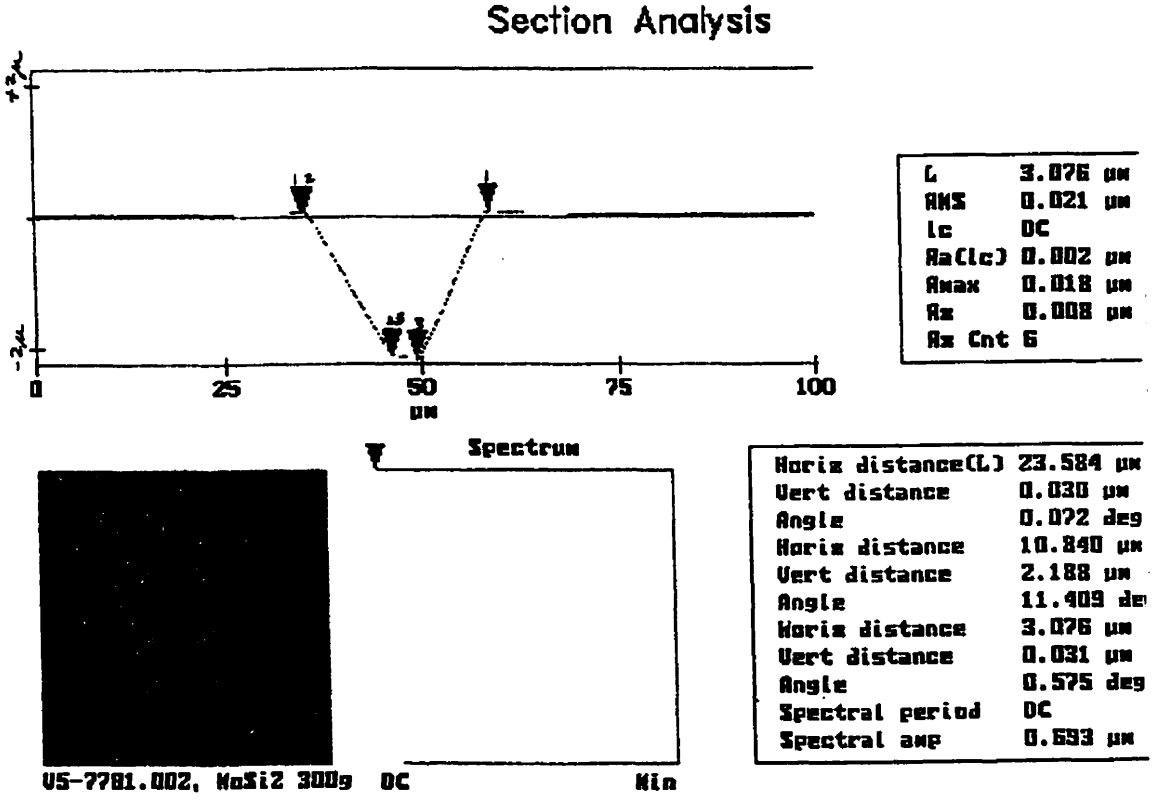

Figure 4.9 Line trace along the diagonal of an indentation.

The volume of the Vickers indenter is given by

$$V = \frac{d^3 \tan\theta_o}{12} \qquad 4.2$$

where d is the indentation diagonal length and θ_o is the angle between the surface and the indenter diagonal. The change in volume associated with a change in angle (i.e. assuming d remains constant) is then given by the equation

$$\frac{\Delta V}{V} = \left(\frac{\tan\theta_1 - \tan\theta_o}{\tan\theta_o} \right) \qquad 4.3$$

where θ_1 is the angle between the surface and the indenter diagonal after load removal.

The value of θ_o in Equation 4.3 is the angle of an ideal Vickers indenter. It is usually assumed that this angle does not change during indentation. However, during indentation of hard materials such as $MoSi_2$ there will be some elastic deformation of the diamond indenter. This should be considered before shape change measurements are made. A correction for the elastic deformation of the diamond indenter followed an approach taken by Stilwell and Tabor (1961). First, it was assumed that the Vickers indenter could be approximated by a cone. With this assumption Boussinesq's solution (Love 1939) for the deformation of the flat surface by a rigid cone was used to calculate the elastic deformation of the indenter. Stilwell and Tabor (1961) stated that the displacement of the surface is given by

$$y = 2pa\left(\frac{1 - \upsilon_1^2}{E_1} \right) \qquad 4.4$$

where p is the pressure, a is one half the diagonal length and υ_1 and E_1 are Poisson's ratio and the elastic modulus of the indented material, respectively. The total displacement of the surface, at the apex, during load is given by

$$d = d_i - \Delta d_{in} \qquad 4.5$$

where d is the total penetration, d_i is the theoretical displacement and Δd_{in} is the elastic deformation of the indenter. Stilwell and Tabor (1961) also stated that the elastic displacement of the indenter can also be calculated by Equation 4.4, using the material parameters for diamond. Substituting Equation 4.4 into 4.5 and replacing d_i by $a.\tan\theta_o$ yields

$$d = a\tan\theta_o - 2pa\left(\frac{1-\upsilon_1^2}{E_1}\right) \qquad 4.6$$

or

$$\frac{d}{a} = \tan\theta_o - 2p\left(\frac{1-\upsilon_1^2}{E_1}\right) \qquad 4.7$$

Assuming a hardness of 8.5 GPa and with υ_{di} =0.1 and E_{di} =1000 GPa the value of $\frac{d}{a}$ from Equation 4.7 is 0.27. Thus, the volume change is

$$\frac{\Delta V}{V} = \frac{\tan\theta_1 - 0.27}{0.27} \qquad 4.8$$

Table 4.1 presents the results of the volume change calculations. As seen in Table 4.1 the shape change, as measured by the changes in the volume of the indentation, is essentially constant at approximately 20% for indentations made with applied loads between 50 and 300 grams. The size of the shape change then begins to increase with further decreases in load. In Section 5.2 the origin of these shape changes and the implication on hardness will be discussed. The diagonal measurements were also used to calculate hardness. The results are similar to those in section 4.1 where it was found that there was little increase in hardness with decreasing load.

LOAD (g)	HARDNESS (GPa)	$-\frac{\Delta V}{V}$	$\Delta\left(-\frac{\Delta V}{V}\right)$[1]
300	8.2	0.2	0.03
200	8.4	0.16	0.04
100	8.4	0.17	0.04
50	8.6	0.21	0.03
25	8.7	0.25	0.03
15	8.3	0.30	0.03

Table 4.1 Change in the volume of an indentation after load removal.

4.1.4. TEM Observations

The SEM observations described in Section 4.1.2. provided information on the macroscopic pattern of deformation and fracture, while the AFM studies added depth information. Both techniques were used to gather detailed information about the surface topography, cracking and deformation around indentations made with a range of loads. However, this information only represents the intersection of the deformed zone with the surface. A complete understanding of the deformation produced during indentation requires that information be gathered from the entire deformed volume and the identification of defects within this volume. These two goals can be readily accomplished with TEM studies. When considering the TEM results in terms of the SEM and AFM results already presented it is important to remember that all of the indentations studied with TEM were made with an applied load of 5 grams. This was the smallest load used in SEM studies.

[1] Based on root mean squrare calculation with 3% error in inputs.

The TEM results will be divided into three groups: the geometry of the plastic zone, defect analysis and analysis of crystal rotations.

4.1.4.1. The Geometry of the Plastic Zone

A low magnification bright field micrograph of an indentation made with the edges of the indenter aligned parallel to ⟨110⟩ directions is shown in Figure 4.10 (a). This micrograph was taken with the beam direction (**B**) parallel to [001]. The accompanying selected area diffraction pattern (SADP) is shown in Figure 4.10 (b). There are three features that dominate the bright field image.

First, there is a high density of traces along ⟨110⟩ directions that form a series of concentric squares directly under the indenter. The square pattern was produced because the traces along [110] ended when they intersected the equivalent traces along $[1\,\bar{1}\,0]$. Extension of a trace beyond this point of intersection was rarely seen and the density of traces was quite high, with one trace approximately every 25 nm (Figure 4.10 (a)). This spacing was constant over the entire region where traces were found. However, in all indentations that were studied these traces were absent from the central portion of the deformed zone.

Second, arrays of dislocations extended away from the indentation along ⟨100⟩ directions. Dislocations lying on either {101}or {103} planes would fit these observations. These arrays appear to originate at the mid-point of the traces along ⟨110⟩ directions. In this orientation this location corresponds to the mid-point of the indenter's edges. In some cases, long straight dislocations that produce a trace along ⟨100⟩ were also seen. Lastly, there were many bend contours around the indentation. These contours, like

the dislocation arrays, appear to originate at the mid-point of the edges (eg. upper left side of indentation in Figure 4.10(a)).

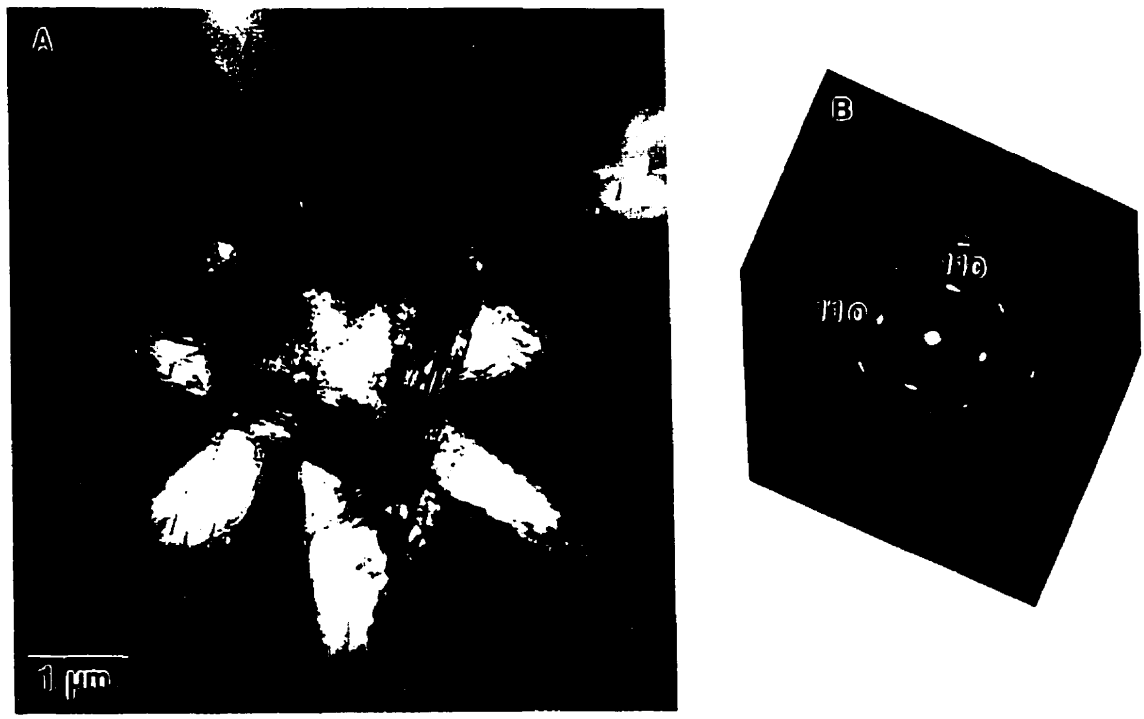

Figure 4.10 (a) Bright Field image, **B**=[001] and (b) SADP of an indentation made with the edges of the indenter aligned with ⟨110⟩ directions.

There are three important features in the accompanying SADP, shown in Figure 4.10 (b). First, streaks along ⟨110⟩ directions connect the (110) diffraction spots. This orientation suggests the streaks are related to the traces along ⟨110⟩ directions seen in the bright field image (Figure 4.10 (a)). Second, the diffraction spots have been radially streaked to form short arcs. Lastly, forbidden diffraction spots are present in the pattern. One example of the extra spots is arrowed in Figure 4.10 (b). Each of these features will be discussed in more detail later.

Figure 4.11 is a stereo pair of an indentation made with the edges of the indenter parallel to ⟨110⟩ directions. The foil was oriented such that the indented surface pointed into the page. The stereo pair indicate that the distance between the squares of slip traces along ⟨110⟩ directions and the indented surface increases as the size of the square decreases. This configuration implies that the defects creating the traces follow the shape of the indentation, i.e. the traces in the centre lie farthest from the indented surface. The configuration of slip on {110} planes also explains the absence of these traces in the centre of the indentation.

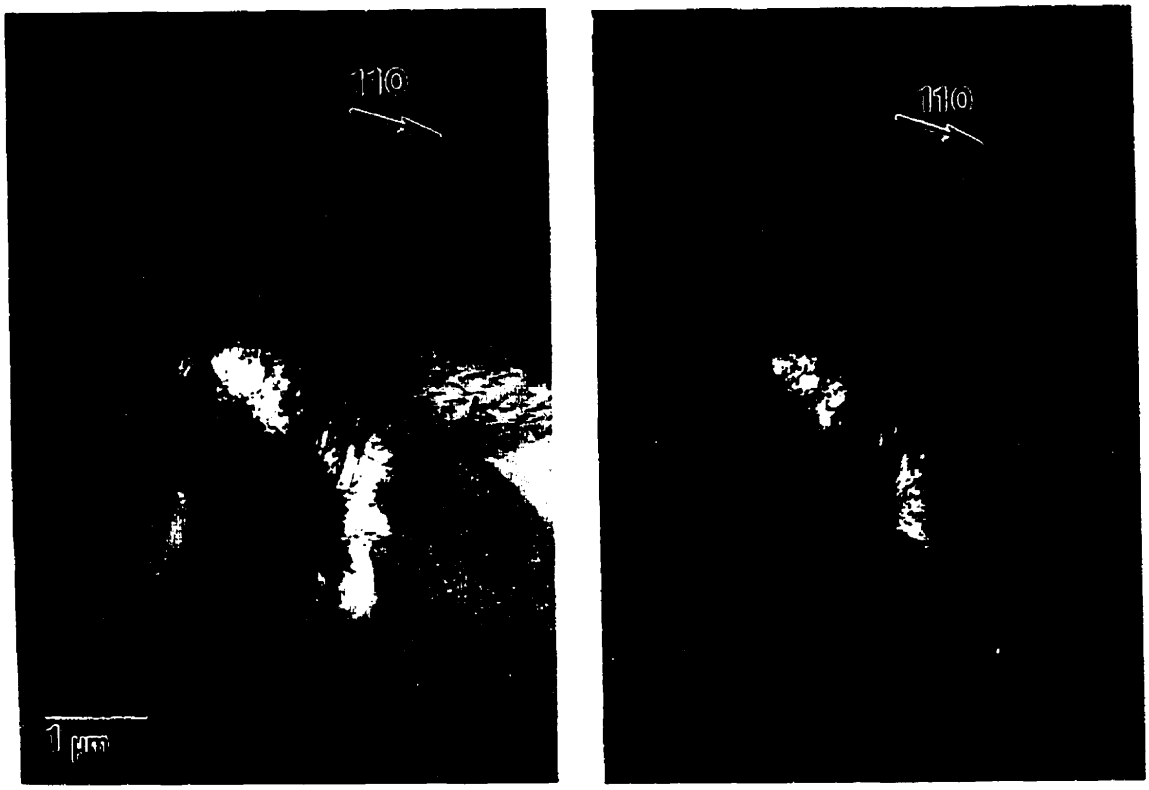

Figure 4.11 Stereo pair of an indentation that was made with the edges of the indenter aligned with ⟨110⟩ directions.

During final thinning of the TEM foil the foil was milled from the back side. Therefore, the traces furthest from the surface, which are found in the centre of the indentation, were probably removed during final thinning. The diagonals of the indentation are also visible in this stereo pair. In this orientation the diagonals lie along ⟨100⟩ directions. The diagonals ended at the corner of the largest of the squares formed by the traces along ⟨110⟩ direction. Thus, the defects creating these traces only occur directly under the indentation as discussed in Section 4.1.2.

When the indentation was made with the diagonals of the indenter aligned parallel to ⟨110⟩ directions the defect structure was very similar to that described above. A low magnification image of an indentation made with this orientation of indenter is shown in Figure 4.12 (a) and the accompanying SADP is shown in Figure 4.12 (b). Again traces lying along ⟨110⟩ directions were seen under the indentation and dislocation arrays extended out from the indentation along ⟨100⟩ directions. In this orientation the dislocations extending along ⟨100⟩ directions originated at the corners of the indentation. It should also be noted that there is much less bending around the indentation. The CBED pattern shown in Figure 4.12 (b) was taken beside the indentation, therefore it does not show any of the additional features noted in Figure 4.10 (b).

A stereo pair of an indentation made with the diagonals of the indenter aligned parallel to ⟨110⟩ directions is shown in Figure 4.13. The geometry of the deformed zone is the same as the other indenter orientation. Once again, the diagonals of the indenter can be seen due to the higher defect density along these directions and the diagonals end at the outermost trace along ⟨110⟩. It is also possible to see the edges of the indentation, which lie along ⟨100⟩ directions. The visibility of the edges is again due to the higher dislocation density along these directions. Since the edges of the indenter form straight lines between

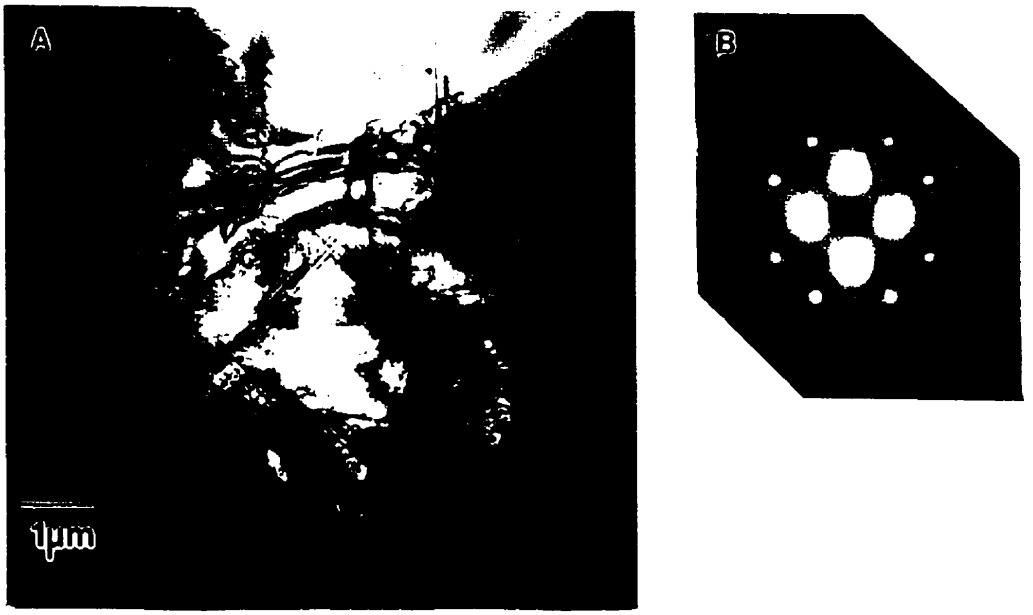

Figure 4.12 (a) Bright Field image, **B**=[001] and (b) SADP of an indentation made with the diagonals of the indenter aligned with ⟨110⟩ directions.

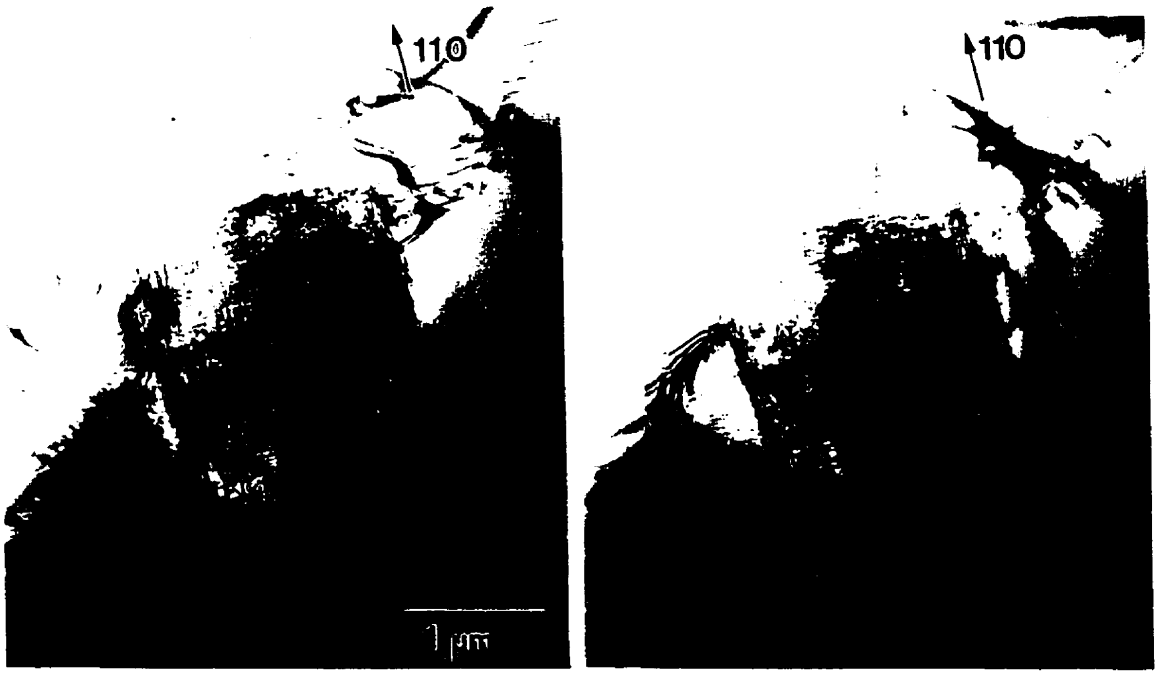

Figure 4.13 Stereo pair of an indentation that was made with the diagonals of the indenter aligned with ⟨110⟩ directions.

the mid-point of the traces along ⟨110⟩ directions, the point where the ⟨110⟩ traces intersect is not under the indentation. This is in agreement with SEM observations. Schematic diagrams of the plastic zones for the two indenter orientations are shown in Figure 4.14.

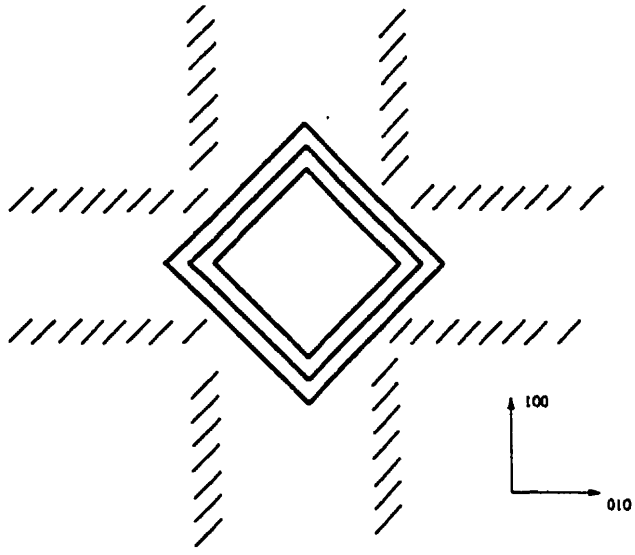

Figure 4.14 Schematic diagram of the plastic zone produced with the two orientations of indentations.

To summarize, a high density of traces along ⟨110⟩ directions form squares directly under the indentation. Stereo pairs have shown that these traces map out a pyramid whose apex points into the sample. A set of dislocations lying along ⟨100⟩ directions extended away from the indentations. These two features were common to indentations made with two different indenter orientations. The most obvious difference between indentations made with different indenter orientations is the extent of foil bending, which is much larger when the edges of the indenter were parallel to ⟨110⟩ directions.

4.1.4.2. Defect Analysis

The details of the defect analysis will not be given separately for each indenter orientation due to the similarity of these structures. The dislocations that form arrays along ⟨100⟩ directions will be discussed first.

A low magnification bright field micrograph of the dislocations that extend along ⟨100⟩ directions shown in Figure 4.15. The labeled dislocations (A-E) will be analyzed in the Burgers vector (**b**) and line direction (**u**) determinations that follow. Four micrographs of the dislocation array containing dislocation 'C' that were taken under different diffracting conditions are presented in Figure 4.16. The dislocations produced strong contrast when the operating reflection (**g**) was equal to $\bar{1}\,\bar{1}0$, $1\,\bar{1}0$ and 200, Figures 4.16 (a), (d) and (c) respectively. Invisibility of the dislocations was obtained when the image was formed with an $0\bar{2}0$ reflection, Figure 4.16 (b). Thus, **b** is equal to [100].

Many of the dislocation images showed considerable residual contrast when the **g**.**b**=0 criterion was satisfied. As outlined in Section 3.6.1 such contrast could result from either the mixed nature of the Burgers vector or the anisotropy of the crystal's elasticity. Therefore, in order to verify the Burgers vector determinations based on the **g**.**b**=0 criterion computer simulations of the experimental images were produced. Successful matching of the simulated and experimental images confirmed the identity of the Burgers vector.

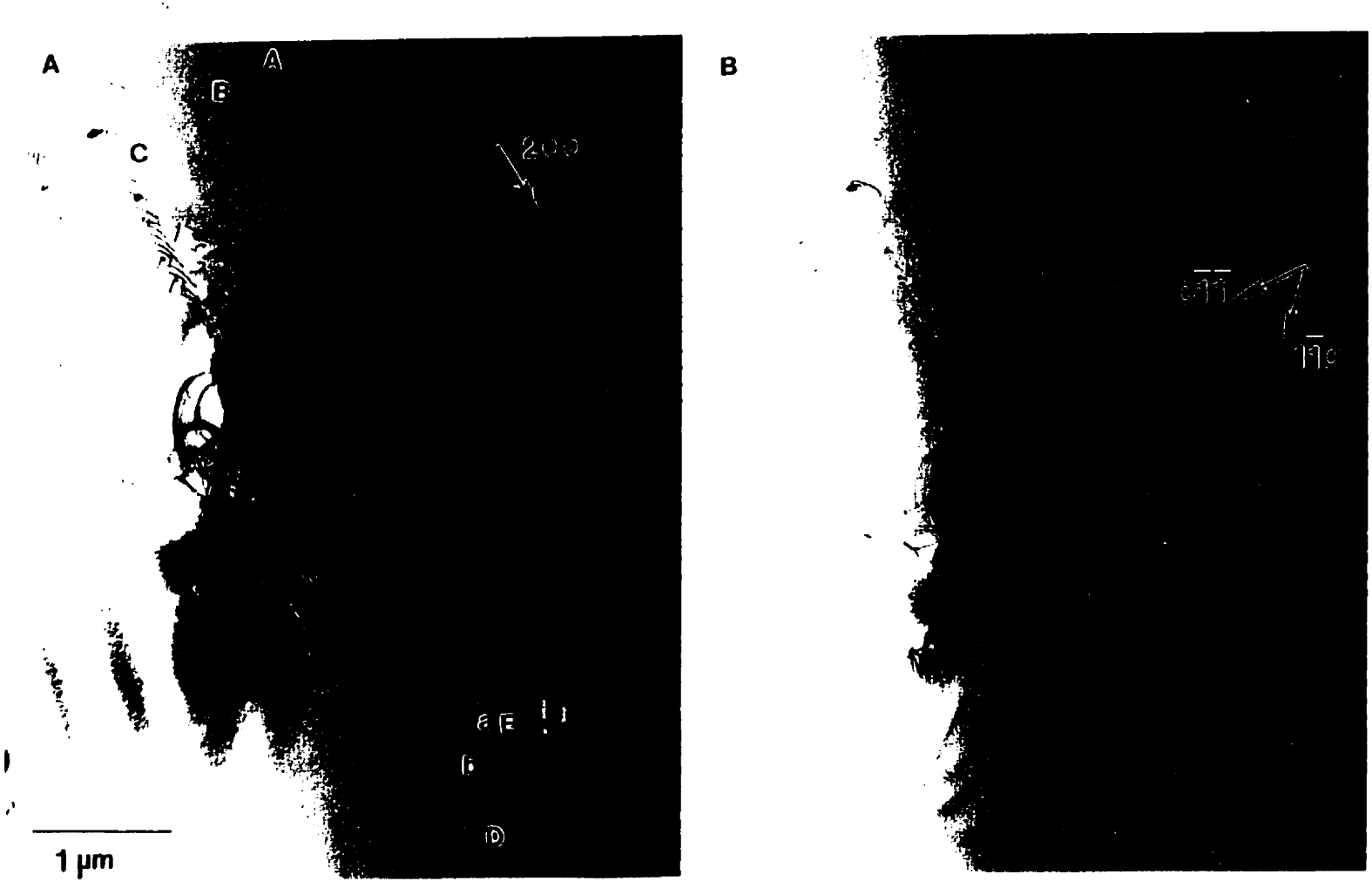

Figure 4.15 Bright Field micrographs of dislocations that extend from the indentation along ⟨100⟩ directions; g= 200 in (a) and g=$1\bar{1}0$ in (b).

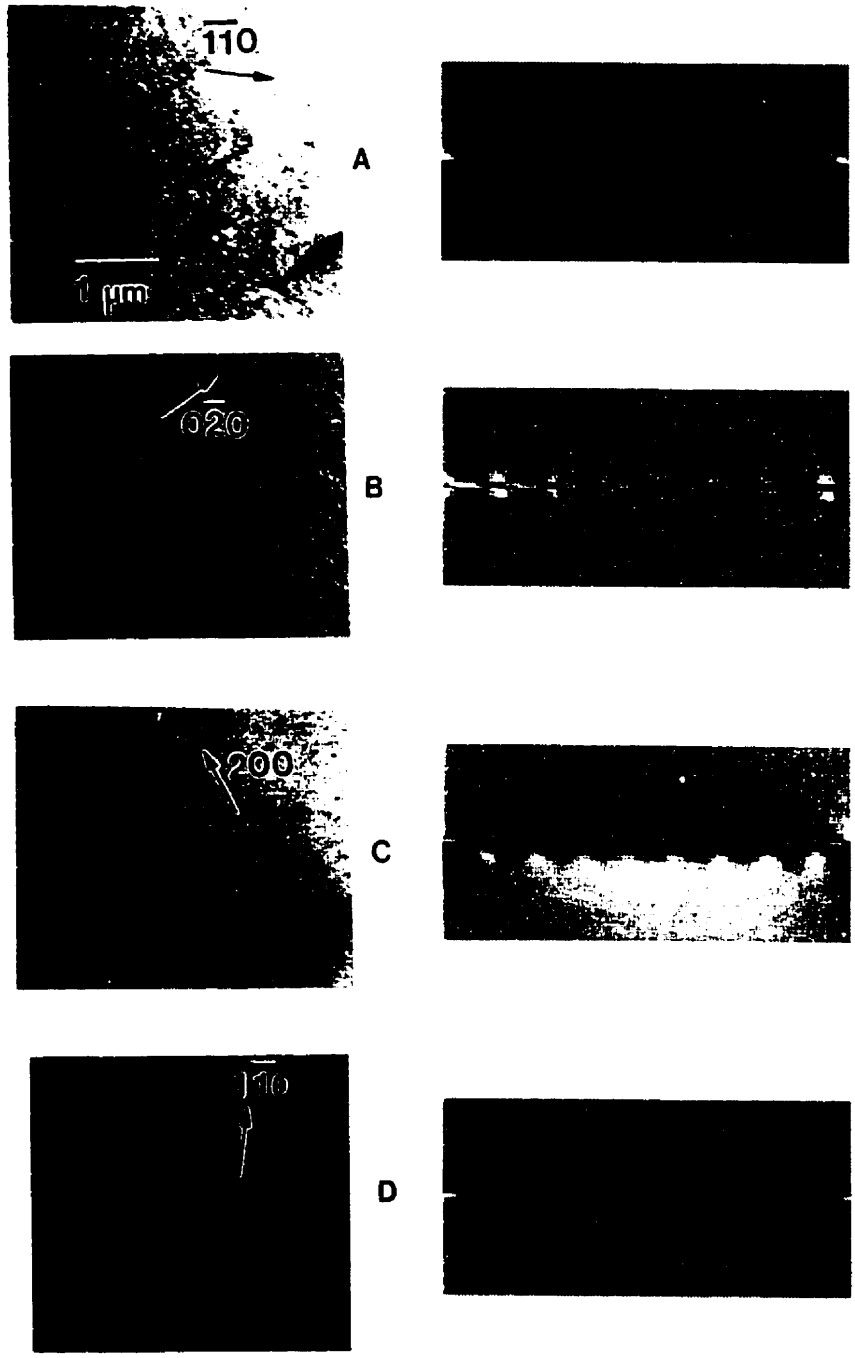

Figure 4.16 Bright Field and simulated images of dislocation 'C' in Figure 4.15; **g**= $\bar{1}\,\bar{1}0$ in (a), **g**= $0\bar{2}0$ in (b), **g**= 200 in (c) and **g**=$1\,\bar{1}0$ in (d).

Simulated images for each diffracting condition are presented in Figure 4.16. The simulations used **b**=[100], **u**=$[1\,\bar{1}\,1]$, and a crystal thickness of 2400 Å. All of the simulated images agree with the experimental images, confirming that the Burgers vector of these dislocations is [100]. During image simulation it was found that the contrast in the computed images was very sensitive to deviations from the Bragg condition.

The line direction of all the labelled dislocations, Figure 4.15, is given in Table 4.2. The details of the line direction determination for dislocation 'C' are presented in Appendix A. As can be seen in Table 4.2, **u** is equal to $\langle 1\,1\,1 \rangle$ and the slip plane is either (011) or $(0\,\bar{1}\,1)$ for all the dislocations. This line direction makes a 63° angle with the Burgers vector. The slip plane was also determined by tilting experiments. For example, the slip plane that contains dislocation 'C' is almost edge on in Figure 4.15 (b). The micrograph was taken with **B**≈[$\bar{1}\,\bar{1}\,1$]. The accompanying diffraction pattern indicates that the $(0\,\bar{1}\,\bar{1})$ plane produces a trace that is parallel to the trace produced by the plane containing the dislocations. Thus, these dislocations lie on an $(0\,\bar{1}\,\bar{1})$ plane, in agreement with the trace analysis results.

Dislocation	Line Direction	Burgers Vector	Slip Plane
A	$[\bar{1}\,1\,1]$	[100]	$(0\bar{1}\,1)$
B	[1 1 1]	[100]	$(0\bar{1}\,1)$
C	$[\bar{1}\,\bar{1}\,1]$	[100]	(0 1 1)
D	$[1\,\bar{1}\,1]$	[100]	$(0\bar{1}\,\bar{1})$
E (a)	$[\bar{1}\,1\,1]$	[100]	$(0\bar{1}\,1)$
E (b)	$[\bar{1}\,\bar{1}\,1]$	[100]	(0 1 1)

Table 4.2 Line direction and slip plane results for dislocations in Figure 4.15.

The second feature noted in Figure 4.10 (a) was the trace along ⟨1 1 0⟩ directions. The first step in identifying these features was to identify the plane on which they lay. Figure 4.17 (a) is a bright field micrograph (**B**=[001]) that clearly shows these traces. In this particular example a portion of the indentation has been removed during foil preparation. The corresponding diffraction pattern, Figure 4.17 (b), contains streaks along ⟨1 1 0⟩ directions. An unambiguous link between the traces and the streaks in the diffraction pattern was obtained with dark field microscopy. Dark field micrographs formed from the streaks along ⟨1 1 0⟩ directions are shown in Figure 4.17 (c) and (d). These dark field micrographs indicate that the defects which produced the traces seen in bright field were also responsible for the streaks in the diffraction pattern.

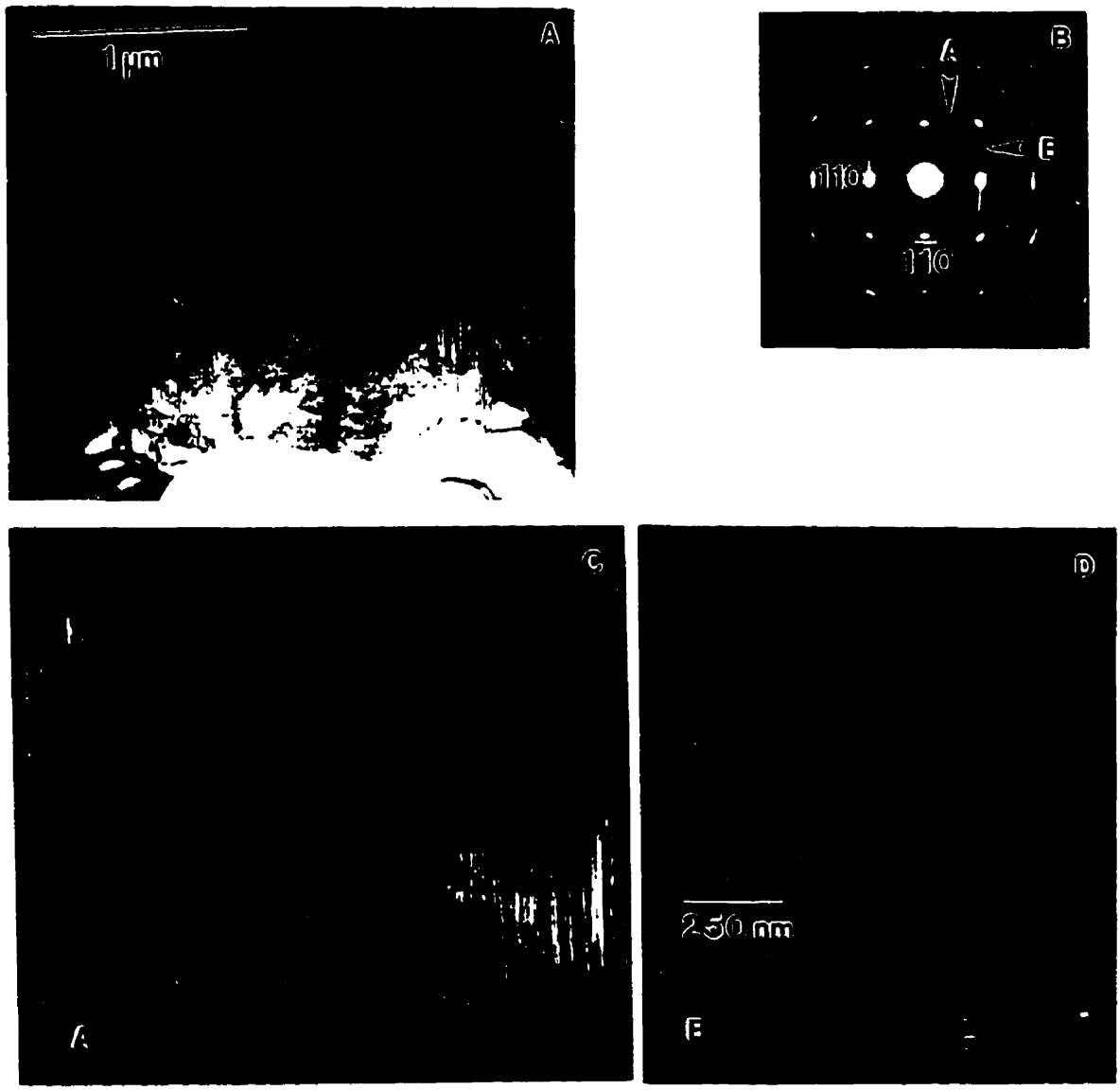

Figure 4.17 Micrographs illustrating the relationship between the features seen in the diffraction pattern and the traces along ⟨110⟩ directions; (a) BF image, **B**=[001], (b) SADP, **B**=[001], (c) and (d) DF micrographs formed with features A and B, respectively, in (b).

Such streaking in a diffraction pattern is a result of the intensity distribution in reciprocal space (Hirsch et.al. 1977). This distribution is a function of the shape of the diffracting body. A plate-like crystal will produce a spike in diffracted intensity along the normal to the plate. Therefore, the defects creating these streaks lie on $\{110\}$ planes and have a plate-like shape. Stacking faults or thin twins are two possible planar defects. It should be noted that the $\{110\}$ planes highlighted in dark field were normal to the streak used to form the image. In Figure 4.10 (a) it was noted that the traces were approximately 25 nm apart. Such a high density of defects is in agreement with the intensity distribution seen in the diffraction patterns.

The planar defects on $\{110\}$ planes were always found in the most highly deformed region directly under the indentation. The high density of defects and large strain gradients in this area made contrast analysis very difficult. Furthermore, analysis of these planar defects required that the crystal be tilted away from the [001] zone. However, tilting experiments in this region of high fault density caused the fault images to overlap. Such overlapping fault images further complicated the contrast analysis. For these two reasons considerable effort was exerted finding isolated examples of faults that were removed from the indentation.

Figure 4.18 shows such an example, although there are regions where there are defects on nearby $\{110\}$ planes. The accompanying diffraction pattern (Figure 4.18 (b)) does not contain any extra diffraction spots. When the foil normal was tilted away from the [001] zone axis a number of narrow sets of fringes were visible (Figure 4.18 (b) and (c)). These two observations suggest that these planar defects are in fact stacking faults. The micrograph in Figure 4.18 (c) does not fully agree with observations made with **B**= [001] (Figure 4.18(a)). In the latter figure the trace along $\langle 110 \rangle$ appears continuous, from the

edge of the indentation to the end of the trace, while, when tilted away from [001], the stacking faults appear to be isolated.

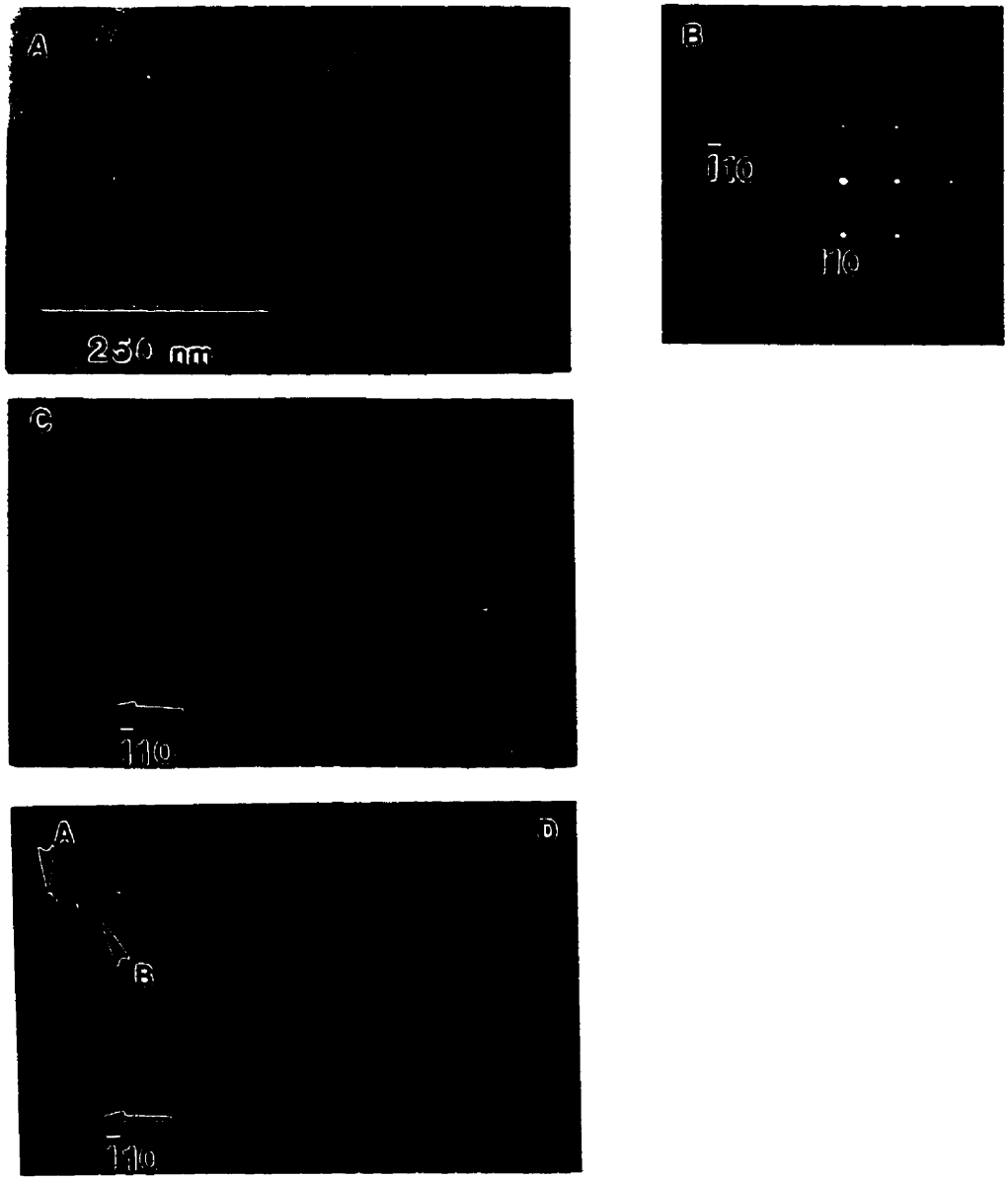

Figure 4.18 Analysis of defects which created the traces along ⟨110⟩ directions; (a) BF image **B**=[001], (b) SADP, **B**=[001], (c) BF image, tilted away from **B**=[001], **g**=$\bar{1}$10 and (d) WBDF, **g**=$\bar{1}$10.

When a weak beam dark field (WBDF) micrograph of the region was formed (Figure 4.18 (c)) a second set of fringes was visible. This suggests that there are stacking faults with different displacement vectors on the {110} planes. These two faults will be referred to as Type A (strong fringe contrast in BF (g=110)) and Type B (weak fringe contrast in WBDF (g=110)). The Type B stacking faults were found to lie between two Type A stacking faults. This arrangement of the two stacking faults was commonly observed. Another example of this stacking fault arrangement is shown in the BF-WBDF pair (g=110) in Figure 4.19. The occurrence of stacking faults with different displacement vectors on {110} planes suggests that slip on {110} planes occurs via the glide of a series of partial dislocations. It should be noted that in some cases (e.g. Figure 4.18(c)) the Type B fault ended without the presence of a Type A fault.

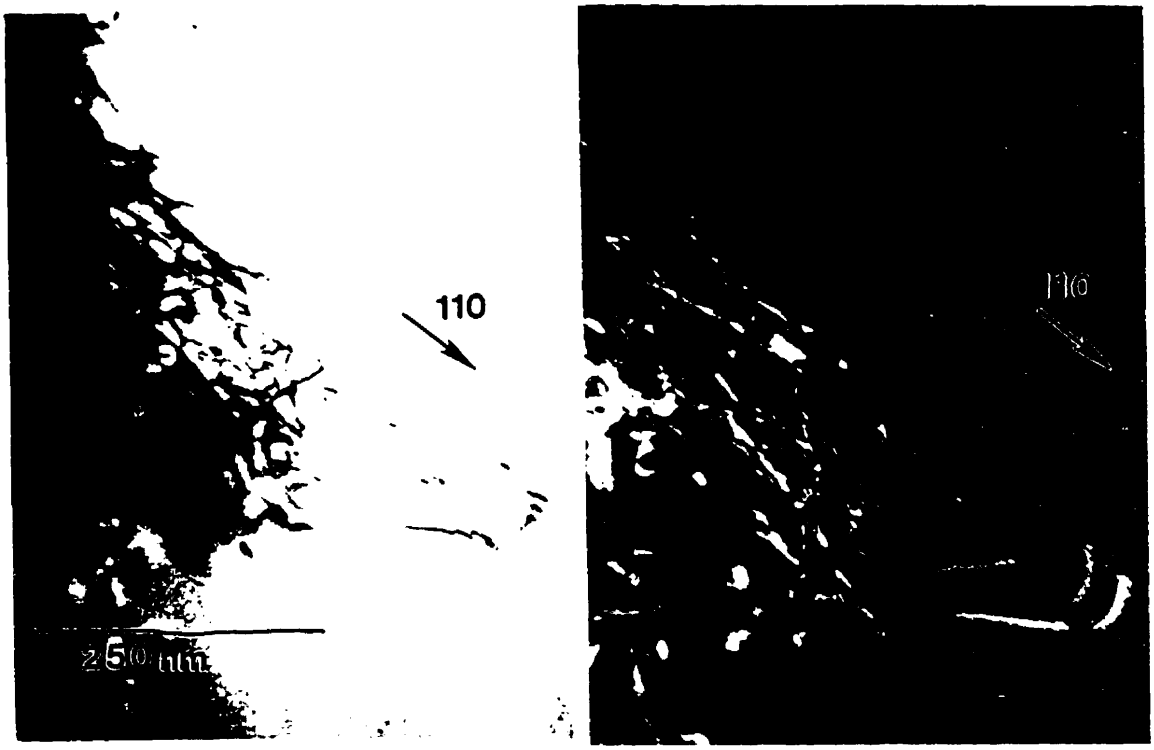

Figure 4.19 BF-WBDF pair illustrating the different displacement vectors of the two stacking faults.

The displacement vector (**R**) of the Type A and B stacking faults was determined for the faults shown in Figure 4.20 (a). This particular example was quite close to the indentation, the corner of which can be seen in the lower right corner of the micrograph. However, there were no faults on adjacent $\{1\,1\,0\}$ planes and the diffracting conditions were constant over a large enough region to conduct contrast analysis.

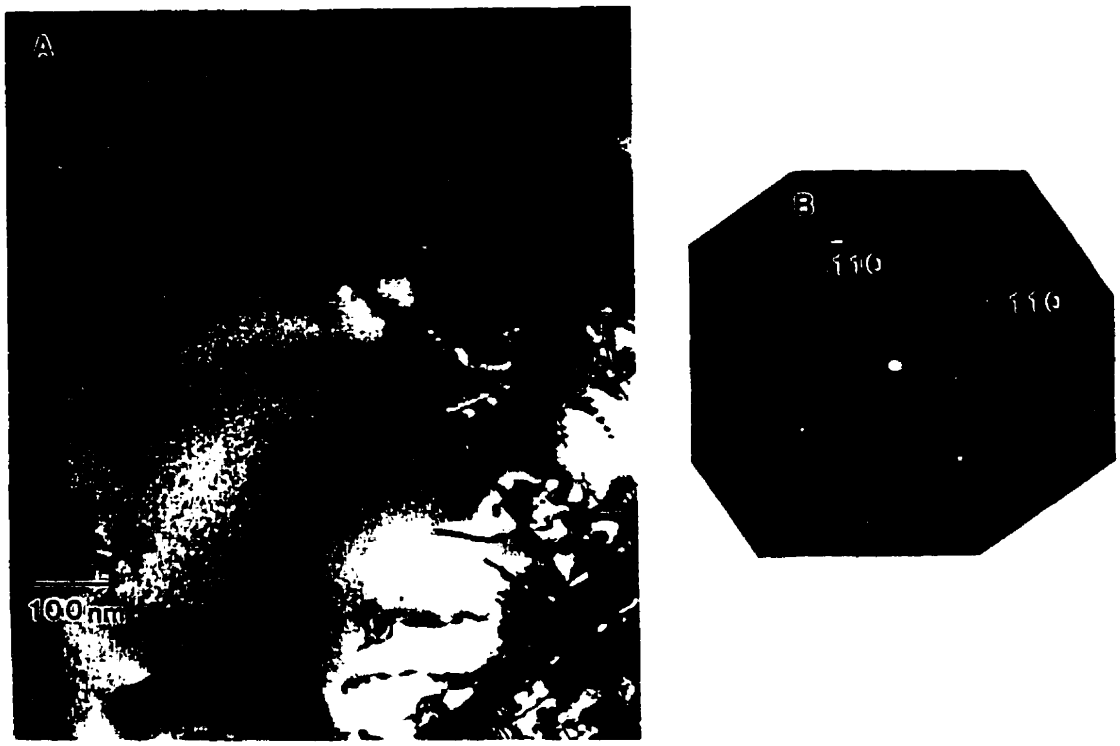

Figure 4.20 (a) BF image, **B**=[001] and (b) SADP, **B**=[001] from region used to identify the displacement vector of the stacking faults on $\{1\,1\,0\}$ planes.

The BF and WBDF micrographs ($\mathbf{g}=\bar{1}\,1\,0$) shown in Figure 4.21 (a) and (b), respectively, again display the same contrast for both Type A and B faults described earlier. The high density of stacking faults directly under the indentation) can also be seen in these micrographs. Figures 4.21(c) to (g) show a series of bright field micrographs taken with

various reflecting conditions. In each case there was no deviation from the Bragg diffracting condition ie. s=o. The fringes of stacking fault A are invisible for **g**= 0 1 1 and 213 while those of stacking fault B are invisible for **g**=$1\,\bar{1}\,0$ and 200. These invisibility conditions are satisfied when **R** equals $\frac{1}{4}[1\,\bar{1}\,1]$ and $\frac{1}{2}[001]$ for Type A and B faults, respectively.

While it was possible to identify the displacement vector of these stacking faults the partial dislocations associated with them could not be conclusively identified. In Figure 4.21 (a) the dislocation at the end of such a fault is marked. In this Figure, it is not apparent that **b**=$\frac{1}{2}[001]$, as the dislocation appears to be in contrast for **g**=1 1 0. However, Kad et.al. (1995) found that $\frac{1}{2}[001]$ dislocations were visible when **g**=1 1 0 due to **g.bxu** contrast. Considering the values found for $\mathbf{R}_f$ and the nature of residual contrast produced by a $\frac{1}{2}[001]$ dislocation by Kad et.al. (1995) it is likely that the dislocation in Figure 4.21 (a) has a $\frac{1}{2}[001]$ Burgers vector.

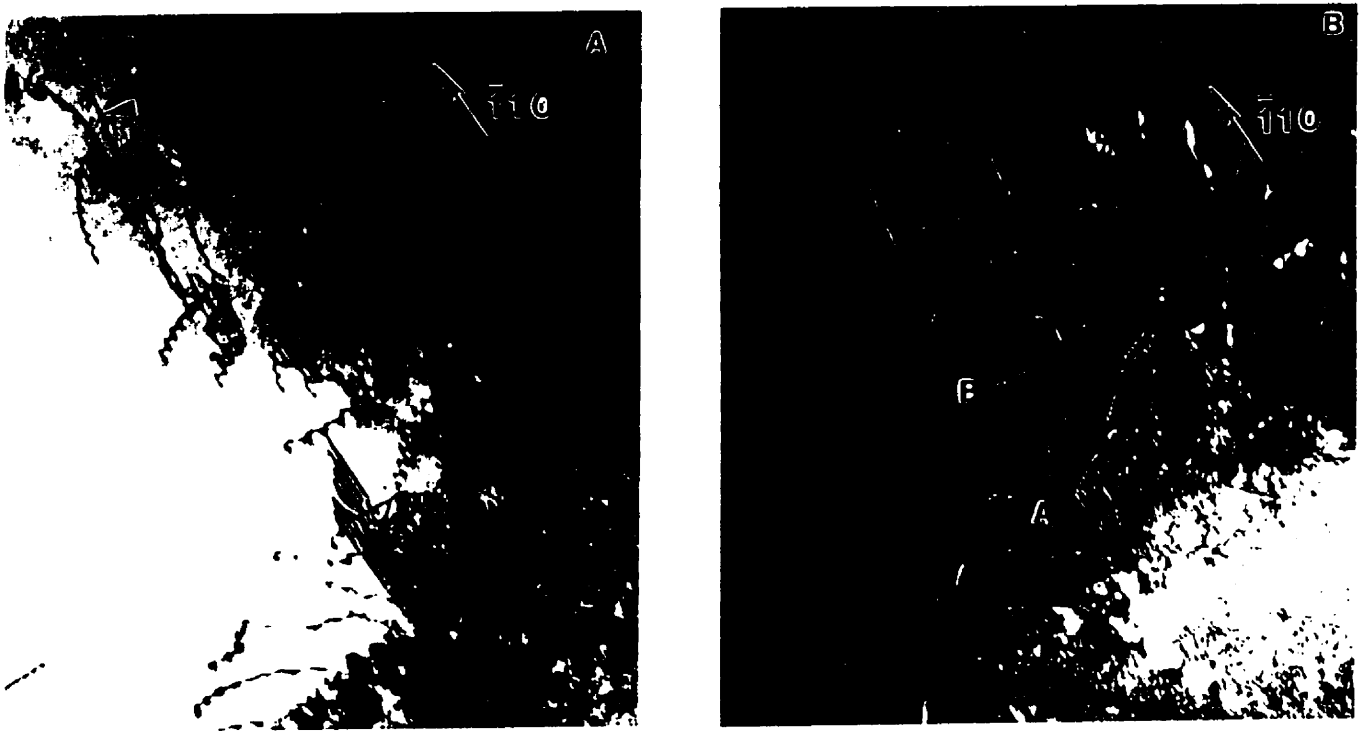

Figure 4.21 Images, formed with various difrracting conditions, of the stacking faults shown in figure 4.20 used to determine $\mathbf{R}_f$ for Type A and B faults; (a) BF **g**= $\bar{1}10$, (b) WBDF **g**= $\bar{1}10$, (c) BF **g**=101, (d) BF **g**=011, (e) BF **g** =020, (f) BF **g**=213 and (g) BF **g**= $21\bar{3}$.

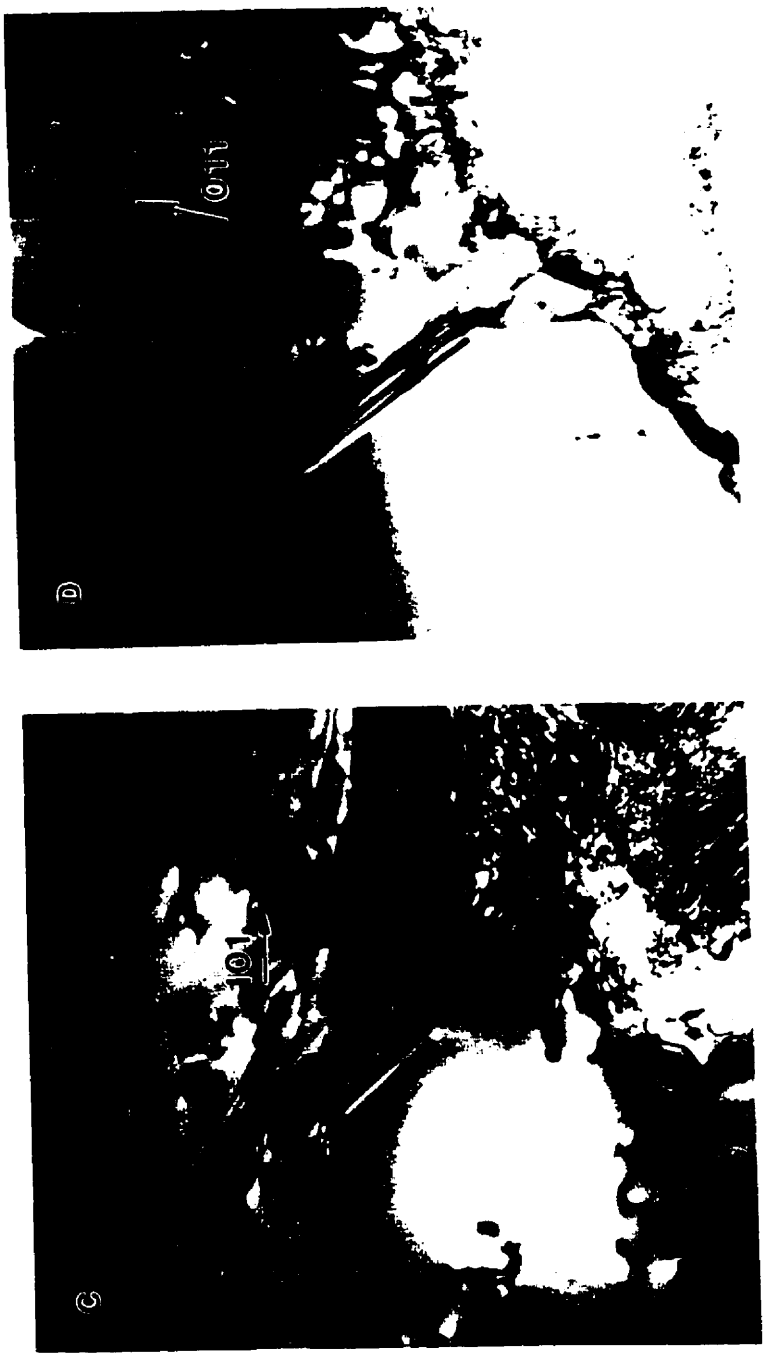
a
[110]
b
[01]

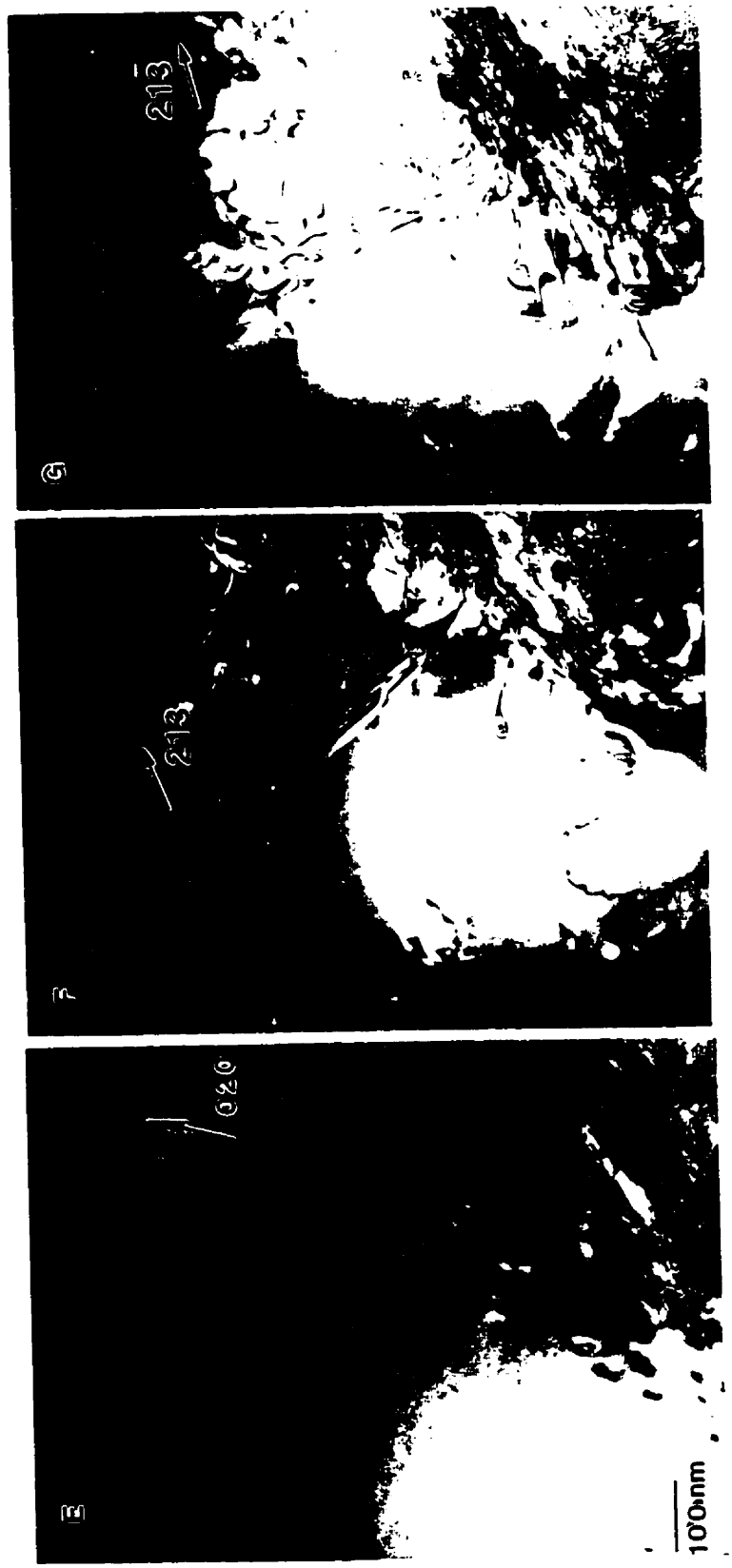
020
213
213
100nm

4.1.4.3. Rotations

The high density of defects in the plastic zone under an indentation was evident in both the bright field images and diffraction patterns. The streaks produced by the high density of stacking faults on $\{110\}$ planes have already been discussed. There are two other features of the diffraction pattern that were related to the deformation produced during indentation. Extra diffraction spots appeared in the pattern, and all the diffracted spots were radially streaked. The origin of these latter two features of the diffraction pattern will now be discussed. The number and intensity of these extra reflections was found to depend on the region of the deformed zone being studied.

Figure 4.22 (a) and (b) are SADPs of an indentation that was made with the edges of the indenter aligned parallel to $\langle 110 \rangle$ directions. Figure 4.22 (c) and (d) are SADPs of an indentation made with the edges of the indenter aligned parallel to $\langle 100 \rangle$ directions. In Figure 4.22 (a) the diameter of the selected area aperture was approximately 1.5 times the edge length of the indentation, while in (b) the aperture had a diameter that was only 0.5 times the edge length. Therefore, only diffraction information from within the area bounded by the stacking faults on $\{110\}$ planes was collected with the smaller diameter aperture. When the large aperture was used (Figure 4.22 (a)), the [001] diffraction spots were the dominant feature. However, when information was only collected from underneath the indentation the extra spots became the dominant feature. In fact only the 110, 200 and 220 primary spots were clearly visible.

The spots that lie within the first order [001] diffraction spots are at a radius (from the transmitted beam) that is 0.76 times the distance to the $\{110\}$ spots. This corresponds to a spacing of 2.96 Å, the interplanar spacing of $\{101\}$ planes. This identification agrees with their position along the 020 systematic row. When the smaller selected area aperture

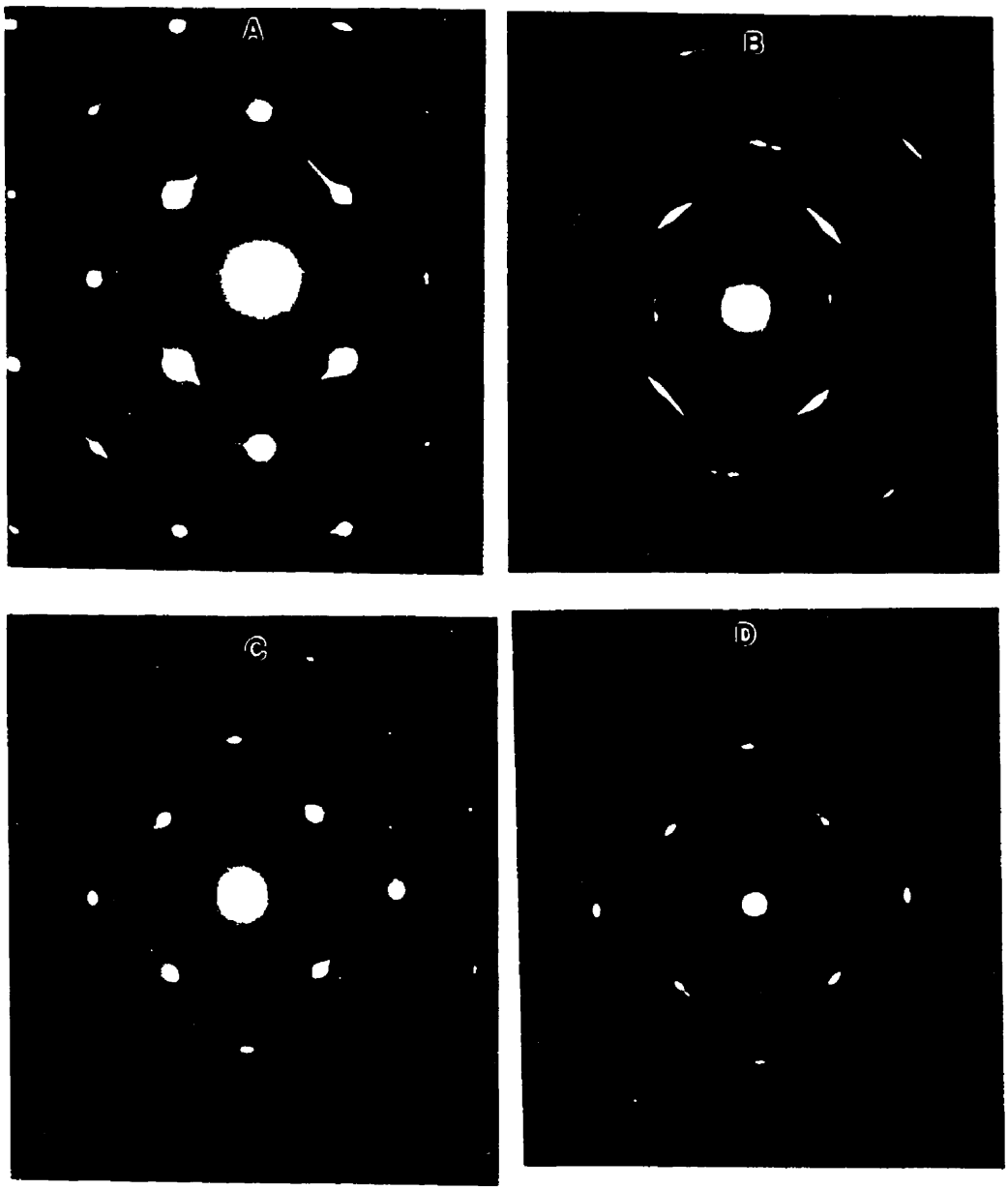

Figure 4.22 SADPs of an indentation made with the edges of the indenter aligned with $\langle 110 \rangle$, (a) and (b), and $\langle 100 \rangle$ directions, (c) and (d).

was used the diffraction spots from the [001] zone were barely visible (Figure 4.22 (b)). It was noted earlier that these spots are actually arcs. In this figure it is apparent that the arcs are a series of discrete spots, each coming from a region in the crystal of slightly different orientation. If the arcs lying at the same distance from the transmitted beam were joined, the $MoSi_2$ ring pattern would be produced. Such a ring pattern is shown in Figure 4.23 (e). This suggests that the crystal under an indentation has been "broken up" into small volumes that have been rotated into a variety of orientations.

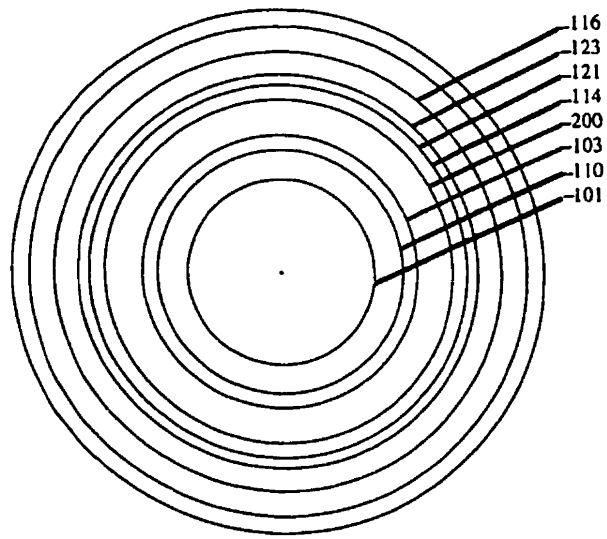

Figure 4.23 Polycrystalline ring pattern for $MoSi_2$.

The origin of these extra diffraction spots was investigated with dark field microscopy. A bright field micrograph (**B**=[001]) and the accompanying SADP are shown in Figure 4.24 (a) and (b), respectively. Again, the selected area aperture was chosen such that only information from the deformed material under the indentation was collected. Dark

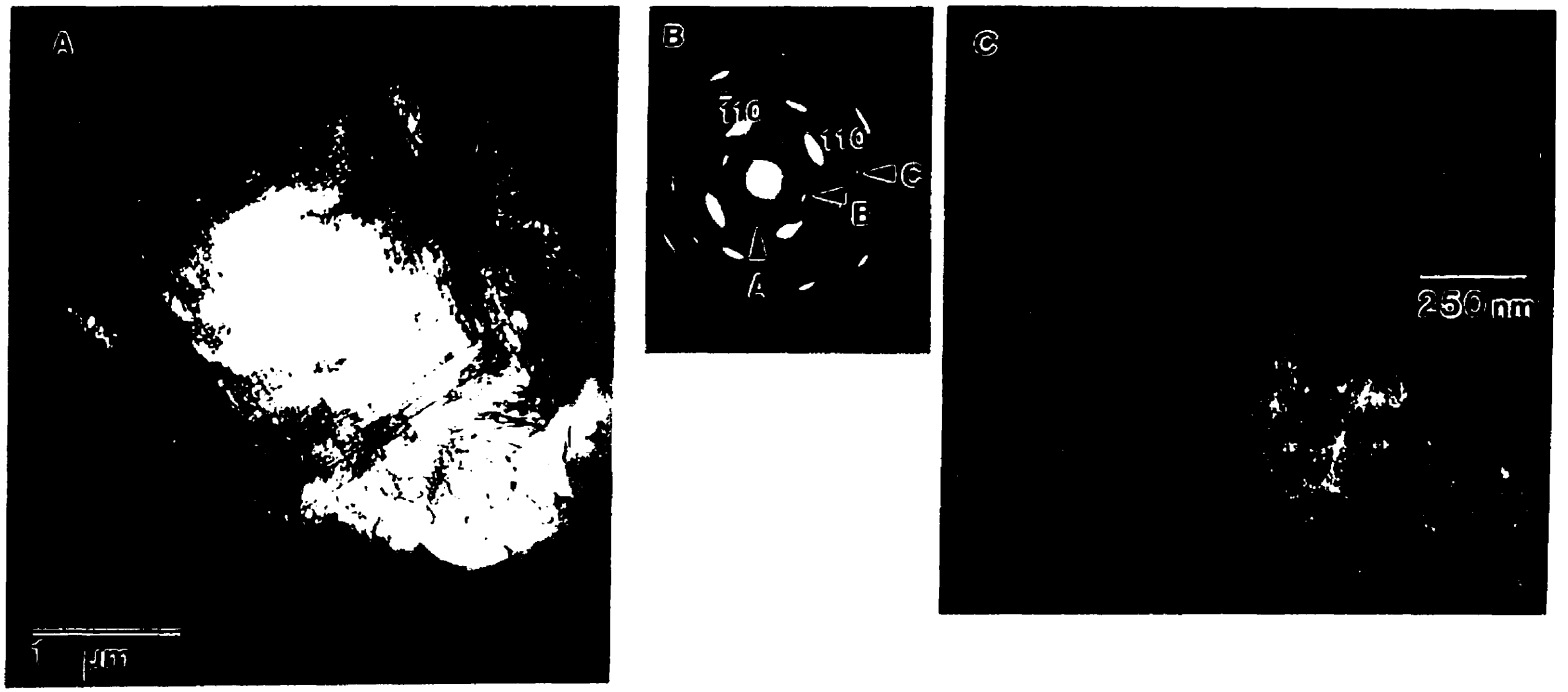

Figure 4.24 Analysis of 'extra' spots seen in SADPs taken from the centre of the indentation. (a) BF micrograph, **B**=[001], (c), (d) and (e) are DF micrographs formed form the diffraction spots A,B and C, respectively.

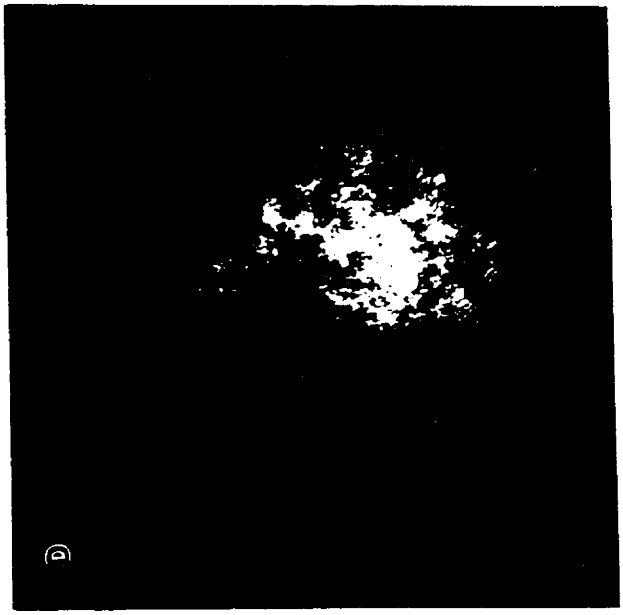

field micrographs using the extra spots A, B and C are shown in Figures 4.24 (c), (d) and (e), respectively. The dark field images have a speckled appearance indicating that there are a large number of small crystallites at this orientation. When the foil was tilted during dark field imaging the location of the areas producing contrast changed. This suggests that these small volumes of material are at slightly different orientations and can be brought into the Bragg diffraction condition by tilting. When the indentation was made with the indenter's diagonals parallel to ⟨1 1 0⟩ the magnitude of the rotations was not as large. This is seen in Figure 4.22 (c) and (d) where the magnitude of both types of rotations is much smaller. Even when the selected area aperture only sampled diffraction information from under the indentation, the intensity of the extra spots was always lower than the primary [001] spots.

The radial streaking of the diffraction spots indicates that material had been rotated by about 15° about the [001] zone axis. The magnitude of this rotation is equal to the angle subtended by the arcs that have been created. This angle was measured for the [001] spots and found to be 15°.

In-situ annealing experiments were conducted on indentations made on (001) planes. Figure 4.25 (a) is a bright field micrograph (**B**=[001]) of an indentation after annealing at 750 °C for two hours. This indentation was made with the edges of the indenter aligned with ⟨1 1 0⟩ directions. The dislocation structure around the indentation appeared quite similar to that in unannealed samples. The only noticeable difference is the absence of bend contours. The SADP has however undergone considerable change. The accompanying SADP is shown in Figure 4.25 (b). Both the radial streaking of diffraction spots and the extra spots are largely absent from this pattern. However, the streaks along ⟨1 1 0⟩ directions are still quite strong. The presence of streaks along ⟨1 1 0⟩ directions is not unexpected since the stacking faults are still visible in the BF image.

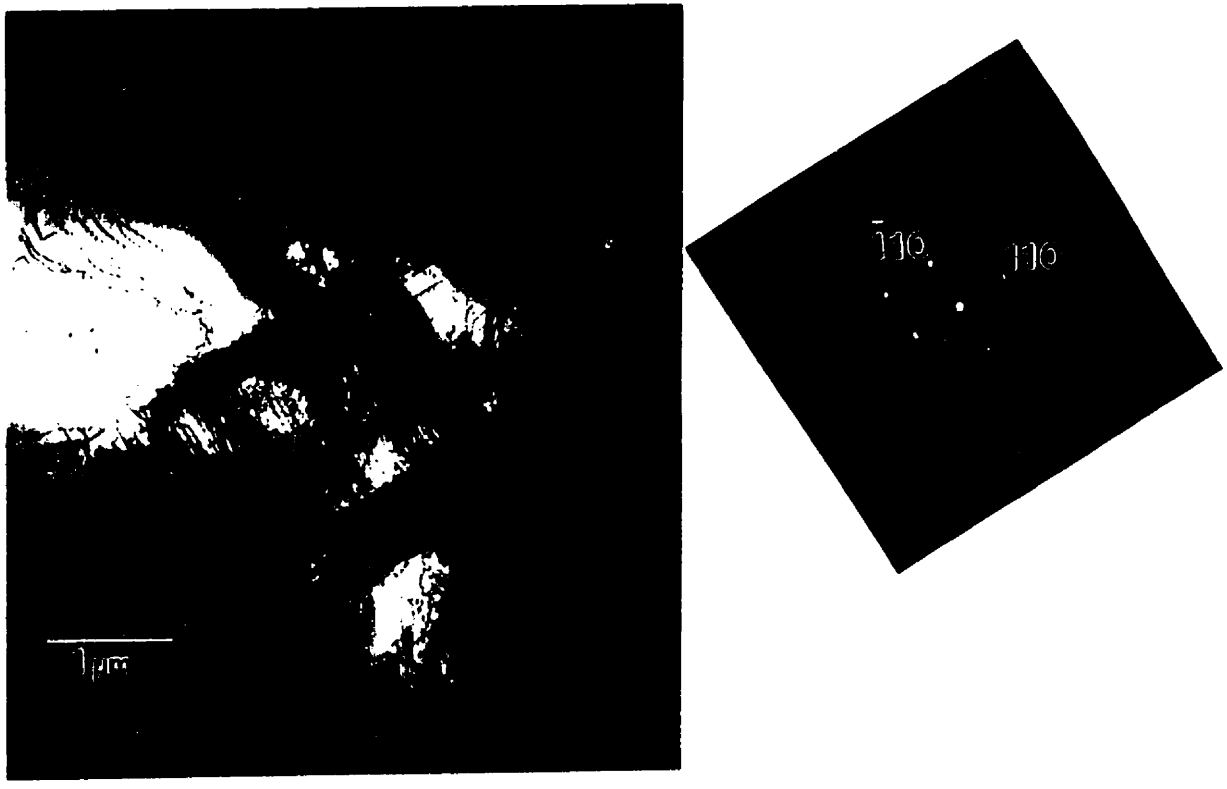

Figure 4.25 Bright Field micrograph (a) and SADP (b) of an indentation that was in-situ annealed for two hours at 750°C.

4.2. (010) Surface

4.2.1. Hardness Measurements

A hardness versus applied load curve for indentations made with the edges of the indenter aligned parallel to [100] and [001] directions is shown in Figure 4.26. The hardness remained constant at approximately 10 GPa for all applied loads. However, there was considerable scatter in the results. This scatter was due to the difficulties measuring the diagonal length. At larger loads (>105 grams) the corners of the indentation were offset on either side of the cracks. At smaller loads the pattern of slip did not produce well defined edges around the indentation.

When the indenter's diagonals were parallel to [100] and [001] directions the hardness versus applied load curve (Figure 4.27) was very similar to the curves for indentations on an (001) plane. The hardness remained constant at 9 GPa when the applied load was between 200 and 500 grams. As the load was reduced below 105 grams the hardness increased and reached a maximum value of 14.5 GPa. It should be noted that only the diagonal parallel to [100] was used in this hardness calculation. In this indenter orientation there was considerable anisotropy in the two diagonal lengths. It is believed the longer diagonal, which was always along [100], was more representative of the diagonal length under load. The justification for this assumption will be discussed in Section 5.2.

4.2.2. SEM Observations

The pattern of deformation and fracture around indentations on (010) planes appeared quite different when the indenter orientation was changed. Indentations made with the edges of the indenter parallel to [100] and [001] directions will be considered first.

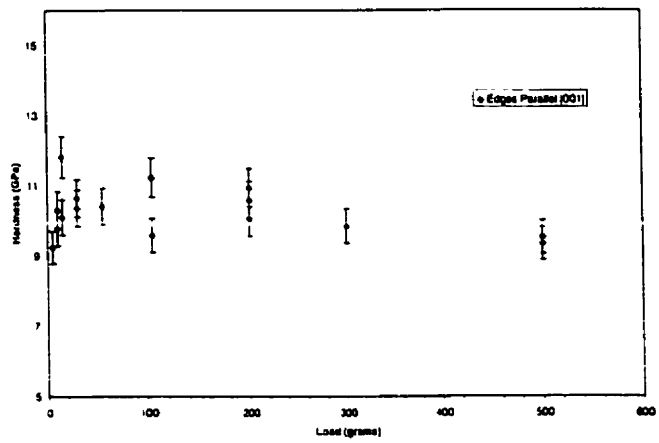

Figure 4.26 Hardness versus applied load for indentations made with the edges of the indenter aligned with [100] and [001] directions.

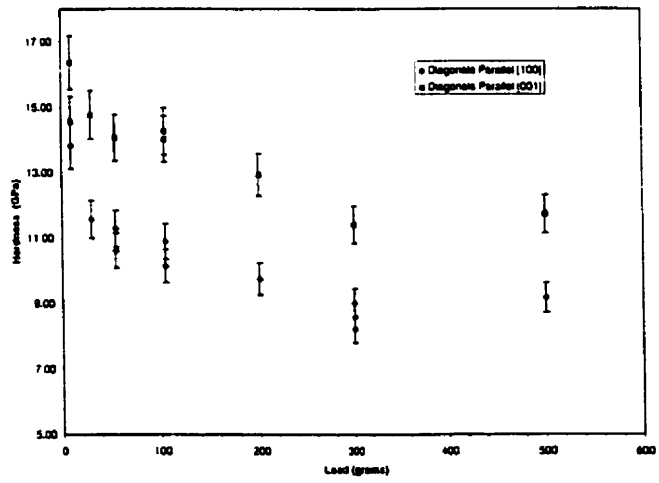

Figure 4.27 Hardness versus applied load for indentations made with the diagonals of the indenter aligned with [100] and [001] directions.

The indentation seen in Figure 4.28 (a) was made with an applied load of 500 grams. The most prominent features of this indentation are the cracks that extend from the corners of the indentation. The net shape of the cracks are arcs. They are tangent to [001] at their origin and then turn away from this direction as they extend away from the indentation. At this scale the cracks do not appear to follow any specific direction. Piled-up material can be seen on the [100] side of the indentation. Within this pile-up there are slip traces along [001] directions. When the applied load was reduced to 105 grams (Figure 4.28 (b)) the size of these cracks was greatly reduced while the slip traces along [001] directions became more apparent. Figure 4.28(c) shows an indentation made with an applied load of 55 g. The cracks that were so prominent at larger loads are now almost non-existent. The slip traces along [001] directions are still visible and piled-up material, forming a semi-circular pattern, is seen on the [001] side of the indentation. Finally, Figure 4.28(d) shows an indentation made with an applied load of 10 grams. There are no cracks seen around this indentation. The movement of material away from the indentation appears to have formed a trough that extends along [001] directions. It appears that this trough is V-shaped with the apex occurring at the mid-point of the indenter's edge.

In the second set of indentations the diagonals of the indenter were parallel to [100] and [001] directions. An indentation made with an applied load of 500 grams is shown in Figure 4.29(a). The cracks around this indentation do not appear to have any particular orientation. However, upon closer examination, the two cracks on the left side of the indentation appear to be the same as those seen when the edges of the indenter were parallel to [100] and [001] directions (Figure 4.28(a)). Figure 4.29(b) shows an optical micrograph of an indentation made with an applied load of 1000 grams. The correspondence of crack configuration between the two indenter orientations is clearly seen in this micrograph. Two sets of slip traces are seen in the deformed zone. The first set lies

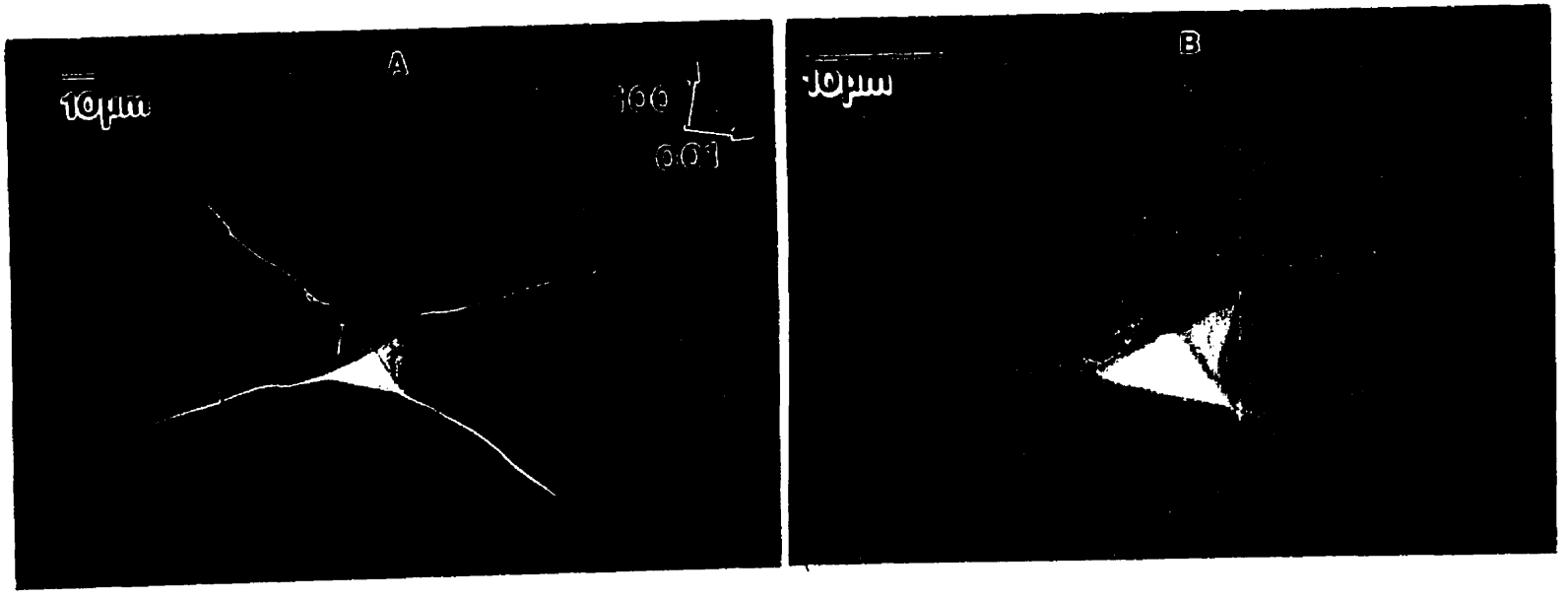

Figure 4.28 SEM images of indentations made with the edges of the indenter aligned parallel to [100] and [001] directions. The indentations were made with an applied load of (a) 500 grams, (b) 105grams, (c) 55 grams and (d) 10 grams.

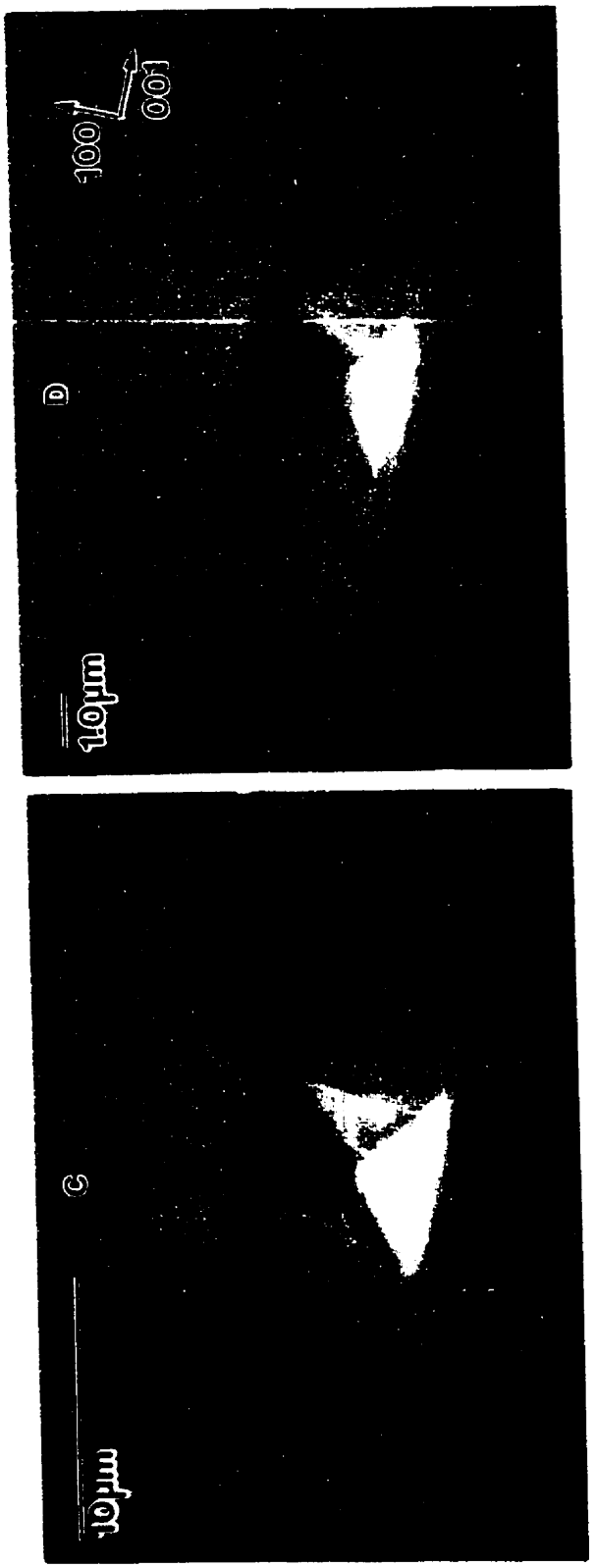
C
10μm
D
10μm
100
001

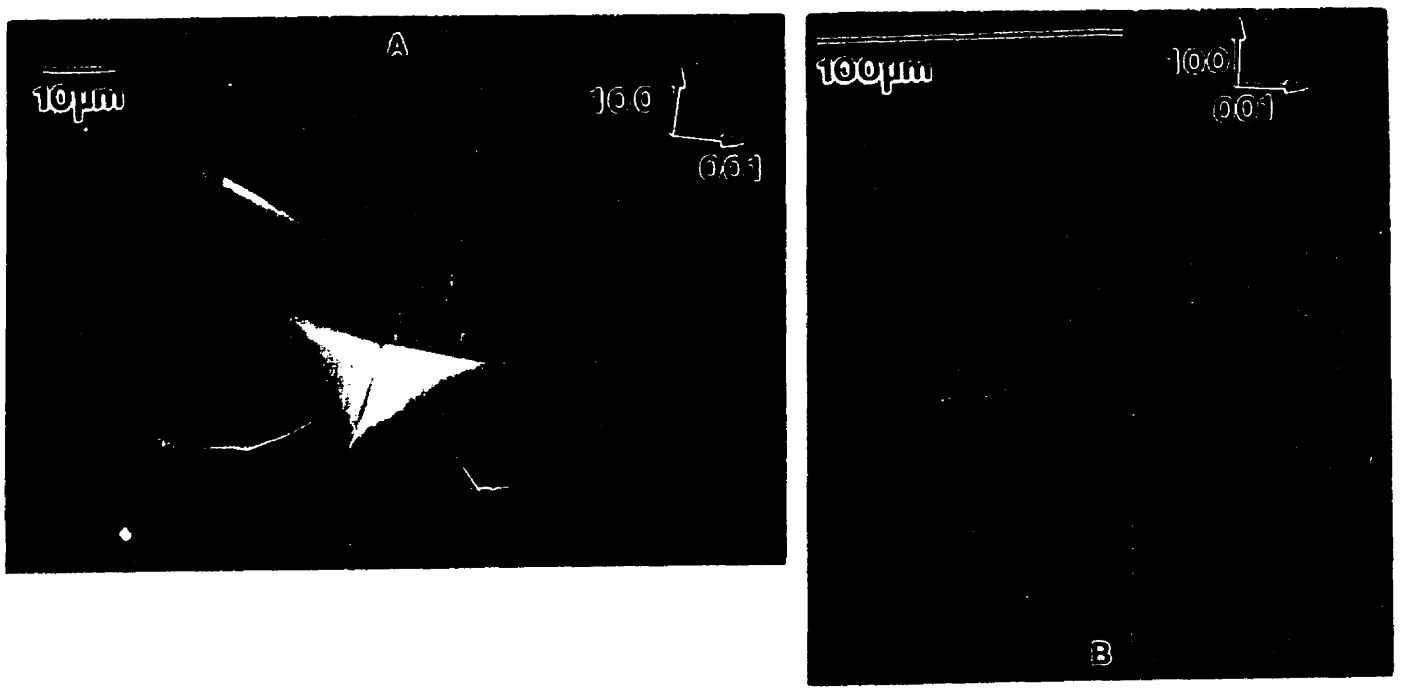

Figure 4.29 SEM images of indentations made with the diagonals of the indenter aligned parallel to [100] and [001] directions. The indentations were made with an applied load of (a) 500 grams, (b) 1000 grams, (c) 105 grams, (d) 55 grams and (e) 10 grams.

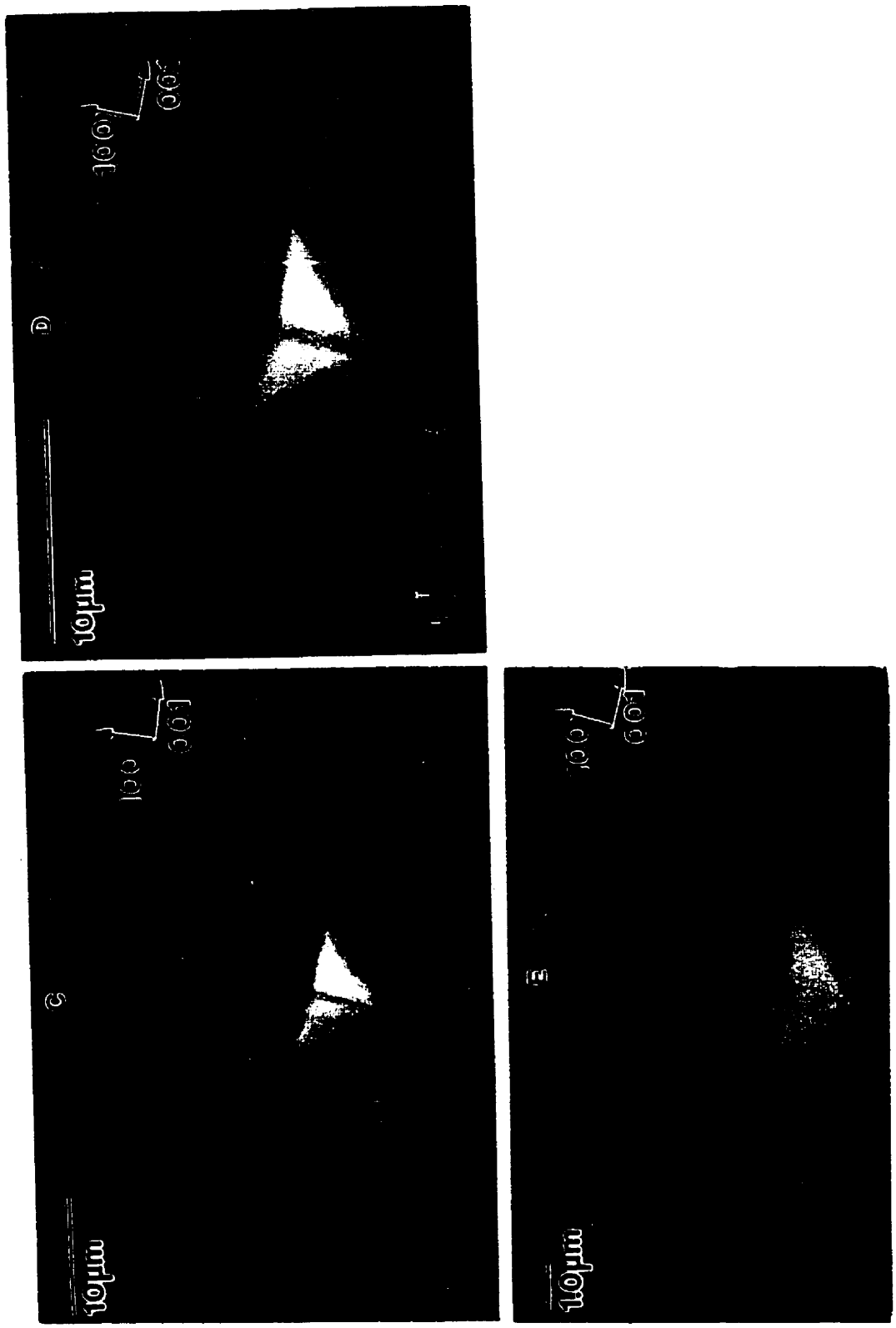
10μm
a
100
100
10μm
c
100
100
10μm
e
100
100

along [001] directions and the second set of slip traces (seen at the bottom of the indentation) lies along ⟨301⟩ directions. These two sets of slip traces are seen more clearly in Figure 4.29(b). When the applied load was reduced to 105 grams (Figure 4.29(c)) there were fewer cracks and those that did form were quite small. Two of the cracks originate at the corners of the diagonal along [100] and extend along [100] directions. Again slip traces that lie parallel to [001] are seen (Figure 4.29(c)). These traces were only seen outside of the region bounded by the corners of the indentation along [100] directions. Within this region, the material again appeared to be in the shape of a trough, with the apex lying along [001]. However the width of the trough is now defined by the diagonal length, not the edge length. The appearance of the indentation made with an applied load of 55 grams, Figure 4.29 (d), is similar to the 105 gram case. Cracks were once again parallel to [100] directions and slip traces were parallel to [001] directions. Lastly, an indentation made with an applied load of 10 g is shown in Figure 4.29(e). As in the other examples at this load there were no cracks present. There were also no slip traces seen along [001] directions.

The [001] axis has the same symmetry as the Vickers indenter and it was found that the indentation maintained this symmetry after the indenter was removed. This was not the case for the [010] axis. This axis contains two mirror planes. It was found that indentations on the (010) plane did not have four fold symmetry. When the edges of the indenter were aligned with [100] and [001] directions the edges did not have the same length (Figure 4.28). Similarly, when the diagonals were parallel to [100] and [001] directions they were not the same length (Figure 4.29). In the latter orientation the difference in diagonal length was approximately 7% ([100] longer than [001]) when the indentation was made with an applied load of 105 grams. This difference increased with decreasing applied load until the diagonal along [100] was 30% longer than the diagonal

along [001] when the indentation was made with an applied load of 10 grams. These observations show that with the correct crystal orientation there can be significant change in the in-plane dimensions when the load is removed.

4.2.3. AFM Observations

It was apparent from SEM observations that the patterns of deformation and fracture reflected the symmetry of the [010] axis. This resulted in differences in the patterns along [100] and [001] directions. AFM studies found that the elevation of material adjacent to an indentation also reflected the symmetry of the (010) plane. When the edges of the indenter were aligned parallel to [100] and [001] directions the SEM images were dominated by the cracks that extend from the indentation's corners. These cracks were also prominent in the AFM images.

An AFM image of an indentation made with an applied load of 300 grams is shown in Figure 4.30. This image shows that there is a large difference in height on either side of the cracks. Material was piled up on the [100] side of the indentation while the surface along [001] remained at the original elevation. This height difference on either side of the cracks suggests that there was a non-Mode I component to the opening of these cracks. Within the material that has piled-up, slip traces along ⟨001⟩ were visible. As the load used to form indentations was lowered, both the fracture and deformation patterns become less prominent. In Figure 4.31. (applied load of 200 grams) the cracks are barely visible and there is only a small difference in elevation on either side of these cracks.

An AFM image of an indentation made with an applied load of 200 grams, with the indenter's diagonals parallel to ⟨100⟩ and ⟨001⟩, is shown in Figure 4.32. Material has been piled-up along ⟨100⟩ directions while the material along ⟨001⟩ remains at the original elevation. This difference in elevation at the corners of the indentation will create some

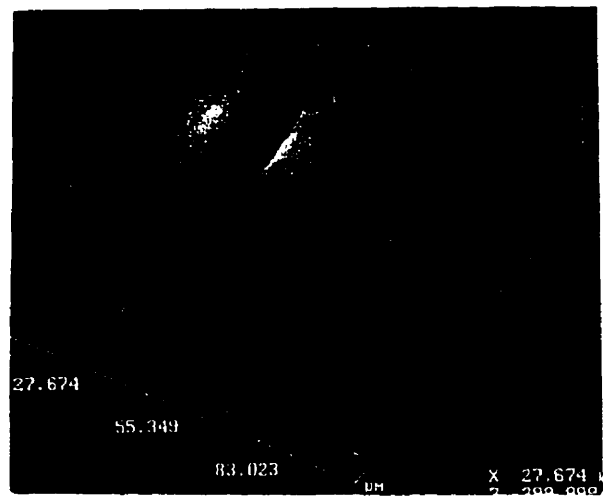

Figure 4.30 AFM image of an indentation made with the edges of the indenter aligned parallel to 100] and [001] directions, applied load is 300 grams.

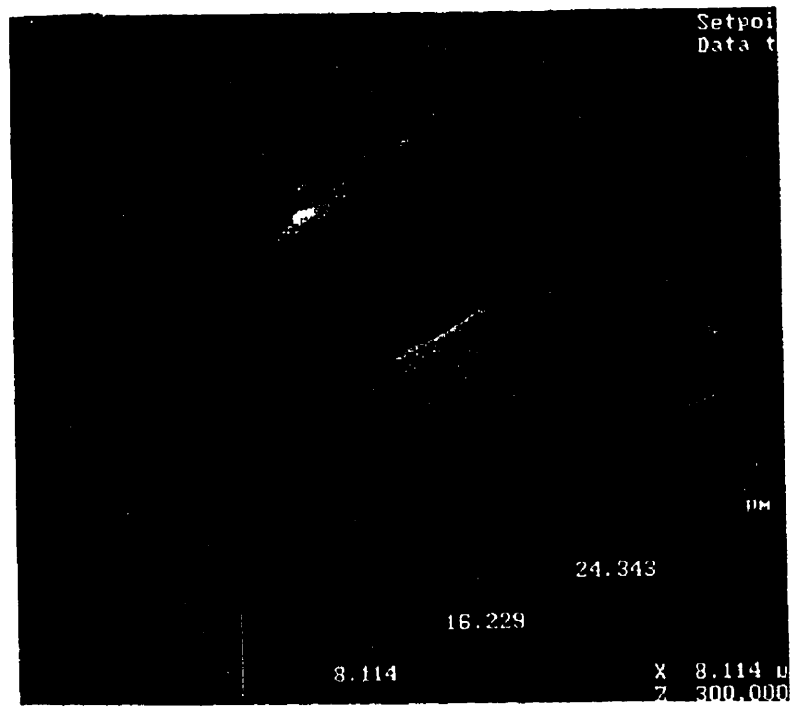

Figure 4.31 AFM image of an indentation, same orientation as figure 4.30, made with an applied load of 200 grams.

difference in the diagonal length. The diagonal along ⟨100⟩ will appear longer because material is pushed further up the sides of the indenter. It was noted in the SEM observations that the diagonal along ⟨100⟩ was longer than that along ⟨001⟩ and the difference increased with decreasing load. The differences due to the height of pile up should decrease with decreasing load as the height of pile up decreases. This is opposite to the trend found in SEM observations. Therefore, the difference in diagonal length must have a different origin. Slip bands along ⟨001⟩ directions are visible at the corner of the indentation at the top of the image. It appears that the elevation of these slip bands does not continually decrease as one moves away from the indentation. A high magnification AFM image of the corner of an indentation made with an applied load of 100 grams is shown in Figure 4.33. In this image the ⟨100⟩ direction runs parallel to the vertical axis and the corner of the indentation lies at the bottom of the image. A fine crack trace is seen along ⟨100⟩. The alternating elevation of slip bands along ⟨001⟩ is evident. It appears that the bands at a higher elevation are wider than those at a lower elevation.

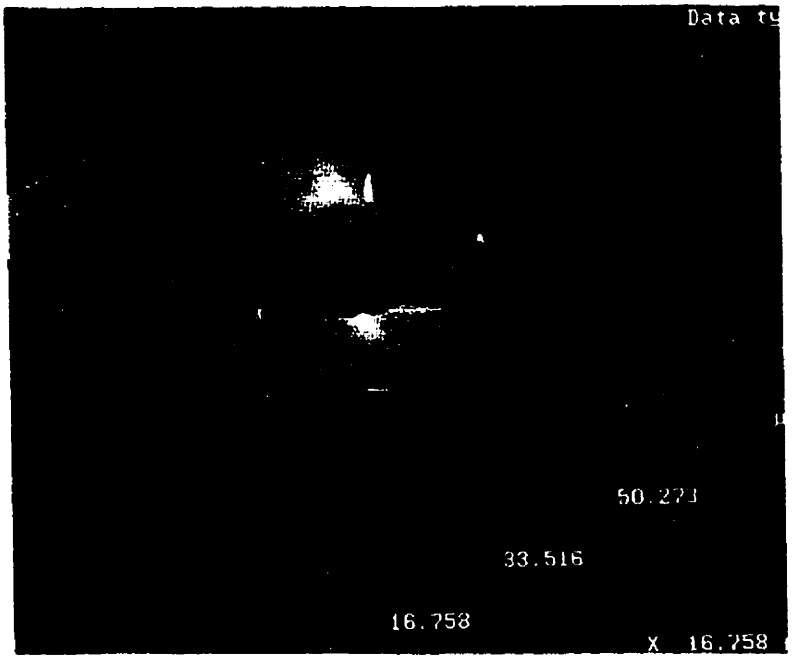

Figure 4.32 AFM image of indentation made with the diagonals of the indenter aligned parallel to [100] and [001] directions, applied load is 200 grams.

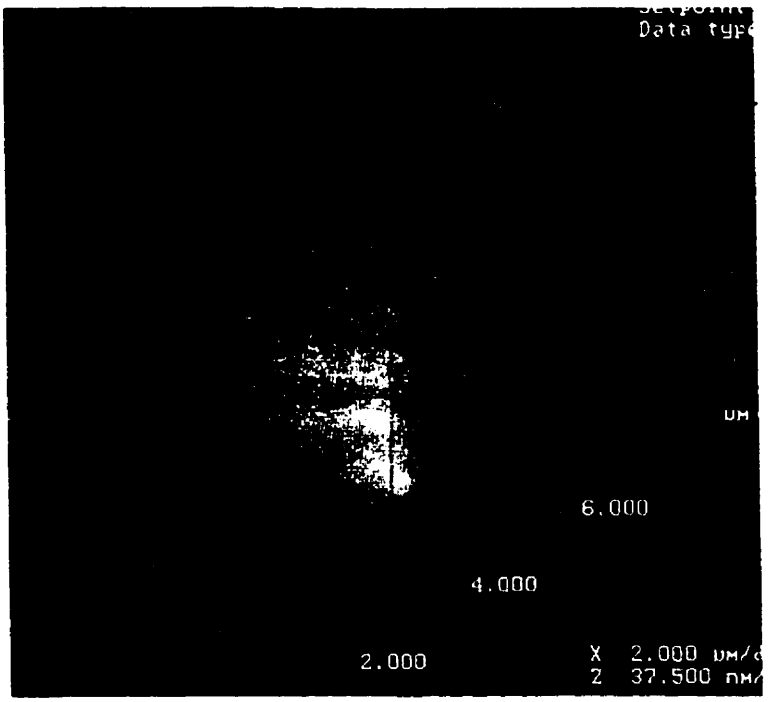

Figure 4.33 High resolution image of the corner of an indentation made with an applied load of 100 grams.

4.2.4. TEM Observations

The anisotropy in the deformation observed in the SEM and AFM studies of the indented surface was also observed in TEM studies. As was the case for the TEM studies of indentations on (001) surfaces the slip systems were found to be the same for both orientations of indentations on (010) surfaces. However, there were differences in the arrangement of slip systems resulting from the orientation of the indenter. Furthermore, it will be shown that the slip systems are the same as those observed during indentation on an (001) surface.

4.2.4.1 The Geometry of The Plastic Zone

A low magnification bright field micrograph (**B**=[010]) of an indentation made with an indenter whose edges were aligned with the [100] and [001] directions is shown in Figure 4.34 (a). The accompanying selected area diffraction pattern (SADP) is shown in Figure 4.34 (b). The arrangement of dislocations around the indenter is complicated. However, there are three basic groups of dislocations in the plastic zone adjacent to the indentation. A schematic diagram showing this arrangement of the three dislocation types is shown in Figure 4.35. Type A dislocations were found in arrays that extended from the indentation along [100] and $[\bar{1}00]$ directions. In Figure 4.34 (a) this extension was approximately 8 μm from the centre of the indentation. The dislocations in this array were long and straight while the same dislocations near to the indentation were curved. The arrays appeared to originate at the corners of the indentation. There were fewer dislocations in the region between these two sources i.e. at the edge mid-point. Type B dislocations were found in arrays that extended along [001] directions. They only extended approximately 5 μm, from the centre of the indentation (Figure 4.34 (a)). They appeared as short segments and were usually curved. In all indentations studied the Type A

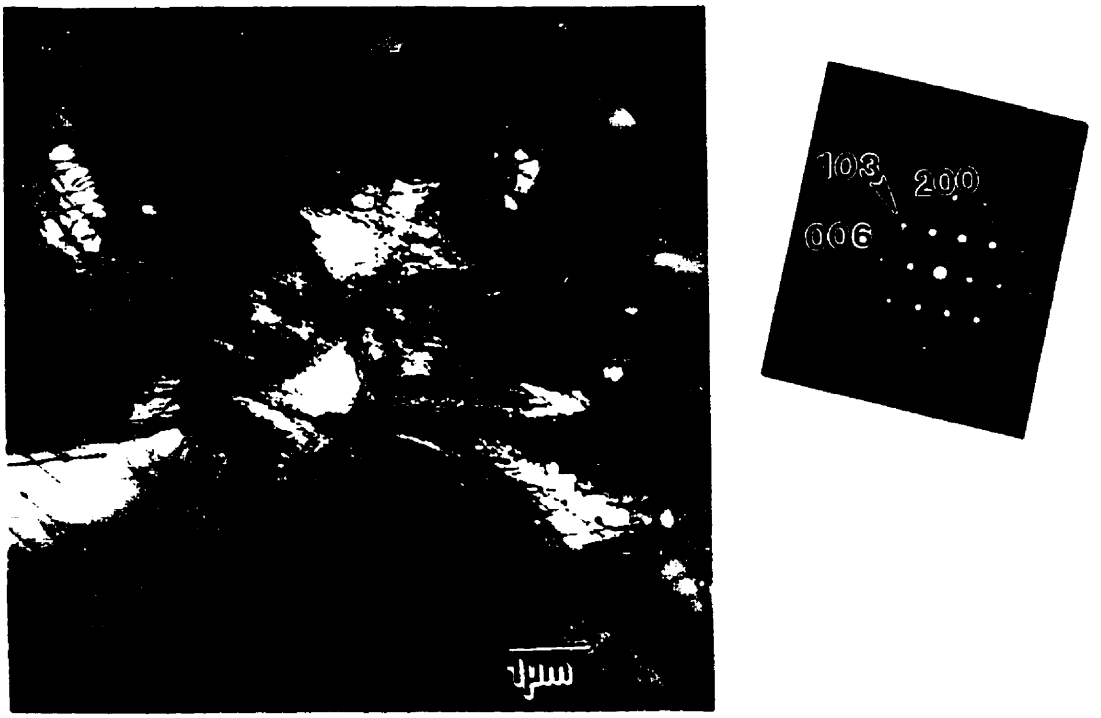

Figure 4.34 Bright Field micrograph (a) and SADP (b) of an indentation that was made with the edges of the indenter aligned with [100] and [001] directions.

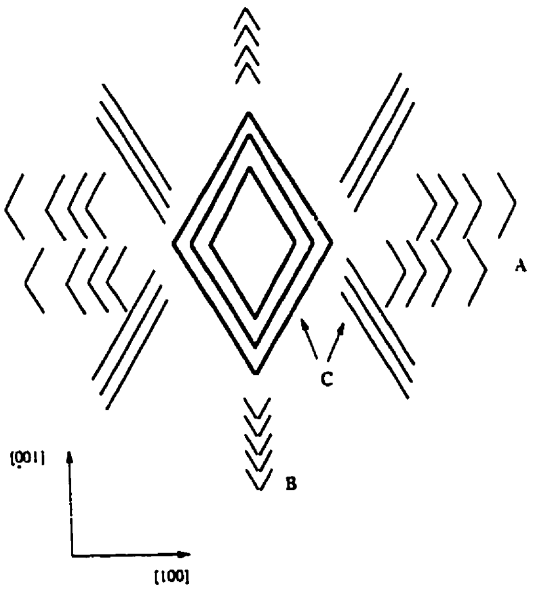

Figure 4.35 Schematic diagram illustrating the arrangement of the three types of dislocations seen under indentations on (010) surface.

dislocations were found to have glided further from the indentation than the Type B dislocations. The third type of dislocations (labeled C) appeared in two configurations. In the first configuration they were in the form of loops whose edges produced traces along directions that were normal to the {101} plane normals. These loops were found directly under the indentation. In the second configuration they were found between type A and B dislocations, originating at the corners of the indentation. Once again they produced traces along directions normal to the {101} plane normals.

There are several other features of interest directly under the indentation (Figure 4.34). First, the diagonals of the indentation can be seen due to the higher dislocation density along these lines. Second, striations along [001] directions can be seen directly under the indentation. These striations do not continue across the indentation. Instead they appear to be truncated by the diagonals of the indenter. The third feature of interest is the dense bands of dislocations along [001] directions that are found at the edges of the indentation. These bands appear to have been formed by dislocations that have piled up at the edge of the indentation. Lastly, in the SEM micrographs (Section 4.2.2) it was noted that the plastic zone was symmetrical about the ⟨100⟩ and ⟨001⟩ axes. i.e. there are two mirror planes. The same symmetry is seen in the TEM images.

Figure 4.36 is a stereo pair of the indentation shown in Figure 4.34. The highly deformed zone under the indentation is in the shape of a pyramid, with the apex being the furthest point from the indented surface. Once again, the features in this region were symmetrical about the ⟨100⟩ and ⟨001⟩ axes. Facets with an edge along [001] were well defined and appeared to have a dense dislocation sub-structure. On the other hand, the facets with edges along [100] were not well defined. In this case there is no clear boundary between the highly deformed region under the indentation and the region beside the indentation. In fact, the highly deformed region extends beyond the edges of the

indentation. There is a high density of the striations along [001] in this region. This stereo pair also shows that the long curved 'A' dislocations beside the bands along [001] lie at various depths in the foil. The band of piled up dislocations along [001] lie near the indented surface; this band formed a barrier between the high and low dislocation density regions of the plastic zone.

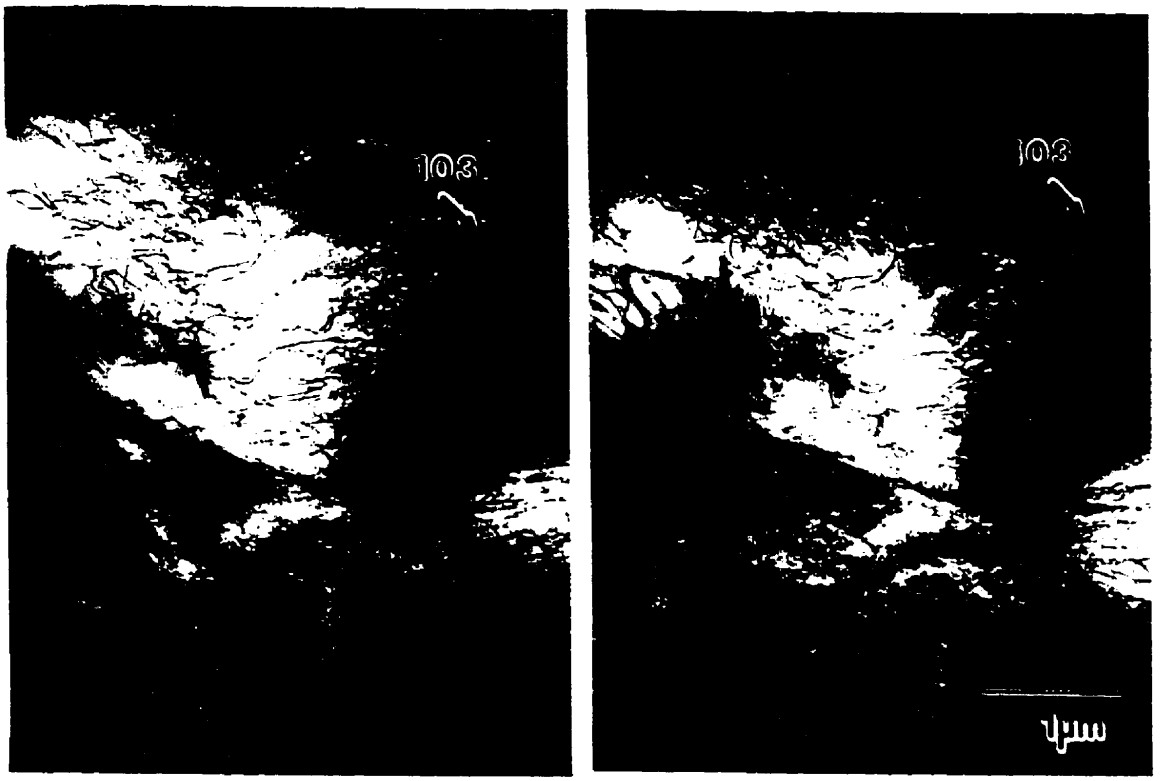

Figure 4.36 Stereo pair if indentation shown in figure 4.34, g=103.

A schematic diagram that illustrates the geometry of the deformed zone under the indentation is shown in Figure 4.37. It should be noted that the deformed zone looks very different along ⟨001⟩ than along ⟨100⟩ directions.

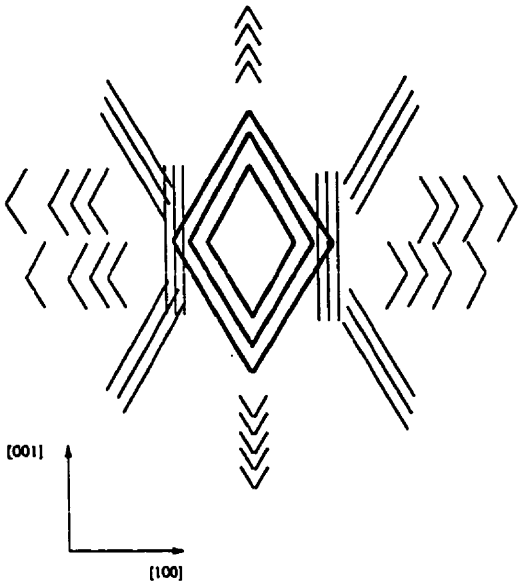

Figure 4.37 Schematic diagram of plastic zone under an indentation on an (010) surface.

A low magnification micrograph (**B**=[010]) of an indentation made with the diagonals of the indenter aligned parallel to [100] and [001] directions is shown in Figure 4.38 (a). The accompanying diffraction pattern is shown in Figure 4.38 (b). The plastic zone beside the indentation appears very similar to that shown in Figure 4.34 (a). There is only one noticeable difference. The Type C dislocations lying between the Type A and B dislocations appear to originate at the corner of the indentation that lies along [100]. With the other indenter orientation these type C dislocations also originated at the corners of the indentation implying they originated at different sources for the different orientations of indenter. Directly under the indentation the plastic zone appeared quite different. First, there were no bands of piled-up dislocations along the edges of the indentation that lie along [001] directions. Thus, a pile-up of dislocations only formed when the edges of the indenter were parallel to [100] and [001] directions. Second, the diagonals of the

indentation were not readily observable. In Figure 4.38 (a) only the diagonal along [100] can be identified.

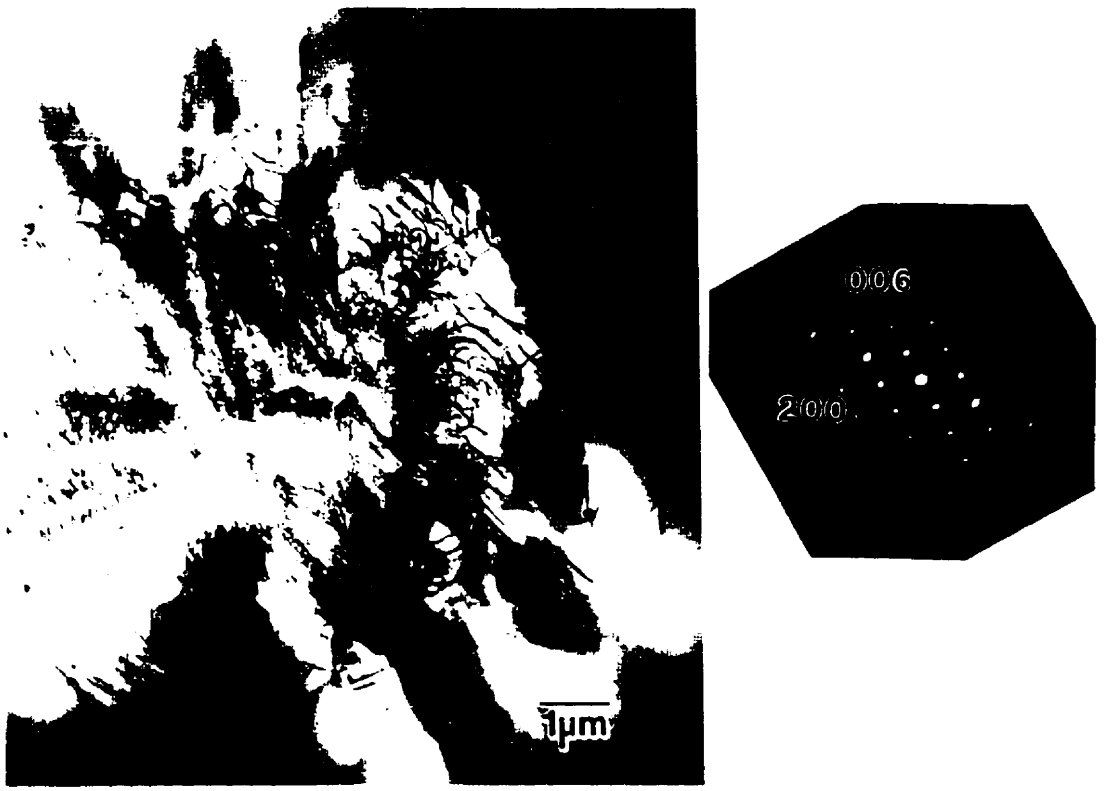

Figure 4.38 Bright Field micrograph (a) and SADP (b) of an indentation that was made with the diagonals of the indenter aligned with [100] and [001] directions.

Figure 4.39 is a stereo pair of an indentation made with the diagonals of the indenter aligned parallel to [100] and [001] directions. In this case there were no facets that defined the highly deformed region of the plastic zone. In fact only the Type C dislocation loops provided depth information under the indentation with the smaller loops lying further from the indented surface. In this figure the Type C prismatic loops were at higher elevations towards the centre of the indentation. Since the indented surface is pointing into the page in these micrographs the geometric arrangement of these loops follows the shape

of the indentation. This is similar to the arrangement of stacking faults on {110} planes for indentations made on (001) planes (Section 4.1.4.).

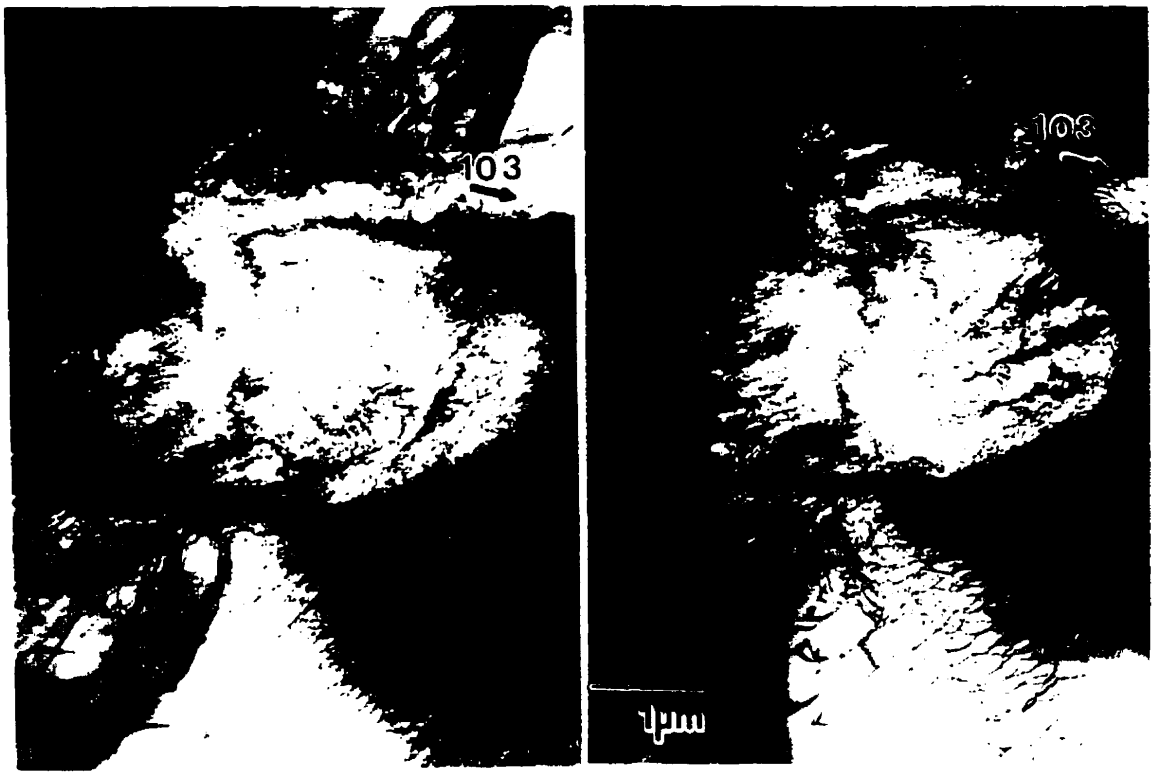

Figure 4.39 Stereo pair of an indentation of the same orientation ass that shown in figure 4.38.

4.2.4.2. Defect Analysis

As noted above indentations made with either indenter orientation contained the same type of dislocations. Therefore only a single contrast analysis will be presented for each dislocation type ie. A, B and C (Figure 4.35). Two differences found in the nature of the dislocation structure beside the indentation will be discussed at the end of the defect analysis.

A set of images of type A dislocations for six different diffracting conditions are shown in Figure 4.40. A simulated image of the dislocation labelled A is also presented

for each set of experimental imaging conditions. The dislocation that was simulated is arrowed in Figure 4.40 (a). All of the dislocations are visible when **g**= 103, $\bar{2}\bar{1}\bar{3}$, $21\bar{3}$ and $10\bar{3}$ and invisible when **g**=$0\bar{1}3$ and 013. Therefore **b** equals [100]. In Figures 4.40 (b) and (f) there is considerable residual contrast. In both cases this residual contrast appears as a series of black and white fringes that lie at an angle to the dislocation. The simulated images are all in agreement with the respective experimental images, thus confirming the Burgers vector determination. Strong residual contrast for dislocations with **b**=[100] was also seen in Section (4.1.4.2) when **g**=020. Therefore, dislocations with this Burgers vector appear to produce strong residual contrast for all cases of **g**.**b**=0.

Trace analysis of the dislocations labelled A and B in Figure 4.40 (a) found that **u**= $[\bar{1}\,1\,1]$ and $[1\,1\,\bar{1}]$ for A and B, respectively. Thus, A and B lie on an $(0\bar{1}\,1)$ and an (011) plane, respectively. Dislocation B has actually cross slipped twice between {011} planes. The cross slip of dislocations with **b**=[100] from one {011} plane to another was quite commonly observed. This type of cross slip is well illustrated in Figure 4.41 (a). Many of the dislocations in the group containing the dislocation set B have cross slipped.

The micrograph in Figure 4.41 (b) was taken closer to the corner of the indentation, which in this example was made with the edges of the indenter aligned parallel to [100] and [001] directions. The dislocations on the right hand side of this micrograph are from the array shown in Figure 4.41 (a). Trace analysis results for dislocations A, B and C (Figure 4.41 (a)), and D and E (Figure 4.41 (b)) are shown in Table 4.3. All of the dislocations have a ⟨111⟩ line direction and lie on {011} planes.

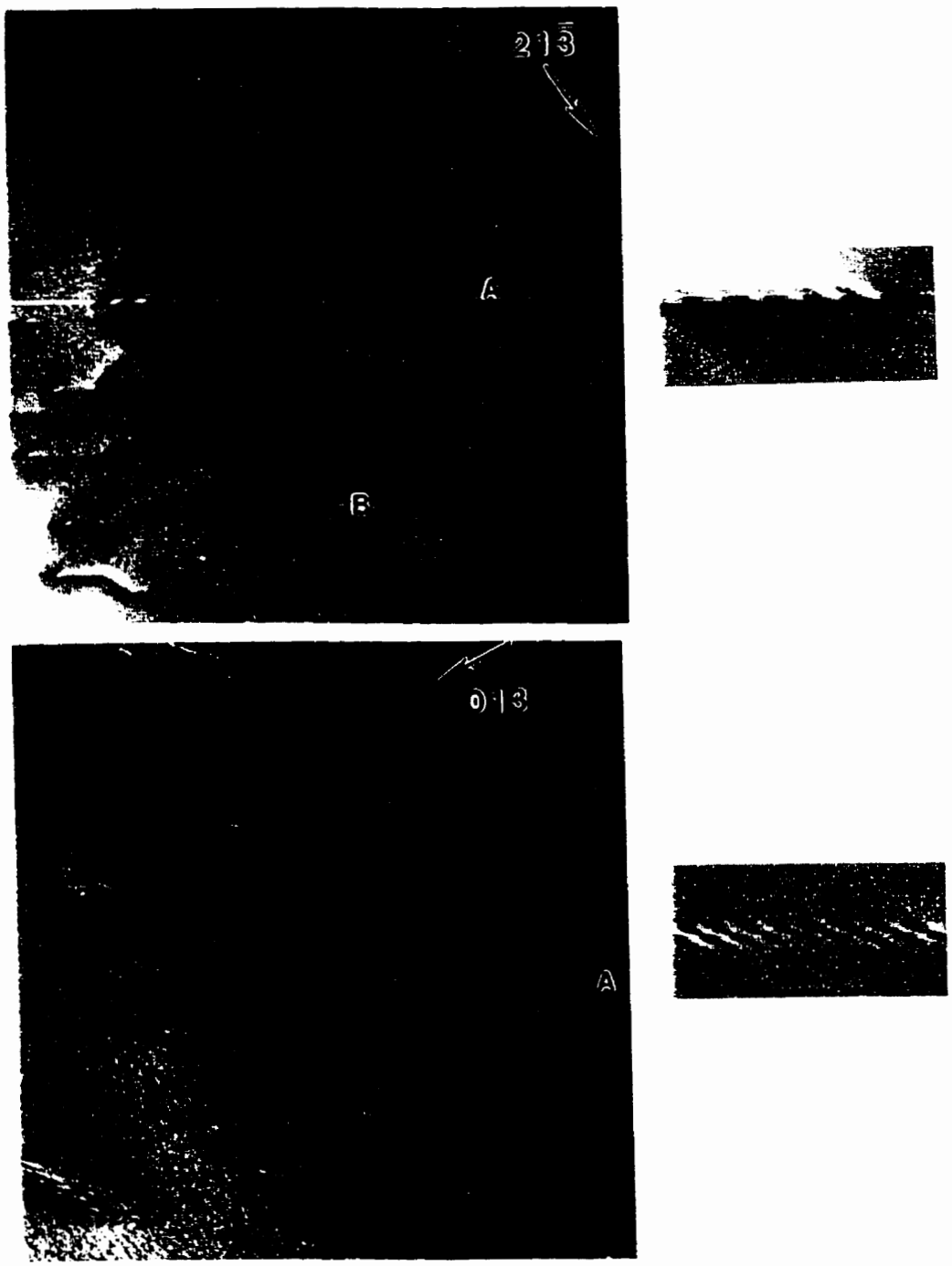

Figure 4.40 Bright Field and simulated images of Type A dislocations. The diffracting conditions are; (a) $\mathbf{g}=21\bar{3}$, (b) $\mathbf{g}=013$, (c) $\mathbf{g}=10\bar{3}$, (d) $\mathbf{g}=\bar{2}\bar{1}\bar{3}$, (e) $\mathbf{g}=103$ and (f) $\mathbf{g}=0\bar{1}3$.

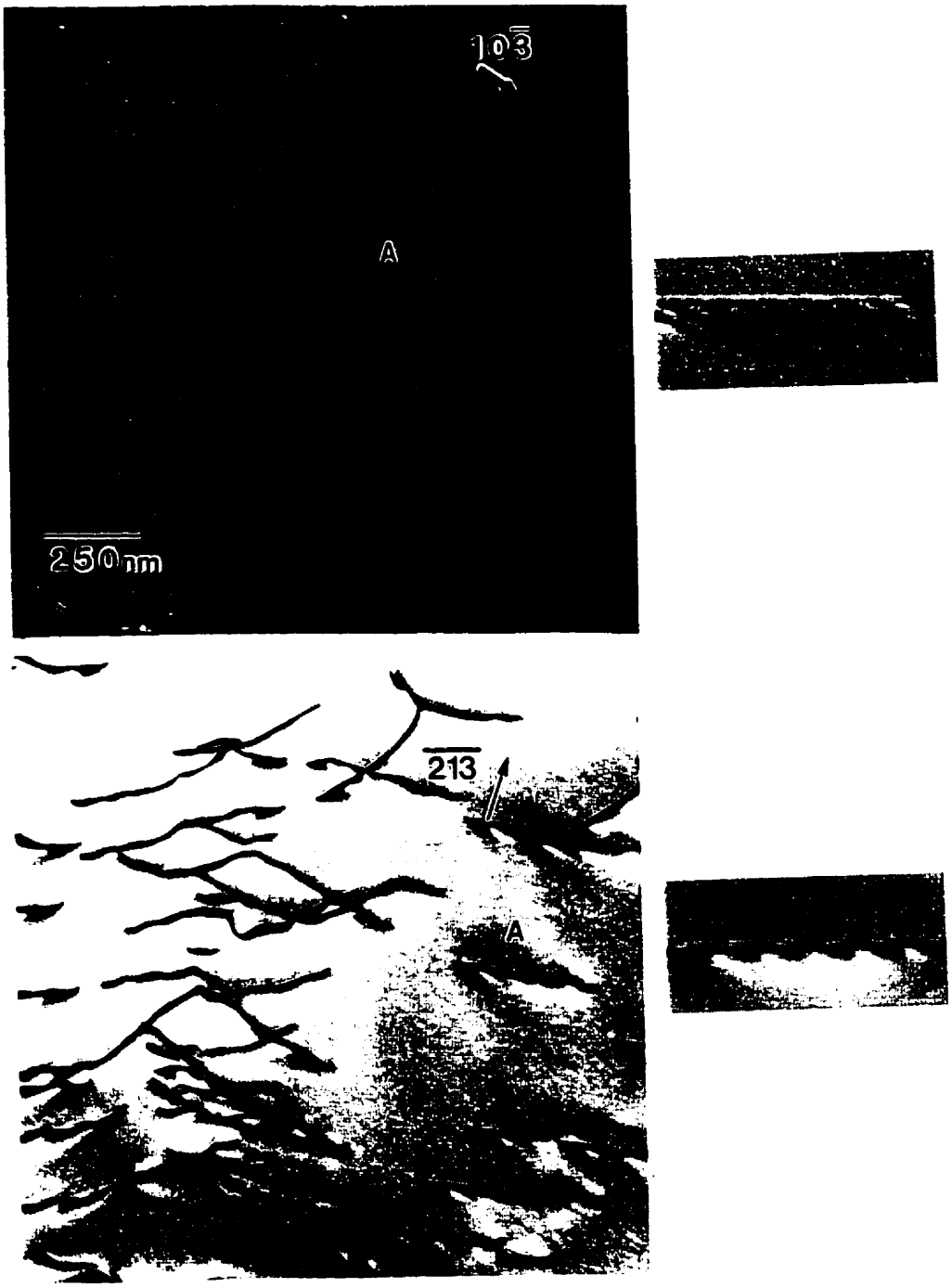
103
A
250nm
213
A

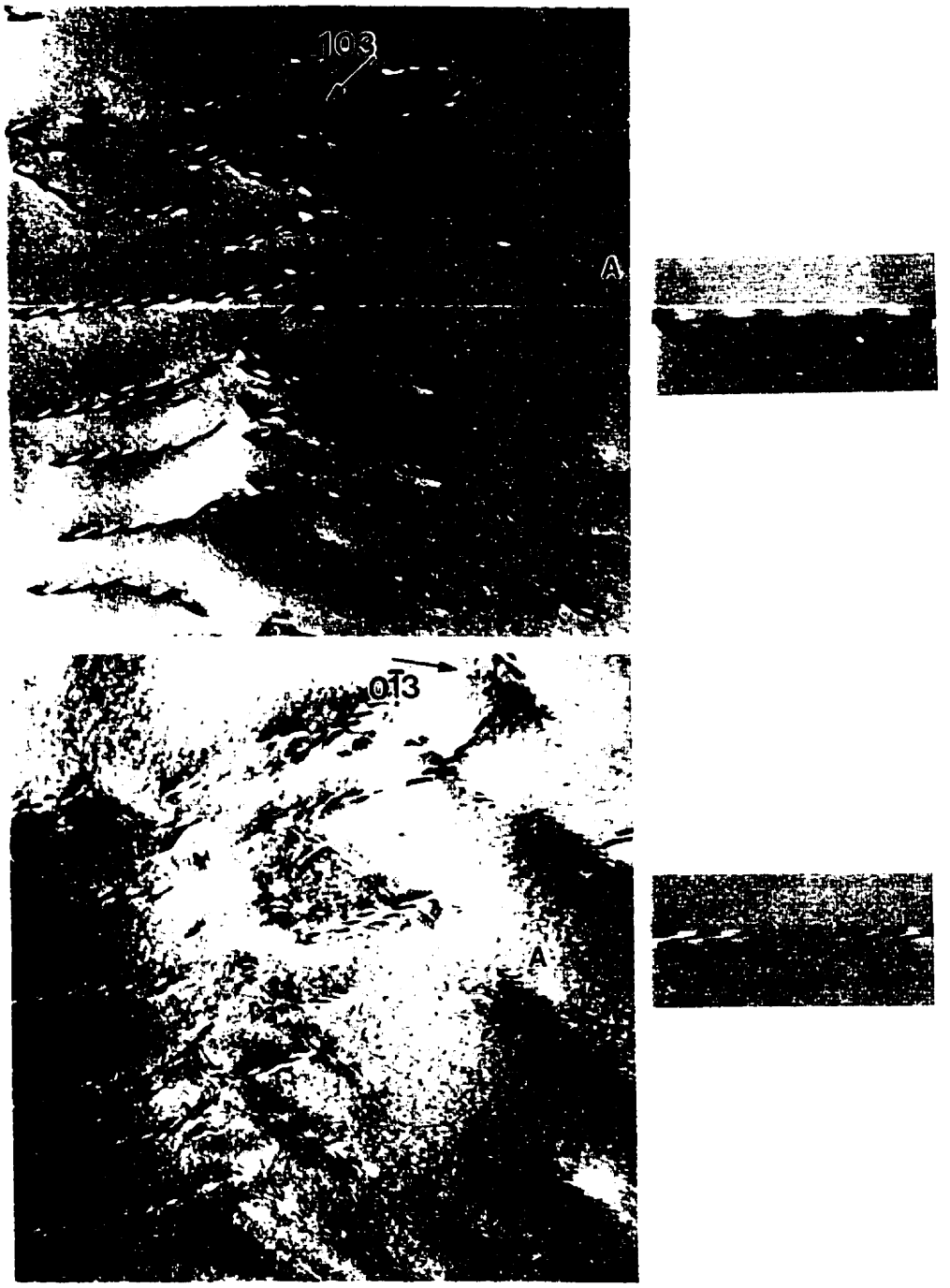
103
A
013
A

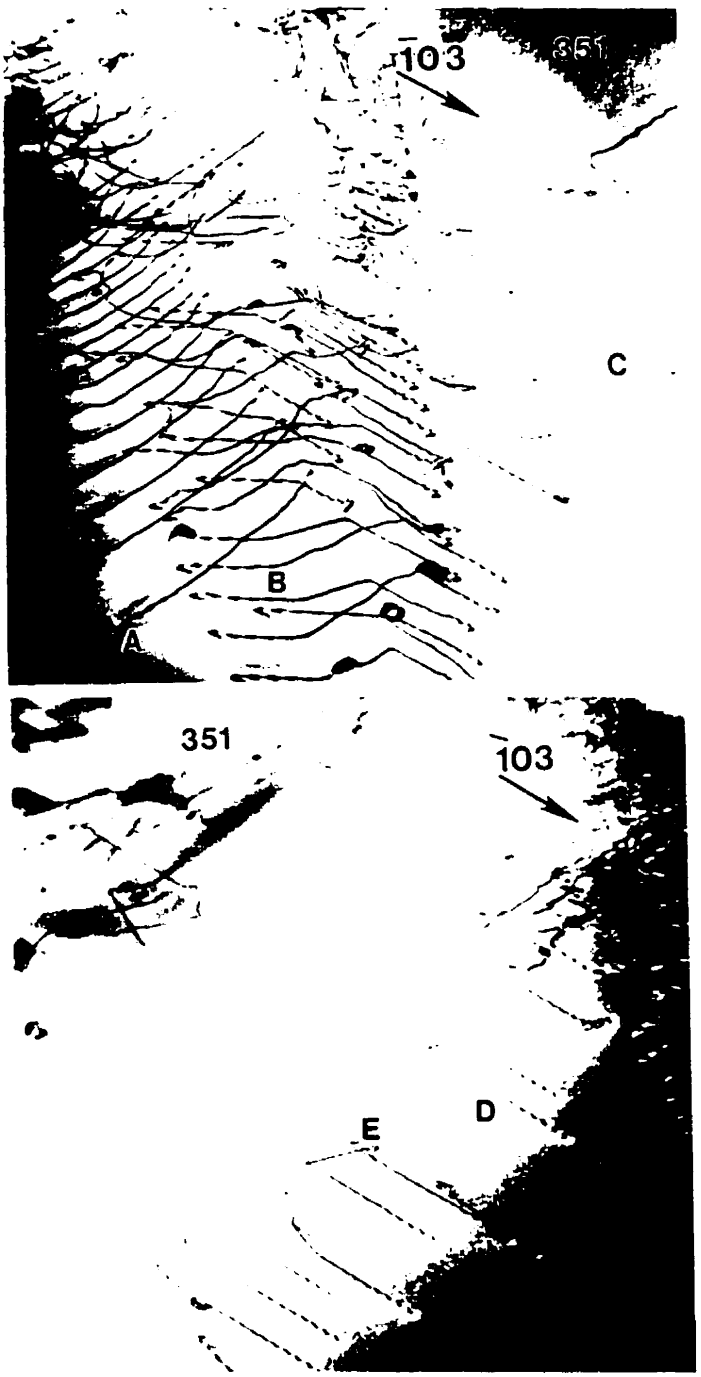

Figure 4.41 Bright Field micrographs showing the arrangement of dislocations around an indentation that was made with the edges of the indenter aligned parallel to [100] and [001] directions.

Dislocation	b	u	Slip Plane
A	[100]	$[\bar{1}1\bar{1}]$	(011)
B	[100]	$[11\bar{1}]$	(011)
C	[100]	$[\bar{1}11]$	$(0\bar{1}1)$
D	[100]	$[\bar{1}11]$	$(0\bar{1}1)$
E	[100]	[111]	$(0\bar{1}1)$

Table 4.3 Trace analysis results for the dislocations labelled in Figure 4.41.

The location of dislocations D and E (Figure 4.41 (a)) was not expected for dislocations having a Burgers vector equal to [100]. Since the indenter was aligned with its edges parallel to [100] and [001] directions the group of dislocations containing D and E lies in the region of the plastic zone where material was anticipated to be moving along [001] not along [100].

Figure 4.42 contains four images of Type A dislocations that were found beside the indentation. Near the top of each image the band of piled-up dislocations along the edge of the indentation can be seen. The visibility conditions for the type A dislocations were consistent with those in Figure 4.40, i.e. they were visible for $\mathbf{g}=\bar{1}03$ and $\bar{1}0\bar{3}$ and invisible for $\mathbf{g}=01\bar{3}$ and 013. In figure 4.42 (c) and (d) Type C dislocations, that occur as loops under the indentation are also visible. These dislocations were invisible when $\mathbf{g}=\bar{1}03$ and $\bar{1}0\bar{3}$, which indicates that **b**=[010]. This Burgers vector gives a displacement parallel to the direction of indentation. The line direction of the loop segment on the left side of Figure 4.42 was found to be $[10\bar{1}]$, i.e. the segment lies on a (101) plane.

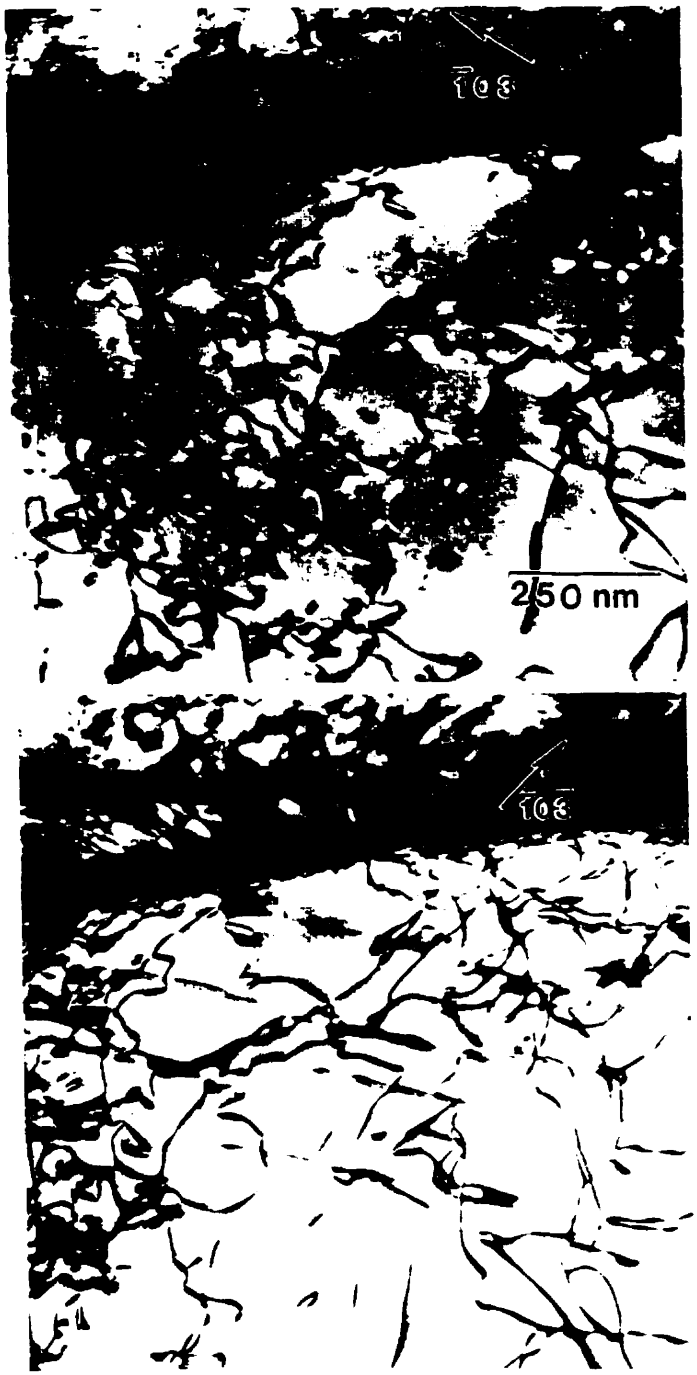

Figure 4.42 Bright Field images of Type 'A' dislocations (figure 4.37) located on the [100] side of an indentation. The diffracting conditions are; (a) $\mathbf{g}=\bar{1}03$, (b) $\mathbf{g}=\bar{1}0\bar{3}$, (c) $\mathbf{g}=01\bar{3}$ and (d) $\mathbf{g}=013$.

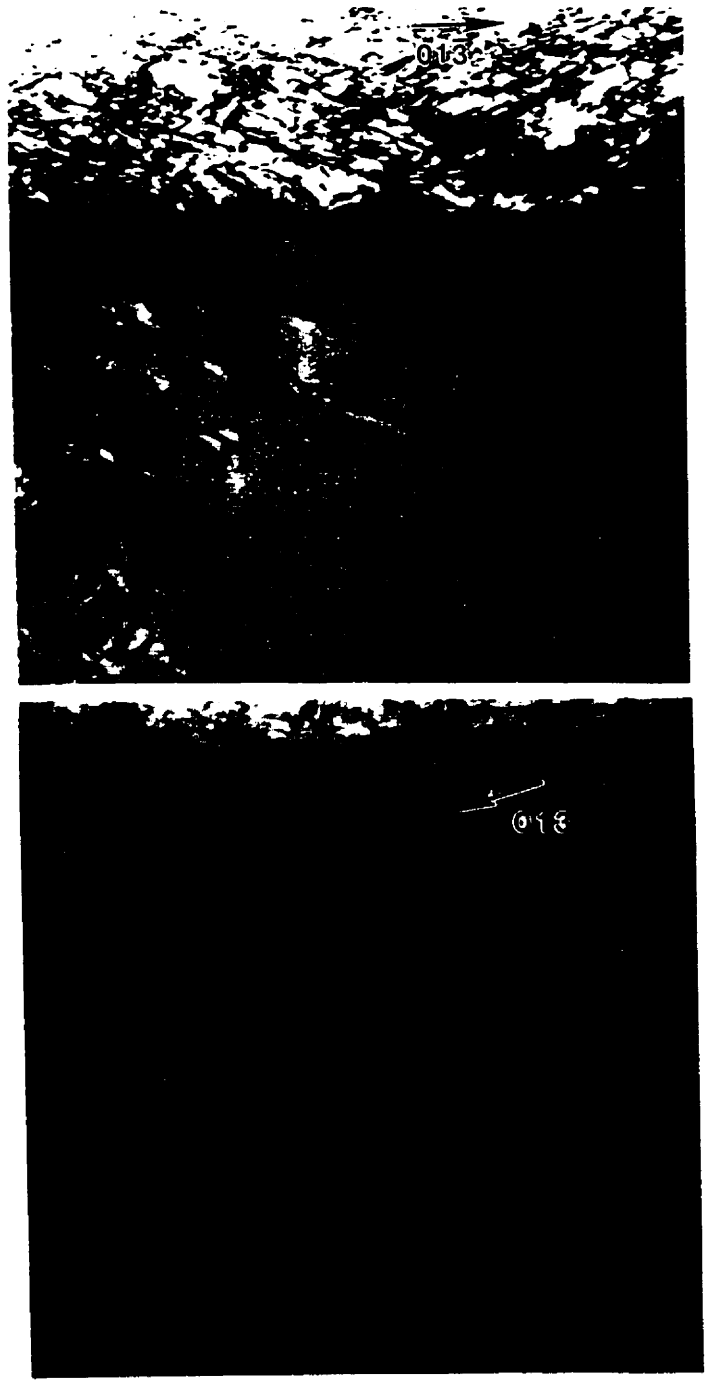

When the indentation was viewed with **B**= [010] (Figure 4.34) all segments of the loop produced traces that formed a 22° angle with the [001] direction. This is also the orientation of traces produced by {101} planes. Thus, these Type C dislocations are prismatic loops that glide on a prismatic cylinder defined by (101) and $(10\bar{1})$ planes.

To this point in the discussion, only the dislocation structure beside the indentation has been considered. There is also considerable information about the dislocation structure under the indentation in Figure 4.42. The band of piled up dislocations along [001] creates a clear demarcation between the different regions of the plastic zone, i.e. between the region under the indentation and the region beside the indentation. However, the [010] prismatic loops were found in both regions of the plastic zone (Figure 4.42 (c)). There appeared to be a second set of dislocations in this figure. However, their high density and the changing diffracting conditions made contrast analysis in this area impossible.

The final type of dislocation found in the plastic zone beside the indentation are those labelled B in Figure 4.35. Two sets of these dislocations are seen in Figure 4.43 (a). The dislocations on the left and right hand sides of the figure will be referred to as group 1 and 2, respectively. In the bright field micrograph (**g**= $\bar{1}03$) the dislocations in group 1 produced a double image while those in group 2 produce only a single image. Six additional reflections (for the dislocations in group 2) are shown in Figure 4.43 (b)-(g). The dislocations were visible when **g**= $\bar{1}03$, $\bar{2}00$, 101, 103 and $\bar{1}10$ while they were invisible when **g**= $10\bar{1}$ and 110. These invisibility conditions are satisfied with **b**= $[\bar{1}1\bar{1}]$ or $[1\bar{1}1]$. In this example, the foil was oriented such that the indented surface was pointing into the page, along $[0\bar{1}0]$. Furthermore, the diffraction pattern was indexed such that the $(00\bar{1})$ plane normal points away from the indentation in this region of the plastic zone.

Since material must move away from the indentation, **b**= $[\bar{1}\,1\,\bar{1}]$. A trace analysis of a dislocation in group 2 found that the line direction was $[\bar{3}3\,\bar{1}]$. Thus, the slip plane of this and all other dislocations belonging to group 2 must be (110). A similar analysis of the dislocations belonging to group 1 found that **b**=$[1\,1\,\bar{1}]$ and the slip plane was a $(1\,\bar{1}\,0)$ plane. Therefore, these two groups of dislocations belong to the same family.

The magnitude of the Burgers vectors of these dislocations was not readily apparent. The dislocations in group 2 produced a single image when **g**=$(\bar{1}03)$ (Figure 4.43 (a)) while a double image was produced when **g**=(103) (Figure 4.43 (e)). A detailed analysis of the contrast of a dislocation from this set is presented in Appendix B. By comparing experimental and simulated images it was found that the $\frac{1}{2}[\bar{1}\,1\,\bar{1}]$ dislocation had dissociated into two equal $\frac{1}{4}[\bar{1}\,1\,\bar{1}]$ partials (Equation 2.6).

An extended stacking fault was found next to an indentation (moving in a direction away from the indentation along $[\bar{1}00]$) that was made with the indenter's diagonals parallel to [100] and [001] directions (Figure 4.44). Most of the indentation had been removed during the thinning procedure leaving only part of the plastic zone, which had a lower dislocation density. Images of this fault and the accompanying partials taken with eight different operating reflections are shown in Figure 4.44. The contrast analysis results obtained from these images are summarized in Table 4.4. The values of $\mathbf{g}.\mathbf{b}_p$ and α ($2\pi.\mathbf{g}.\mathbf{R}$) for $\mathbf{b}_p$ and **R** equal to $\frac{1}{4}[\bar{1}\,1\,1]$ are also presented in this table. Both partials and the stacking fault have a displacement vector equal to $\frac{1}{4}[\bar{1}\,1\,1]$. This is another case of a

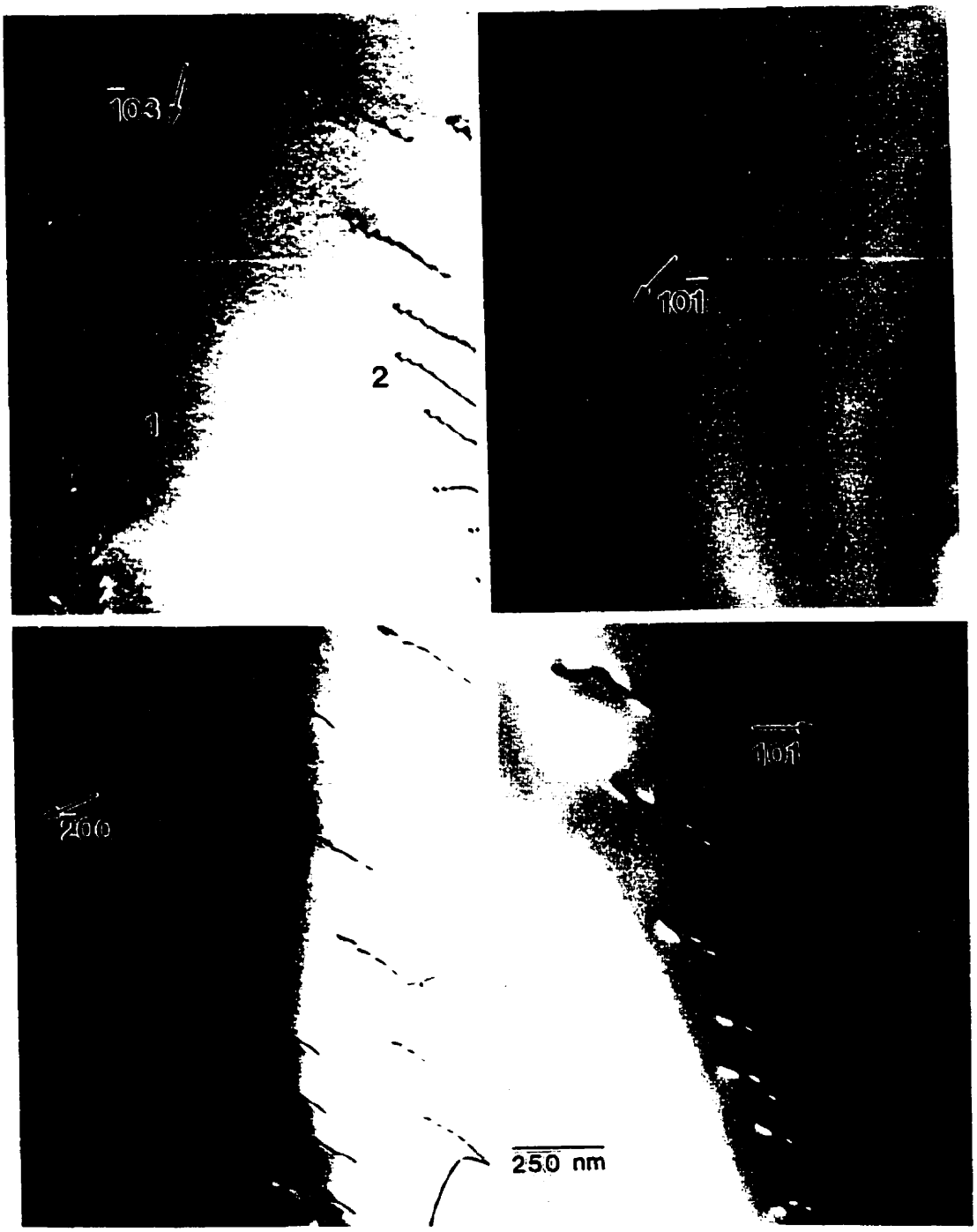

Figure 4.43 Bright Field images of Type 'B' dislocations (figure 4.37) located on the [100] side of an indentation. The diffracting conditions are; (a) $\mathbf{g}=\bar{1}03$, (b) $\mathbf{g}=10\bar{1}$, (c) $\mathbf{g}=\bar{2}00$, (d) $\mathbf{g}=101$, (e) $\mathbf{g}=\bar{1}10$, (f) $\mathbf{g}=110$ and (g) $\mathbf{g}=110$.

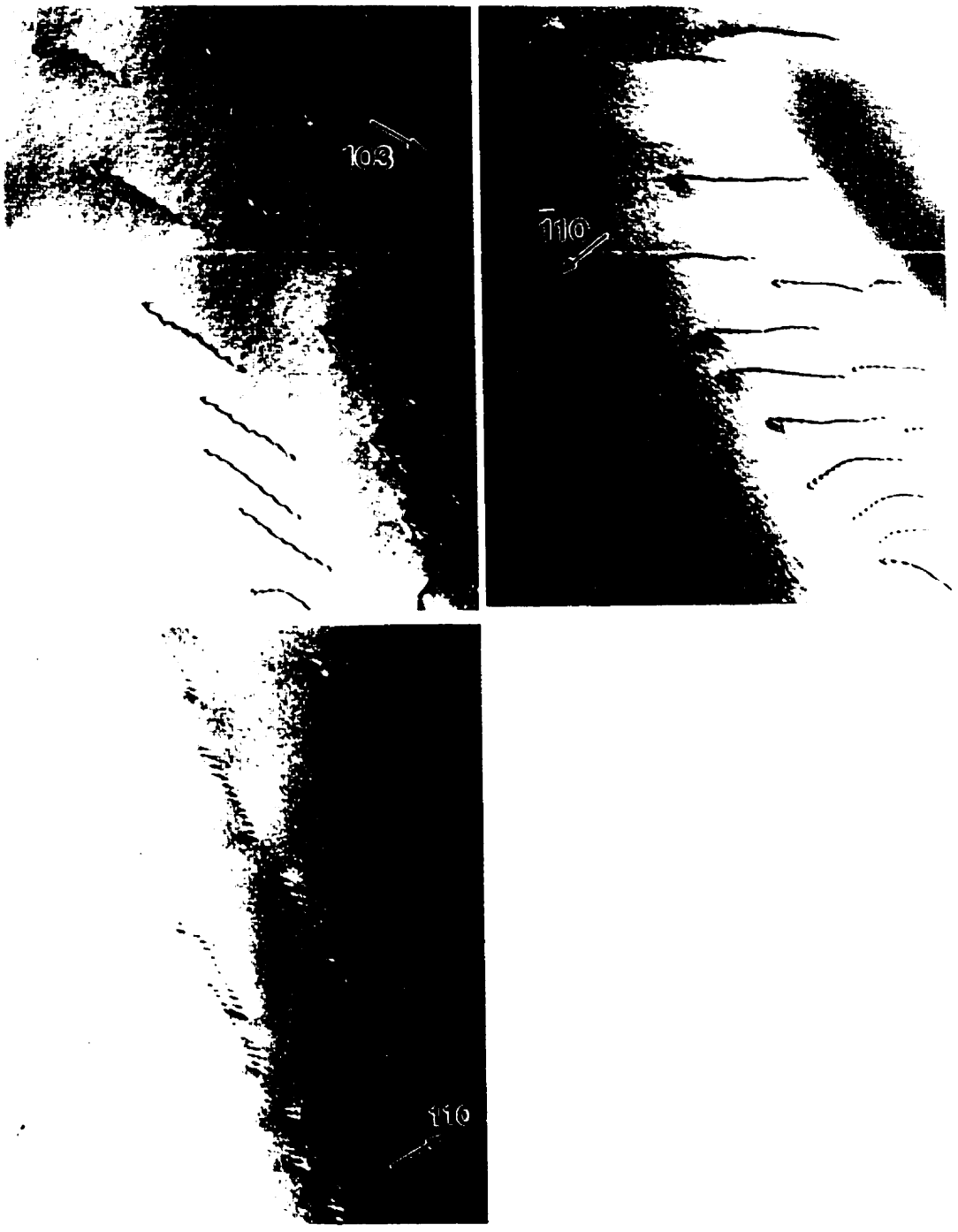
103
110
110

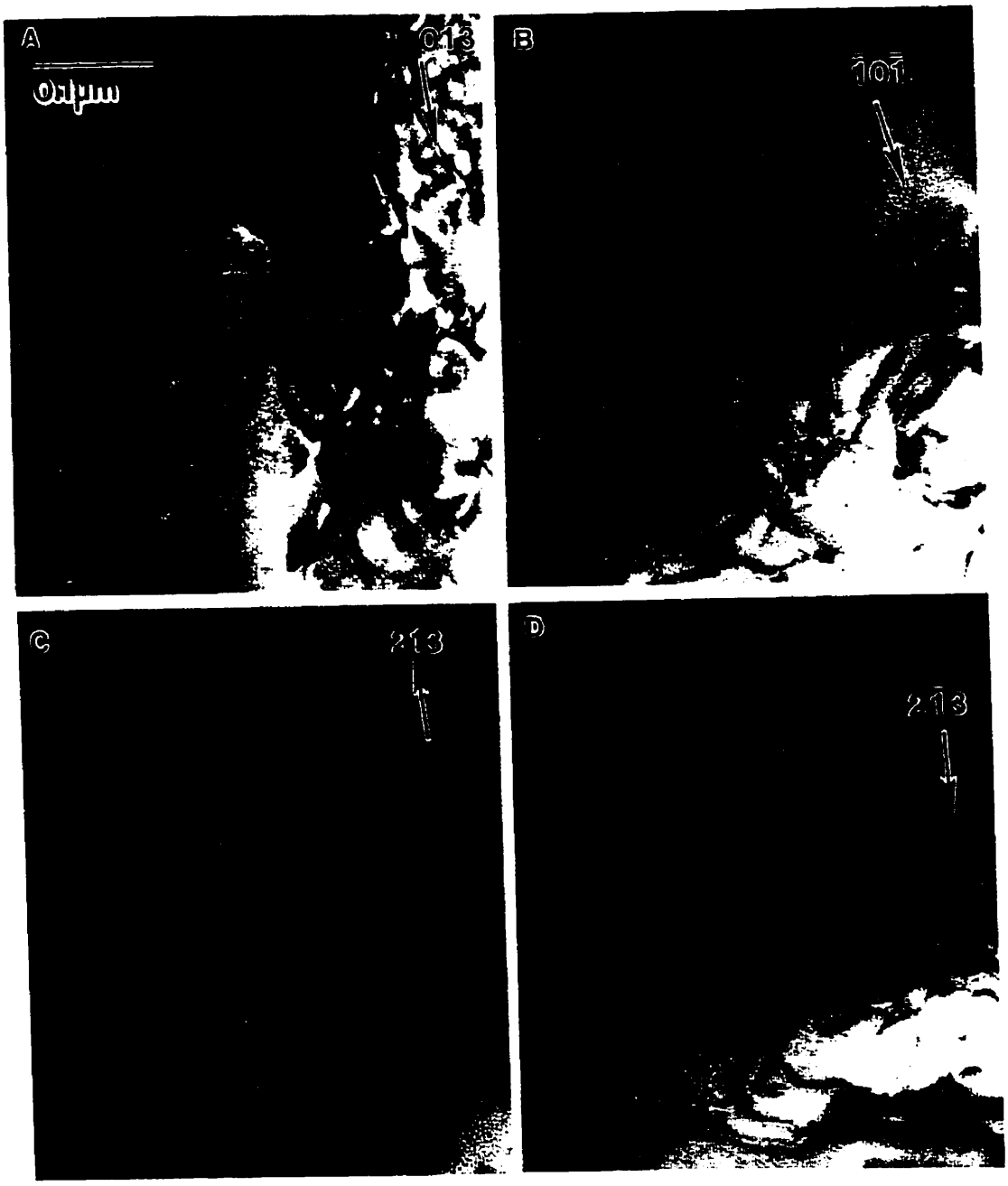

Figure 4.44 Bright Field images of an extended stacking fault that was observed directly beside the indentation. The diffracting conditions are; (a) g=013, (b) g= $\bar{1}0\bar{1}$, (c) g=213, (d) g= $2\bar{1}3$, (e) g= 103 (f) g= $01\bar{3}$, (g) g= $00\bar{6}$ and (h) g= $21\bar{3}$.

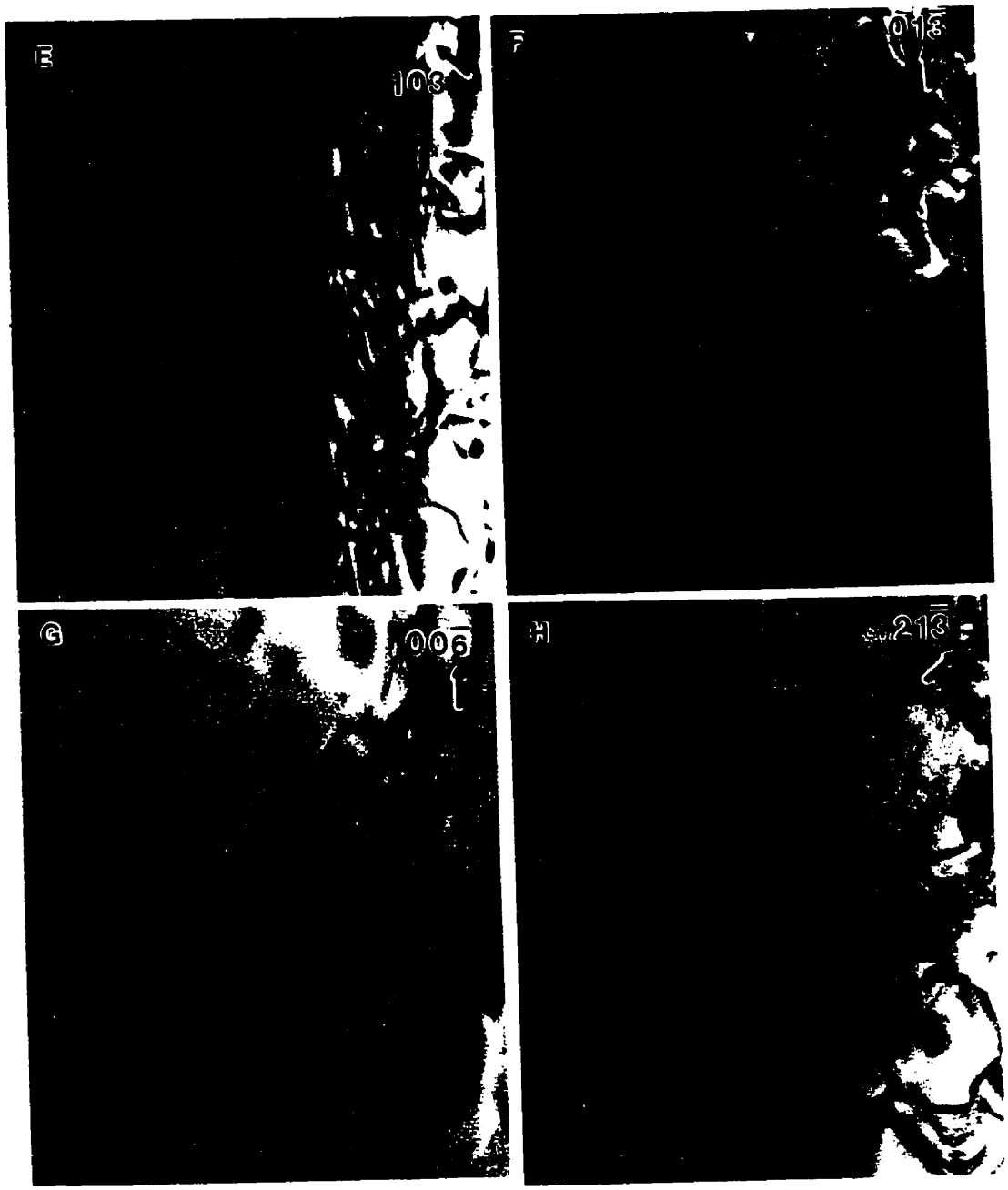
E
103
F
013
G
006
H
213

$\frac{1}{2}\langle 1\,1\,1\rangle$ dislocation that had dissociated into two identical partials. However, in this example, located very close to the indentation, the partials had a much wider separation (700 Å). This suggests that the separation of $\frac{1}{4}\langle 1\,1\,1\rangle$ partials is a function of the position of the stacking fault with respect to the indentation. Furthermore, in several of the images weak fringe contrast could be seen outside the partials. This weak contrast did not behave like that due to a fault with $\mathbf{R}=\frac{1}{2}[001]$ (Figure 4.21 (b)). Such fringe contrast could result from movement of the partials during foil preparation. Since this contrast is seen outside of the partials, the partials must have moved closer together during thinning, i.e. they probably moved as the pressure was relaxed.

Lastly, in many of the images the $\frac{1}{4}[\bar{1}\,1\,1]$ partials were invisible even though $\mathbf{g}.\mathbf{b} \neq 0$. For example, when $\mathbf{g}=0\bar{1}3$ (Figure 4.44 (b)) $\mathbf{g}.\mathbf{b}_p=\frac{1}{2}$ and the partials are invisible. This was true for all other cases where $\mathbf{g}.\mathbf{b}=\frac{1}{2}$. The partials were only visible when $\mathbf{g}.\mathbf{b} \geq \pm 1$ (Figure 4.44 (c),(d) and (e)).

Figure 4.44	g	$\mathbf{g}.\mathbf{b}_p$	$2\pi\ .\mathbf{g}.\mathbf{R}$
A	$01\bar{3}$	1	2π
B	$\bar{1}0\bar{1}$	0	0π
C	$21\bar{3}$	$\frac{1}{2}$	π
D	$2\bar{1}3$	$\frac{1}{2}$	π
E	$10\bar{3}$	$-\frac{1}{2}$	$-\pi$
F	$01\bar{3}$	$-\frac{3}{2}$	3π
G	$00\bar{6}$	-1	-2π
H	$21\bar{3}$	0	0

Table 4.4 Summary of contrast for partial dislocations, $\mathbf{b}_p = \frac{1}{4}[\bar{1}\,1\,1]$, and stacking fault, $\mathbf{R} = \frac{1}{4}[\bar{1}\,1\,1]$, shown in figure 4.44.

Two differences were noted in the dislocation structure when the diagonals of the indenter were aligned parallel to [100] and [001] directions. The first of these can be seen in Figure 4.45 (a). This bright field micrograph ($\mathbf{g}=\bar{1}03$, $\mathbf{B}=[\bar{3}151]$) was taken just beyond the corner of the diagonal aligned parallel to [001]. There appear to be several dislocation reactions. Two nodes and the three dislocations that meet node 1 are labelled 1

and 2 and A, B and C, respectively. Dislocation A is lying in the plane of the foil at the same depth as the node it ends at, while dislocations B and C travel from the node to the indented surface. In Figure 4.45 dislocations B and C produced contrast that was very similar to the dissociated dislocations ($\mathbf{b}=\frac{1}{2}[\bar{1}\,1\,\bar{1}]$ and $\frac{1}{2}[1\,1\,\bar{1}]$) in Figure 4.43. In both of these figures one set of dislocations produced a single image while the other produced a double image. Contrast analysis (Figure 4.45) found that dislocations B and C have Burgers vectors equal to $\frac{1}{2}[\bar{1}\,1\,\bar{1}]$ and $\frac{1}{2}[1\,1\,\bar{1}]$, respectively. The Burgers vector of dislocation A was found to be equal to [100]. Therefore, the net reaction between these dislocations is

$$\frac{1}{2}[\bar{1}\,1\,\bar{1}]+[100]=\frac{1}{2}[1\,1\,\bar{1}] \qquad 4.9$$

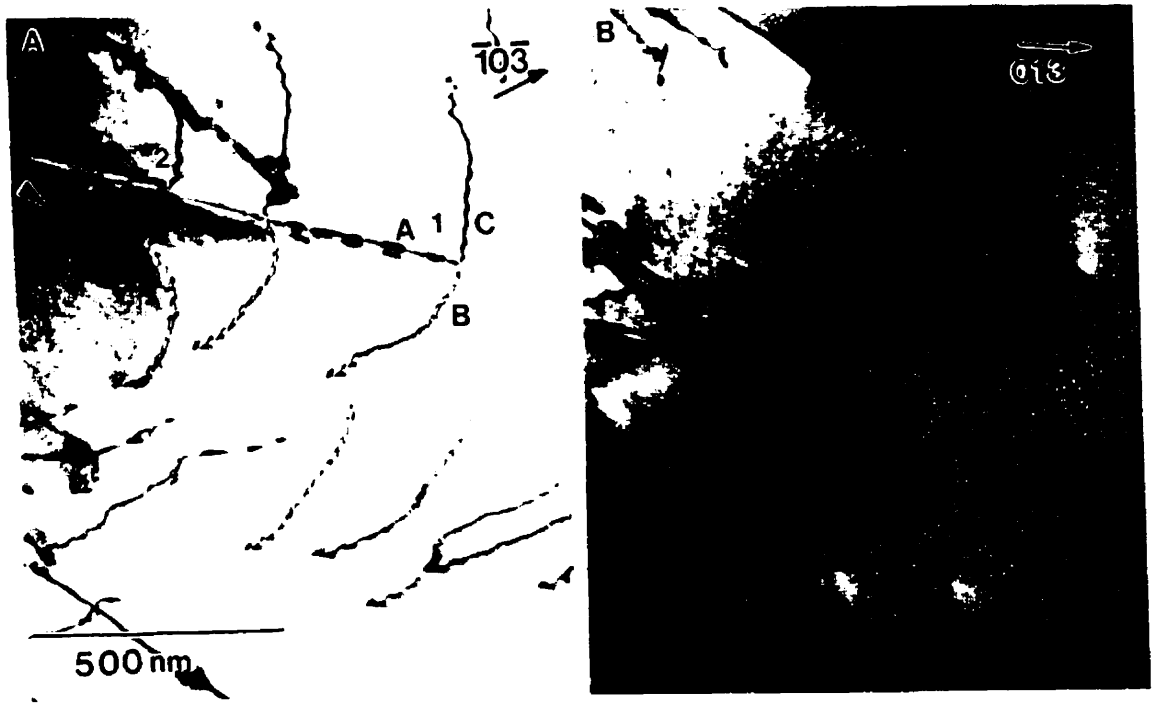

Figure 4.45 Bright Field micrographs of dislocation reactions occurring near an indentation. The diffracting conditions are; (a) $\mathbf{g}=\bar{1}0\bar{3}$, (b) $\mathbf{g}=013$, (c) $\mathbf{g}=006$, (d) $\mathbf{g}=\bar{2}00$, (e) $\mathbf{g}=\bar{1}01$ and (f) $\mathbf{g}=\bar{1}0\bar{1}$.

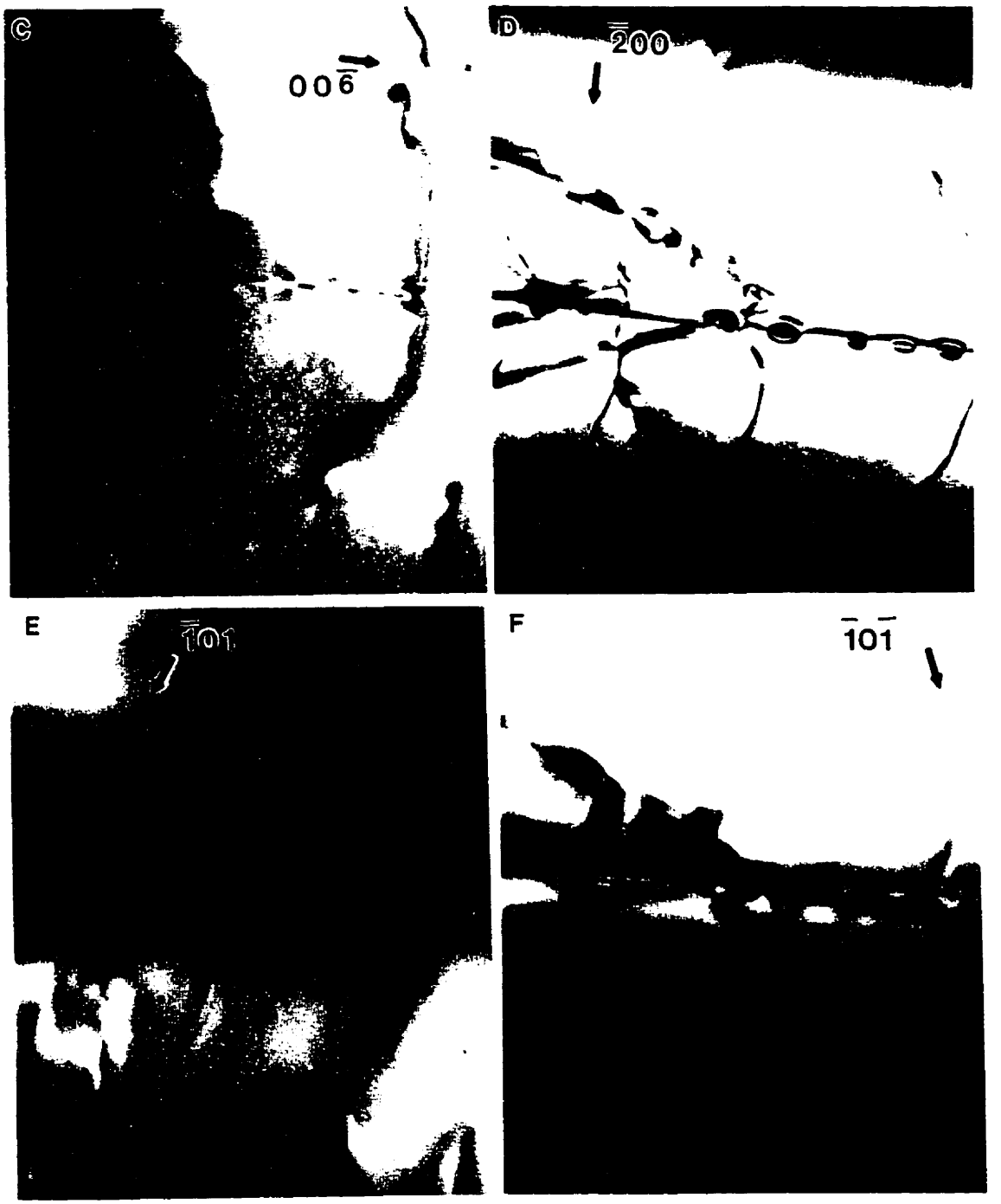
C
00$\bar{6}$
D
$\bar{2}$00
E
$\bar{1}$01
F
$\bar{1}$0$\bar{1}$

It should be noted that $\mathbf{u}=[00\bar{1}]$ for dislocation A; it lies on an (010) plane. This was the only example of the (010)[100] slip system found in this study. A stereo pair that was taken of this area illustrated that node 2 lies closer to the indented surface (which points towards the page) than node 1.

The second difference in the dislocation structure is shown in Figure 4.46. These two bright field micrographs were taken in the region of the plastic zone adjacent to that contained in Figure 4.45. In fact, the dislocation marked in Figure 4.46 (a) is also marked in Figure 4.45 (a). The dislocation structure in this area was formed from $\langle 100 \rangle$ and $\frac{1}{2}\langle 111 \rangle$ dislocations. The $\langle 100 \rangle$ dislocations were invisible in Figure 4.46 (b) ($\mathbf{g}=002$) while the $\frac{1}{2}\langle 111 \rangle$ dislocations were visible in both micrographs. The identity of the $\frac{1}{2}\langle 111 \rangle$ dislocations was confirmed with 101 type reflections (not shown) and the similarity of the contrast in Figures 4.46 (a) and 4.45 (a). Trace analysis found that all of the $\langle 100 \rangle$ and some of $\frac{1}{2}\langle 111 \rangle$ (arrowed) dislocations had a line direction that was equal to $\langle 111 \rangle$. Dislocations with this line direction were long and straight. This configuration of $\langle 100 \rangle$ dislocations was found around indentations made with the edges of the indenter parallel to [100] and [001] directions (eg. Figure 4.41 (b)). However, the density of these dislocations was much higher in this case. This type of $\frac{1}{2}\langle 111 \rangle$dislocations was only seen around indentations made with the diagonals of the indenter parallel to [100] and [001].

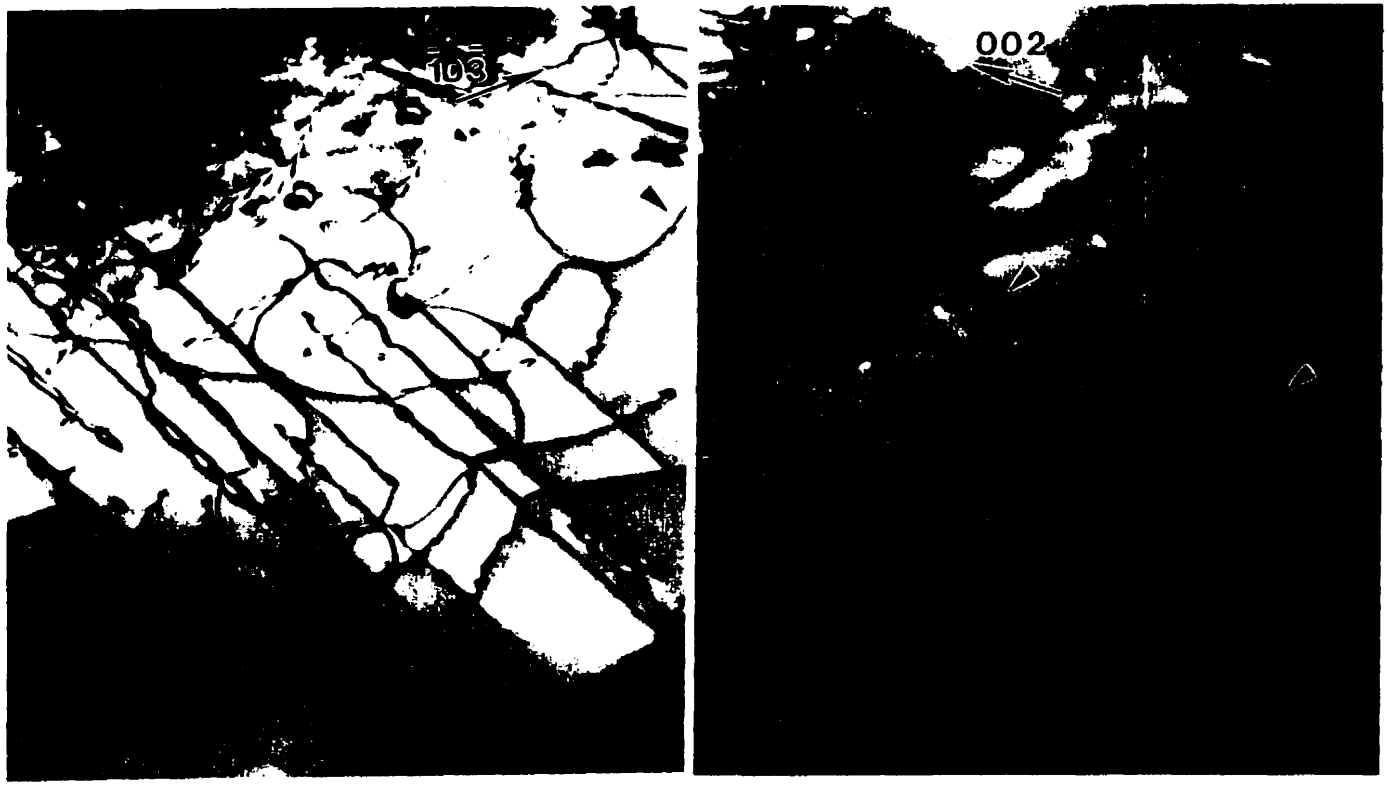

Figure 4.46 Bright Field micrographs of the dislocation arrangement near indentations made on an (010) plane with the diagonals of the indenter aligned parallel to [100] and [001] directions.

4.2.4.3. Rotations

The rotations associated with indentations on (010) surfaces were neither as large nor as well defined as those produced during indentation of (001) surfaces. Two SADPs of an indentation made with the edges of the indenter aligned parallel to [100] and [001] directions are shown in Figures 4.47 (a) and (b). In Figure 4.47 (a) the selected area aperture only collected information from the most highly deformed area, i.e. within the bands of high dislocation density along [001], while the SADP in Figure 4.47 (b) contained information from the lower dislocation density region of the plastic zone. There is no marked difference in these two diffraction patterns, unlike the case of indentations on (001) surfaces. In both SADPs there were rotations of approximately 10° about the [010] zone. There were also some extra spots but these spots were only seen around higher order reflections (further from the transmitted beam). Similar SADPs for an indentation that was made with the diagonals of the indenter aligned parallel to [100] and [001] directions are shown in Figure 4.47(c) and (d). These two diffraction patterns are very similar to the patterns of Figures 4.47 (a) and (b).

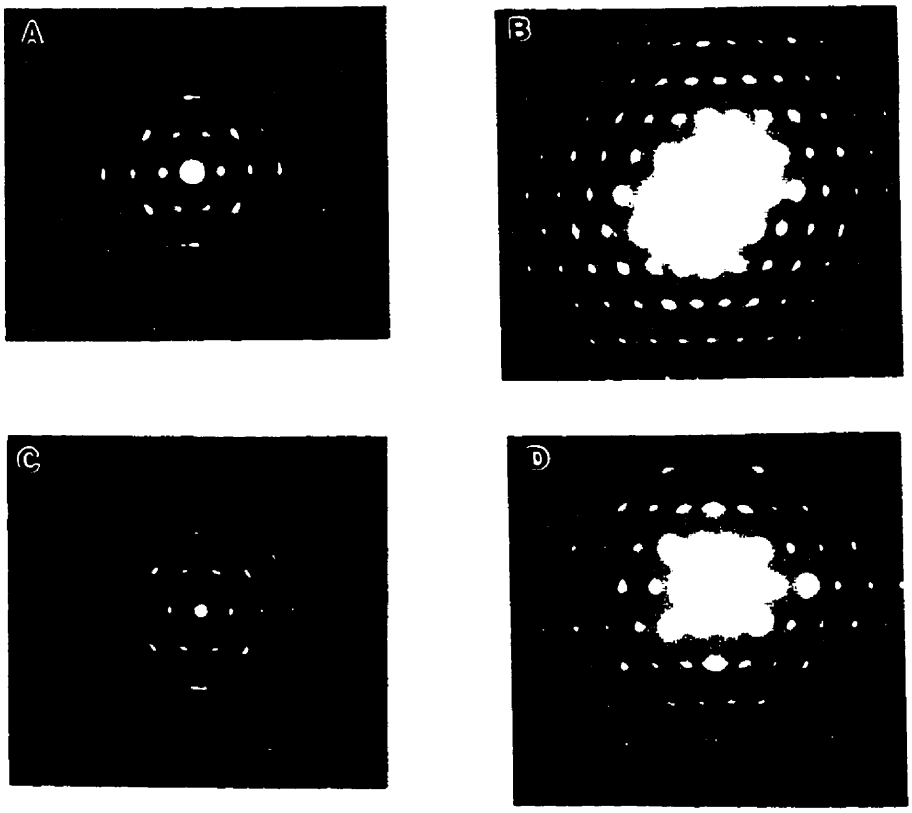

Figure 4.47 SADPs taken under indentations made with the two orientations of indenter. The edges and diagonals of the indenter were parallel to [100] and [001] directions in (a) & (b) and (c) & (d), respectively.

In Figure 4.42 it was noted that the diffracting conditions were different on either side of the band of piled-up dislocations. A more detailed analysis of this change in diffracting conditions is presented in Figure 4.48. A bright field micrograph of the band of piled-up dislocations and the material on either side of this band is shown in Figure 4.48(a). Outside the band **B**=[010], as seen in the CBED pattern in Figure 4.48 (b). On the other side of the band, i.e. in the highly deformed area, the centre of the pattern has been rotated approximately 9° about the [001] axis. A similar rotation was seen on the other side of the indentation. There were no rotations of this type observed around

indentations that were made with the diagonals of the indenter aligned with [100] and [001] directions.

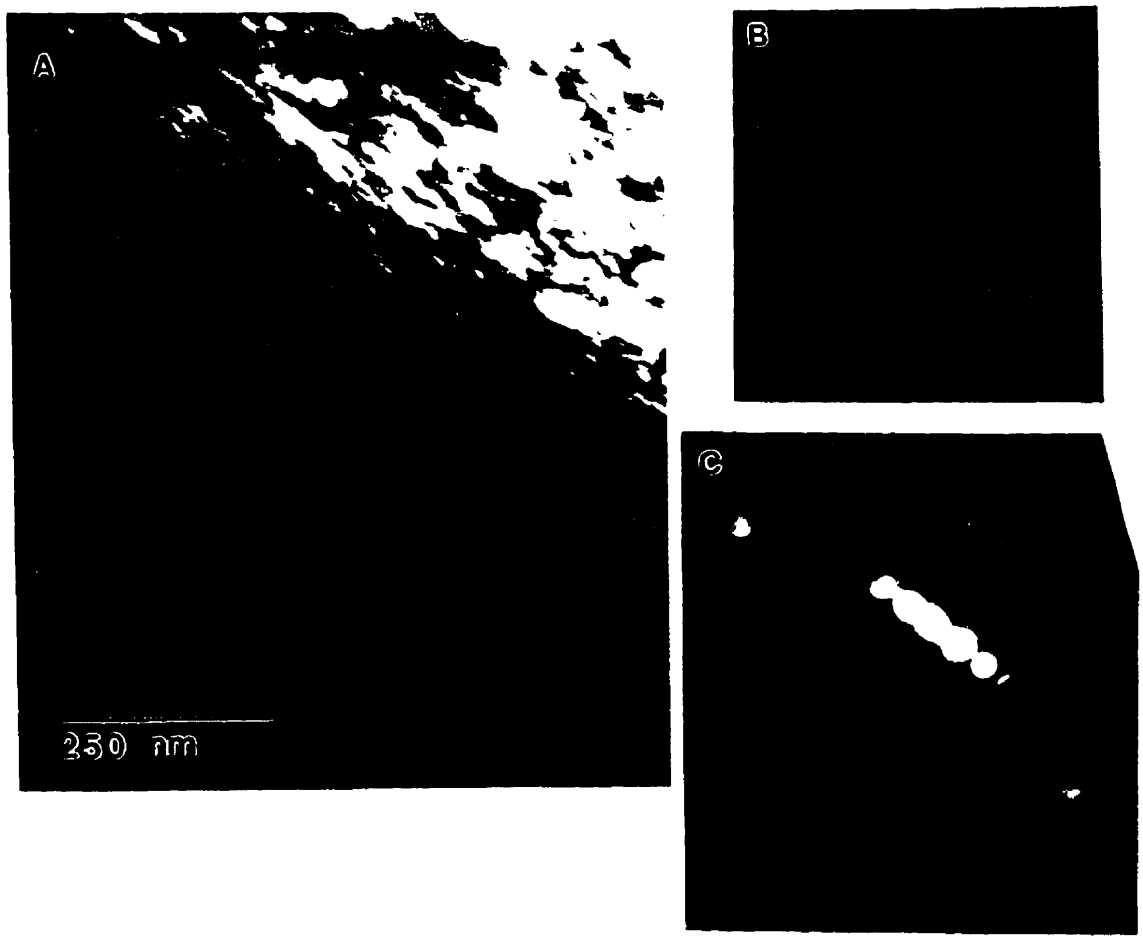

Figure 4.48 Bright Field micrographs (a) and difraction patterns (b) and (c) illustrating the rotation around an indentation on an (010) plane.

Chapter 5

Discussion

This discussion is divided into three sections: slip system analysis, analysis of small indentations i.e. those without cracks and less than 10 μm in size, and an analysis of large indentations i.e. those with cracks and greater than 10 μm in size.

In the first section the observations of slip systems will be analyzed in terms of the slip system selection criteria outlined in Section 2.1.3. and then compared to the published literature on the mechanical properties of $MoSi_2$. This comparison with the published literature will include a discussion of the dislocation contrast observed during TEM analysis.

In the second section the combination of elastic and plastic deformation processes that accommodate small indentations will be discussed. The sequence of events from the first elastic deformation to the onset of plastic flow and the shape change that occurs during unloading will be discussed. Again the results will be compared to the published literature. Finally, the development of the observed hardness versus applied load curves from the microstructural deformation events will be discussed. Of particular interest is the orientation dependence of these processes and how it can be incorporated into models of hardness at low loads.

In the final section of the discussion the results from indentations whose edge length was greater than 10 μm will be discussed. Plastic deformation and fracture are now

the dominant methods of accommodation. The plasticity processes operative during the formation of large indentations are much closer to those found in the bulk. This is demonstrated in the hardness versus applied load curves, where the hardness is constant at higher applied loads. The evolution of slip system activity including the appearance of slip systems that transport material towards the surface will also be discussed. The discussion will consider where and why fracture is initiated at an indentation size of about 10 μm. These issues will be discussed in terms of the slip systems identified during TEM analysis of the deformation produced around small indentations.

5.1 Slip System Observations

There were six slip systems observed in this study: $\{011\}\langle 100\rangle$, $\{110\}\langle 001\rangle$, $\{110\}\langle 111\rangle$, $\{010\}\langle 100\rangle$, $\{101\}\langle 111\rangle$ and $\{013\}\langle 331\rangle$. To the authors knowledge this is the first time the $\{110\}\langle 001\rangle$ slip system has been identified and the first report of the $\{110\}\langle 001\rangle$, $\{110\}\langle 111\rangle$, $\{010\}\langle 100\rangle$ and $\{101\}\langle 111\rangle$ slip systems being operative at room temperature. The $\{013\}\langle 331\rangle$ and $\{101\}\langle 111\rangle$ slip systems was inferred from observations of the slip traces around large indentations. This will be discussed in Section 5.3. An analysis of the first three slip systems listed, with reference to results in the literature, will be presented first.

5.1.1. {011}[100] Slip

Dislocations with a ⟨100⟩ Burgers vector were observed around all indentations. They were usually found to lie on {011} planes, and were frequently observed to cross slip between {011} planes. The dislocations were often very long and straight (e.g. Figure 4.15 and 4.41), lying along ⟨111⟩ directions. This line direction gave the dislocation a predominantly edge character (70°). The tendency to align along ⟨111⟩ directions decreased when the dislocations were closer to the indentation (Figure 4.42), i.e. in regions of higher stress.

There were two exceptions where straight ⟨100⟩ dislocations did not have a ⟨111⟩ line direction. First, to maintain a pure edge character the segments of the [010] prismatic loops seen directly under indentations were required to lie along ⟨101⟩ directions. Second, dislocations from the {010}⟨100⟩ slip system had an [001] line direction.

Similar observations of ⟨100⟩ dislocations were made by Ito et.al. (1995) and Maloy et.al. (1992). In the former study, ⟨100⟩ dislocations were found in samples (with the appropriate orientation) deformed at all temperatures. These authors also noted that ⟨100⟩ dislocations tended to align along ⟨111⟩ directions but found this tendency was not as pronounced in samples tested at higher temperatures (Ito et.al. 1995, Figure 9). Maloy et.al. (1992) made similar observations in samples indented at 100 °C. Although they did not report the exact line direction of the ⟨100⟩ dislocations, Maloy et. al. (1992) did find that they were straight and lay on {011} planes.

The observations in this study and the other studies cited are reminiscent of observations made in Si deformed at low temperatures (Dash 1956) where the dislocations

tended to align along simple crystallographic directions. Nabarro (1967) suggested that the formation of straight dislocations is indicative of a large Peierls barrier that must be overcome by thermal activation.

It is worth considering why ⟨100⟩ dislocations were often found on {011} planes, occasionally on (010) planes and were never found on {013} planes. In Section 2.1.4. it was shown that τ_{max}, the maximum shear stress, varies linearly with the ratio $\frac{|\mathbf{b}|}{h}$, where **b** is the Burgers vector and h is the interplanar spacing. Therefore, one would anticipate slip on a system with a low value of τ_{max} $\left(\frac{|\mathbf{b}|}{h}\right)$ would be favoured. In Table 2.3 it was shown that the value of $\frac{|\mathbf{b}|}{h}$ was largest for {013} slip, less for {011} slip and the smallest for {010} slip. However, only one case of {010}⟨100⟩ slip was found in this study and Ito et.al. (1995) only observed {010}⟨100⟩ slip in samples deformed at temperatures between 600 and 800 °C.

The preference for {011} slip planes may be related to the tendency for the dislocations to lie along a simple crystallographic direction. Kelly and Macmillan (1985) noted that this tendency to lie along simple crystallographic directions is due to a deep potential well along this direction. In $MoSi_2$ it appears that such a potential well lies along ⟨111⟩ directions. This may result in the preference of {011} slip planes. There were no observations of the {013}⟨100⟩ slip system in this study. The only observations of {013}⟨100⟩ slip in the literature were made in samples deformed at high temperatures. Unal et.al. (1990) reported {013} to be the predominant slip plane of [100] dislocations in

samples deformed at 1400 °C while Mitchell et.al. (1993) observed the {013}⟨100⟩ slip system in [021] oriented single crystals deformed at 1300 °C.

In Sections 4.1.4.2. and 4.2.3.2. strong residual TEM contrast was always present when [100] dislocations were imaged in the **g.b**=0 condition. Such residual contrast had been noted by Maloy et.al. (1992) and Unal et.al. (1990). In the latter study this contrast was attributed to the edge character of the dislocations. However, in Figure 4.16 (b) it is apparent that there are two components to this residual contrast. First, the image is actually a double image that is symmetrical about the dislocation line. This type of contrast is characteristic of edge dislocations when **g.b**=0 but **g.bxu** ≠0 (Hirsch et.al. 1967).

Second, and more striking, are the alternating black and white fringes which appear along the dislocation. In Figure 5.1 the simulated image from Figure 4.16 (b), **u**= $\langle \bar{1}\,1\,1 \rangle$, is compared to a simulated image that was calculated under the same diffracting conditions but with **u**=$\langle \bar{9}01 \rangle$. A line direction of **u**=$\langle \bar{9}01 \rangle$ produces a dislocation that is 15° away from pure screw orientation. The double image resulting from the edge component of the dislocation with **u**= $\langle \bar{1}\,1\,1 \rangle$ should disappear with this new line direction. This is in fact the case.

However, the alternating black and white contrast is still present. A similar situation was discussed by Humble (1970) for a pure screw dislocation in β-brass. Humble showed that the alternating black/ white contrast was due to anisotropic elasticity. Considering the anisotropy of the elastic constants in $MoSi_2$ (Table 2.2) it is quite probable that this is the origin of the residual contrast produced by ⟨100⟩ dislocations in $MoSi_2$.

Figure 5.1 Two computer simulated images of a ⟨100⟩ dislocation. (a) **b**=⟨100⟩, **g**=$0\bar{2}0$ and **u**=$\langle\bar{1}\,1\,1\rangle$ (b) **b**=⟨100⟩, **g**= $0\bar{2}0$ and **u**= $\langle\bar{9}01\rangle$.

5.1.2. {110}[001] Slip

A characteristic feature of the deformed zone produced by an indentation on an (001) surface were the traces along ⟨110⟩ directions. It was shown in Section 4.1.4.2 that these traces were due to stacking faults with displacement vectors, **R**, equal to $\frac{1}{2}[001]$ or $\frac{1}{4}\langle 1\,1\,1\rangle$. It was also found (Figure 4.21) that the fault with **R**=$\frac{1}{2}[001]$ was bounded by partial dislocations with **b**=$\frac{1}{2}[001]$ and $\frac{1}{4}\langle 1\,1\,1\rangle$. This system of partial dislocations and stacking faults is a result of the dissociation of a unit [001] dislocation.

It is anticipated that an [001] dislocation will dissociate due to its large Burgers vector (7.85 Å). Three possible dissociations are shown in Figure 5.2. Dissociations A and C produce a partial dislocation with a Burgers vector of $\frac{1}{2}[001]$ while dissociations B

and C create stacking fault with **R**= $\frac{1}{2}[001]$. Dissociation A creates a stacking fault with a displacement vector equal to $\frac{1}{4}[1\bar{1}3]$.

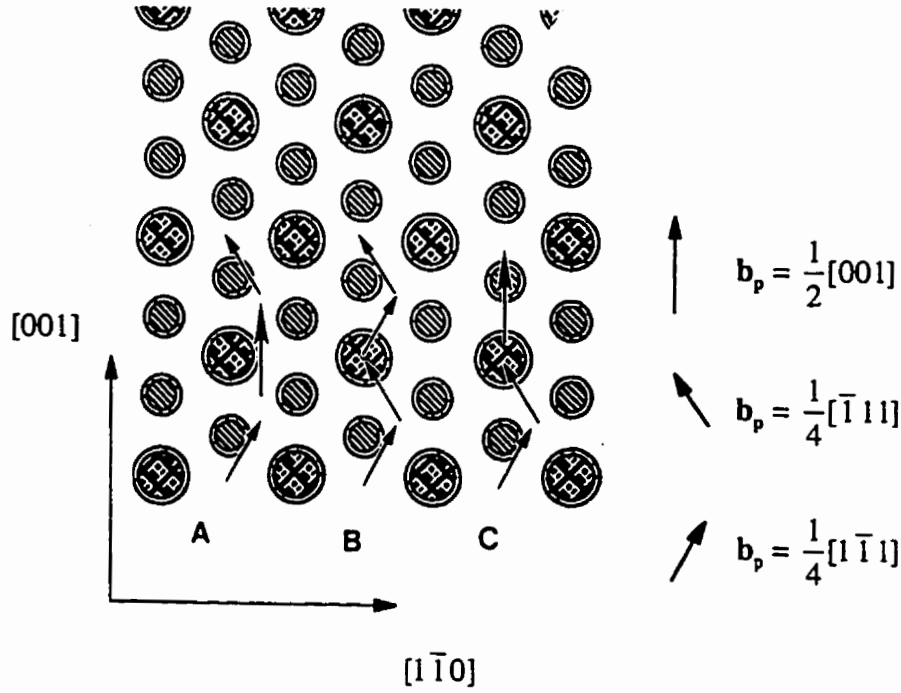

Figure 5.2 Possible dissociations of a [001] dislocation.

In Figure 4.21 a stacking fault with a $\frac{1}{2}[001]$ displacement vector was seen to be bounded by a partial dislocation with the same vector. This configuration is only possible if dissociation C (Figure 5.2) has occurred. This dissociation is also consistent with the adjacent $\frac{1}{4}\langle 111\rangle$ stacking fault seen in Figure 4.21.

Dissociation B was also commonly observed. An example of this dissociation is seen in Figure 4.19. This dissociation was identified by two end faults that produced strong residual contrast in certain WBDF conditions (Figure 4.19). In this case the [001]

dislocation has dissociated into four $\frac{1}{4}\langle 1\,1\,1\rangle$ type partial dislocations. In this scenario the two 'end' faults have displacement vectors equal to $\frac{1}{4}[1\,\bar{1}\,1]$ and $\frac{1}{4}[1\,\bar{1}\,1]$ while the central fault has a displacement vector of $\frac{1}{2}[001]$. This dissociation is shown schematically in Figure 5.3.

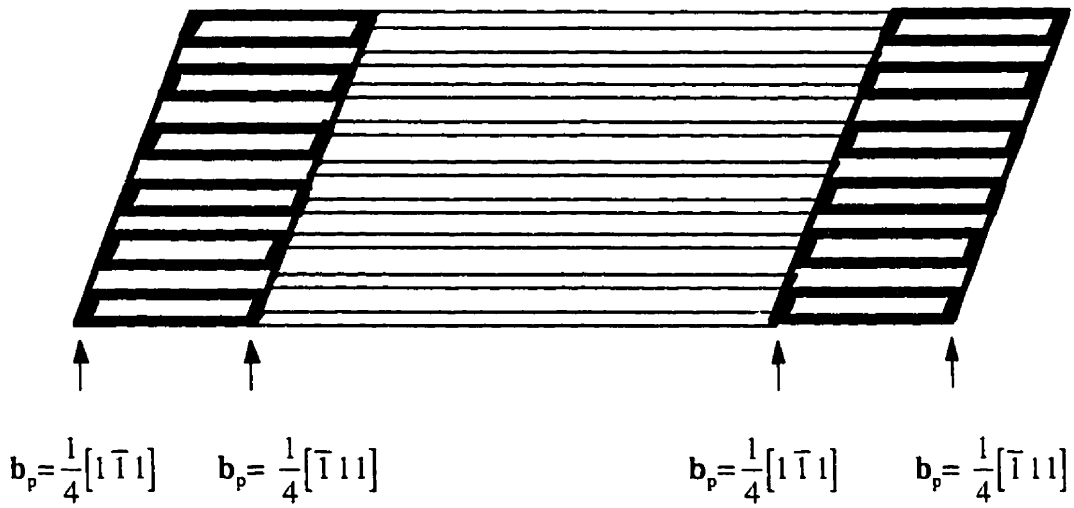

Figure 5.3 Schematic diagram showing the arrangement of stacking faults produced during the dissociation of a [001] dislocation.

In Table 2.4 it was shown that $\sum|\mathbf{b}_{product}|^2$ is 20% lower for dissociation B than for either dissociation A or C. Therefore, the more frequent observation of dissociation B agrees with the strain energy calculations presented in Table 2.4.

A key element in the identification of stacking faults with a $\frac{1}{2}[001]$ displacement vector was the residual contrast produced by these faults. A fault with $\mathbf{R}=\frac{1}{2}[001]$ will cause the Mo atoms of the B layer, in the ABAB stacking sequence of $MoSi_2$, to lie directly over the Mo atoms in the A layer. Such a configuration is probably quite unstable due to the proximity of Mo atoms. The stability might be increased by a small displacement out of the slip plane thereby increasing the spacing between Mo atoms in the two layers. This additional displacement vector would be in contrast when $\mathbf{g}.\mathbf{R}=2n\pi$. Thereby producing the residual contrast observed in Figure 4.19. van Tendeloo and Amelinckx (1974) found similar residual contrast in $NiMo_3$ for cases where there was a small additional displacement at the anti-phase boundary, which was created by an excess of Mo atoms there.

The only previous report of faults with $\mathbf{R}=\frac{1}{2}[001]$ was by Kad et.al. (1995). These authors only observed these faults in unannealed samples and considered them to be formed during growth and to be metastable. They proposed that a $\frac{1}{2}[001]$ fault could be formed from the dissociation

$$[001] \Rightarrow \frac{1}{4}[1\bar{1}1] + SISF + \frac{1}{2}[001] + SISF + \frac{1}{4}[\bar{1}11] \qquad 5.1$$

This is dissociation A in Figure 5.2. It is evident in Figure 5.2 that this particular dissociation produces faults with $\mathbf{R} = \frac{1}{4}\langle 113\rangle$ and $\frac{1}{4}\langle 111\rangle$ and not faults with $\mathbf{R}=\frac{1}{2}[001]$.

5.1.3. $\{110\}\langle 111\rangle$ Slip

Partial $\frac{1}{4}\langle 111\rangle$ dislocations and stacking faults with $\mathbf{R}=\frac{1}{4}\langle 111\rangle$ are produced by the dissociation of either [001] or $\frac{1}{2}\langle 111\rangle$ dislocations. This section will only consider the dissociation of $\frac{1}{2}\langle 111\rangle$ dislocations into two identical partial dislocations (Equation 2.6). This dissociation was only observed in the plastic zone of indentations on (010) surfaces. There were three important observations made with respect to $\frac{1}{2}\langle 111\rangle$ dislocations and their dissociation.

First, there were no examples of whole $\frac{1}{2}\langle 111\rangle$ dislocations found in this study. It is shown in Appendix B that two closely spaced $\frac{1}{4}\langle 111\rangle$ partial dislocations can only be resolved when $\alpha = 2n\pi$ (i.e. the fault is invisible) and $\mathbf{B}$ is close to the foil normal. Therefore, the two reported observations of whole $\frac{1}{2}\langle 111\rangle$ dislocations (Unal et.al 1990 and Maloy et.al. 1992) may be unresolved $\frac{1}{4}\langle 111\rangle$ partial dislocations. Since, neither study presented images that satisfy the above diffracting conditions it is unclear whether or not these authors actually observed whole $\frac{1}{2}\langle 111\rangle$ dislocations.

Second, $\frac{1}{4}\langle 111\rangle$ dislocations were observed in samples that were indented at room temperature. Prior to this observation the lowest temperature at which the $\{110\}\frac{1}{2}\langle 111\rangle$ slip system was found to be active was 300 °C (Ito et.al. 1995).

Third, the separation of the observed $\frac{1}{4}\langle 111\rangle$ partial dislocations varied with location of the dislocations around an indentation. When the partials were located in a region of the plastic zone that was not directly under the indentation, their separation was between 70 and 75 Å, which is in general agreement with the two previous determinations of the separation of partial dislocations (Evans et.al. 1993 and Ito et.al. 1995). The exact separation was difficult to determine because of the nature of the contrast produced by the two closely spaced partials and the associated stacking fault. As mentioned above $\frac{1}{4}\langle 111\rangle$ partial dislocations can only be resolved when $\alpha = 2n\pi$ and **B** is close to the foil normal. Since the exact separation is most easily determined when **B** is close to the slip plane ($\{110\}$) it is desirable to image the partials with a diffracting plane that belongs to the $\langle 110\rangle$ zone axis.

However, there are no planes from this zone axis that would cause the fault to be invisible. Therefore, one must tilt away from the $\langle 110\rangle$ zone axis to obtain the appropriate diffracting conditions. The two determinations of the separation of the partial dislocations in the literature (Evans et.al. 1993 and Ito et.al. 1995) used a 103 type reflection. Since neither paper accounted for the 30° tilt away from the $\langle 110\rangle$ zone axis required to access a 103 diffracting vector these determinations underestimates the true separation of the partial dislocations.

The most striking observation concerning the $\{110\}\frac{1}{4}\langle 111\rangle$ slip system was that the separation of $\frac{1}{4}\langle 111\rangle$ partial dislocations was much larger (up to a factor of 10) underneath an indentation than it was in regions removed from the indentation. For indentations on an

(001) surface this change can be seen by comparing the stacking fault width in Figure 4.18 or Figure 4.19 to that in Figure 4.21. The situation is more evident around indentations on an (010) surface (Figure 4.43 versus Figure 4.44). It was also noted that the dislocations in Figure 4.44 had probably moved closer together during the thinning process. All of these observations suggest some component of the stress state under the indentation influences the separation of these partial dislocations.

The separation of partials is determined by an energy balance between the repulsive forces of the partials and the attractive force which acts to minimize the surface area of the stacking fault. In Section 2.1.2. it was shown that a stacking fault with $\mathbf{R}=\frac{1}{4}\langle 111\rangle$ creates four layers where Mo atoms are in ABCD stacking. Such a change in the stacking sequence could be of importance if the local density of the ABCD stacking sequence of {110} planes is different from the original ABAB sequence of {110} planes. The theoretical density of the tetragonal (C11b) and hexagonal (C40) structures is 6.24 $g.cm^{-3}$ and 6.42 $g.cm^{-3}$, respectively. This is a 3% difference in density for the change of the stacking sequence from ABAB to ABCABC. This suggests that there may be a further increase in density when all four possible Mo sites are occupied i.e. ABCD packing. Therefore, the four layers of atoms around the stacking fault may be more densely packed than the surrounding material. This higher density structure will be favoured directly under the indenter where there is a large compressive hydrostatic pressure (several GPa). Moreover, high pressure may help to promote the extension of the $\frac{1}{4}\langle 111\rangle$ stacking faults due to the increased density of the stacking sequence produced by the fault. During the thinning process some of this pressure is released and the extension of the stacking faults decreases.

5.2 Elastic and Plastic Accommodation Processes of Small Indentations

Small indentations are defined in this study as indentations whose edge length is less than 10 μm. This is not an arbitrary demarcation between indentations of different sizes. Distinct changes in the hardness versus applied load curve and the nature of the deformed zone were observed at this size of indentation.

First, as seen in the curves of hardness versus applied load (Figures 4.1, 4.2, 4.26 and 4.27) the hardness was constant when the indentation was larger than 10 μm (which corresponds to loads greater than approximately 100 grams) while any increase in hardness with decreasing load occurred below this point. Second, the shape of the deformed zone around the indentation also changed as the size of the indentation was reduced below 10 μm. There was no cracking associated with small indentations and the plastic zone did not extend significantly beyond the indentation.

Before the specific features of the elastic and plastic deformation are discussed it will be useful to review the patterns of plastic flow that have been observed. Two slip systems: {110}[001] and {011}[100] were active during indentation of an (001) surface. A schematic diagram showing the configuration of slip on these two systems is given in Figure 5.4. These two slip systems transport material along the indentation axis ({110}[001]) or along directions contained in the indented surface ({011}⟨100⟩).

The {110}[001] slip system moved material into the sample along the axis of indentation, [001]. The stereo pair of Figure 4.11 illustrated that slip on this system outlined the shape of the indenter, i.e. the smallest squares produced by the dislocation traces on {110} planes were at the centre of the indentation and lay furthest from the indented surface. This slip system was only active directly under the indentation.

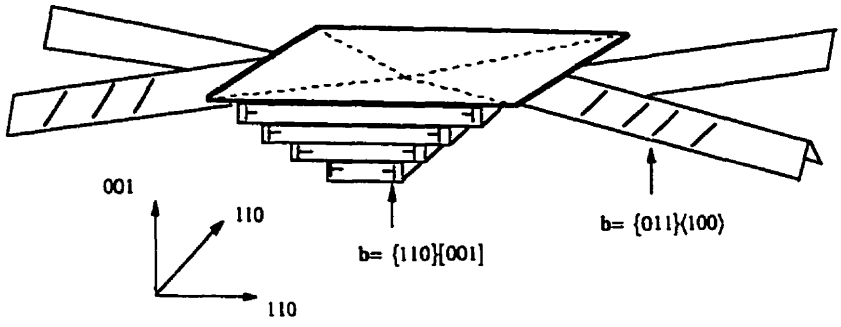

Figure 5.4 Schematic diagram showing the configuration of the {110}[001] and {011}[100] slip systems. The [100] dislocations have cross-slipped onto similar {101} planes, Figure 4.12 (a).

The second slip system, {011}[100], moved material along directions that are contained in the indented surface. Dislocations from this slip system were observed both underneath and beside the indentation. Dislocations on the {110}[001] slip system only traveled a few hundred nanometers beyond the indented surface while dislocations from the {011}[100] slip system traveled more than a micron (the exact distance depended on the applied load) away from the edge of the indentation. The pattern of deformation shown in Figure 5.4 was found around indentations that were made with either the edges or the diagonals of the indenter parallel to ⟨110⟩ directions.

The pattern of material movement was more complicated when the indentation was made on an (010) surface because of the lower symmetry of the [010] axis. However, material was again transported along the indentation axis and along directions that were either normal to or nearly normal to the indentation axis. The $\{110\}\frac{1}{2}\langle 111\rangle$, {011}⟨100⟩ and (010)⟨100⟩ slip systems were operative during indentation of an (010) surface. The configuration of slip on these systems is shown in Figure 5.5.

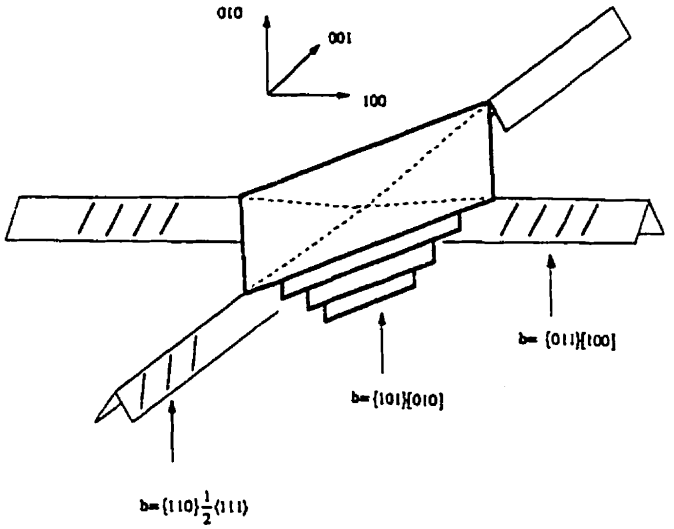

Figure 5.5 Configuration of the $\{110\}\frac{1}{2}\langle 111\rangle$ and $\{011\}\langle 100\rangle$ slip systems.

Prismatic dislocation loops of the $\{101\}[010]$ slip system transported material along the indentation axis into the sample. Again a slip system whose slip direction was parallel to the indentation direction was only active directly under the indentation. The $\{011\}\langle 100\rangle$ and $(010)\langle 100\rangle$ slip systems transported material away from the indentation along the indented surface. Finally, the $\{110\}\frac{1}{2}\langle 111\rangle$ slip system transported material into the sample at a 30° angle to the surface. It was generally found that slip system activity was determined by the orientation of the indenter. A given slip system would only be activated to transport material away from a given facet if the normal to that facet had a component in the slip direction. For example, when the indenter was aligned with its edges parallel to [100] and [001] directions there were no dislocations with a $\langle 100\rangle$ Burgers vector seen adjacent to the facets whose edges lay along $\langle 100\rangle$. One would anticipate the slip direction to be either [010] or have a component along [001]. This is in agreement with these observations.

The plastic deformation responsible for the formation of small indentations on either (010) or (001) surfaces transported material either parallel to the indented surface or into the sample. There were no slip systems found that transported material to the surface, suggesting a local increase in density. This observation seems counter intuitive. One might anticipate that the material displaced by the indenter should be transported to the free surface to conserve volume. The formation of pile up at the free surface and the overall deformation that occurs during indentation can be considered in terms of the indentation models presented in Section 2.2. Continuum models will be considered first.

In Section 2.2.1.2. the use of slip line field theory and the expansion of a hemispherical cavity were presented as two approaches for describing the plastic flow during indentations in polycrystals. Hill et.al. (1947) demonstrated that slip line field theory could be used to describe the plastic deformation during indentation of a material that demonstrated rigid plastic behaviour and the indentation was made with a sharp indenter (included angle is <60°) . When these two conditions were satisfied the volume of material that piled up around the indentation was equal to the volume of the indentation.

On the other hand, in cases where the indented material was not an ideal rigid plastic material or the included angle of the indenter was greater than 60° the plastic deformation had radial symmetry (Mulhearn 1957 and Samuels and Mulhearn 1959). In these cases the volume of material that was displaced by the indenter could not be accounted for by material that had piled up beside the indentation. Marsh (1964) showed that this latter type of behaviour would be anticipated when the ratio of Young's modulus to yield strength $\left(\frac{E}{Y}\right)$ was less than 100. This criterion is generally satisfied by materials that have a high yield strength, which is usually the case for brittle solids.

$MoSi_2$ has a Young's modulus of 440 GPa (Nakamura et.al. 1990) and the room temperature yield stress along [001] can be crudely approximated as 5 GPa ($\frac{1}{3}$ of the measured hardness for an applied load of 5 grams (Figure 4.2)). This produces a value of 90 for $\frac{E}{Y}$. Further, the Vickers indenter has an included angle of 168°. Based on an $\frac{E}{Y}$ ratio of 90 and an included angle of 168 ° one might anticipate that an indentation made with a Vickers tip in $MoSi_2$ would have radial symmetry with no significant pile up. The material displaced by plastic deformation will move into the surrounding matrix and not towards the surface. This is in fact the case. There is no significant pile up formed and the active slip systems move material away from the indenter into the surrounding matrix. However, since the indentations were formed in single crystals the plastic zone is not anticipated to display the radial symmetry observed around large indentations with similar material properties (e.g. Mulhearn 1957). The shape of the plastic zone will be defined by the available slip systems. Therefore, while the overall geometry of the plastic zone is anticipated by the continuum models the details of deformation require knowledge of the elastic and plastic deformation. The best approach for this is to look at the sequence of deformation that occurred during indentation between the time of first contact and complete unloading.

It was shown in Section 2.2.2.1 that elastic deformation occurs when first contact is made during the indentation of single crystals. In theory this elastic deformation might be identified through the shape change that takes place when the applied load is removed. However, it was noted (Section 4.1.2) that reverse plastic flow occurs when the applied load is removed. This is the second component to the shape change that must be quantified if the amount of elastic deformation is to be determined. The separation of the two components of the shape change will be discussed after the magnitude and orientation of

the observed shape change has been discussed. The discussion of these latter two concepts will look at whether elastic recovery and reverse plastic flow combine to produce the observed shape change.

Large anisotropic changes in the shape of the indentation were noted in Sections 4.1.3 and 4.2.2. In Section 4.1.3 AFM techniques were used to measure the change of shape of indentations on an (001) surface made with the edges of the indenter aligned parallel to ⟨110⟩ directions. It was found that the volume of the indentation decreased when the load was removed. The magnitude of this decrease in volume increased with decreasing load until the change was approximately 30% for indentations made with an applied load of 15 grams. This represents a 15 % decrease in the depth of the indentation parallel to the [001] axis. It is assumed that indentations made with their diagonals parallel to [110] directions experienced similar recovery.

When indentations were made on an (010) surface an in-plane shape change was observed. For example, when the diagonals of the indentation were aligned with the [100] and [001] directions, the diagonal along [001] was almost 30% shorter than the diagonal along [100], for an indentation made with an applied load of 10 grams. A similar pattern of recovery was observed for indentations on both (001) and (010) surfaces. When the edges of the indentation were parallel to [001] and [100] the edge along [001] was shorter than that along [100]. Therefore, there is considerable change in the dimension along the [001] direction while there did not appear to be any change in the [100] dimension. Finally, the magnitude of the shape change increased with decreasing applied loads.

The largest dimensional change observed was the 30% difference in the diagonal length for indentations made on an (010) surface with an applied load of 10 grams. A similarly large shape change was noted by Page et.al. (1992). These authors observed that

one half of the total displacement of the indenter was recovered when the load was removed during nano-indentation of sapphire. This observation (Figure 3(b), Page et.al. 1992) was made for an indentation that had a total depth of 500 nm and the applied load was 8 grams. This indentation is comparable in size to those in the current work which displayed a 30% difference in diagonal length. In their paper Page et.al. (1992) determined that this shape change was due to elastic recovery. Considering the similarity of the indentation size and material properties (sapphire, E= 390 GPa, versus $MoSi_2$, E=440 GPa) it is possible that a large fraction of the observed shape change in $MoSi_2$ is also due to elastic recovery.

The second element of any shape change is the effect of crystallography i.e. is the shape change the same in all directions? It cannot be assumed that the shape change will be isotropic. In this study it was found that any change in the shape of the indentation was due to a dimensional change along the [001] axis. When the indentation was on an (001) surface the dimensional change along [001] resulted in a change in the depth of the indentation while on (010) surfaces this change of the [001] dimension created a difference in diagonal lengths of indentations.

A similar result was obtained by Sargent and Page (1985). These authors pointed out that the largest elastic recovery will occur along the direction with the largest yield stress to modulus ratio $\left(\frac{Y_\theta}{E_\theta}\right)$. It has been shown (Umakoshi et.al. 1990, Mitchell et.al. 1993 and Ito et.al. 1995) that the highest yield stress in $MoSi_2$ single crystals occurs along the [001] axis. A first approximation to $\frac{Y_{100}}{E_{100}}$ and $\frac{Y_{001}}{E_{001}}$ can be made using the data of Ito et.al. (1995) and Nakamura et.al. (1990). Y_{100} can be roughly approximated by Y_{0151} which is 1 GPa at 295 K and Y_{001} can again be approximated to be 10 GPa. Dividing these yield stress values by the stiffness constants found by Nakamura et.al. (1990) a value of

0.0025 is obtained for $\frac{Y_{100}}{E_{100}}$ while $\frac{Y_{001}}{E_{001}}$ is greater than 0.01. Thus, the ratio of $\frac{Y_\theta}{E_\theta}$ is at least four times larger for [001] than for [100], which suggests the elastic recovery along [001] will be larger than that along [010]. This agrees with observations where the largest dimensional change occurred along [001] directions regardless of crystal orientation. The exact nature and origin of this reverse plastic flow will be discussed in detail later when the evolution of plastic deformation during indentation is considered.

The separation of the elastic and plastic components of the overall shape change is not straightforward. This requires that one of these components can be independently quantified. It is not possible to quantify the elastic portion of the deformation without a load displacement curve that covers the entire loading cycle. However, it is possible to approximate the amount of plastic back flow from the pattern of slip traces. Slip traces along ⟨110⟩ directions were seen on the facets of the indentation (Section 4.1.2). These traces could have only been formed during unloading. Therefore, the step height of these traces will indicate the amount of reverse plastic flow. This could be determined by stereo-microscopy in the SEM. This quantity could then be compared to the overall shape change and the fraction of elastic deformation determined.

Changes in the shape of an indentation that occur during unloading have been used to explain Indentation Size Effect (ISE) i.e. increasing hardness with decreasing load. In such explanations it is assumed that any shape change is due solely to elastic recovery. For example, Bull, Page and Yoffe (1989) developed a model of ISE where the increase in hardness was due to an increasing fraction of elastic deformation with reductions in the applied load. In this model it was assumed that each increment of plastic deformation was preceded by elastic deformation. It was further assumed that the deformed zone was hemispherical in shape. While the authors stated this was an ideal case it does not reflect

the situation present during the formation of small indentations in brittle materials. It has been shown here that the shape change is dictated by crystallography. It has also been shown that the shape change does not necessarily influence the hardness i.e. when the depth is the only dimension that changes. Therefore, any discussion of ISE that involves the change in shape of the indentation that occurs during unloading should consider the influence of crystallography.

Elastic recovery will only alter the measured hardness if the crystal is oriented such that the direction(s) with a significant amount of elastic recovery have a component in the plane of the indentation. This is illustrated by considering indentations on an (001) surface. When the edges of the indenter were aligned with [110] directions there was only a small increase in hardness with decreasing load (Figure 4.1), although there was a 15% elastic recovery in the depth of the indentations. The hardness increase was considerably larger when the diagonals of the indenter were aligned with ⟨110⟩ directions (Figure 4.2). It is believed the change in hardness found by simply rotating the indenter by 45° can be explained by considering the microscopic nature of plasticity in $MoSi_2$.

The second stage in the sequence of deformation is plastic flow. As discussed in Section 2.2.2.2 the onset of plasticity probably occurs at the theoretical strength due to the absence of pre-existing dislocations in such small volumes of crystal. The first slip system to be activated can be determined by resolving shear stresses on to the available slip systems. The approach of Brookes et. al. (1971) has been used for this calculation because of its simplicity and ability to correctly predict the first slip system to be activated. The result of this calculation will be divided by the CRSS of the slip system in question to reflect the anisotropic nature of deformation in $MoSi_2$. The final number will be referred to as the Modified Resolved Shear Stress (MRSS). The room temperature CRSS values that

were determined by Ito et. al. (1995) will be used here. Furthermore, since the [001] displacement is a result of the motion of $\frac{1}{4}\langle 111\rangle$ partials the CRSS of the $\{110\}\langle 111\rangle$ slip system will be used for $\{110\}[001]$. The MRSS produced on each of the observed slip systems, for each orientation of indenter, is presented in Table 5.1.

Slip System	Edges ∥ [110]	Diagonals ∥ [110]	Edges ∥ [100] & [001]		Diagonals ∥ [100] & [001]
			Facet ∥ [100]	Facet ∥ [001]	
$\{110\}[001]$	0.24	0.06	0.0	0.06	0.08
$\{1\bar{1}0\}[11\bar{1}]$	0.18	0.10	0.03	0.05	0.08
$\{10\bar{1}\}[010]$	0.04	0.04	0.15	0.04	
$\{0\bar{1}1\}[100]$	0.03	0.0	0.15	0.0	0.12

Table 5.1 MRSS for the observed slip systems.

The MRSS created during indentation of an (001) surface will be considered first. When the edges of the indenter were aligned parallel to $\langle 110\rangle$ directions, the largest MRSS was developed on the $\{110\}[001]$ slip system with that on the $\{1\bar{1}0\}\langle 11\bar{1}\rangle$ system very close to this value. The MRSS values for the $\{011\}\langle 100\rangle$ slip systems are significantly lower (0.04 versus 0.24) than those on the slip systems with a $\{110\}$ slip plane. Therefore, slip likely occurs on the $\{110\}[001]$ slip system first.

When the diagonals of the indenter were parallel to $\langle 110\rangle$ directions the highest MRSS was once again found for slip systems with a $\{110\}$ slip plane. However, there is a much smaller difference in the MRSS values for systems with a $\{110\}$ slip plane than those

with {101} type slip planes. This convergence occurs because of a decrease in the MRSS value for systems with a {110} slip plane. This decrease in MRSS on {110} planes is in agreement with the higher hardness found for this orientation of indenter.

It is known from the microstructural observations that several slip systems are activated during indentation. The activation of slip systems other than those on which the initial slip occurred suggests that slip on the first system to be activated was not capable of producing the necessary strain. During indentation of an (001) surface slip is initiated on the {110}[001] slip system.

The first dislocation produced on this system will glide along the {110} plane until its motion is stopped by the lattice resistance, which is equal to the force produced by the indenter. The second dislocation will glide away from the indenter and stop when the force from the indenter equals the interactive force with the first dislocation. This process will continue until a pile up of dislocations is formed. This pile up produces a back stress against the indenter which increases in magnitude until it is easier to activate another slip system than it is to push out more dislocations on this original system. The magnitude of this back stress can be calculated with a simple model of dislocation pile up.

The first step in this calculation of back stress is to determine the geometry of the pile up producing it. It should be reiterated that these dislocations are actually loops. It was pointed out that the absence of dislocations from the {110}[001] slip system in the centre of the indentation (Figure 4.10 (a)) was a result of foil thinning. Therefore, the smallest loops are a foil thickness away from the indented surface. This thickness is approximately 250 nm. From Figure 4.10 (a) the total width of the indentation is 2.2 μm and the width of the band of slip traces along ⟨110⟩ directions is 0.7 μm. From these

values and by assuming the indented surface is flat it can be determined that the dislocations at the apex are 390 nm away from the indented surface. In other words the dislocation pile up is approximately 390 nm long.

The interaction energy between two loops of equal radius was calculated by deWit (1960). This energy is given by the expression

$$W_{12} \approx \frac{\mu b^2 a}{1-\upsilon}\left(\ln\frac{8a}{z} - 1\right) \qquad 5.2$$

when z<<a and

$$W_{12} \approx \frac{2\pi\mu b^2 a}{1-\upsilon}\frac{a^3}{z^3} \qquad 5.3$$

when z>>a

where z is the distance between loops and a is the loop radius. The separation (along [001]) between loops can also be approximated from the information in Figure 4.10 (a). The edge length of the indentation is 2.2 μm, which implies the depth under load is 440 nm. If it is assumed that 30 % of the total depth of the indentation is accommodated elastically, 310 nm of the 440 nm is accommodated plastically. From Figure 4.10 (a) it is seen that there are approximately 50 loops along z, therefore the spacing of loops is approximately 6 nm. If the average loop diameter is 500 nm, $\frac{z}{a} = 0.012$. Therefore, z<<a and Equation 5.2 is applicable. This equation is very similar to that for the self energy of two straight dislocations. Therefore, these loops can be approximated as straight dislocations because their separation is so much smaller than their radius. Therefore, the back stress created by this pile up of loops can be calculated using a simple model of a

dislocation pile up. The back stress created by a dislocation pile up was given by Cottrell (1953) as

$$\sigma_B = \frac{\mu N b}{2\pi(1-\upsilon)x} \qquad 5.4$$

where μ is the shear modulus, b the Burgers vector, N the number of dislocations and x is the length of the pile up. Assuming $\mu = \frac{3}{8}E$, Nb = 310 nm and x=390 nm, σ_B=0.06 E ($\sigma_B = \frac{E}{18}$). This is the back stress along [001] if all of the loops are co-linear. However the loops do not lie above one another; they lie at a 22° angle to the surface (under load). The back stress along [001], when the pile up is 68° from this direction, can be calculated using Cottrell's (1953) calculation of the force between two nonparallel dislocations. The force between two non-parallel dislocations is given by

$$F_y = \frac{\mu b^2}{2\pi(1-\upsilon)} \bullet \frac{y(3x^2+y^2)}{(x^2+y^2)^2} \qquad 5.5$$

where y is parallel to [001] and x is parallel to [110]. If x=0 the two dislocations are directly above one another along [001] and $F_y = \frac{\mu b^2}{2\pi(1-\upsilon)} \bullet \frac{1}{y}$. If x=2.5y, which is the geometry under load, $F_y = \frac{\mu b^2}{2\pi(1-\upsilon)} \bullet \frac{0.4}{y}$. Thus, the force along [001] is only 40% of that calculated when the dislocations lie above one another, i.e. $\sigma_B = \frac{E}{45}$ when the dislocations follow the shape of the indenter. This stress is of the order of the theoretical strength. Thus, it is not surprising that other slip systems are activated when the

dislocation pile up on the first slip system produces a stress equal to $\frac{E}{45}$. In particular the $\{011\}\langle 100\rangle$ slip system must be activated at some point in the development of this pile up.

Dislocations produced by the $\{011\}\langle 100\rangle$ slip system travel further from the indenter than those on $\{110\}\langle 001\rangle$ (Figure 4.10 (a)). There is, at the same time, a large gradient in the density of dislocations upon approach to the centre of the indentation. The density of dislocations with $\mathbf{b}=\langle 100\rangle$ directly under the indentation can be calculated from the rotations that were noted in Section 4.1.4. In Figure 4.24 extra spots were found within the first order pattern of [001] diffraction spots. It was shown that their spacing from the transmitted beam corresponded to the d-spacing of (101) planes. A rigid body rotation of 22° would be required to rotate the (101) planes to a position where they are parallel to the (100) plane and produce the observed diffraction spots. The actual rotation may be less than this due to streaking of the reciprocal lattice points i.e. a rotation less than 22° would be required to bring some portion of a rod into the zero order Laue zone than the reciprocal lattice point itself. A rotation of this type can be produced by a pile up of dislocations with $\mathbf{b}=\langle 100\rangle$.

The density of dislocations required for the observed rotation can be calculated from the expression of crystal bending developed by Nye (1953). Nye (1953) gave the dislocation density required to bend a crystal into an arc with radius r as

$$\rho = \frac{1}{r|\mathbf{b}|} \qquad 5.6$$

Using r= 1 μm and $|\mathbf{b}|$ =0.32 nm ρ is found to be 1.2 x10^{16} m^{-2}. This is an extremely high dislocation density for a material with a high yield stress that has been deformed at room

temperature. With this model the three other {101} spots in Figure 4.24 would be attributed to the pile up of other, analogous ⟨100⟩ type dislocations produced at the other facets of the indentation.

A point of considerable interest is the variation in the magnitude of these rotations with changes in orientation. The above calculation has used information from an indentation that was made with the edges of the indenter aligned parallel to ⟨110⟩ directions. When the diagonals of the indenter were parallel to ⟨110⟩ directions the {011} diffraction spots were not as intense (Figure 4.24). In this case the dislocation density is probably lower, reducing the magnitude of the rotation and therefore only the end of the reciprocal lattice rod intersects the zero order Laue zone. This difference in density of ⟨100⟩ dislocations indicates the difference in the plastic zone required to accommodate an indentation in this orientation.

The rotations observed on (010) surfaces were not of the same magnitude as those on (001) planes. There were no extra diffraction spots seen under indentations made on this surface. There was however a 9° rotation (Figure 4.48) observed between the crystal beside the indentation and just inside the edge that lies along [001]. This rotation is also due to a pile up of ⟨100⟩ dislocations that locally bend the crystal. However, in this case the rotation is not large enough to bring extra reciprocal lattice points into the zero order Laue zone. The smaller rotation implies that the pile up contains fewer dislocations.

The rotations that have been observed indicate that very large dislocation densities are produced at small indentations. Large lattice rotations under an indentation were observed by Brown et.al. (1988) in their study of indentations in MgO. Like $MoSi_2$, MgO has a high yield stress and a limited number of slip systems at room temperature. The

lattice rotations observed in both materials are reminiscent of those produced during indentation of a rigid plastic metal (Hill et.al. 1947). In fact, the model of indentation of Hill et.al. is based on the rotation of material along slip lines. However, $MoSi_2$ and MgO have quite different flow characteristics. The SEM observations agree with the non-metallic character of $MoSi_2$, showing no pile up around the indentation. This apparent contradiction in behaviour is resolved with consideration of the scale of the observations.

Rotations were always limited to the material directly under an indentation. In all examples the lattice remains in the original orientation until the edge of the indentation was encountered. In the case of indentations on an (001) surface rotations were only observed inside the slip traces on {110} planes. Therefore, the only material that deforms like a metal with a low yield stress is the volume directly under the indentation ($\approx 1\mu m^3$) . It is only in this region that the stresses are large enough to produce this type of deformation. This interpretation is in agreement with the large dislocation densities that have been calculated in this region of the indentation. The stresses quickly decrease in magnitude such that this type of flow is not observed beside the indentation.

The rotations under an indentation on an (001) surface were removed during annealing experiments. While dislocations from the {011}⟨100⟩ slip system were still present after annealing sufficient recovery took place to remove the rotations. This occurred at a relatively low temperature ($0.4\ T_m$) due to the initial high dislocation density. Dislocations from the {110}[001] slip system were also still present after annealing. It is likely that the density of these dislocations was also reduced.

To this point in the discussion the nature of the shape change that occurs during unloading and the nature of plastic flow have been discussed. It is now important to

consider how these events relate to the hardness of small indentations, in particular to any changes in hardness with changes in applied load. This discussion will use indentations on (001) surfaces as an example, as indentations on an (010) surface follow the same argument.

The difference in hardness, at a given load, between indentations made with the two indenter orientations has been discussed in terms of the differences in the resolved stresses for the two indenter orientations. This issue is separate from the changes in hardness with changing load. Indentation Size Effect (ISE) has been attributed to both shape changes that occur when the load is removed and to plastic deformation. The influence of shape changes that occur during unloading have already been discussed. As pointed out in Section 2.2.3. geometrically necessary dislocations will dominate plastic flow and strength when the scale of deformation is below 10 μm. For this reason geometrically necessary dislocations have been cited in explanations of ISE that are based on plasticity.

Brown (1988) developed a model of ISE that was based on geometrically necessary dislocations. The model described both the hardness and rotation observations. In this model material was assumed to move away from the indentation via rotating blocks that were separated by geometrically necessary dislocations. Agreement was found between the model's predictions and the experimental hardness measurements. Variations in the hardness curves resulting from orientation differences were handled by variation of the constant A, the ratio between the hardness and flow stress (Equation 2.20). However, there is no clear indication of what the physical significance of A is. Ma and Clarke (1995) derived a very similar expression using strain gradient plasticity concepts. These authors also found good agreement with their experimental results. However, they too were unable to fully describe the influence of orientation on their measurements.

In this study it was found that there was a dramatic change in the hardness versus load curves when the indenter was rotated by 45° with a much lower ISE when the edges of the indenter were parallel to ⟨110⟩. TEM studies indicated that the same slip systems were active for these two orientations of indentation. It was also found that the orientation that displayed the largest ISE (diagonals parallel to [110]) had smaller rotations i.e. a smaller density of ⟨100⟩ dislocations. Therefore a model of ISE that only considers the density of geometrically necessary dislocations is inadequate for the observations made in this study the model must also consider the geometric arrangement of the indenter with respect to the available slip systems.

The largest ISE was observed when the diagonals of the indenter were aligned with ⟨110⟩ directions. This orientation also produced smaller rotations i.e. lower dislocation density on the {101}⟨100⟩ slip system. Further, it is believed that the {101}⟨100⟩ slip system is the second to be activated. These points suggest the {101}⟨100⟩ slip system is not responsible for ISE.

When the edges of the indenter are parallel to ⟨110⟩ directions the slip planes of the {110}⟨001⟩ slip system are aligned with the facets of the indentation. When the diagonals of the indenter are parallel to ⟨110⟩ directions the slip planes of the {110}⟨001⟩ slip system are at 45° to the facets of the indenter. In this latter arrangement more material is displaced to accommodate the indenter and may be a cause of the difference in ISE. One approach that might help to model this situation is that taken by Orowan (1941) in his discussion of slip band spacing. This discussion states that the spacing of slip bands is based on the size of the stress free zone surrounding a slip band. Thus, as the stresses become larger the slip band spacing is reduced to relieve the increased stress. In the models of hardness based on geometrically necessary dislocations the strength is based on the density of dislocations,

which in turn is based on the volume of the indentation. There also appears to be a geometric factor at work i.e. a specific orientation of indenter may be more easily accommodated by the available slip systems. Thus, there is a certain density of dislocations required to accommodate the volume of the indentation and there is a configuration of slip planes required to reproduce the shape of the indenter. This configuration might be considered in terms of Orowan's approach.

5.3. Accommodation of Large Indentations

When the edge length of the indentation was larger than 10 μm the deformation processes were different than those found around small indentations. Elastic deformation ceased to be a significant fraction of the total deformation while plastic deformation remained important and fracture processes were initiated. This discussion of large indentations will consider why fracture is initiated and how it evolves with changes in the applied load. The pattern of material movement away from the indentation will also be considered. As in previous sections, particular attention will be paid to the role crystallography plays in the accommodation processes.

All of the information for this discussion was obtained from analysis of the surface features around an indentation. However, TEM information from small indentations will provide an important reference from which inferences about slip systems can be made. It is important to remember that only slip systems with a Burgers vector that was parallel to or normal to the surface were observed around small indentations. There were no systems that moved material away from the indentation towards the sample surface. This is not the case for large indentations.

Indentations made with the two different orientations of indenter on an (001) surface looked quite different. When the diagonals of the indenter were parallel to $\langle 110 \rangle$ directions, broad bands, elevated above the surface, were observed parallel to $\langle 110 \rangle$. These bands extended at least one indentation diagonal length away from the indentation. The location of these bands indicates it is unlikely they were produced by reverse plastic flow on the $\{110\}[001]$ slip system. It is more likely they were probably produced by material moving to the surface during indentation i.e. material has piled up around the indentation. Since the only slip plane in $MoSi_2$ that produces a trace along $\langle 110 \rangle$ directions on an (001) surface is (110), these bands are probably due to plastic flow on the $\{110\}\frac{1}{2}\langle 1\bar{1}1 \rangle$ slip system.

Because the $\{110\}$ planes are perpendicular to the surface being indented the edges of the indenter must be at an angle to them in order for material to move directly from underneath the indentation to the free surface. This is true when the diagonals of the indentation were parallel to $\langle 110 \rangle$ directions. Further, it was noted in Section 4.1.2 that the slip bands along $\langle 110 \rangle$ directions were bounded by the bands of dislocation etch pits lying along $\langle 100 \rangle$ directions i.e. the latter dislocations have traveled further from the indentation. The etch pits are formed by dislocations from the $\{011\}\langle 100 \rangle$ slip system. Since this slip system was observed in the TEM studies it must have been activated early in the development of the plastic zone. These two observations suggest that during the formation of large indentations the $\{110\}\frac{1}{2}\langle 1\bar{1}1 \rangle$ slip system is activated after the $\{011\}\langle 100 \rangle$ slip system.

A similar scenario was found when the edges of the indenter were aligned with $\langle 110 \rangle$ directions. Again broad bands that were elevated above the surface were seen along $\langle 110 \rangle$ directions. However, in this orientation these bands are parallel to the edges of the indentation so they can no longer move material directly from the indentation to the surface. The question of moving material from under the indenter to the surface is solved if the dislocations forming these traces originated on another plane and cross-slipped onto $\{110\}$ planes to reach the surface. It is postulated that $\frac{1}{2}\langle 1\bar{1}1 \rangle$ dislocations first traveled on $\{011\}$ planes and then cross slipped onto $\{110\}$ planes to form the observed slip bands.

A cross slip scenario was used by Hirsch et.al. (1985) to interpret their slip trace observations in GaAs. Hirsch et.al. (1985) postulated that dislocations traveled along one slip system into the sample until a pile up formed. The stress developed at the front of this pile up was then relieved by cross slip of the dislocations onto planes that allowed them to travel to the free surface. When an indentation was formed with the indenter's edges parallel to $\langle 110 \rangle$ directions, slip traces, not a series of etch pits, were formed along $\langle 100 \rangle$ directions. Therefore the Burgers vector of these dislocations cannot be $\langle 100 \rangle$. The most likely slip system to produce these traces is $\{011\}\langle 111 \rangle$. Thus, another slip system has been activated to accommodate large indentations of this orientation. Again it is a slip system that transports material from under the indentation to the surface.

At least two additional slip systems have been activated with the increase in the size of the indentation. Indentations of both orientations on (001) surfaces produced slip on the $\{110\}\langle 111 \rangle$ slip system, while slip on $\{011\}\langle 111 \rangle$ was observed when the indenter was aligned with its edges parallel to $\langle 110 \rangle$ directions. This indicates a change in the pattern of material movement. During the formation of small indentations there are no slip systems

that move material to the surface. During the formation of a large indentation the slip systems that move material to the free surface are activated. This picture of indentation for large indentations is similar to the continuum picture developed by Hill et.al. (1947). Thus, the material displaced by the indenter could no longer be accommodated without pile up and material is displaced towards the surface.

While this movement of material is dictated by crystallography (i.e. the available slip systems), it is still in agreement with the overall pattern of material movement assumed in continuum models. Indentations on (010) surfaces undergo a similar change in the active slip systems. In this case there are two differences in the nature of plastic deformation. First, the most prominent slip traces are those parallel to $\langle 100 \rangle$ (Figures 4.28(a) and 4.29(b)). These traces are produced by slip on the $\{1\,1\,0\}\langle 1\,\bar{1}\,1 \rangle$ slip system. However, these traces were found around all sides of the indentation not just beside the facets with an edge parallel to $\langle 100 \rangle$. Again this system, which moves material to the surface is more pronounced around large indentations. Second, slip traces were seen along $\langle 301 \rangle$ directions (Figure 4.29 (b)). Such traces could be produced by slip on $\{103\}$ planes with a dislocation that contains a component that is parallel to [010]. Such a dislocation is $\langle 33\,\bar{1} \rangle$. Therefore it appears that the $\{103\}\langle 33\,\bar{1} \rangle$ slip system has been activated at indentations with larger plastic zones.

To summarize, the $\{1\,1\,0\}\langle 1\,\bar{1}\,1 \rangle$ and $\{0\,1\,1\}\langle 1\,\bar{1}\,1 \rangle$ slip systems became active when a large indentation is formed on an (001) surface and the $\{103\}\langle \bar{3}31 \rangle$ slip system became active when a large indentation was formed on an (001) surface. The activation of additional slip systems reflects the inability of the original slip system to provide the required plastic flow. Finally, there is a considerable increase in the activity on the

$\{1\,1\,0\}\langle 1\,\bar{1}\,1\rangle$ slip system as material moves away from the indentation towards the free surface.

These plasticity observations should be compared to the results from compression testing in the literature. The results of Ito et.al. (1995) will be used for this comparison as these authors conducted tests at temperatures near or at room temperature. Ito et.al. (1995) observed slip on the $\{0\,1\,1\}\langle 1\,0\,0\rangle$ slip system in samples that were deformed at temperatures as low as -100 °C, the $\{1\,0\,3\}\langle \bar{3}\,3\,1\rangle$ slip system was active at room temperature, the $\{1\,1\,0\}\langle 1\,\bar{1}\,1\rangle$ slip system became active in samples that were deformed at 300 °C or higher and the $\{0\,1\,0\}\langle 1\,0\,0\rangle$ and $\{0\,2\,3\}\langle 1\,0\,0\rangle$ slip systems were only observed in samples that were deformed at temperatures between 600 and 900 °C. These slip system observations were a function of crystal orientation. The slip systems that Ito et.al. (1995) found became active at temperatures above room temperature are in general agreement with those found to become active when the indentation had an edge length that was larger than 10 μm. At low temperatures and small indentation sizes only those slip systems with a low critical resolved shear stress are active. As the deformation temperature was raised additional slip systems were activated because of the decreased critical resolved shear stress required for their operation. During indentation additional slip systems are required to accommodate the larger volumes of deformed material produced by large indentations.

An important part of the accommodation of large indentations is fracture. In fact, the appearance of fracture has been used to identify large indentations. The initiation of fracture processes and the changes in these processes with increases in the applied load will now be considered. Again it is worth considering the salient features of the fracture observations presented in Sections 4.1.2 and 4.2.2 before a detailed analysis of the

observed fracture behaviour is presented. Two quite different cracks were observed around indentations on (001) surfaces. The first set of cracks were straight and aligned along ⟨100⟩ directions. These cracks are most likely on {100} planes as this has been found to be a cleavage plane in $MoSi_2$ (Wade et.al. 1992). The second type of cracks were only observed around indentations that were made with the diagonals of the indenter aligned with ⟨110⟩ directions. These cracks were semi-circular and located at the intersection of slip traces along ⟨110⟩ directions. They appeared to be responsible for the shallow, clam shell shaped regions where material had been removed. In both cases cracks were only present when the applied load was equal to or larger than 55 grams.

Like the plasticity observations the fracture patterns observed on (010) surfaces were not as transparent as those observed on (001) surfaces. The most consistent fracture patterns were observed when the edges of the indenter were aligned with [100] and [001] directions. Cracks originated at the corners of the indentation and traveled away from it along an arc that was parallel to the [001] at the corner of the indentation. AFM observations (Section 4.2.3) showed that there was a large uplift of material on the outside of the crack i.e. away from the indentation. This Mode III opening accommodates the material that wants to pile up beside the indentation. These cracks were also observed around indentations made with the other orientation of indenter on (010) planes. However, in this orientation the cracks were not as large or as well defined. Cracks along [100] directions were also observed around these indentations. Again these cracks probably lie on (100) planes.

These observations demonstrate that crystallography is an important factor in fracture processes, in agreement with the discussion of fracture processes during indentation of single crystals presented in Section 2.2.2.3. Any explanation of the fracture

patterns must describe both the influence of crystallography and the threshold behaviour, i.e. why fracture was only observed around indentations that had an edge length of at least 10 μm.

Crack formation requires a nucleus and a tensile stress that can open this nucleus to form a macroscopic crack. Lawn and Wilshaw (1975) pointed out that there is always a tensile component to the stress state formed during indentation with a pointed indenter. The independence of crack orientation from indenter orientation found in this study indicates that the variation in stress around the indentation is not the governing factor in the orientation of the cracks. Therefore, the formation of a crack nucleus must be the critical factor in the formation of cracks in $MoSi_2$.

Nuclei can form at either a critically sized pile up of dislocations or at a much smaller flaw on a plane with a lower surface energy. Both of these sources appear to be operative in $MoSi_2$. Cracks that originated at a pile up of dislocations will be considered first. Both the semi-circular cracks around indentations on (001) surfaces and the arc shaped cracks around indentations on (010) surfaces appear to originate from dislocation sources. The semi-circular cracks seen on (001) surfaces formed at the intersection of $\{110\}$ slip planes. If slip is occurring on the $\{110\}\langle 1\bar{1}1\rangle$ and $\{1\bar{1}0\}\langle 111\rangle$ slip systems the intersection of these two will produce dislocations with a $\langle 101\rangle$ type Burgers vector. A pile up of dislocations with this Burgers vector would create a crack on $\{101\}$ planes.

The arc shaped cracks produced around indentations on (010) surfaces have a Mode I opening that is parallel to [100] directions. This opening occurs in the same region where there is a large pile-up of [100] dislocations, as noted in Section 4.2.4.3. Therefore, it appears that this pile up of $\langle 100\rangle$ dislocations is the origin of these cracks. The large Mode

III opening is then created by the pile up of dislocations from the $\{110\}\langle 1\bar{1}1\rangle$ slip system beside the indentation. Cracks on (100) planes form around indentations on both surfaces. In all cases the dislocations from the $\{011\}\langle 100\rangle$ slip system that is operative around a given {100} crack contains a Burgers vector that is at 90° to the crack opening. Thus, the cracks cannot be formed from a pile up of these dislocations.

All of the cracks discussed above only formed at a minimum indentation size. This threshold occurred when the indentation was approximately 10 μm in size. Therefore any models of crack nucleation must predict such threshold behaviour in order to be applicable to cracking in $MoSi_2$. The model of crack nucleation at a pile up of dislocations will be discussed first. In this theory a dislocation pile up is large enough to form a critical flaw that will grow spontaneously under the application of a tensile stress. There have been several presentations of the calculation of the stress necessary to form the required pile up. Hirth and Lothe (1992) considered a dislocation pile up of length l. They give this stress as

$$\sigma \geq \left[\frac{8\mu\gamma}{\pi(1-\upsilon)}\right]^{\frac{1}{2}} l^{-\frac{1}{2}} \qquad 5.7$$

where γ is the surface energy, μ is the shear modulus and υ is Poisons ratio. Using data for $MoSi_2$ (μ=170 GPa, υ=0.15 and γ= 1 J.m^{-2}) the stress to open a crack is

$$\sigma \geq 9\times10^{5} l^{-\frac{1}{2}} \ \text{Pa}\sqrt{m} \qquad 5.8$$

Therefore, if it is assumed that the largest pile up will be one half of the indentation size the stress required to form a critical flaw when the indentation has an edge length of 10 μm is 400 MPa.

Cracks formed with a much smaller flaw, if any, on a low energy plane include the {010} cracks seen around indentations on an (001) surface. The maximum stress required to form these cracks can be estimated from an energy balance. The strain energy released during cracking in an indentation test must equal that required to create the new surfaces formed during crack formation. A first approximation can be made by considering the elastic energy stored in a hemispherical volume. It can also be assumed that two half penny cracks form, i.e. one crack associated with each diagonal. The elastic energy per unit volume stored during loading with a tensile stress σ is

$$\frac{\sigma^2}{2E} \qquad 5.9$$

where E is Young's modulus. The energy in the hemispherical cavity is equal to the product of equation 5.9 and the volume of a hemisphere with radius r. This energy is given as

$$\frac{2\pi r^3\sigma^2}{3E} \qquad 5.10$$

and the surface energy required to form the two half penny cracks is equal to $2\pi\gamma r^2$. Equations 5.9 and 5.10 can then be equated if, as noted earlier, it is assumed that all of the energy is stored in a hemisphere and this energy is consumed during crack formation. Therefore, the stress required to form a critical flaw is given by

$$\sigma = \left(\frac{6E\gamma}{r}\right)^{\frac{1}{2}} \qquad 5.11$$

Using the elastic constants for $MoSi_2$ and setting r equal to 10 μm, σ is calculated to be 520 MPa. This value is in good agreement with the stress required to form a crack from a dislocation pile up. This agrees with the experimental observation that all cracks form at roughly the same size of indentation. Both values of stress are considerably lower than the hardness at this size of indentation. However, it was shown by Lawn and Wilshaw (1975) that the maximum tensile stress during a point contact is considerably lower than the hardness. In both equations 5.7 and 5.11 the stress varies inversely with the square root of the indentation dimension. Therefore, if the stress required for crack nucleation increases quickly with decreasing indentation size, a minimum indentation size (stored energy) is required to initiate fracture and this occurs locally at a lower stress than the overall stress required to make an indentation.

Chapter 6.0

Conclusions

By using indentation testing to study the mechanical properties of $MoSi_2$, new information about both the mechanical properties of $MoSi_2$ and the nature of indentation testing has been collected. This information resulted from a detailed microstructural analysis of deformed single crystals. The large stresses and hydrostatic pressures created under the indenter allowed crystals that could not be plastically deformed in compression below 1200 °C to be deformed at room temperature. Furthermore, by studying indentations with a range of plastic zone sizes information on the evolution of slip system activity was gathered. At the same time the tetragonal crystal structure and anisotropic elasticity of $MoSi_2$ allowed novel insights into the nature of indentation testing.

Six slip systems were operative during room temperature indentation. $\{011\}\langle 100\rangle$, $\{110\}\langle 001\rangle$, $\{010\}\langle 100\rangle$, $\{110\}\langle 111\rangle$, $\{101\}\langle 111\rangle$ and $\{013\}\langle 331\rangle$. The $\{101\}\langle 111\rangle$ slip system has not been reported previously and only the $\{011\}\langle 100\rangle$ and $\{013\}\langle 331\rangle$ slip systems were previously found to be active during room temperature deformation of single crystals (Ito et.al. 1995). The last two systems listed above were not conclusively identified by TEM analysis. However, when the surface observations were correlated with the anticipated slip systems and the nature of material movement during indentation testing was considered the listed slip systems could be inferred to be operative.

Of particular interest is the identification of the $\{110\}\langle 001\rangle$ slip system. It was previously thought that dislocations from this system were only associated with growth faults (Kad et.al. 1995). It is clear from this study that this system can be activated during

room temperature deformation. It was found that an overall $\langle 001 \rangle$ displacement was produced by a combination of $\frac{1}{2}\langle 001 \rangle$ and $\frac{1}{4}\langle 1\,1\,1 \rangle$ partial dislocations. Furthermore, the arrangement of partial dislocations and stacking faults was stable up to a temperature of 750 °C. Moreover, the $\{1\,1\,0\}\langle 0\,0\,1 \rangle$ slip system was observed during room temperature deformation and the configuration of these dislocations was stable.

Considerable insight into the nature of $\frac{1}{2}\langle 1\,1\,1 \rangle$ dislocations has been gained. First, it was shown that two closely spaced $\frac{1}{4}\langle 1\,1\,1 \rangle$ partial dislocations could appear as a single dislocation under a variety of diffracting conditions. Second, there were no examples of whole $\frac{1}{2}\langle 1\,1\,1 \rangle$ dislocations found in this study. This suggests that the two early reports of $\frac{1}{2}\langle 1\,1\,1 \rangle$ dislocations (Unal et al. 1990 and Maloy et.al. 1992) may have actually been observations of two partial dislocations. A wide variety of diffraction conditions is required to conclusively identify the exact Burgers vector of $\langle 1\,1\,1 \rangle$ dislocations. The reaction

$$\frac{1}{2}\langle 0\,0\,1 \rangle \Rightarrow \frac{1}{4}\langle 1\,1\,1 \rangle + \frac{1}{4}\langle \bar{1}\,\bar{1}\,1 \rangle \qquad 6.1$$

has been found for the first time in this study.

Lastly, it was noted that the separation of $\frac{1}{4}\langle 1\,1\,1 \rangle$ partial dislocations varied with location around the indentation. When the partial dislocations were far from the centre of the indentation their separation was similar to that reported previously (Evans et.al. 1993 and Ito et.al. 1995). However, when the two $\frac{1}{4}\langle 1\,1\,1 \rangle$ partial dislocations were located very close to the centre of the indentation their separation was larger by up to a factor of ten. It

appears that this difference in partial separation may be caused by the large hydrostatic pressure directly under the indentation.

The understanding of indentation testing of single crystals has also been advanced by the current study, largely due to the detailed observations that illustrate the importance of crystallography during each stage of the indentation cycle: elastic deformation, plastic deformation and fracture.

First, it was clearly shown that the nature of the shape change that occurs during unloading was dictated by crystallography. In $MoSi_2$ the largest dimensional change occurred along [001] regardless of whether this direction was parallel to or normal to the indentation axis. It was found that this shape change was a combination of elastic recovery and reverse plastic flow. Therefore, the separation of these two components would be necessary before any conclusions concerning shape change could be made.

Second, the nature of plastic deformation within the plastic zone was determined by the available slip systems. In $MoSi_2$ slip was initiated on systems that moved material either directly into the sample or along the surface. It was only at larger plastic zone sizes that additional slip systems were activated and material moved towards the surface and material is piled up dbeside the indentation. The limited number of active slip systems in the early stages of plastic deformation caused large stresses to form as dislocations piled up along the active slip systems. These stresses eventually led to the activation of other slip systems.

An important outcome of the observations concerning elastic and plastic deformation was insight into the nature of Indentation Size Effect (ISE). It was shown that explanations of ISE, whether based on elastic recovery or the nature of plastic flow, are not easily generalized. In both cases the effects of crystallography were shown to be of

paramount importance. For example, it was shown that ISE could not be explained by models based solely on the density of geometrically necessary dislocations. A model based on plastic deformation must include a term that reflects the geometric correspondence between the slip systems and the orientation of the indenter.

Finally, great effort was made to ensure a defect free surface was being indented. This implied that crack nuclei had to be formed during indentation. Cracks that were formed by either a pile up of dislocations and or by cleavage were observed around indentations made on both surfaces. It was shown that both models of crack formation would display the observed threshold behaviour i.e. there was a minimum size of indentation below which cracks did not form. Once cracks were nucleated they became an important part of the accommodation of the indenter.

In conclusion, the formation of an indentation in a single crystal is a complicated process that is governed by the crystal structure of the material under test. This leads to unique geometries of deformation for materials with different crystal structures. In the case of materials with a limited number of active slip systems at the test temperature, stresses approaching the theoretical strength may be reached under the indentation.

Chapter 7.0

Future Work

The current study has looked at indentations on two orientations of $MoSi_2$ single crystals over a range of applied loads. The indentations were studied by three microscopic techniques. The work has provided a good physical understanding of the accommodation processes that occur during indentation. There are several areas where this work can be expanded to fill out the understanding of indentation in $MoSi_2$ and more generally anisotropic materials.

First, indentations on {110} and {111} surfaces would add insight into the nature of indentation. There is only one family of slip planes parallel to the axis of indentation for indentation of an {110} surface while there are no slip planes parallel to the axis of indentation for {111} surfaces. These two cases would be interesting with respect to the early stages of the development of the plastic zone as slip systems whose slip plane contains the axis of indentation are the first to be activated. The absence of such slip systems would provide interesting insight into the initial stages of plasticity.

Second, there is a great need for accurate quantitative indentation data i.e. load displacement curves at low loads. While the current study provides a good qualitative picture of the indentation process, quantitative data would provide insight into the sequence of events during the formation of an indentation. This would in turn allow more accurate modeling of the indentation process. An automated indenter capable of producing very fine loads could provide the required quantification of the indentation process.

Finally, there is also an aspect of sample preparation that would shed further light on the current results. TEM information from a cross-sectional sample through an indentation would provide interesting insight into the plastic zone. Preparation of such a section was attempted during the current study but proved unsuccessful. Therefor information along the axis of indentation was inferred from stereo microscopy results. A cross-sectional sample through an indentation may be produced by Focused Ion Beam (FIB) milling techniques. FIB techniques could produce a sample of uniform thickness with a large thin area. Cross-sections along both ⟨110⟩ and ⟨100⟩ directions could be produced. Cross-sections parallel to the axis of indention might elucidate elements of the plastic zone that may not have been seen in the current study that used plan view samples.

APPENDIX A

LINE DIRECTION DETERMINATION

The unique determination of the line direction (**u**) of a dislocation requires that projections of this direction be recorded from three traces corresponding to different beam directions. The accuracy of the analysis is improved if the traces are from directions spanning a large angular range. The following example demonstrates the procedure used in all trace analyses. Figure A.1 shows three micrographs of the dislocation labeled 'C' in Figure 4.15. Two directions are shown on each of these images. The first is the normal to the diffracting planes (**g**) and the second is a low index direction from a neighbouring zone. While this second direction is not accurate it allows the correct sense of the angle between the dislocation trace and **g** to be determined. Table A.1 shows this angle, **B** and **g** for each micrograph. This information was plotted on a stereographic projection using the procedure outlined in Section 3.6.2. The resulting stereographic projection is shown in Figure A.2. It can be seen that the three traces intersect at $\mathbf{u}=[\bar{1}\,\bar{1}\,1]$ for dislocation C. Since the slip plane contains both **u** and **b** the normal of this plane is equal to the cross product of these two vectors. Thus, the slip plane is (0 1 1).

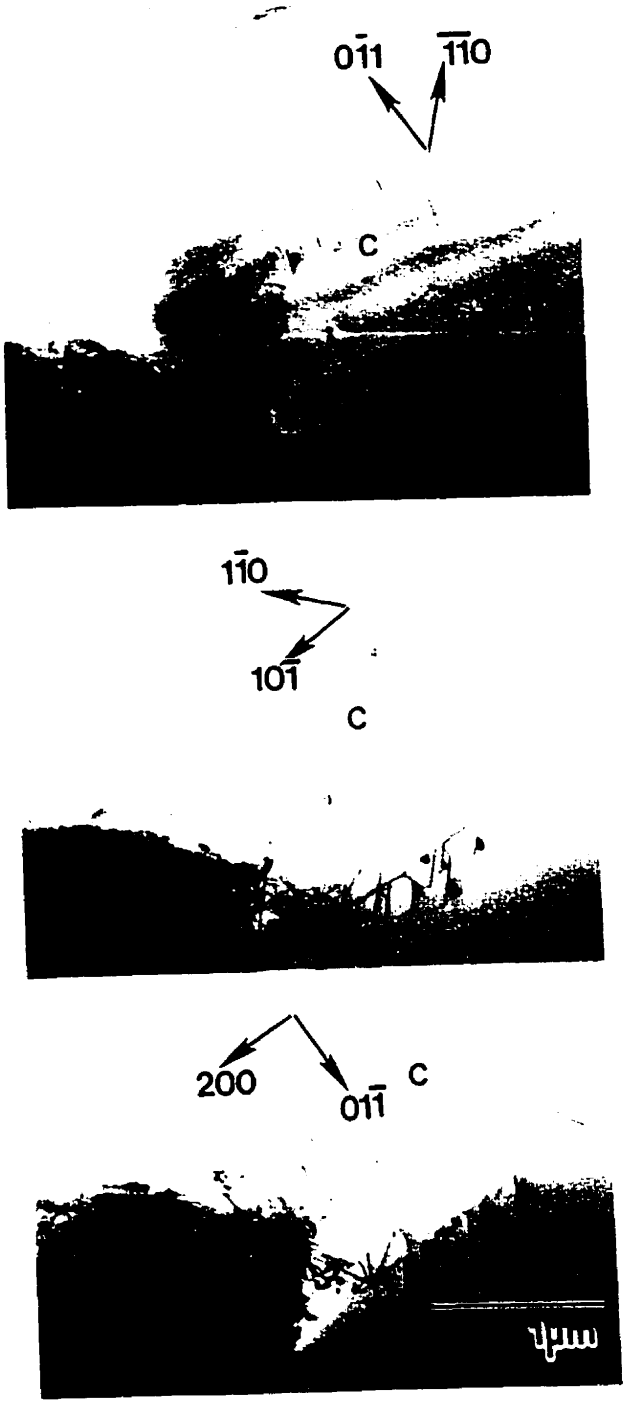

Figure A.1 Three BF micrographs of dislocations C. g and another direction in the nearby zone axis are marked in each micrograph.

Figure	B	g	Angle (°)
A.1 (a)	111	$1\bar{1}0$	88 from: $\bar{1}10$ to: $10\bar{1}$
A.1 (b)	$\bar{1}11$	$\bar{1}\bar{1}0$	37 from: $\bar{1}\bar{1}0$ to: $0\bar{1}1$
A.1 (c)	011	200	65 from: 200 to: $01\bar{1}$

Table A.1 Trace information used for stereographic projection in Figure A.2.

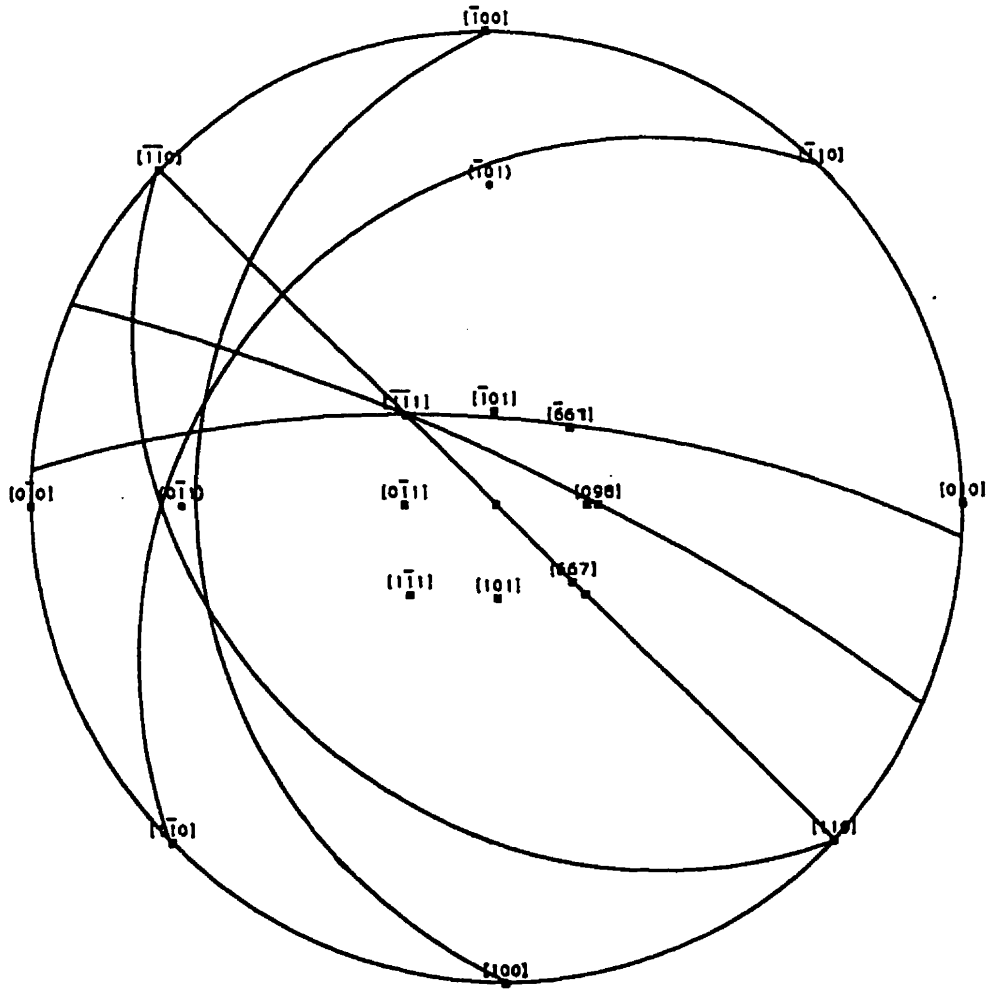

Figure A.2 [010] stereographic projection, based on the information in Table A.1, used to determine the line direction of dislocation C in Figure A.1.

Appendix B

Contrast Analysis for ⟨111⟩ Type Dislocations

During contrast analysis studies of ⟨1 1 1⟩ dislocations it was found that the nature of the images depended on the operating reflection and the angle between the beam direction (**B**) and the slip plane normal. In some cases a single dislocation image was seen while in others two images were observed. A detailed analysis of this contrast was undertaken to determine if the dislocation producing this contrast was perfect ie. $\mathbf{b}=\frac{1}{2}\langle 1\,1\,1\rangle$ or had dissociated according to Equation 2.6 with $\mathbf{b}=\frac{1}{4}\langle 1\,1\,1\rangle$ for the resulting partials. The dislocations studied were from group 2 in Figure 4.43 (a), with a Burgers vector of the $[\bar{1}\,1\,\bar{1}]$ type.

For the purpose of image simulation it was assumed that a $\frac{1}{2}[\bar{1}\,1\,\bar{1}]$ dislocation had dissociated according to Equation 2.6,

$$\text{i.e.} \qquad \frac{1}{2}[\bar{1}\,1\,\bar{1}]=\frac{1}{4}[\bar{1}\,1\,\bar{1}]+\frac{1}{4}[\bar{1}\,1\,\bar{1}]$$

It was also assumed that the partials had a separation of 75 Å. The separation is based on the value experimentally determined by Evans et.al. (1993). These authors had reported a partial separation of 65Å. Their measurements were made on images formed with **g**=103. $\mathbf{B}=[\bar{3}31]$ is the closest zone, with respect to the slip plane normal, that contains this reflection and it is 30° from $[\bar{1}\,10]$. Therefore, the measured separation of 65 Å corresponds to a true separation of 75 Å.

Table A.2 shows $\mathbf{g}.\mathbf{b}_p$ and α ($2\pi.\mathbf{g}.\mathbf{R}$) values for the dissociated dislocation and $\mathbf{g}.\mathbf{b}$ values for the whole dislocation. Of the five diffracting conditions shown in Table A.2, $\alpha=2n\pi$ only when $\mathbf{g}=103$ or 011. When $\mathbf{g}=011$ both $\mathbf{g}.\mathbf{b}_p$ and α are zero, therefore it is only when $\mathbf{g}=103$ that the partials should be visible when the fault is in extinction. On the other hand, when $\mathbf{g}=\bar{1}03$ the partials and stacking fault should all produce contrast. The other diffracting conditions produce similar contrast to that found with $\mathbf{g}=\bar{1}03$. Therefore, only the two 103 type diffracting vectors were required to study the contrast produced by the stacking fault and partials. It should be noted that the line direction used in the simulation is the overall line direction of the dislocation. However, there were changes in this line direction along the length of the dislocation. This creates some difficulties in image matching.

The effect of the geometry of observation was studied by making observations along four different beam directions (**B**). Figure A.4 is a stereographic projection of directions that shows the four $\langle 391 \rangle$ type beam directions, the slip plane normal ([110]) and the dislocation Burgers vector ($[\bar{1}\,1\,\bar{1}]$). When $\mathbf{B}=[391]$ or $[39\bar{1}]$ **B** is 30° from the (110) plane normal. This angle is increased to 64° when $\mathbf{B}=[\bar{3}91]$ or $[\bar{3}9\bar{1}]$. Thus, the effect of this change in viewing angle can be studied for both **g**s. For each **g** and **B** combination, images were taken with $\pm$ **g** and $s \geq 0$. These experimental images were then compared to the simulated images.

Six experimental images and simulations using $\mathbf{b}=\frac{1}{4}[\bar{1}\,1\,\bar{1}]$ and $\mathbf{b}=\frac{1}{2}[\bar{1}\,1\,\bar{1}]$ are shown in Figure A.5. The two simulated images were calculated using the same diffracting conditions. In Figure A.5 (a) and (b) ($\mathbf{g}=\bar{1}03$) there is only a single image seen in the

experimental images. These images are quite diffuse with lobes extending away from the dislocation. Careful examination of these images shows that the contrast along the dislocation line is not uniform. It oscillates between light and dark sections. These two features are reproduced in the simulated images of the dissociated dislocation. These two images were taken at different angles to the slip plane, but the observed contrast is very similar.

When the diffracting vector is changed to $\bar{1}0\bar{3}$ or 103 the image is quite different. A bright field image taken with $\mathbf{g}=\bar{1}0\bar{3}$ and $\mathbf{B}=\left[\bar{3}91\right]$ is shown in Figure A.5 (c). On the left side of the dislocation two dark fringes separated from one another with a thin connection at the one side of the fringe pattern is seen. This again agrees quite well with the simulated images of the dissociated dislocation. From Table A.2 it is anticipated that the fault is not producing contrast. In this case **B** is 64° from the slip plane normal causing the images of the closely spaced partials to overlap. When the same reflection is used, but **B** is changed to $\left[39\bar{1}\right]$ two distinct lines of contrast are seen (Figure A.5 (d)). In this case **B** is only 30° from [110], implying that the projected separation of partials will be larger than when $\mathbf{B}=\left[\bar{3}91\right]$ (Figure A.5 (c)). Again the simulation confirms that two images should be seen with these imaging conditions. This difference in projected separation determines whether one or two images are seen when $\mathbf{g}=\bar{1}0\bar{3}$. In the simulated image (s=0) the two images are symmetrical about the fault while there is a slight asymmetry in the experimental images. Because of the large strains present around the indentation it was difficult to ensure that s=0 along the entire dislocation length. Therefore, the right hand portion of the dislocation agrees well with the simulation while the subtle change in contrast of the dislocation suggests that s>o here. When there was a deviation from the Bragg

condition this asymmetry of the two images became quite pronounced (Figure A.5 (e)). In this image **g** and **B** are the same as in Figure A.5 (a) while s≠0. When the sign of **g** was reversed, Figure A.5 (f), the asymmetry was reversed. The asymmetry of the two images with non zero s and the reversal of this asymmetry with a change in the sign of **g** are all confirmed in the simulated images. In all cases the experimental and simulated images that used $\mathbf{b}=\frac{1}{2}[\bar{1}\,1\,\bar{1}]$ did not show any agreement. Thus, the dislocations in Figure 4.59 are dissociated according to Equation 2.6.

Two conclusions come from this analysis. First, the dissociated dislocations will produce a single image under many diffracting conditions. In fact, it is only when $\alpha=2n\pi$ and $\mathbf{g}.\mathbf{b}_p \neq 0$ that the two partials might be imaged. Further, because the separation of partials is quite small in this system (≈ 75 Å) the geometry of observation becomes very important. When **B** forms a large angle with the slip plane normal the images from each partial become inseparable. Second, the true separation of partials will be quite difficult to determine. Observations with **B**=[1 1 0] would require $\mathbf{g}=1\,\bar{1}\,0$. The image using this **g** vector should be similar to those in Figure A.5 (a) and (b), i.e. a single image would be produced. The separation would have to be determined with a 103 reflection and then the true separation calculated from the observed separation.

g	$\mathbf{g.b_p}$	α	**g.b** (**b**= $\frac{1}{2}[\bar{1}1\bar{1}]$)
103	-1	-2π	-2
$\bar{1}03$	$-\frac{1}{2}$	$-\pi$	-1
$\bar{1}10$	$\frac{1}{2}$	π	1
101	$-\frac{1}{2}$	$-\pi$	-1
011	0	0	0

Table A.2 $\mathbf{g.b_p}$ and α ($2\pi.\mathbf{g.R}$) values for a partial dislocation and stacking fault for which **g** and **R** equal $\frac{1}{4}[\bar{1}1\bar{1}]$.

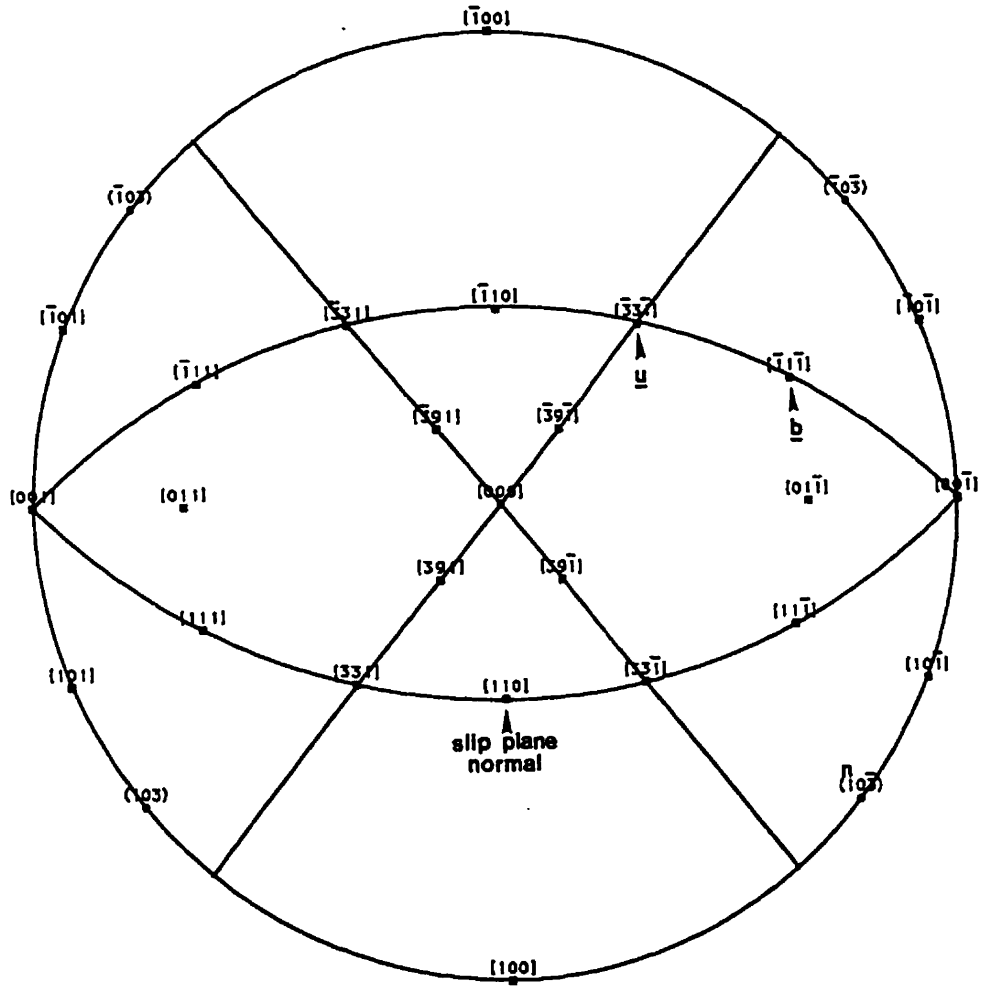

Figure A.4 [001] stereographic projection showing **u** and **b** for the dislocation studied. Also shown is the orientation information for the micrographs in Figure A.5.

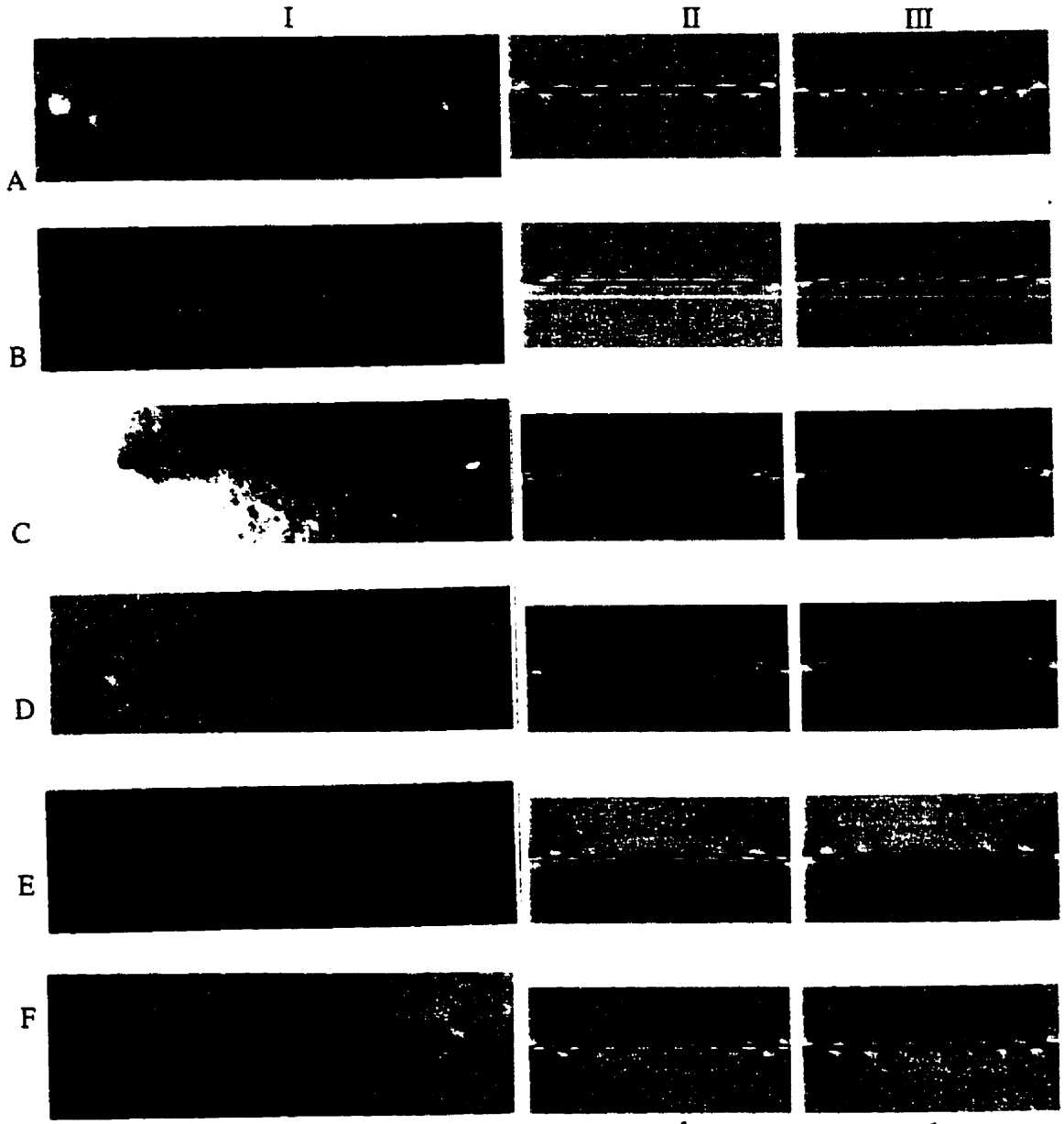

Figure A.5 Experimental and simulated images for $\mathbf{b} = \frac{1}{4}[\bar{1}\,1\,\bar{1}]$ (II) and $\mathbf{b} = \frac{1}{2}[\bar{1}\,1\,\bar{1}]$ (III) for the following diffracting conditions; (a) $\mathbf{g} = \bar{1}03$, $\mathbf{B} = 391$ and $w = 0$ (b) $\mathbf{g} = 10\bar{3}$, $\mathbf{B} = \bar{3}9\bar{1}$ and $w = 0$ (c) $\mathbf{g} = \bar{1}0\bar{3}$, $\mathbf{B} = \bar{3}91$ and $w = 0$ (d) $\mathbf{g} = \bar{1}0\bar{3}$, $\mathbf{B} = 39\bar{1}$ and $w = 0$ (e) $\mathbf{g} = \bar{1}0\bar{3}$, $\mathbf{B} = 39\bar{1}$ and $w = 0.54$ (f) $\mathbf{g} = 103$, $\mathbf{B} = 39\bar{1}$ and $w = 0.59$.

References

Alman, D.E., Shaw, K.G., Stoloff, N.S. and Rajan, K., 1992, Mat.Sci and Eng. **A155**, 85

Argon, A.S., Hori,Y. and Orowan, E., 1960, J.Am.Ceram.Soc., **43**, 86

Armstrong, R.W. and Wu, C.C., 1974, J.Am.Ceram.Soc. **61**, 102

Ashby, M.F., 1970, Phil.Mag. **21**, 399

Atkins, A.G. and Tabor, D., 1965, J.Mech.Phys.Solids **13**, 149

Bhattacharya, A.K. and Nix, W.D., 1991, Int.J.Solids Structures, **27**, 1047

Bhattacharya, B.K., Bylander, D.M. and Kleinman, l., 1985, Phys. Rev.B. **32**, 7973

Boettinger, W.J., Perepezko, J.H. and Frankwicz, P.S., 1992, Mat.Sci. and Eng., **A155**, 33

Boyarskaya, Y.S., Grabko, D.Z. and Pishkova, D.S., 1985, phys.stat.sol.(a) **87**, 175

Brewer, L.and Lamoreux, R.H., 1980, Atomic Energy Review, Special Issue #7, edited by L.Brewer (Vienna: IAEA) p.320

Brookes, C.A., O'Neill, J.B. and Redfern, B.A.W., 1971, Proc.Roy.Soc.A. **322**, 73

Brown, L.M., Khan, M.Y. and Chaudhri, M.M., 1988, Phil.Mag.A. **57**, 187

Brown, L.M., 1988, unpublished

Bull, S.J., Page, T.F. and Yoffe, E.H., 1989, Phil.Mag.Lett. **59**, 281

Cai, X., Zhou, P.N., Wagendristel, A. and Bangert, H., 1992, Scripta Met. **27**, 347

Cook, R.F. and Pharr, M., 1990, J.Am.Ceram.Soc. **73**, 787

Cotton, J.D., Kim, Y.S. and Kaufman M.J., 1991, Mat. Sci. and Eng. **A144**, 287

Daniels, F.W. and Dunn, C.G., 1949, Trans.Am.Soc.Metals **41**, 419

Dash, W.C., 1956, J. apple. Phys. **27** 1193, 1387

de'Heurle, F.M., Peterson, L.S. and Tsai, M.Y., 1980, J.appl.Phys. **51**, 5976

deWit, R., 1960, Solid State Phys., **10** 249

Dominguez-Rodriguez,A.H., Cheong, D.S. and Heuer, A.H., 1991, Phil.Mag.A **64**, 923

Evans, D.J., Court, S.A., Hazzledine, P.M. and Fraser, H.L., 1993, Phil.Mag.Lett. **67**, 331

Farber, B.Y., Chiarelli, A.S. and Heuer A.H., 1994, Phil.Mag.A **70**, 201

Fleck,N.A., Muller, G.M., Ashby, M.F. and Hutchinson, J.W., 1994, Acta metall.mater, **42**, 475

Fleischer, R.L., 1987, J. Mat. Sci., **22**, 2281

Fleischer, R.L., Dimiduk, D.M. and Lipsitt, H.A., 1989, Ann.Rev.Mater.Sci., **19**, 231

Frank, F.C., 1949, Physica **15**, 31

Frenkel, J., 1926, Z.Phys. **37**, 152

Gane, N., 1970, Proc.Roy.Soc.A. **317**, 367

Gane, N. and Cox, J.M., 1971, Phil.Mag.A. 881

Head, A.K., Humble, P., Clarebrough, L.M., Morton, A.J. and Forwood C.T., Computed Electron Micrographs and Defect Identification, North-Holland, Amsterdam (1973)

Hertz, H., 1881, J. Reine Angew. Math **92**, 156

Hertz,H., 1882, Verhandlungen des Vereins zur Betorderung des Gewerbefleisses, **61**, 449

Hill, M.J. and Rowcliffe, D.J., 1974, J.Mat.Sci. **9**, 1569

Hill, R.,1950, The Mathematical Theory of Plasticity, Oxford: Clarendon Press.

Hill, R., Lee E.H. and Tupper S.J., 1947, Proc.Roy.Soc.A. **188**, 273

Hirsch, P.B., Howie, A., Nicholson, R.B., Pashley D.W. and Whelan, M.J., Electron Microscopy of Thin Crystals, Butterworths, London (1977)

Hirsch, P.B., Pirouz,P.,Roberts, S.G. and Warren, P.D.,1985 Phil.Mag.B, **52**, 759

Hirst, W. and Howse, M.G.J.W., 1969, Proc.Roy.Soc.A. **311**, 429

Hirth, J.P. and Lothe J., Theory of Dislocations, Kreiger Pulishining Co. (1992)

Holmes, D., Heuer, A.H. and Pirouz,P., 1993, Phil.Mag.A **67**, 325

Humble, Modern Diffraction Imaging Techniques in Materials Science, eds. Amelinckx S., Gevers R., Renalt G. and Van Landuyt J., North-Holland, Amsterdam (1970)

Ito, K., Inui, H., Shirai, Y. and Yamaguchi, M., 1995, Phil.Mag.A., **72**, 1075

Johnson K., 1970, J.Mech.Phys.Solids **18**, 115

Kad, B.K., Vecchio, K.S., Bewlay, B.P. and Asaro, R.J., 1994, Mat.Res.Soc.Symp.Proc. **322**, 49

Kad, B.K., Vecchio, K.S. and Asaro, R.J., 1995, Phil.Mag.A **72**, 1

Kelly A. and Macmillan N.H., Strong Solids, Claredon Press, Oxford (1986)

Khan, M.Y., Brown, L.M. and Chaudhri, M.M., 1992, J.Phys. D: Appl.Phys. **25**, A257

Lawn, B.R. and Howes, V.R., 1981, J.Mat.Sci. **16**, 2745

Lawn, B.R. and Wilshaw, R., 1975, J.mater.Sci. **10**, 1049

Lograsso, T.A., 1992, Mater.Sci.Eng. **A155**, 115

Love, A.E.H., 1939, Quart. J. Math., **10**, 161

Ma, Q. and Clarke, D.R., 1995, J.Mat.Res. **10**, 853

Maloy, S.A., Lewandowski, J.J., Heuer, A.H.and Petrovic, J.J., 1992, Mat.Sci. and Eng., **A155**, 159

Maloy, S.A., Mitchell, T.E., Lewandowski, J.J. and Heuer, A.H., 1992, Acta metall.mater. **40**, 3159

Maloy, S.A., Mitchell, T.E., Lewandowski, J.J. and Heuer, A.H., 1993, Phil.Mag.Lett. **67**, 313

Maloy, S.A., Xiao, S-Q, Heuer, A.H., and Garrett J., 1993, J.Mater.Res. **8**, 1993

Marsh, D.M., 1964, Proc.Roy.Soc.A. **279**, 420

Meyer, E, 1908, Z.Ver.Dtsch.Ing., **52**, 645

Mitchell, T.E., Maloy, S.A. and Heuer, A.H., 1993, Critical Issues in the Development of High Temperature Structural Materials, 279

Mulhearn, T.O., 1959, J.Mech.Phys.Solids **7**, 85

Nabarro, F.R.N., 1950, Phys.Rev. **79**, 894

Nabarro, F.R.N., Theory of Crystal Dislocations

Nakamura, M., Matsumoto, S., and Hirano, T.,1990, J.Mat.Sci. **25**, 3309

Nye, J.F., 1953, Acta metall. **1**, 153

Orowan, E., 1941, Nature **147**, 452

Page, T.F., Oliver, W.C. and McHargue, C.J., 1992, J. Mater.Res., **7**, 1992

Pearson, W.B., The Chemistry and Physics of Metals and Alloys, New York: Wiley, p.589 (1972)

Pethica, J.B. and Tabor, D., 1979, Surf.Sci., **89**, 182

Rao, S.I., Dimiduk, D.M.and Mendiratta, M.G., 1993, Phil.Mag.A. **68**, 1295

Samuels, L.E. and Mulhearn, T.O., 1957, J.Mech.Phys.Solids **5**, 123

Sargent, P.M. and Page, T.F., 1985, J.Mater.Sci. **20**, 2283

Schmid, E. and Boas, W., 1950, Plasticity of Crystals, London, F.A. Hughes & Company p.105

Seitz, F., 1950, Phys.Rev. **79**, 723

Shaffer, P.T.B., Plemum Handbook of High-Temperature Materials, No. 1, Materials Index, New York: Plenum Press (1964)

Smakula, A. and Klein, M.W., 1949, J.Opt.Soc.Amer. **39**, 445

Stilwell, N.A. and Tabor, D., 1961, Proc.Phys.Soc.Lond. **78**, 169

Svechnikov, V.N., Kocherzhinskii, Y.A. and Yupko, P.S., 1970, DAN Ukr. SSR **A6**, 85

Swain, M.V. and Lawn, B.R., 1969, phys.stat.sol. **35**, 909

Tabor, D. 1951, The Hardness of Metals, Claredon Press, Oxford

Thomas, O., Senateaur, J.P., Madar, R.,Laborda, O. and Resencher, E., 1985 Solid State Comm. **55**, 629

Umakoshi, Y., Hirano, T., Sakagami,T. and Yamane, T., 1989a, Scripta Met. **23**, 87

Umakoshi, Y., Sakagami, T., Yamane, T. and Hirano, T., 1989b, Phil.Mag.Lett. **59**, 159

Umakoshi, Y., Sakagami, T., Hirano, T. and Yamane, T., 1990, Acta metall.mater. **38**, 909

Unal, O., Petrovic, J.J., Carter, D.H. and Mitchell, T.M., 1990, J.Am.Ceram.Soc. **73**, 1752

Vahldiek, F.W. and Mersol, S.A., 1968, J.Less.Comm.Metals **15**, 165

van Ommen, A.H., Reader, A.H. and deVries, J.W.C., 1988, J.Appl.Phys., **64**, 3754

van Tendeloo, G. and Amelinckx, S., 1974, phys.stat.sol. **22**, 621

Vasudevan, A.K. and Petrovic, J.J., 1992, Mater. Sci. Engn. **A155**, 1